Øyvind Sunde Sortland

Boron removal from silicon by steam and hydrogen

◨ NTNU

Norwegian University of
Science and Technology

This work is dedicated to beings suffering from climate change
and anyone who does not yet enjoy energy security.

Abstract

Solar cells are among the most promising technologies for development of sustainable power generation in terms of environmental impact and resource availability, and crystalline silicon cells dominate the present market expansion. Cost reductions are still necessary for this technology to become a major global energy producer. Development of metallurgical refining processes for solar grade silicon has potential to drastically decrease energy consumption, but face challenges to effectively remove the important impurities boron and phosphorus. For boron removal, refining by an oxidizing reactive gas show potential for low energy consumption and promising refining rates.

Previous investigation of reactive gas boron removal is limited, while related plasma refining has been developed to pilot scale. This experimental study seeks to reveal the potential and limits of reactive gas refining for boron removal. First and foremost at a fundamental level to understand the removal process and what determines the rate of removal. Boron was removed from high-purity silicon and metallurgical grade silicon at 1500-1800 °C by blowing steam in hydrogen and/or argon onto the melt surface. The rate of boron removal was calculated from inductively coupled plasma mass spectrometry analyzes of the boron content in samples periodically extracted from the melt. The fastest rate of boron removal was achieved at the highest gas flow rate. Increasing the partial pressure of steam was also found important to increase the removal rate and simultaneously reduce gas consumption.

Supply of steam as the oxidizing agent to the interface is the only identified rate determining step for boron removal, like for active oxidation of silicon to SiO gas at the interface. At least 50% of the steam in the feed did not reach the surface in representative experiments and this is attributed to essentially stoichiometric Reactions (0.1) in the gas and (0.2) for active oxidation of silicon at the interface. Diffusion of steam accounts for increasing losses with increasing gas flow rate. The fraction of steam in the feed gas that was supplied to the melt surface was estimated by comparing weightloss by active silicon oxidation in experiments to equilibrium in Reaction (0.2) if all of the feed gas had reacted.

$$H_2O + SiO = SiO_2 \text{ (s)} + H_2 \tag{0.1}$$

Boron removal in experiments was found to proceed at equilibrium between HBO in the gas flow and boron in the melt, which was determined from the estimated supply of steam to the interface Reactions (0.2) and (0.3). No resistance was identified for the mass transfer of boron as such.

$$H_2O + [Si] \rightleftharpoons SiO + H_2 \tag{0.2}$$
$$[B] + SiO + \tfrac{1}{2} H_2 \rightleftharpoons HBO + [Si] \tag{0.3}$$
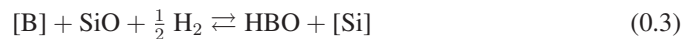
Equilibrium at the interface also agreed with observations that silica passivation forms if the steam supply is above the saturation pressure of SiO in Reaction (0.4). Silica formed continuous layers and stopped boron removal if formed on the entire surface. A clean melt surface could be maintained with steam partial pressures less than twice the saturation pressure of SiO at the temperature of the melt. Additionally, CO reacted to SiC particles on the surface and was found less effective for boron removal than steam. Atmospheric partial pressure of steam was tested at $1800\,^{\circ}\mathrm{C}$, and exploration of such conditions is suggested for further developments.

$$2\,\mathrm{SiO} \rightleftarrows [\mathrm{Si}] + \mathrm{SiO_2}\ (\mathrm{s/l}) \tag{0.4}$$

Preface

This thesis is submitted to the Norwegian University of Science and Technology (NTNU) for partial fulfillment of the requirements for the degree of philosophiae doctor.

This doctoral work has been performed mainly at the Department of Materials Science and Engineering (DMSE), NTNU, Trondheim, with Merete Tangstad as main supervisor. The work was carried out from August 2011 until August 2015, including teaching duties at NTNU. Part of the work was carried out at the group Elaboration par procédés magnétiques (EPM) at the laboratory Science et Ingénierie des Matériaux et Procédés (SiMaP) in Grenoble, France, between October and December 2014, with travel grant from Håkon Styris Fond.
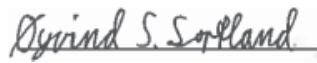
Experiments and use of models have been conducted by the author. Used models have been developed by Kai Tang at SINTEF (description in Section 3.6.1), the author (Section 3.6.2 and in part Mark William Kennedy (DMSE) (Section 3.6.3). ICP-MS analyzes were conducted by Syverin Lierhagen at Department of Chemistry, NTNU. Samples were prepared in collaboration with Torild Krogstad (DMSE). Microprobe analyzes in Section 4.5 (except 4.5.1) were conducted in collaboration with Morten Peder Raanes (DMSE), and SEM imaging in Section 4.5.1 was conducted in collaboration with Yingda Yu (DMSE).

During the course of the doctoral work, parts have been presented at the following Norwegian and international conferences.

1. Prospects of Using Syngas for B Removal from Si. *UMG-Silicon seminar*, Trondheim-Tromsø, April, 2012.

2. B Removal from Si by Reactive Gas Refining. *Nasjonal Konferanse for Materialteknologi*, Trondheim, May, 2012.

3. Removal of Boron from Silicon by Reactive Gas Refining, *TMS 2013 142ndANNUAL MEETING & EXHIBITION*, San Antonio, March, 2013.

4. Boron Removal from Silicon Melts by H_2O/H_2 Gas Blowing - Gas-phase Mass Transfer. *TMS 2014 143rd ANNUAL MEETING & EXHIBITION*, San Diego, February, 2014.

5. Boron Removal from Silicon Melts by H_2O/H_2 Gas Blowing - Steam Supply and Boron Removal. *Norwegian Solar Cell conference*, Son, May, 2014.

6. Boron Removal from Silicon Melts by H_2O/H_2 Gas Blowing - Mass Transfer in Gas and Melt. *Nasjonal Konferanse for Materialteknologi NMS+NMF Sommermøte*, Oslo, June, 2014.

Results of experiment and modeling in Sections 4.1.3-4.1.7 and 4.1.9 have been used in the paper "Boron Removal from Silicon Melts by H_2O/H_2 Gas Blowing - Mass Transfer in Gas and Melt", published in *Metal. Mater. Trans. E*, 1(3):211-225, 2014, together with modeling in Section 5.4.2. The results in Section 4.1.2 have been discussed similarly to Section 5.4.1 in the paper "Boron Removal from Silicon Melts by H_2O/Ar Gas Blowing", submitted for publication in *Metal. Mater. Trans. B*. Abstract of these papers are included in Appendix A.

Øyvind Sunde Sortland
Trondheim, August 17, 2015

Acknowledgements

Contents

List of Tables

xii

List of Figures

xiv

List of Symbols and Abbreviations

A	Area (of reaction).
A_c	Area of free horizontal cross-section in crucible.
C	Concentration.
ΔC	Driving force.
C_4	Concentration in gas flow out of system.
$C_{[j]}$	Concentration of "j" in bulk melt.
C_b	Concentration in bulk gas (flow over surface).
C_{eq}	Concentration for equilibrium (modeling).
C_i	Concentration around interface.
D	Diffusion coefficient.
E	Enrichment ratio.
E_a	Activation energy.
$\Delta G^{\ominus}$	Gibbs free energy of reaction at standard state.
H	Height of lance exit above melt surface.
$\Delta H^{\ominus}$	Enthalpy of reaction at standard state.
$\Delta_f H^{\ominus}$	Enthalpy of formation at standard state.
$\Delta_{trs} H^{\ominus}$	Enthalpy of transition at standard state.
J	Flux.
K	Equilibrium constant.
L	Characteristic length.
M	Molar mass (of silicon melt).
Q	Total gas flow rate.
R	Gas constant ($8.314\ \mathrm{J/mol/K}$).
Re	Reynolds number.
$S^{\ominus}$	Entropy at standard state.
$\Delta S^{\ominus}$	Entropy of reaction at standard state.
$\Delta_{trs} S^{\ominus}$	Entropy of transition at standard state.
Sc	Schmidt number.
Sh	Sherwood number.
T	Temperature (of melt).
T_Q	Temperature at condition of gas flow rate ($293\ \mathrm{K}$ for Q in [l_N/min]).

U	Uncertainty at approximately 95% confidence level.
U_r	Relative uncertainty at approximately 95% confidence level.
V	Volume (of melt).
Θ	Angle.
α_{j}	Reaction order (apparent for "j" in feed).
$\alpha_{\mathrm{H_2O}}^s$	Reaction order for steam supply to interface reactions.
$\alpha_{eq,\mathrm{j}}$	Reaction order for "j" in interface reactions for equilibrium (modeling).
δ	Boundary layer thickness.
γ	Activity coefficient.
γ^0	Activity coefficient at infinite dilution.
μ	Dynamic viscosity.
ρ	Density (of silicon melt).
σ_r	Relative standard error.
τ	Mean exposure time of eddy currents.
$\frac{k_t}{k_{eq}}$	Gas utilization, equivalently $\frac{p_{4,\mathrm{HBO}}}{p_{eq,\mathrm{HBO}}(p_{\mathrm{H_2O}})}$.
ζ	Distance above interface as fraction of boundary layer thickness ($\zeta = \frac{z}{\delta}$).
Δc_p	Heat capacity change of reaction at constant pressure.
d	Inner diameter of lance (at exit).
d_c	Inner crucible diameter.
e_r	Relative error.
k	Mass transfer coefficient.
k_0	Frequency factor.
k_1	Mass transfer coefficient for step 1 (in melt).
k_2	Rate constant for step 2 (reaction at interface).
k_3	Mass transfer coefficient for step 3 (diffusion into gas).
k_4	Mass transfer coefficient for step 4 (gas flow out of system).
k_{HBO}	Fluid dynamic mass transfer coefficient for diffusion of HBO gas in step 3.
k_{eq}	Mass transfer coefficient in equilibrium simulation using feed gas.
$k_{eq}(p_{\mathrm{H_2O}}^s)$	Mass transfer coefficient in equilibrium simulation using steam supply ($p_{\mathrm{H_2O}}^s$).
k_t	Total mass transfer coefficient for boron removal.
m	Mass (of melt).
$-\Delta m$	Weightloss of charged crucible during experiment (by active silicon oxidation).
$-\Delta m_{eq}$	Silicon weightloss using feed gas in equilibrium simulation (for interface).
n	Amount of substance.
$\frac{\mathrm{d}n}{\mathrm{d}t}$	Rate (of removal).
$\frac{\mathrm{d}n_{\mathrm{H_2O}}}{\mathrm{d}t}$	Rate of steam feeding.
$\frac{\mathrm{d}n_{\mathrm{H_2O}}^s}{\mathrm{d}t}$	Rate of steam supply to interface.

p	Pressure (total).
$p^{\ominus}$	Standard pressure (1 bar).
p^{sat}	Saturation pressure.
$p^s_{H_2O}$	Part of the partial pressure in feed that is supplied to interface.
p_4	Partial pressure in gas flow out of system.
p_j	Partial pressure of "j" (in feed).
p_b	Partial pressure in bulk gas (flow over surface).
p_{eq}	Partial pressure for equilibrium (modeling).
p_i	Partial pressure around interface.
r	Radius (from center of melt surface).
r_c	Inner crucible radius.
r_s	Radius at end of stagnation region.
r_w	Radius at end of wall jet region.
t	Time.
$t_{1/2}$	Half-life (of removal).
t_r	Duration of reactive gas blowing.
u	Standard uncertainty.
v	Velocity.
x	Mole fraction.
x_4	Mole fraction in gas flow out of system.
$x_{[j]}$	Mole fraction of "j" in bulk melt.
x_{hyp}	Mole fraction for hypothetical bulk equilibrium.
x_i	Mole fraction around interface.
$\frac{x_{HBO}}{x_{[B]}}$	Distribution coefficient for boron between melt and gas.
z	Distance normal from interface.
BSE	Back-scattered electrons.
CFD	Computational fluid dynamics.
DMSE	Department of Materials Science and Engineering.
EDS	Energy dispersive X-ray spectroscopy.
EG	Electronic grade.
ICP-MS	Inductively coupled plasma mass spectrometry.
MG	Metallurgical grade.

MHD   Magnetohydrodynamic.

NEDO   New Energy and Industrial Technology Development Organization.
NTNU   Norwegian University of Science and Technology.

SEM   Scanning electron microscopy.
SoG   Solar grade.

WDS   Wavelength dispersive X-ray spectroscopy.

Chapter 1

Introduction

1.1 Problem Outline

Global warming and predictions of increasing energy consumption and diminishing fossil fuel resources have initiated a search for environmentally friendly and renewable energy sources. Solar energy is considered one of the most attractive sources for viable energy production, both in terms of environmental impact and resources [1]. Lorenz et al. [2] predicted the average annual growth of roughly 30%-35% in installed global solar power capacity from 2008 to 2020. The photovoltaic market is dominated by silicon solar cells. An important limitation to the industrial expansion is the production costs compared to electricity output. Reduced production costs are necessary to realize the potential photovoltaic systems have to become a major source of electric energy as predicted in Figure 1.1 based on the vast and renewable resources of solar energy.

Production of solar grade silicon (SoG-Si) accounts for 25% of the production costs of photovoltaic panels with multicrystalline silicon and 40% of monocrystalline silicon systems [3], and remains the largest cost component of solar cells SEMI [4]. The potential for reducing costs in this part of the value chain is particularly large as the photovoltaic industry has a tradition of using waste from the electronic industry. In addition to the high production costs of electronic grade silicon (EG-Si), the amount of silicon from this source is no longer sufficient for the photovoltaic industry. Accordingly, the photovoltaic industry has started to make use of metallurgical processes for producing SoG-Si [4]. SoG-Si has a target purity in the order of 99.9999% (6N) while the purity of EG-Si is approximately 9 nines. Different impurity elements have different impact on the efficiency of solar cells. Boron and phosphorus are used for p- and n-type doping and control of their amounts is vital for solar cell operation. The impurities in SoG-Si should be less than $0.3 \ \mathrm{ppmw}$ boron and $0.1 \ \mathrm{ppmw}$ phosphorus [5]. Since highly efficient solar cells can be achieved with SoG-Si, the expensive Siemens process used to upgrade metallurgical grade silicon (MG-Si) of 95-99% purity [6] has become sub-
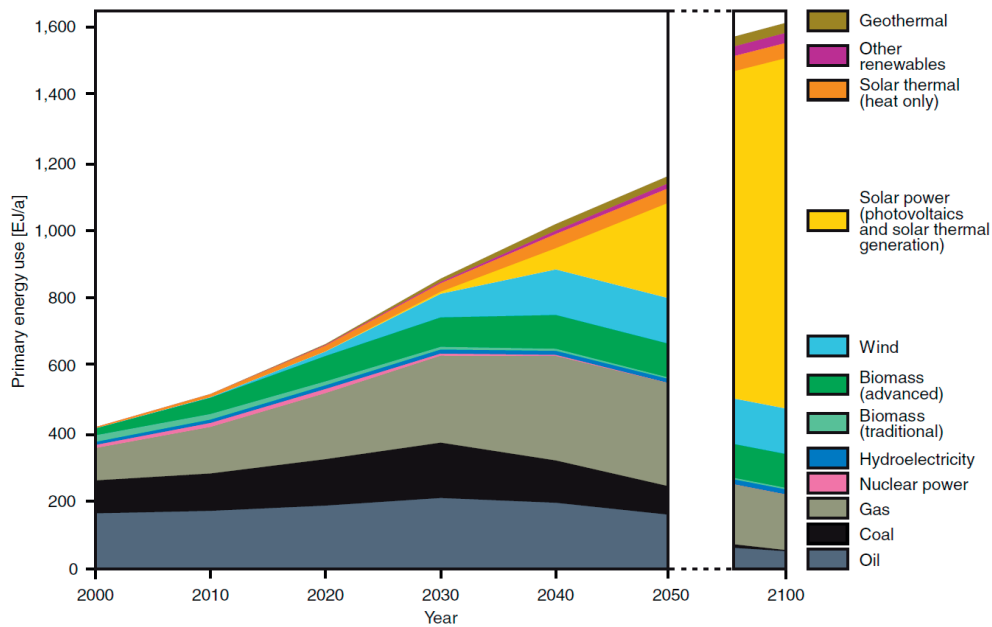
Figure 1.1: Predictions by Graßl et al. [1] of different energy technologies' contribution to meet future global energy demands.

ject to modification. These processes are represented by the chemical route in Figure 1.2, in which Delannoy [7] summarized the production routes to solar cells. Furthermore, emerging technologies for SoG-Si production have been developing, and metallurgical routes aim to significantly reduce the cost of purification of MG-Si with sufficient purity for solar cells. Metallurgical processes are also typically suitable for large scale production. An important development challenge for metallurgical processes lies in achieving sufficient purity of the product material.

The Siemens process converts silicon to silanes using HCl. After redistribution and distillation of the silanes, they are decomposed to pure polysilicon by chemical vapor deposition. Modifications to the Siemens process aim to reduce the energy consumption and increase silicon yield. REC has developed a fluidized bed reactor which allows at least 30% reduction of costs for SoG-Si production and Tokuyama Corporation has developed a vapor to liquid deposition technique for increased throughput [8].

In metallurgical routes, MG-Si is purified in its elemental form. It avoids formation and handling of toxic and potentially explosive chlorosilane compounds. Furthermore, the energy consumption has been lowered to one fifth of that of the traditional Siemens process [8], which significantly lowers production costs compared to chemical routes. Several processes

2
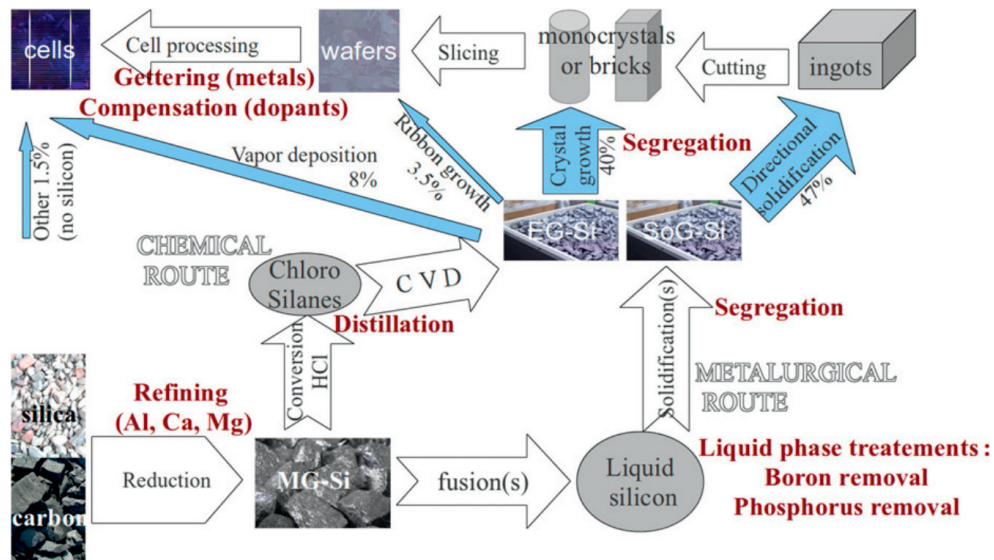
Figure 1.2: Overview by Delannoy [7] of routes for production of solar cells. Metallurgical grade silicon produced by reduction of quartz with carbon materials is predominately refined in a chemical route and emerging metallurgical routes, of which boron removal is studied in this work.

have been developing. The SOLSILC and SPURT projects investigated utilization of pure quartz and carbon raw materials in silicon production to obtain a pure product, and FESIL had a pilot plant for this purpose. Elkem Solar has an industrial plant for upgrading of MG-Si using slag treatment, leaching and directional solidification at a scale of $6000 \, \mathrm{tonne/year}$ [9]. New Energy and Industrial Technology Development Organization (NEDO) and Kawasaki Steel Corporation in Japan had in 2004 developed a process involving electron beam melting in vacuum for phosphorus removal, plasma treatment for boron removal and two directional solidification steps [8, 10, 11]. A similar process utilizing plasma refining and directional solidification steps has also been developed to pilot scale in the PHOTOSIL project in France [12], subsequent to the Joule-III ARTIST project that studied plasma refining with electromagnetic stirring of the melt [13]. The PHOTOSIL route [12] used feedstock of upgraded MG-Si, partially purified by one directional solidification process. After optimization of the process, $0.3 \, \mathrm{ppmw}$ boron was achieved and solar cells demonstrated 16.4% average efficiency [14] in 2010. In the PVMaT (Photovoltaic Manufacturing Technology) project, Khattak et al. [15] at Crystal Systems had in 2001 developed a pilot scale furnace for reactive gas and slag refining of up to $300 \, \mathrm{kg}$ silicon. They ended the process with directional solidification before test solar cells were made with efficiencies of 7.3%, and 13.5% for subsequent Czochralski crystallization.

1.1.1   Boron Removal in Metallurgical Silicon Refining

Directional solidification efficiently removes metal impurities due to their low solubility in solid compared to liquid silicon. This is not the case for phosphorus and boron due to their high segregation coefficients of respectively 0.35 and 0.8 [16], and research has focused on removal of these elements [3]. Phosphorus is volatile compared to silicon and can be evaporated by vacuum treatment of molten silicon, like in the NEDO route. The vapor pressure of boron is however lower than that of silicon and boron can not be removed by direct evaporation. As such, dedicated processes are developed to remove boron, which includes the topic of this thesis.

Boron is typically removed by oxidation, either to form a slag compound like in the Elkem process or volatile compounds like in the NEDO and PHOTOSIL and PVMaT projects. Both reactive gas and plasma refining removes boron to volatile compounds, and experiments of reactive gas refining are reported in this thesis. The difference is that plasma refining used a plasma torch to blow highly reactive species like radicals onto the silicon surface, which is depicted in Figure 1.3, while reactive gas refining does not superheat the gas and may use lances for blowing [17] or bubbling the gas through the melt [15]. The reactive species in a plasma can generally form non-equilibrium products, but Altenberend [18] argued that equilibrium products are formed in plasma refining experiments like in reactive gas experiments, and that the radicals does not make a difference for boron removal. On this basis, literature on plasma refining is included in this thesis to supplement the scarce literature on reactive gas refining. The temperature of the melt is typically not much higher than the melting point and below 1600 °C [11], and few vol% steam or oxygen are most frequently used with hydrogen and/or argon at atmospheric pressure (summarized in Table 2.4). This work studies boron removal in reactive gas refining experiments.

In slag refining at 1600 °C, Jakobsson [19] found the distribution coefficient between the slag and the melt boron contents at final equilibrium to be around 2 for silicate slags with magnesia and calcium oxide. Accordingly, a high-purity slag is required to reduce the boron content below 0.3 ppmw in SoG-Si, and large amounts of slag is required for refining of MG-Si, which typically contain more than 5 ppmw boron [5]. Slag refining is typically studied in batch experiments with slag and silicon resting in a crucible, for which Nishimoto and Morita [20] reported a mass transfer coefficient of 1.4 μm/s for the kinetics of boron removal from silicon to $CaO\text{-}SiO_2$ slags at 1550 °C. They found the rate of boron removal to be limit by diffusion in the slag, correlating to relative high viscosities of silica-containing slags. Consequently, there is a possibility for achieving increased refining rates by boron removal to gas, and reactive gas and plasma refining typically achieve mass transfer coefficients for boron removal above 10 μm/s (summarized in Figure 2.3). Elkem [21] has developed a technical solution for semi-continuous slag refining, in which slag can flow out of the reactor and any amount of slag can be used over time. The flow of slag in the semi-continuous reactor by Elkem [21] may also be expected to increase the mass transfer and rate of boron removal.
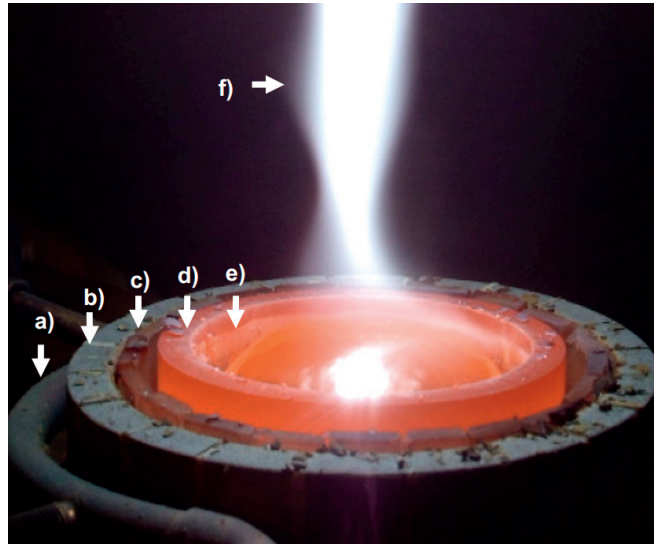
Figure 1.3: Image of plasma refining (Altenberend [18]), including a) induction coil, b) segmented cold crucible, c) thermal insulating silica plates, d) graphite crucible, e) molten silicon, f) plasma.

Reactive gas and plasma refining also benefit from semi-continuous operation with a flow of gas through the furnace holding the melt, as large amounts of gas is used for boron removal. For pilot scale plasma refining in the NEDO project, Nakamura et al. [11] used flow rates of argon and hydrogen up to a total of $4.26\ m_N/min$. They refined 300 kg silicon from 8 ppmw to 0.3 ppmw boron in 4.5 h with 50.6 vol% hydrogen and 4.3 vol% steam, for which a total gas consumption calculates to $579\ m_N^3$ of both argon and hydrogen.

In principle, there is no final equilibrium in the open system represented by gas flow through the furnace, and any SoG-Si purity target for boron can be achieved in a single process step by blowing enough gas for long enough time, regardless of the initial boron content of the feedstock. Boron impurities in the feed gas and dissolution of boron impurities in the crucible into the melt can however be expected to cause a low boron content at final equilibrium in practice. Such limitations have not been reported in experiments. Gas reactant are readily available in high purity, and dedicated purification techniques have not been necessary for reactive gas refining or plasma experiments. Instead the final boron content can be determined by the economics of gas consumption, silicon loss and throughput, as the boron content follows the law of exponential decay over time. Khattak et al. [15] demonstrated reactive gas refining of highly doped EG-Si scrap with about 20-150 ppmw boron to below 0.4 ppmw, and they proposed that the process could make doped EG-Si scrap available as a low-cost silicon feedstock, which in 2001 was available at a scale for solar cell production of

100-200 MW/year. They also refined MG-Si with $5 - 50$ ppmw boron to 0.1 ppmw boron by reactive gas refining.

For economic reasons, it is desirable to minimizing costs related to gas and energy consumption as well as maximize the refining rate and throughput. For plasma refining by Nakamura et al. [11] with 300 kg melt, Altenberend [18] assumed the 650 kW plasma torch to dominate the energy consumption, and neglected the energy for heating the melt in an economic evaluation. Reactive gas refining thus appear favorable in terms of energy consumption, which is not further assessed in this thesis. For plasma refining of 300 kg silicon from 8 ppmw to 0.4 ppmw boron by Nakamura et al. [11], Altenberend [18] calculated an electricity cost of 1.3 €/kg. The cost of argon and hydrogen gas was estimated to 2.50 €/kg and 2.40 €/kg, respectively, assuming 1 €/m$_N^3$ costs for both gases. Gas consumption was estimated to the largest operational cost (excluding labor costs). Optimizing the gas composition will thus be important for development towards an industrial process of reactive gas refining. Khattak et al. [22] proposed that their process with boron removal by steam in reactive gas refining, phosphorous removal by slag treatment and finally directional solidification, could be implemented in a MG-Si production plant at a scale of 1000 tons/year with variable costs of SoG-Si production of \$7.62/kg.

Khattak et al. [22] also tested simultaneous refining with slag and gas bubbling and found it to be beneficial for the removal rate. They attributed this to increased stirring by injection and the possibility of sequential reactions like segregation of impurities to slag and subsequent volatilization. Nishimoto and Morita [20] found that chlorine gas blowing removed boron from CaO-SiO$_2$ slags, but not directly from silicon, and proposed the possibility of removing boron through a slag to chlorine gas. Similarly, Bjerke [23] found the efficiency of slag refining to increase in a hydrogen atmosphere. When combining slag and plasma treatment, Suzuki et al. [24] found plasma treatment to be more effective for boron removal than slag treatment with silicates of alkaline earth metals. Suzuki et al. [25] observed about 20% increased boron removal with up to 10 weight% CaF$_2$ additions to the silicon melt, possibly by formation of BF$_3$ or BOF gases.

Other gases than steam, oxygen and hydrogen have also been explored for removal of boron directly to gas. Suzuki et al. [25] found boron removal with low fractions of CO$_2$ in argon plasma to be as efficient as with oxygen, while the removal rate was faster with steam. A reactive gas of HCl has also been studied thermodynamically by Yvon et al. [26]. Based on a thermodynamic study, they expected boron to form volatile species of mainly BCl$_2$H, BCl, BCl$_2$ and BClO. Contradictory to the thermodynamic calculations, the ratio of B/Si in the gas flow out of the furnace was significantly lower with HCl compared to oxygen and hydrogen in plasma experiments. This was due to a dramatic increase in silicon volatilization, but only a weak increase in boron volatilization with increasing HCl flow rate. Ammonia was used as reactive gas at low pressure for refining of MG-Si by Van Den Avyle et al. [27]. Ammonia was found ineffective for boron removal, possibly due to formation of solid boron nitride that re-dissolved into the melt.

1.2 Motivation

While removal of boron from silicon to gas is an attractive semi-continuous process for the metallurgical production route to SoG-Si, it has not been extensively explored. Theuerer [28] first observed that boron could be removed by steam and hydrogen gas during zone refining in 1956. However, plasma refining was first started to be developed as a dedicated process in the late 1980's [29]. Gas was not used again until the turn of the century [15]. Experiments of gas blowing onto the melt surface [17] have revealed that also reactive gas refining can achieve high rates of boron removal like plasma refining. It was recently found that the rate of boron removal was higher in experiments than what could be expected from tabulated thermodynamic data [30]. The present work explores this discrepancy further by estimating the fraction of steam in the feed gas that actually reacts with the melt surface.

Further study is also desirable in order to complement and unify the literature regarding the kinetics of boron removal in the process in terms of what limits the rate of boron removal to gas. The rate has been proposed to be limited by diffusion and convection of boron in the melt without stirring [25]. With induction stirring however, mass transfer in the melt is found to be fast [11, 18] compared to the net rate of boron removal in plasma experiments. Altenberend [18] found that the effect of hydrogen and temperature on the boron removal rates in reactive gas refining by Nordstrand and Tangstad [17] and in plasma refining experiments were consistent with equilibrium for the reactions at the melt surface. He proposed that the rate of boron removal is limited by supply of steam to the interface reactions. Steam supply through the mechanism of active oxidation of silicon is considered in this work and estimated in experiments. So far, low fractions of steam have been used in experiments, as transition to passive oxidation with formation of silica at the melt surface has proved detrimental to the process Alemany et al. [13]. The threshold steam content and ways to increase it is also assessed in this work.

The study of process kinetics focuses on assessing what limits the refining rate in experiments. Experimental parameters are varied separately to identify which have an important effect on the refining rate. Furthermore, the dependencies between the removal rate and experimental parameters are compared to relevant theory and models of individual steps in the process kinetics. Knowledge of the process kinetics and how the removal rate depend on different experimental parameters is a basis for optimizing the removal rates, the time required for removing boron to a specified target and the throughput of the process. Additionally, the degree to which the reactive gas is utilized in reactions provides a measurement for the loss due to kinetic limitations. Conceptually, the reactive gas can be fully utilized to equilibrium during the passage of gas at a low gas flow rate, although this may require a long time for supplying all the gas necessary to reach the targeted boron concentration in the melt. The refining rate can be increased by increasing the gas flow rate, but kinetic limitations will eventually take effect at which equilibrium may no longer be approached during the passage of gas. The gas utilization starts to reduce and gas consumption in practice becomes higher

than the thermodynamic minimum.

The first reactive gas experiments at NTNU by Nordstrand and Tangstad [17] serves as the basis for the present experimental work. Gas blowing appears suitable for the large amounts and flow rates of gas used for boron removal. Although the reaction area and residence time available for gas-melt reactions can be increased by bubbling the gas through the melt, the risk of splashing represent a practical limit to the flow rate. This might rationalize why Khattak et al. [15] obtained significantly lower rates with bubbling compared to blowing the gas or plasma onto the melt (Table 2.4 show comparison to plasma refining by Einhaus et al. [12] for the same scale of $60\,\mathrm{kg}$ melt). Splashing of droplets into the gas at high flow rate could however be favorable for the removal rate and gas utilization, and development of an experimental setup for this purpose is proposed for further work. The rate of removal of boron across the surface of the melt is directly dependent on the available surface area, but also the kinetic limitations may change between different experimental setups, scales and ranges of experimental parameters. The rates and kinetic limitations may thus not be directly comparable between different facilities, so the focus is on the effects of experimental parameters and assessing theory and models for process kinetics, which can set a basis for further development towards an industrial process.

1.2.1 Research Questions

The PhD project is part of the research project Pure Silicon Production using Natural Gas (ReSiNa), which investigates the possibility to utilize natural gas in metallurgical production of SoG-Si and other silicon materials. Thus, the potential of natural gas or its derivatives for boron removal in SoG-Si production is investigated first. To provide boron removal by oxidation, CO and hydrogen (in syngas) is used as reactive gases, and compared to steam and hydrogen. In this respect, selecting reactive gases according to research question one (RQ1) in the list below is the starting point for the PhD project.

The selected gas system for boron removal is further studied to develop a knowledge base on which the reactive gas refining process can be improved for industrialization. This includes defining important reactions (RQ2) and investigate the kinetics of these (RQ3-4) in terms of varying experimental parameters (RQ5-6). The potential for optimization (RQ6) are revealed by exploring experimental limits, predominately for formation of an inhibiting surface layer (RQ7) and possibilities of circumventing or minimizing its effects to further increase the boron removal rate (RQ8).

RQ1 Is CO and hydrogen suitable for boron removal in SoG-Si production, as compared to a reactive gas of steam and hydrogen?

RQ2 Which reactions are important for boron removal and byproduct formation?

RQ3 What limits the rate of boron removal from silicon to gas?

RQ4 How does the rate of boron removal depend on gas composition?

RQ5 What experimental parameters are important for the rate and efficiency of boron removal?

RQ6 How does important experimental parameters influence the rate of boron removal and surface coverage, and how can boron removal be optimized?

RQ7 What are the limitations for surface coverage by byproducts in reactive gas refining?

RQ8 How can inhibition by surface layer formation be minimized or prevented?

1.3   Thesis Outline

Theoretical background regarding thermodynamics and relevant kinetic theory is reviewed in Chapter 2. It includes thermodynamic considerations and equilibrium modeling relevant for boron removal from silicon to a gas phase with emphasis on reactive gases of steam and hydrogen, but also considering CO. The refining rate is further defined as used in the thesis, and a distinction is drawn between the terms rate and kinetics. A literature review of refining rates achieved in reactive gas and related plasma refining experiments follows. An overview of process kinetics is presented and relevant theory for mass transfer through each step of boron removal is presented with emphasis on the expected effect of experimental parameters on the mass transfer coefficient. The theories are combined to a total mass transfer coefficient for boron removal. Finally, supply of steam and oxidation of silicon is considered, including passivation by silica formation on the surface.

Chapter 3 presents the experimental setups and procedures for reactive gas refining and lists the variation of parameters in different experimental series. Furthermore, the method for preparation and inductively coupled plasma mass spectrometry (ICP-MS) analysis of samples extracted from the melt during experiments are presented, and also preparations and microprobe analysis to investigate the silicon surface after experiments. Calculations of mass transfer coefficients from boron concentrations in samples and uncertainty are presented, and finally models used for comparison and discussion of experimental results.

Experimental results and their uncertainties are presented in Chapter 4. Experiments in which an experimental parameters is varied are compared, firstly in terms of boron concentration over time and secondly in terms of mass transfer coefficients and gas utilization compared to equilibrium modeling. Also the weightloss of the crucible during experiments was measured to assess loss of silicon in the most recent experimental series. Observations of passivation and threshold steam partial pressures are presented and solid byproducts are characterized after experiments.

The results from Chapter 4 are further used in discussions of process kinetic theory in Chapter 5. Silicon loss is compared to equilibrium modeling and incorporated in the assessment of

boron removal. The mass transfer coefficients are plotted as function of individual parameters varied in experimental series, and the dependencies are compared to theory in Chapter 2 and models. Finally, the understanding of process kinetics in the experiments is incorporated in an overview of the refining process. Main conclusions are summarized in Chapter 6 together with suggestions for further development.

Chapter 2

Theory and Literature

The general principle of metallurgical refining of silicon is extraction of the impurity elements into a phase that can be separated from silicon and does not itself introduce significant amounts of impurities into silicon or take up a large fraction of the silicon melt. The latter reduces the recovery of silicon and thus the throughput of the refining process.

An oxidizing agent (compared to boron) is used to extract boron by oxidation. Silicon may be completely oxidized to SiO_2 as a stable phase and boron may to B_2O_3, which is utilized in slag refining. Reactive gas and plasma refining relies on partial oxidation to gas species, for which boron form various boron suboxides with and without hydrogen as well as boron hydrides form volatile molecules as modeled in Section 2.1. There is an inconsistency in the literature as to which is the principal gaseous product of boron oxidation (Table 2.4). Increased removal rates achieved by introducing hydrogen in the oxidizing gas and thermodynamic modeling with re-evaluated data for the HBO stability [30] suggests HBO to be dominant. Silicon may be partially oxidized to SiO gas, which is sufficiently stable at the high temperatures of silicon melt ($> 1414\,°C$) to allow a practical operational window in terms of the partial pressures of oxidizing gases like steam, CO and oxygen in which the silicon surface remains clean and exposed to the gas. Formation of SiO does however represent a loss of silicon from the melt, and is found to be a thermodynamic requirement for removal of boron to gas. HBO is more stable than SiO at refining temperatures, and refining is possible as boron can be enriched in the gas (achieve a higher concentration ratio of boron to silicon in the gas than in the melt as explained in Section 2.1.4). However, most of the oxidizing agent reacts with silicon as the host material in the melt and not with boron at comparably low impurity contents.

In experiments, the rate of boron removal consistently follow a first order rate law (Section 2.2), with exponential decay of the rate as the boron content in the melt is gradually reduced. The state of the art is summarized in terms of refining rates achieved in previous reactive gas and plasma refining experiments. The main focus is on process kinetics, for which an overview of mass transfer steps for boron removal from the melt to the gas is presented in Section 2.3 for the experimental setup of gas blowing. Section 2.3 also defines the open

system from which boron leaves with the gas flow. Diffusion of boron from the melt to the interface is enhanced by convection in the melt as shown in Section 2.3.1. In the first study of reactive gas refining with steam in hydrogen, Theuerer [28] proposed boron to be removed in reactions at the interface and this was experimentally supported by Nakamura et al. [11]. The literature is however not unified about whether the reaction represents a kinetic limitation to boron removal or if they are fast enough for local equilibrium at the interface. The gas is blown from a tubular lance to make an impinging jet onto the surface in experiments. Theory for diffusion to/from the gas flow pattern has been developed and the mass transfer coefficient for diffusion to gas is expected to depend on radius from the point of jet impingement point on the surface, gas flow rate, velocity and thus lance diameter (Section 2.3.3). HBO accumulates in the gas flow along the surface and the rate of boron removal in the gas flow out of the system is given by the flow rate and HBO concentration. Thermodynamics provide a limit to the HBO concentration depending on the concentration of reactive gases and also temperature and boron content of the melt, so the removal rate of boron can also be limited by the flow rate of gas for a given composition as shown in Section 2.3.4. Finally the different theories and mass transfer coefficients for each step is combined to a total mass transfer coefficient in Section 2.3.5, which can be calculated from experimental measurements of the boron removal rate.

The oxidizing gas is supplied to the silicon surface through the mechanism of active oxidation presented in Section 2.3.6, in which it may be partly consumed by reaction with SiO before it reaches the interface. The reaction produces silica fume in the gas flow as the main byproduct, which from metallurgical silicon production is filtered and sold as a valuable byproduct. Næss et al. [31] found that the reaction between oxygen and SiO reduces mass transfer of oxygen to interface and enhance mass transfer of SiO, and concluded that supply of oxygen is determining the rate of oxidation. Most studies of active oxidation is concerned with oxygen as the oxidizing agent, and possible adaptions to supply of steam is presented.

Complete oxidation to silica typically inhibit boron removal to gas by separating the melt and gas phases if silica forms directly onto the interface, in what is called passive oxidation. Consequently, oxygen potential at the interface should be maintained below saturation which is represented by the saturation pressures $p_{O_2}^{sat} = 3 \cdot 10^{-18}$ bar or $p_{H_2O}^{sat} = 4 \cdot 10^{-5}$ bar at 1500 °C. SiO has a high saturation pressure of $p_{SiO}^{sat} = 3.5 \cdot 10^{-2}$ bar at 1500 °C and can accommodate substantial amounts of oxygen at the interface until silica start to form. The fuming reaction and the concentration profiles for diffusion of oxidizing agents towards the surface also contributes to maintain a lower oxygen potential at the interface compared to the feed. Section 2.3.7 focuses on the operational window in which a clean surface can be maintained.

2.1 Thermodynamic Study

The highest rates in previous studies of reactive gas and plasma refining experiments are achieved with reactive gases containing hydrogen and oxygen, particularly steam and hydrogen [11, 17, 18, 25, 28]. Thermodynamic studies in previous works have suggested boron to be removed as different principal boron-containing species in the gas phase (summary in Table 2.4). Wu et al. [32] suggested that hydrogen boron suboxides ($H_x B_y O_z$) may achieve greater partial pressures than boron suboxides ($B_x O_y$), and HBO is identified as the principal specie for boron removal to gas in most studies [13, 15, 17, 18, 33], although BO has been suggested in some plasma refining studies [11, 25]. A thermodynamic study by Alemany et al. [13] indicated that BHO is ten times more volatile than BO at $1577\,°C$, which correlate to a roughly 8 times increase in the B/Si ratio in the flue gas with addition of an equal amount of hydrogen to that of oxygen in the plasma. Similarly, Altenberend [18] found hydrogen boron suboxides to form higher contents in the gas when combining oxygen and hydrogen reactants in the plasma, compared to boron suboxides and boron hydrides formed respectively when supplying only oxygen or hydrogen.

Consequently, focus is given to thermodynamics of the H-B-O-Si system. The efficiency of refining depends directly on the activity of boron in the melt and the stability of the gas product. A review of relevant literature values for boron is presented first and a selection is made for use in thermodynamic modeling. The model is used to predict dominant species and reactions, and to assess efficiency and optimization of the process with steam and hydrogen reactants. This serves as the basis for assessing use of CO as the oxidizing agent. The possibility of removing boron to gas in the B-O-Si and H-B-Si subsystems is also assessed.

2.1.1 Thermodynamic Data for Boron

The thermodynamic data for boron in liquid silicon and for HBO as the principal product of boron removal to a gas with oxygen and hydrogen are of particular importance for the expected efficiency of the reactive gas refining process. Furthermore, studies have not converged on a consensus for these values. In 2015, Vadon et al. [34] compiled and reevaluated literature values for the activity of boron in liquid silicon ($\gamma_{[B]}$) as shown in Figure 2.1 and the standard enthalpy of formation of HBO ($\Delta_f H_{HBO}^{\ominus}$) in Table 2.1.

Impurities contents in relevant silicon materials are typically orders of magnitude below $1\,\mathrm{wt\%}$ and Vadon et al. [34] focused on the activity coefficient of boron at infinite dilution ($\gamma_{[B]}^0$) and its variation with temperature (T). Vadon et al. [34] reevaluated equilibrium conditions in experiments by Noguchi et al. [35], Tanahashi et al. [36] and Inoue et al. [37], and made new calculations for the activity coefficients. Dalaker [38] reported the activity coefficient for boron from thermodynamic modeling using the SINTEF database for SoG-Si materials by Tang et al. [39], which reproduces the activity coefficient at infinite dilution
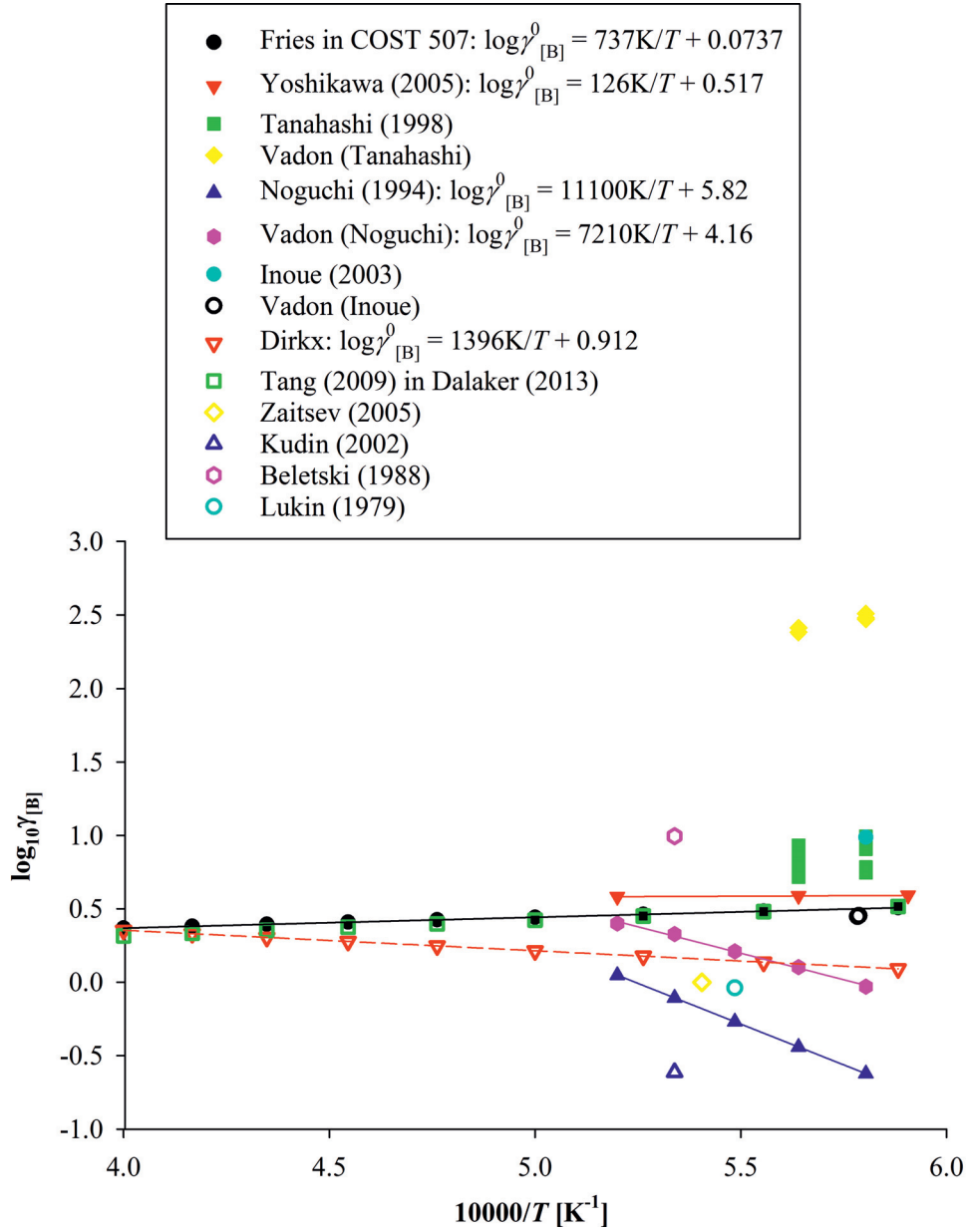
Figure 2.1: Literature values for the activity coefficient for boron in liquid silicon, compiled and reviewed by Vadon et al. [34]. Formulas in legends describe the regression lines for the activity coefficient at infinite dilution.

by Fries and Lukas in COST 507 [40] Thermochemical Database for Light Metal Alloys. The database by Tang et al. [30] provide a boron solubility of 5.1 weight%, oxygen solubility of 56 ppmw, carbon solubility around 96 ppmw and hydrogen solubility of 1.3 ppmw (36 ppma Safarian et al. [41]) in a high-purity silicon melt at 1500 °C under 1 bar hydrogen atmosphere. All of these solubilities increase with increasing temperature.

Vadon et al. [34] considered optimization methods, used by Fries and Lukas [40] and Dirkx and Spear [42], to be most robust for determining thermodynamic data of boron in liquid silicon because such methods can use the most available thermodynamic data. They considered the activity coefficient by Fries and Lukas [40] to be most realistic as it shows a tendency towards ideal solution $\gamma^0_{[B]} \approx 1$ with increasing temperature. The data by Fries and Lukas [40] are also relatively close to the final determination by Yoshikawa and Morita [43] from equilibrium experiments, including experiments by Noguchi et al. [35], Tanahashi et al. [36] and Inoue et al. [37]. The proposed activity coefficient reveals an increasing stability of boron in liquid silicon with increasing temperature, and this contributes to increase the efficiency of boron removal with decreasing temperature towards the melting point of silicon of 1414 °C.

The review of the standard enthalpy of formation of HBO is motivated by the observation by Tang et al. [30] that equilibrium simulations with the tabulated value in JANAF [44] Thermochemical Tables were not able to explain the high rate in experiments of boron removal by steam and hydrogen. This means that the concentration of boron in the gas flow was higher in experiments than the presumably highest possible limit from equilibrium modeling. To resolve this discrepancy, they conducted a new ab-inito study of the thermodynamic data for HBO and found a lower value for the enthalpy of formation of HBO. The entropy of $S^\ominus_{\mathrm{HBO}}(298\,\mathrm{K}) = 202.6$ J/mol/K in JANAF [44] Thermochemical Tables was however closely reproduced. The large spread of 60 kJ/mol between literature values in Table 2.1 suggest a large uncertainty in the enthalpy of formation of HBO. The spread in the formation enthalpy translates through an exponential relation to orders of magnitude spread in the equilibrium concentration of HBO and thus expectations for the efficiency of the gas refining process. Indeed, equilibrium modeling with the value in JANAF [44] Thermochemical Tables near the upper end of the range in Table 2.1 does not explain that it is possible to remove boron in the experiments by Nordstrand and Tangstad [17] with steam in argon and reduced hydrogen contents. Vadon et al. [34] assessed the reactions from which $\Delta_f H^\ominus_{\mathrm{HBO}}(298\,\mathrm{K})$ was calculated in the original studies and made recalculations so that their reviewed values refer to thermodynamic data by Gurvich et al. [45] for reference species in the reactions. The review of value (2) by Gorokhov et al. [46] is an exception as Jacobson and Myers [47] was used for B_2O_2 data. Based on their reviewed values, Vadon et al. [34] calculated an average of $\Delta_f H^\ominus_{\mathrm{HBO}}(298\,\mathrm{K}) = -231 \pm 13.5$ kJ/mol.

Table 2.1: Literature values for the standard enthalpy of formation of HBO, compiled and reviewed by Vadon et al. [34].

Reference (Year)	Method	$\Delta_f H_{\mathrm{HBO}}^{\ominus}(298\ \mathrm{K})$ [kJ/mol]
Gurvich et al. (1994) [45]	Review of Farber and Frisch [48]	-188.6 ± 25
Farber and Frisch (1969) [48]	Mass Spectrometry	-196 ± 13
JANAF (1985) [44]	Review	-198.3 ± 3.0
Vadon et al. (2015) [34]	Review of Farber and Frisch [48]	-211.8 ± 12
Vadon et al. (2015) [34]	Review of Dill et al. [49]	-212.8 ± 19.5
Vadon et al. (2015) [34]	Review of Gorokhov et al. [46] (1)	-228.0 ± 27.0
Gurvich et al. (1994) [45]	Review of Gorokhov et al. [46]	-228.6 ± 20
Tang et al. (2012) [30]	Ab initio	-229.4
Duan et al. (1999) [50]	Ab initio	-233.9
Vadon et al. (2015) [34]	Review of Tang et al. [30]	-234.7
Vadon et al. (2015) [34]	Review of Page [51]	-236.7
Vadon et al. (2015) [34]	Review of Duan et al. [50]	-242.8 ± 8.4
Vadon et al. (2015) [34]	Review of Gorokhov et al. [46] (2)	-250.2 ± 38.0
Page (1989) [51]	Ab initio	-251

2.1.2 Thermodynamic Model

A module in HSC Chemistry 7 [52] for minimizing the Gibbs free energy is used for modeling of a small amount (10 $\mathrm{l_N}$) of hydrogen gas with 3.7 vol% steam at 1 bar in contact with a surplus amount (40 g) of silicon melt with 0.3 ppmw boron. A normal liter ($\mathrm{l_N}$) refers to the volume of gas at normal conditions of 20 °C and 1 atm pressure. The amounts are selected to estimate the composition of the last volume of gas to leave the furnace for refining to SoG-Si, to assess the potential for refining silicon to this extent using hydrogen- and oxygen-containing reactive gases.

The steam content was selected to the upper threshold that can be input without forming silica at 1500 °C. Avoiding silica formation at the interface is important because it floats and forms a layer on the silicon surface and passivates the melt from further reactions with the gas. A different threshold for silica formation of 2.8 vol% steam was however found in a different model developed by Tang et al. [30], and Yvon et al. [26] calculated that silica does not form at oxygen contents up to 10 vol% at 1507 °C. The thermodynamic value for this threshold is however not directly related to experiments. The threshold steam content in the feed in experiments is typically higher than the thermodynamic threshold (Section 2.3.7) because the steam contents that reaches the interface where the thermodynamic models apply is lower than the concentration in the reactive gas feed, as explained in Section 2.3.6.

Equation (2.1) is used for the activity coefficient at infinite dilution of boron in silicon calculated by Vadon et al. [34] from data in COST 507 [40] Thermochemical Database for Light Metal Alloys ($\gamma_{[B]}^0 = 3.1$ at 1500 °C). An increased enthalpy of formation of HBO in the thermochemical data by Tang et al. [30] compared to the HSC database is implemented in the model through the activity coefficient in Equation (2.2), where $R = 8.314$ J/mol/K is the gas constant. The value by Tang et al. [30] is used in this model as they used it to model gas refining experiments that is the basis for the present work. Altenberend [18] suggested that boron does not interact significantly with other impurities in MG-Si as equal removal rates were obtained with MG-Si and EG-Si feedstock, so the infinite dilution approximation $\gamma_{[B]} = \gamma_{[B]}^0$ is used in the thermodynamic modeling.

$$\log_{10} \gamma_{[B]}^0 = \frac{737 \text{ K}}{T} + 0.0737 \tag{2.1}$$

$$RT \ln \gamma_{\text{HBO}} = -31000 \text{ J/mol} \tag{2.2}$$

In addition to boron and silicon in the melt and a slag phase to allow silica and B_2O_3 formation, the model includes all gases in the H-B-O-Si system in the HSC database with reliable sources above 1414 °C, which are listed Table 2.2. The gases in Table 2.2 are ordered after increasing partial pressures at 1500 °C and the topmost species with partial pressures at least an order of magnitude higher than all species below are considered as dominant species. With the re-evaluated stability of HBO, it dominates among the boron-containing products the O-H-B-Si system with oxygen input in the order of 1 vol% (and higher) in hydrogen between $1410 - 2000$ °C and SiO is the dominating by-product. The model results in Figure 2.2 shows the partial pressures of relevant product gases and steam (hydrogen is at atmospheric pressure) in equilibrium with SoG-Si with 0.3 ppmw boron.
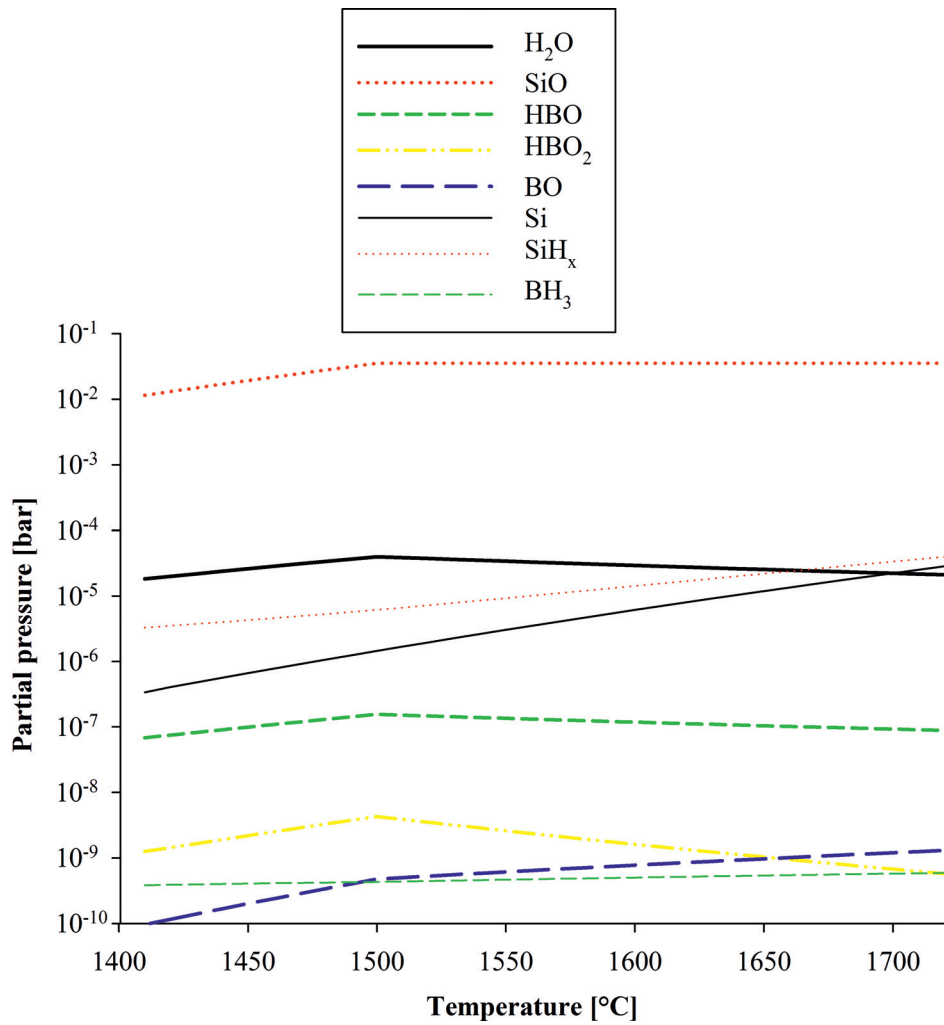
Figure 2.2: Equilibrium partial pressures of selected gas species established from 3.7 vol% steam in hydrogen (1 bar total pressure) over liquid silicon with 0.3 ppmw boron in the thermodynamic model.

Table 2.2: Gaseous species modeled in HSC Chemistry 7 [52] in the H-B-O-Si system and subsystems defined to the lower left. Highlighted species are considered dominating among each group, and those in highlighted groups are dominant in the H-B-O-Si model.

$\mathbf{H}_x\mathbf{B}_y\mathbf{O}_z$	H_xO_y	B_xH_y	Si_xH_y	$\mathbf{H}_x$	B_x	Si_x	O_x	B_xO_y	$\mathbf{Si}_x\mathbf{O}_y$
HBO	**H₂O**	**BH₃**	SiH	**H₂**	**B**	**Si**	**O**	**BO**	**SiO**
HBO_2	OH	BH_2	SiH_2	H	B_2	Si_2	O_2	B_2O_2	Si_2O_2
H_2BOH	H_2O_2	BH	SiH_4			Si_3	O_3	BO_2	SiO_2
BOH	HO_2	B_2H_6	SiH_3					B_2O_3	
H_3BO_2								B_2O	
HBOH									
$B(OH)_2$									
$B(OH)_3$									
$H_3B_3O_3$						B-O-Si system			
$B_2(OH)_4$					B-Si system				
$H_3B_3O_6$			H-B-Si system						

2.1.3 Boron Distribution

Equilibrium between the dominant species in the gas and the melt is summarized in Reaction (2.3), in which brackets denotes the silicon melt. Khattak et al. [15] was the first to construct Reaction (2.3) from thermodynamic modeling. The heterogeneous reaction distributes boron across the melt-gas interface, depending on SiO and hydrogen partial pressures at the interface (p_i). Equation (2.4) presents the distribution of boron from melt to HBO gas for equilibrium at the interface. The activity of silicon is approximated to unity as the silicon the feedstock selected for refining to SoG-Si would typically be MG-Si close to the upper purity range near 99% [16]. The mole fraction of boron at the interface is represented by $x_{i,[\mathrm{B}]}$ and $p^{\ominus} = 1\,\mathrm{bar}$ is the standard pressure.

$$[\mathrm{B}] + \mathrm{SiO} + \tfrac{1}{2}\,\mathrm{H}_2 \rightleftarrows \mathrm{HBO} + [\mathrm{Si}] \tag{2.3}$$

$$\frac{p_{i,\mathrm{HBO}}}{x_{i,[\mathrm{B}]}} = \gamma_{[\mathrm{B}]} \frac{K_{\mathrm{HBO/SiO}}}{p^{\ominus\frac{1}{2}}} p_{i,\mathrm{SiO}} p_{i,\mathrm{H}_2}^{\frac{1}{2}} \tag{2.4}$$

At $1500\,^{\circ}\mathrm{C}$, the equilibrium constant in Equation (2.4) is $K_{\mathrm{HBO/SiO}} = 1.85$ and the distribution coefficient for boron for the conditions in Figure 2.2 is $\frac{x_{i,\mathrm{HBO}}}{x_{i,[\mathrm{B}]}} = 0.20$ for equilibrium at the interface. A large amount of gas is thus necessary for refining MG-Si to SoG-Si, even compared to the amount of slag necessary in slag refining. The minimum volume of gas necessary to completely extract boron is 96000 times the melt volume at normal conditions ($20\,^{\circ}\mathrm{C}$ and atmospheric pressure), or $37\,\mathrm{m_N^3/kg}$. Refining at an industrial scale of $7500\,\mathrm{ton/year}$ thus requires a gas flow rate per melt mass of $123\,\mathrm{l_N/min/kg}$.

Figure 2.2 includes two domains separated at $1500\,°C$. Silica forms below $1500\,°C$ and the oxide contents in the gas is limited to saturation partial pressures. It is thus seen that the steam content in the reactive gas increases can be increased with increasing temperature. Above $1500\,°C$, silica is not formed from $3.7\,\text{vol}\%$ steam and the amount of oxygen in the gas is constant with temperature. The partial pressure of HBO decreases with increasing temperature for a constant oxygen potential in the gas (above $1500\,°C$ in Figure 2.2) as a result of a decreasing ratio of the HBO and SiO stabilities. However, the steam content can be increased with increasing temperature, which also is found by Yvon et al. [26]. The increasing partial pressure of HBO below $1500\,°C$ in Figure 2.2 shows that the partial pressure of HBO can be increased by increasing the steam content simultaneously with temperature. Thus, thermodynamic modeling suggests a high temperature with the steam content at the threshold for passivation in a hydrogen atmosphere to be optimal for maximizing the HBO pressure at the surface and potentially the rate of boron removal. The same conclusion was drawn by Altenberend [18]. According to Altenberend [18], operation of plasma torches typically requires argon, so there is a trade-off between increased steam contents at higher temperatures and reduced hydrogen content in plasma compared to reactive gas refining.

Wu et al. [32] suggest a temperature just above the melting point of silicon to be advantageous for boron removal as their equilibrium calculations shows a decrease in the partial pressures of hydrogen boron suboxides, except the nearly constant equilibrium partial pressure of HBO, which is not dominant in their study. Nordstrand and Tangstad [17] found the rate of boron removal to increase for lower temperatures between $1450 - 1600\,°C$ in reactive gas refining with $3.2\,\text{vol}\%$ steam in hydrogen. The same effect was observed by Altenberend [18] when the induction heating power was decreased. The rate of boron removal was not affected by changing only the plasma power between $25 - 45\,\text{kW}$. The decreasing temperature dependence is consistent with equilibrium since the steam content was held constant through these experiments, assuming the fraction of steam reaching the interface to be constant.

Optimization by increasing the steam content and temperature simultaneously was demonstrated in plasma refining experiments by Fourmond et al. [53]. The refining rate was almost doubled by increasing the O_2 content from $0.8 - 1.8\,\text{vol}\%$ in a plasma with $3.2\,\text{vol}\%$ hydrogen in argon simultaneously with a $150 \pm 20\,°C$ temperature increase. Additionally, Altenberend [18] increased the O_2 fraction in argon (without preheating to plasma) from $3.6\,\text{vol}\%$ at the silicon melting point to $19\,\text{vol}\%$ at $1680\,°C$ and calculated a doubling of the boron removal rate at equilibrium.

The equilibrium HBO partial pressure and the distribution coefficient increases with the square root of the hydrogen partial pressure. The boron removal rate has been found to show the same dependence on the hydrogen fraction in the reactive gas in reactive gas and plasma refining experiments by for instance Nordstrand and Tangstad [17] and Altenberend [18] (further discussion in Section 2.3.2). Consistently, Theuerer [28] found a reactive gas of water vapor in hydrogen to be more effective for reactive gas boron refining compared to inert gases and water vapor. Furthermore, Sulentic [54] achieved a faster removal rate in an

experiment with 3.2 vol% steam and 48.4 vol% hydrogen and argon compared to 3.2 vol% in a pure argon atmosphere. Replacing the Ar atmosphere with an equal mixture of hydrogen and argon for 3.2 vol% steam decreased the final boron content achieved after 1.5 h refining from 104 ppmw to 1 ppmw.

Increasing the total pressure of a reactive gas composition with hydrogen, while keeping the steam content below the threshold for passivation, also promotes HBO formation and increases the distribution coefficient. The larger number of gaseous reactants than products in Reaction (2.3) causes the equilibrium to shift towards higher contents of products at increasing total pressure according to Le Châtelier's principle.

Since SiO is produced from steam to an essentially stoichiometric amount, the equilibrium HBO partial pressure increases proportionally with the partial pressure of steam at the interface, until passivation removes the melt-gas interface. Additionally, the input steam content threshold for silica formation was found independent of hydrogen content, since oxygen does not bind in significant amounts to hydrogen compared to the dominant oxide SiO. Contradictory, Suzuki et al. [25] explained how silica formed in Ar/O$_2$ and Ar/CO$_2$ plasmas, but not a Ar/H$_2$O plasma, by formation of hydrogen as steam reacts with the melt and subsequent volatilization of silica according to Reaction (2.5). Nakamura et al. [11] also suggested addition of hydrogen to increase the reaction area as Reaction (2.5) is shifted to the right by increasing hydrogen contents in the reactive gas.

$$\text{SiO}_2 \text{ (l)} + \text{ H}_2 \rightleftarrows \text{SiO} + \text{ H}_2\text{O} \tag{2.5}$$

2.1.4   Silicon Loss and Boron Enrichment

Silicon is lost from the melt by oxidation to SiO. SiO is further oxidized to silica as it diffuses from the interface due to shifting of Reaction (2.6). At the interface, the partial pressure of steam at equilibrium with silicon is low ($p_{i,\text{H}_2\text{O}} = 4 \cdot 10^{-5}$ bar at 1500 °C in Figure 2.2) compared to the supplied steam content ($p^s_{\text{H}_2\text{O}} = 0.037$ bar is input to calculations for Figure 2.2). Thus, Reaction (2.6) is shifted to the right as SiO is transferred from the interface to the bulk gas, and the saturation pressure of SiO in Equation (2.7) is reduced from approximately $p_{i,\text{SiO}} = 0.037$ bar at the interface to $p_{b,\text{SiO}} = 4 \cdot 10^{-5}$ bar in the bulk gas for the steam contents presented above and unit activity of silica. Section 2.3.6 explains the mechanism of active oxidation further. The order of magnitude reduction in the SiO partial pressure from the interface to the bulk gas dictates that the silica becomes the dominant silicon product in the bulk gas. The majority of silicon in the off-gas is according to Næss [55] and other investigations in Section 2.3.6 found as silica fume particles below its melting point of 1723 °C [52] or droplets in an aerosol in plasma refining as observed by Altenberend [18].

21

$$\text{SiO} + \text{H}_2\text{O} \rightleftarrows \text{SiO}_2 \text{ (l/s)} + \text{H}_2 \qquad (2.6)$$
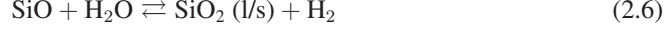
$$p_{\text{H}_2\text{O}} p_{\text{SiO}} = \frac{p^{\ominus}}{K_{\text{H}_2\text{O}+\text{SiO}}} p_{\text{H}_2} \qquad (2.7)$$

Silicon oxidation represents a loss of melt and reduced silicon recovery, and concequently causes an up-concentration of boron and other impurities in the remaining melt. The loss of silicon was measured in experiments by Nordstrand and Tangstad [17] to an average of 10.7% during 4.5 h reactive gas refining using 3.2 vol% steam in a 3 l_N/min gas flow. This silicon loss represents 12% up-concentration of boron after 4.5 h, while the reduction in boron concentration during the refining was more than two orders magnitude, which makes the effect of up-concentration negligible.

Refining is only possible if the rate boron is removed from the melt is higher than the rate of up-concentration. Assuming that HBO and silica particles have equal velocities in the bulk gas flow, the ratio of boron to silicon concentrations in the off-gas must be greater than the ratio of boron to silicon concentrations in the melt [56]. Accordingly, up-concentration sets a requirement to the enrichment ratio $E > 1$ in Equation (2.8) for the H-B-O-Si system. In the thermodynamic model for the H-B-O-Si system (Figure 2.2), HBO is the only gas with a partial pressure above the limit for boron removal.

$$E = \frac{\frac{C_{\text{HBO}}}{C_{\text{SiO}_2}}}{\frac{x_{[\text{B}]}}{x_{[\text{Si}]}}} \qquad (2.8)$$

The concentration of silica (C_{SiO_2}) in Equation (2.8) represents the amount of silicon ($n_{\text{Si}_t} \approx n_{\text{SiO}_2}$) in a volume ($V$) of gas after reactions. Equation (2.9) also show that the concentration of HBO relates proportionally to the partial pressure (p_j) of this presumably ideal gas and mole fractions (x) are in Equation (2.8) used to represent concentration in the approximately pure silicon melt. The density of the melt (ρ) can be approximated to that of pure liquid silicon, like the molar mass $M \approx M_{\text{Si}}$.

$$C_j = \frac{n_j}{V} = \frac{p_j}{RT} = \frac{\rho}{M} x_{[j]} \qquad (2.9)$$

The enrichment ratio can be related to thermodynamics in the scenario that equilibrium is established between the bulk phases, so that concentrations of species in Reaction (2.3) at the interface equals the bulk concentrations. Since SiO is the dominant oxide in equilibrium with silicon, $C_{\text{SiO}_2} = \frac{p_{i,\text{SiO}}}{RT}$ is used for the combination of Equations (2.8) and (2.4) to Equation (2.10). The resulting equilibrium enrichment ratio (E_{eq}) only depends on the hydrogen partial pressure and temperature through $K_{\text{HBO/SiO}} \gamma_{[\text{B}]}$.

22

$$E_{eq} = \frac{K_{\text{HBO/SiO}}}{p^{\ominus \frac{1}{2}}} p_{i\text{H}_2}^{\frac{1}{2}} \gamma_{[\text{B}]} \tag{2.10}$$

Equation (2.10) suggests the enrichment ratio to be independent on the boron concentration in the melt and thus does not change during refining. Consequently, there is no principal limit to the purities that can be obtained provided the reactive gases are clean from boron-containing impurities is (except complete volatilization of the melt). In practice however, the extent of refining is limited by economics of gas consumption [18] and time in addition to melt recovery, which drives research for optimizing the enrichment ratio and the rate of boron removal. Reactive gas and plasma refining may be used for recycling of electronic scrap which is EG-Si with high boron contents (4-10 times higher than MG-Si [15]). Khattak et al. [15] first demonstrated reactive gas refining of electronic scrap and obtained a purity close to SoG-Si quality (achieved less than 1 ppmw boron) in 2002. They thus saw the potential for electronic scrap to become an additional silicon feedstock for the photovoltaic industry, as electronic scrap annually amounted to $100 - 200$ MW capacity of produced modules in 2002. Nordstrand and Tangstad [17] also used highly doped EG-Si with $130 - 150$ ppmw boron, which in several experiments was refined below 1 ppmw within 4.5 h.

With the re-evaluated HBO thermochemical data by Tang et al. [30], modeling of the H-B-O-Si system with HBO and SiO as dominant products gives $E_{eq} = 5.7$ at 1500 °C in a hydrogen atmosphere. The enrichment ratio decreases slightly with temperature ($E_{eq} = 3.2$ at 1720 °C) due to the decreasing ratio of the HBO and SiO stabilities as indicated by the decreasing HBO partial pressure above 1500 °C in Figure 2.2.

Enrichment ratios measured experimentally are according to calculations by Altenberend [18] in Table 2.3 almost an order of magnitude higher than thermodynamic calculations. Reasons for the deviation from equilibrium calculations may relate to kinetics of both boron and silicon volatilization, measurement uncertainty, assumptions in calculations or inaccurate thermodynamic data. Altenberend [18] particularly discussed the influence of silica droplets or particles in relation to spectroscopic gas analysis to explain the deviation. A minimum estimate for the enrichment ratio in Experiment 9 by Nordstrand and Tangstad [17] was calculated by assuming complete utilization of steam in the reactive gas. It is also worth noting that the equilibrium enrichment factor Altenberend [18] calculated for this experiment is

Table 2.3: Comparison of enrichment ratios for experiments (E_{exp}) and equilibrium (E_{eq}) (modified from Altenberend [18]).

Mehtod [Author]	Melt temperature	Reactive gas	E_{exp}	E_{eq}	E_{exp}/E_{eq}
Plasma [18]	1410 °C	Ar/3.2% H_2/1.8% O_2	136	15	9
Plasma [11]	$1600 - 1700$ °C	Ar/5% H_2O	36	5.5	7
Reactive gas [17]	1500 °C	Ar/3.2% H_2O	>11	6	>2

23

higher than the enrichment factor of 5.7 calculated from partial pressures modeled in Figure 2.2, which includes 96.8 vol% hydrogen in the reactive gas. Accordingly, comparison of experiments to the H-B-O-Si equilibrium model provides even larger deviations than those in Table 2.3.

Nakamura et al. [11] observed formation of dust containing both boron and silicon in the plasma refining furnace. By assuming the mole ratio of boron to silicon in the dust to equal that in the gas, they reported a 36-fold enrichment of boron in the gas phase. In comparison, Altenberend [18] calculated $E_{eq} = 5.5$ for their experiments (although using 2.5 vol% steam in the calculations). Compared to Nakamura et al. [11], Alemany et al. [13] measured a much lower B/Si ratio in the gas of approximately 0.017, which was persistent through variations of O_2 and hydrogen contents.

2.1.5 Oxidation by CO

The equilibrium model of the H-B-O-Si system was extended by introducing 3.7 vol% CO as the oxidizing agent instead of steam in hydrogen, and also CO_2 and a SiC phase was included. CO contains the same amount of oxygen as steam, and the same threshold for silica formation is found for for both oxidizing agents. Like steam, CO reacts essentially stoichiometrically to SiO and Equation (2.3) describes boron distribution across the interface. Accordingly, the partial pressures of SiO and HBO at equilibrium equals those in Figure 2.2 and the equilibrium enrichment ratio is the same for CO and steam as oxidizing agent. However, CO can not remove boron at equilibrium without additional hydrogen in the reactive gas, which is needed for HBO formation.

Nevertheless, Suzuki et al. [25] was able to remove boron with CO_2 in argon plasmas. They obtained a maximum boron elimination of about 90% after 30 min treatment with 0.7 vol% CO_2 in the argon plasma, which was the same found for 0.7 vol% O_2 in the plasma. A plasma of 1.24 vol% steam in argon achieved 98.9% boron elimination during 25 min refining and was found more efficient for boron removal compared to 0.44 vol% hydrogen and CO_2 with an equal content of oxygen in the plasma.

An important difference between oxidation by CO and steam is that carbon released by decomposition of CO binds with silicon to form solid SiC in Equation (2.11) and not volatile species like hydrogen, which is produced from decomposition of steam. Thus, surface coverage of SiC must be considered in addition to passivation by silica.

$$CO + 2\,[Si] \rightleftarrows SiC\,(s) + SiO \qquad (2.11)$$

At equilibrium, SiC formation can not be prevented with CO as the reactive gas in the way that silica formation can be avoided at low oxygen contents. Reaction (2.11) between CO and

silicon does not produce a volatile carbon-containing specie like SiO is a volatile oxygen-containing specie. Hence, carbon in the form of SiC is expected to accumulate in the crucible during refining to the same extent that silicon is lost by oxidation.

SiC is however observed to efficiently settle in liquid silicon Çiftja [57], as the density of SiC (3.2 g/cm^3 [58]) is greater than that of liquid silicon (2.59 g/cm^3 near the melting point [59]). High-frequency magnetic field induction can also enhance settling of SiC particles to crucible walls [60]. In contrast, silica has a lower density (2.2 g/cm^3 for β-Cristobalite [61]) than liquid silicon and is expected to accumulate at the surface.

Suzuki et al. [25] found an increasing trend of the boron removal rate with increasing contents of O$_2$ and CO$_2$ to level off beyond about 0.2 vol% in argon plasmas, as they observed a silica surface film by the Ar/O$_2$ and Ar/CO$_2$ plasmas. SiC formation was however not reported. Microprobe analyzes by Sulentic [54] did however reveal that SiC formed particles at the surface in graphite crucibles. SiC particles were observed at the melt surface also after an experiment with quartz crucible in an alumina tube furnace and without carbon-containing reactive gases. Thus, oxidation of carbon contaminants to CO appears to be a sufficient source for partial SiC coverage at the melt surface.

2.1.6 Potential for Hydrogen or Oxygen as Reactive Gas

The lower limit to the total boron partial pressure in the off-gas for boron removal to be possible is presented in Equation (2.12), for which $E = 1$ and the silicon melt is approximated to be pure ($x_{[\text{Si}]} = 1$) in Equation (2.8). The total boron partial pressures (p_{B_t}) is a sum over all boron-containing gases times the number of boron or silicon atoms in each molecule, and vice versa for the total silicon partial pressure p_{Si_t}. In case there is a dominant specie for boron or silicon, this can be used to approximat the total partial pressure of the element.

$$p_{\text{B}_t} = p_{\text{Si}_t} x_{[\text{B}]} \tag{2.12}$$

BO is the dominating boron-containing gas in the B-O-Si system (gases shown in Table 2.2) up to around 2300 °C with a gas input of 3.7 vol% oxygen atoms in argon. The stability of BO is not sufficient compared to SiO for removal at equilibrium for any temperature of liquid silicon. However, boron removal by O$_2$ in argon plasmas has been proven experimentally in plasma refining by Suzuki et al. [25] and Ikeda and Maeda [62], which is an indication of non-equilibrium, and BO has been reported as the principle specie for boron removal [11, 25]. Suzuki et al. [25] found the Ar/H$_2$O plasma achieved faster boron removal compared to Ar/O$_2$ plasmas. With 1.24 vol% steam in argon, the boron content was reduced from 35.7 ppmw to 0.4 ppmw during 25 min refining, which is sufficient for refining of MG-Si to SoG-Si. This represents 98.9% boron elimination and compares to a maximum of 90% boron elimination after 30 min treatment with an equal oxygen amount in 0.7 vol% O$_2$. When considering BO

25

to be the dominant boron-containing specie, Nakamura et al. [11] could not explain increased removal rates observed with increasing hydrogen contents in the reactive gas, as hydrogen shifts Reaction (2.13) to the left. This trend can be explained by HBO formation, while Nakamura et al. [11] proposed the reaction area to increase with hydrogen due to shifting of Reaction (2.5).

$$[B] + H_2O \rightleftarrows BO + H_2 \tag{2.13}$$

Refining with pure hydrogen produces silicon hydrides of which no specie is dominant (H-B-Si system in Table 2.2). The dominant boron-containing specie BH_3 is thus stable enough at equilibrium to remove boron as its equilibrium enrichment ratio is $E_{eq} = 17.8$ at 1500 °C. Nordstrand and Tangstad [17] showed that boron can be removed by pure hydrogen in reactive gas refining experiments at 1500 °C. The rate obtained was significantly lower than the rates obtained with 3.2 vol% steam in the reactive gas, as the absolute partial pressure of BH_3 in a hydrogen atmosphere is at equilibrium three orders of magnitude lower than that of HBO shown at 1500 °C in Figure 2.2 for 3.7 vol% steam in hydrogen. The equilibrium enrichment ratio in the H-B-Si system decreases significantly with temperature and is below the limit for boron removal ($E_{eq} = 1$) above approximately 1850 °C.

Imler et al. [63] compared plasma refining with pure argon to introduction of oxygen and hydrogen reactive gases. They were not able to measure accurately any reduction in boron concentration by in an argon atmosphere. Also Flamant et al. [64] found experimentally that boron could not be removed in a pure argon atmosphere at a reduced pressure of 0.05 bar. Consistently, modeling of the B-Si system in Table 2.2 the vapor pressures of boron an silicon provides $E_{eq} = 0.007 - 0.031 < 1$ in the temperature interval $1500 - 1700$ °C of their experiments. Imler et al. [63] was able to remove boron by adding hydrogen in the reaction chamber, which agrees with $E_{eq} > 1$ in the H-B-Si system. They found the boron removal rate to be relatively insensitive to the amount of hydrogen. The combination of hydrogen and oxygen, even in small amounts, was considered necessary to achieve increased refining rates. Over an order of magnitude higher rates was demonstrated with both oxygen and hydrogen compared to only hydrogen additions in the reaction chamber. Consistently, the partial pressure of HBO is orders of magnitude higher in the H-B-O-Si model compared to the partial pressure of BH_3, which is dominant in the H-B-Si model with no source of oxygen. The equilibrium enrichment ratio is however lower for the H-B-O-Si model than the H-B-Si model, and thus the absolute partial pressure of boron-containing species in the gas can be considered more important for the refining rate than the enrichment ratio. Provided that the enrichment ratio is sufficient for up-concentration due to silicon loss to be negligible, as in experiments with steam in hydrogen by Nordstrand and Tangstad [17], the enrichment ratio does not influence the rate of removal directly like the absolute partial pressures obtained in the gas flow (Section 2.3.4).

2.2 Rate of Boron Removal

The rate ($\frac{\mathrm{d}n}{\mathrm{d}t}$) of boron removal is the amount of boron removed from the melt per time unit (t), while the flux (J) is a local flow of boron out of the melt. If the flux varies across the surface, it must be integrated or averaged over the reaction area (A) to be directly related to the rate of removal. Equation (2.14) is the mass balance for removal of boron from the top surface of a melt in a crucible. This mass balance states that the rate of change of the amount of boron in the melt equals the rate at which boron is transferred across the melt surface. The free horizontal cross-section area in the crucible (A_c) approximates the area of the melt surface. The rate is calculated from experimental measurements of concentrations, for instance in consecutive samples, while the flux relates to theory of reaction kinetics (Section 2.3).

$$\frac{\mathrm{d}n}{\mathrm{d}t} = \int_{A_c} J \mathrm{d}A \tag{2.14}$$

The reaction area between the melt and gas is not readily known, so the crucible cross-section area A_c is used in Equation (2.14), which assumes a flat melt surface. Deviation from a flat and clean surface in experiments is thus pronounced through the flux and kinetic parameters. Fluid dynamic calculations by Nordstrand and Tangstad [17] for $3 \, \mathrm{l/min}$ gas blown from $5 \, \mathrm{cm}$ above the melt surface indicate ripples on the surface that increases the surface area and causes overestimation of the flux and kinetic parameters.

The gas-melt interface area can also be reduced by surface coverage for instance by passivation and possibly SiC formation, which causes calculated kinetic parameters to represent slower kinetics than reality. In plasma refining experiments, Suzuki et al. [25] suggested that reactions with boron only occurred in the area where the plasma jet was impinging the melt surface. Nakamura et al. [11] arrived at the same conclusion as the melt the surface was covered by silica outside the dimple and the removal rate in their experiments was proportional to the measured dimple area. A non-transfer type plasma was found to provide a larger dimple area and thus faster boron removal compared to a transfer type plasma.

Kinetic theory in Section 2.3 relates the flux to a driving force in the form of a concentration difference (ΔC) in Equation (2.15). The mass transfer coefficient k is a measure of the reaction kinetics. A high mass transfer coefficient is desirable for achieving high rates of boron removal with the low concentrations and driving forces encountered in refining of MG-Si to SoG-Si.

$$J = k\Delta C \tag{2.15}$$

27

2.2.1 Rate Law

The overall kinetics for removal of boron is represented by the total mass transfer coefficient for boron k_t, and the total driving force is the concentration of boron in the bulk of the melt ($C_{[B]}$, see Section 2.3). The rate of removal can be calculated from the concentration of boron by using these values in Equation (2.15) and insert this into Equation (2.14). The resulting differential rate law in Equation (2.16) is obtained by expanding $n = CV$ in Equation (2.14) and averaging the flux over the crucible cross-section area. V is the volume of the melt.

$$\frac{\mathrm{d}n_{\mathrm{B}}}{\mathrm{d}t} = V\frac{\mathrm{d}C_{[B]}}{\mathrm{d}t} = -k_t A_c C_{[B]} \tag{2.16}$$

The rate of boron removal is proportional to the concentration of boron in the melt provided that mass transfer coefficient is independent of the boron concentration. This is referred to as first order kinetics (reaction orders are further explained in Section 2.3.2), for which Equation (2.16) integrates to the integral rate law in Equation (2.17). The integral rate law shows the evolution of the concentration during refining, referred to the initial concentration ($C(t = 0)$). The concentration decreases exponentially with time for first order kinetics.

$$\ln \frac{C_{[B]}}{C_{[B]}(t = 0)} = -k_t \frac{A_c}{V} t \tag{2.17}$$

The integral rate law allows the mass transfer coefficient to be directly calculated from concentration measurements during refining. Plots of measured concentrations ($C_{[B]}$) and the time of measurement or sampling (t) in the form of $\ln \frac{C_{[B]}}{C_{[B]}(t=0)}$ as function of $\frac{A_c}{V} t$ fit to a straight line for first order kinetics and provides the mass transfer coefficient as the negative slope. Figure 2.3 shows this plot for previous works, which all fit to Equation (2.17), with constant mass transfer coefficients. Nakamura et al. [11] found the rate of concentration reduction ($\frac{C_{[B]}}{C_{[B]}(t=0)}$) to scale inversely to the melt volume and proportionally to the melt-gas interface area, which also is consistent with the rate laws in Equations (2.16) and (2.17). An inverse relation between the melt volume and refining rate was also observed by Imler et al. [63].

The half-life $t_{1/2}$ of reaction shown in Equation (2.18) is a commonly used measure of the rate for first order kinetics, in addition to the mass transfer coefficient. It represents the time period in which the concentration is reduced to the half as shown in Equation (2.18) by setting $\frac{C_{[B]}}{C_{[B]}(t=0)} = \frac{1}{2}$ in Equation (2.17). This time period is only constant for exponential reduction of the concentration and thus only applies to first order kinetics. The half-life can not be related to mass transfer coefficients and reaction kinetics without knowledge of the reaction area and melt volume.

28

$$t_{1/2} = \frac{ln\frac{1}{2}}{ln\frac{C_{[B]}}{C_{[B]}(t=0)}}t = -\frac{ln\frac{1}{2}}{k_t\frac{A_c}{V}} \tag{2.18}$$

2.2.2 Achievements in Literature

Previous experimental works on the kinetics of plasma and reactive gas refining are summarized in Figure 2.3 in terms of the mass transfer coefficients achieved. The concentration scale is selected to represents refining from MG-Si to SoG-Si. The time scale shows that the mass transfer coefficients obtained by Nordstrand and Tangstad [17], Safarian et al. [41], Altenberend [18] and Suzuki et al. [25] requires 1 h refining time for a 1 cm deep cylindrical melt (assuming constant mass transfer coefficient over the surface area).

Suzuki et al. [25] calculated mass transfer coefficients related both to the cross-section of the plasma torch nozzle and the entire melt surface area. The mass transfer coefficients they calculated based on the nozzle cross-section area was found to decrease with decreasing initial concentration of boron in spite of the data for each experiment fitting to the apparent first order model for boron, which was explained by reactions outside the plasma-impinging area at relatively high boron contents. In Figure 2.3 the mass transfer coefficients are calculated as averages over the crucible cross-section area in all experiments except zone refining by Theuerer [28], which provide an estimated area for the entire melt-gas surface area in his zone refining experiments.

Nakamura et al. [11] report mass transfer coefficient assuming boron removal only in the area of a dimple forming beneath the plasma torch. They measured the diameter and depth of the dimple and their kinetic parameters are related to the calculated surface area of the dimple and not the entire crucible cross-section. The highest of their mass transfer coefficient are in Figure 2.3 recalculated as an average over the crucible cross-section area for comparison. The highest mass transfer coefficient they report over the crucible cross-section area is $1.18 \cdot 10^{-4}$ m/s, and is in the same in the same order as the mass transfer coefficient Suzuki et al. [25] calculated over the cross-section of the plasma torch nozzle ($1.4 \cdot 10^{-4}$ m/s).

Ikeda and Maeda [62] used a rotating plasma torch to supply plasma over a larger surface area of the melt, with the same reactants used by Suzuki et al. [25]. Ikeda and Maeda [62] calculated a mass transfer coefficient of $7.7 \cdot 10^{-5}$ m/s as an average over the entire surface of the molten silicon. The increased mass transfer coefficient compared to $1.3 \cdot 10^{-5}$ m/s found by Suzuki et al. [25] was attributed to rotation of the plasma torch. Rotating the plasma torch can be expected to heat a larger area of the surface.

Boron removal from the liquid zone during zone refining to a reactive gas of steam and hydrogen produced the highest mass transfer rates in the work by Theuerer [28] in 1956. The mass transfer coefficients he obtained relates to an estimated area and volume for the molten section of the ingot, which during refining is moved across the ingot. Boron is presumably

not removed from solid silicon, which at any time constitutes the majority of the ingot. Thus the rate of removal through the molten section equals that for the whole ingot and the overall flux or rate constants averaged over the entire ingot is slower than those calculated for the molten volume of the ingot. The boron removal rates achieved in previous investigations are further compared in terms of refining method and experimental parameters in Table 2.4.
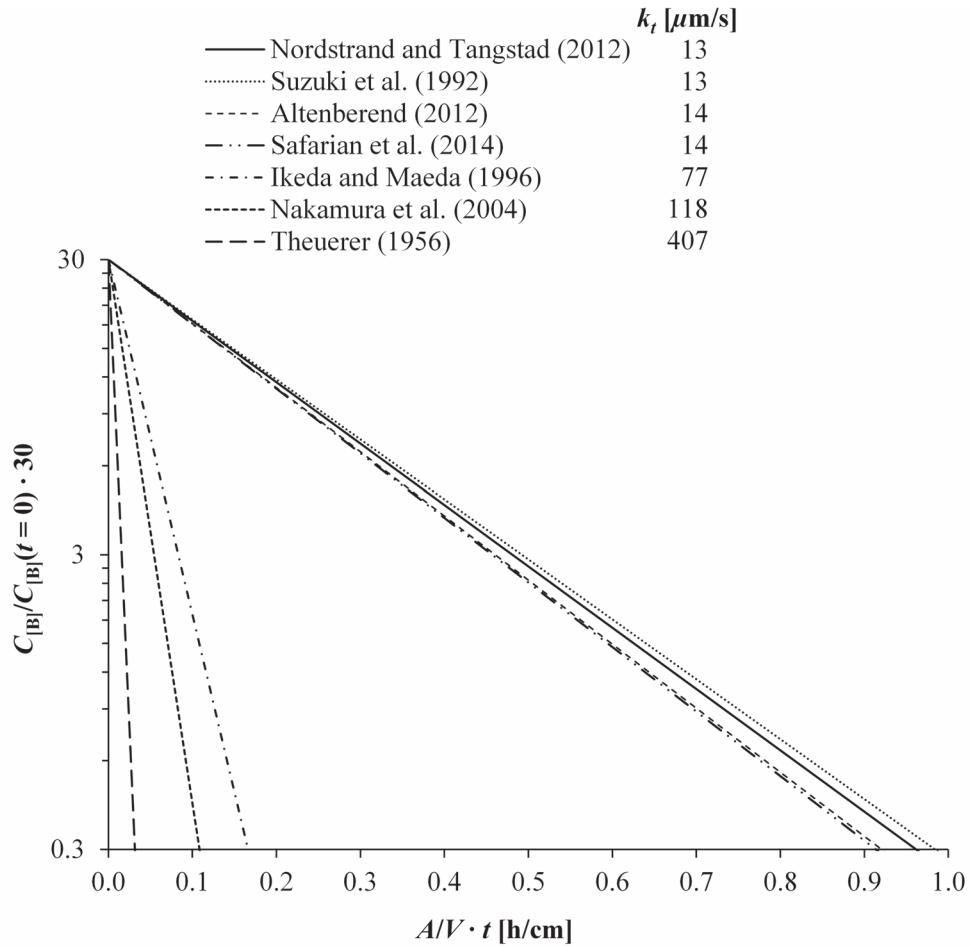
Figure 2.3: Boron removal achievements in previous works of oxidizing gas and plasma refining. Experiments with the highest total mass transfer coefficient in each study are compared on a normalized concentration axis, with scale representing a refining ratio 100 from typical MG-Si (~ 30 ppmw) to SoG-Si (≤ 0.3 ppmw). Selection of reaction area in calculations may account for large differences in estimates of the total mass transfer coefficient.

Table 2.4: Summary of gaseous boron removal experiments in literature. Two lines are used to describe the experiment with fastest boron removal in each reference, and each additional line show changes in additional experiments. *Values with units are half-lives and expressions or values without units are total mass transfer coefficients [μm/s].

Author Method (Year)	Reactants Atmosphere	Scale Temperature	Gas flow [l_N/min/kg]	Volatile B species	Half-life* k_t [μm/s]
Theuerer [28]	1.3%H_2O	Lab	2993		2 s
Zone refining (1956)	in H_2	1414 °C			$3.6 \cdot 10^3 \sqrt{[\text{vol}\%]_{H_2O}}$
Suzuki et al. [25]	1.24%H_2O	5.5 g	21	BO, BO_2,	38 min
Plasma (1992)	in Ar	1414 °C		B_2O_3	13
Ikeda and Maeda [62]	1.24%H_2O	10 g	750		3 min
Rotating plasma (1996)	in Ar	1414 °C			77
Khattak et al. [15]	H_2O	<300 kg		HBO,	97 min
Bubbling/slag (2001)	in H_2	1450 °C		HBO_2	(60 kg)
Alemany et al. [13]	H_2/O_2	<10 kg		BOH	
Plasma (2002)	in Ar				
Fourmond et al. [53]	1.8%O_2	3-10 kg	26-7.8	BOH	34 min
Plasma (2004)	3.2%H_2/Ar				35-41
Nakamura et al. [11]	4.3%H_2O	<300 kg	7.4	BO	144 min
Plasma (2004)	50.6%H_2/Ar		$[\text{vol}\%]_{H_2O}(2.5 \cdot 10^{-5} + 1.8 \cdot 10^{-10}[\text{vol}\%]_{H_2}^{3.2})$		
Einhaus et al. [12]	H_2/O_2	<60 kg	26-7.8	BOH	34 min
Plasma (2006)	in Ar				
Wu et al. [32]	H_2O/O_2			BH_3O_6,	3.2 min
Plasma (2009)	in Ar			BHO_2	
Lee et al. [33]	H_2/H_2O			BOH	3.3 min
Plasma (2011)	in Ar				
Imler et al. [63]	H_2/O_2	<2.6 kg			24 min
Plasma (2011)	in Ar				
Nordstrand and	3.2%H_2O	200 g	15	HBO	18 min
Tangstad [17]	in H_2	1450 °C			13
Gas blowing (2012)	in H_2	1500 °C			10
	in Ar	1500 °C			1.2
	100%H_2	1500 °C		BH_2	0.75
Sulentic [54]	3.2%H_2O	40 g	33		8 min
Gas blowing (2012)	48.4%H_2/Ar	1500 °C			20
Altenberend [18]	0.8%O_2	2.9 kg	40	HBO	95 min
Plasma (2012)	4.2%H_2/Ar	1414 °C		HBO_2	13
Safarian et al. [41]	5.9%H_2O	400 g	3	HBO	36 min
Gas blowing (2014)	in H_2	1500 °C			14

One plasma refining experiment by Wu et al. [32] in 2009 with an Ar/H$_2$O/O$_2$ plasma at vacuum of 10^{-8} bar show a very high removal rate with half-life of close to 3 min in the first 10 min, but then the reaction stopped. In 2011, Lee et al. [33] compared plasma refining of MG-Si with argon, Ar/H$_2$, Ar/H$_2$O and Ar/H$_2$/H$_2$O plasmas, for which an increasing removal ratio of boron of respectively 39%, 50%, 52% and 65% was achieved after 5 min. This converts to half-lives of 7.0 min, 5.0 min, 4.7 min and 3.3 min if a first order dependence of the boron concentration is assumed, although no significant boron removal was observed in the first 3 min of the plasma treatment. The empirical rate expression found by Nakamura et al. [11] in Table 2.4 relates to the dimple area.

2.3 Process Kinetics

Removal of boron proceeds through a series of steps outlined in Figure 2.4. Steps 1-3 transfer boron across the melt surface and step 4 moves boron away from the surface. The melt is considered as a reservoir from which boron is removed across the interface. Step 1 of boron removal is thus supply of boron from the melt, which at the interface proceeds by diffusion. Convection is important for transport of boron within the melt reservoir. Section 2.3.1 explains that convection inside the melt also is important for diffusion of boron to the interface, for instance by bringing a body of melt with bulk boron concentration close to the interface. The effect of melt convection on the rate of boron removal is expressed through the extent at which it enhances diffusion to the interface.

The melt and gas flow over the surface represents an open system into which gas enters from the lance exit and leaves in step 4. Instead of defining an exact border for the system, step 4 is considered to include all of the gas flow and condensed matter that permanently leaves the surface. Although boron has been observed in the silica fume [11], condensation of HBO in the gas is not expected to affect boron removal from the melt. Equilibrium modeling with a relatively high partial pressure of HBO (0.24 mbar) together with silica fume in hydrogen does not indicate B$_2$O$_3$ formation above 430 °C, and the gas is assumed to leave the system before HBO condenses.

The removal of boron depends on the supply of steam presented in Section 2.3.6 as well as the concentration of hydrogen as reactants for HBO formation at the interface. SiO formed at the interface leaves the system as silica fume particles. Fuming is in Section 2.3.6 considered to occur within the gas boundary layer and consume part of the steam in Reaction (2.19) before it can be supplied to the interface. Its equilibrium constant is high ($K_{H_2O+SiO} = 9 \cdot 10^5$ for partial pressures in Figure 2.2 at 1500 °C) and the reaction tends towards the stoichiometric limit where it consumes 50% of the steam (with the remaining 50% producing SiO and minor amounts of HBO at the interface). The fraction of steam in the feed that is supplied to the interface ($\frac{p^s_{H_2O}}{p_{H_2O}}$) depends on the extent at which Reaction (2.19) reaches completion within the gas boundary layer and diffusion of steam towards the interface.

$$H_2O + SiO = SiO_2 \text{ (l/s)} + H_2 \tag{2.19}$$
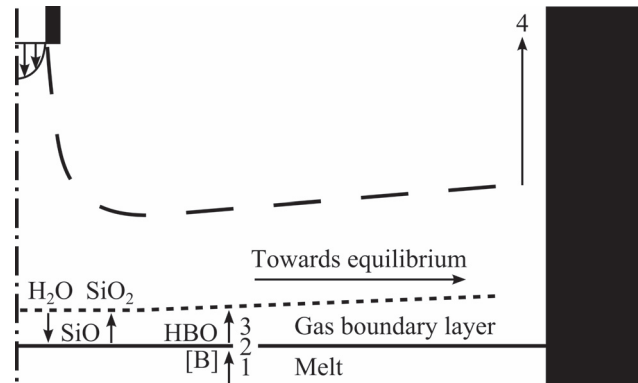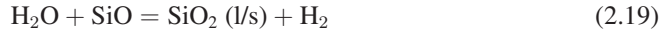
Figure 2.4: Overview of boron removal process with supply of steam to the melt surface, active oxidation of silicon and mass transfer for boron through steps 1-4. The crucible center is to the left of the figure and the crucible wall to the right. The gas is blown from the lance in the upper left corner an flows along the melt surface according to the impinging jet flow pattern indicated by stapled lines before leaving the surface in step 4. The flow pattern does not include effects of deflection by the crucible wall.

To sum up, boron is removed from the melt through the following mass transfer steps.

1. Diffusion from the melt to the interface (depends on convection inside the melt).

2. Interface reactions, which transfer boron from the melt to the gas at the interface.

3. Diffusion from the interface to the bulk of the gas.

4. Convection by bulk gas flow.

Mass balance over a differential area (start of Equation (2.20)) defines the flux to be positive into the melt (downwards), while boron is removed out of the melt (upwards in Figure 2.4) and the fluxes have negative values. It is worth noting that the rate is directly related to the flux since the area considered is constant (i.e. the crucible cross-section). Continuity requires the transfer of boron to be equal through all the steps as shown in Equation (2.20) at steady state, for which the total driving force is distributed over each step ($\Delta_{1\text{-}4}C$) according to the mass transfer coefficients for the different steps ($k_{1\text{-}4}$). Each step poses a resistance to mass transfer of boron. The resistance is inverse to the mass transfer coefficient.

$$-\frac{\mathrm{d}n_{[\mathrm{B}]}}{\mathrm{d}A\mathrm{d}t} = -J_{\mathrm{B}} =$$

$$k_1 \underbrace{(C_{[\mathrm{B}]} - C_{i,[\mathrm{B}]})}_{\Delta_1 C} = k_2 \underbrace{(C_{i,[\mathrm{B}]} - C_{i,\mathrm{HBO}})}_{\Delta_2 C} = k_3 \underbrace{(C_{i,\mathrm{HBO}} - C_{b,\mathrm{HBO}})}_{\Delta_3 C} = k_4 \underbrace{C_{4,\mathrm{HBO}}}_{\Delta_4 C} \qquad (2.20)$$

In Equation (2.20), $C_{[\mathrm{B}]}$ is the bulk concentration of boron in the melt and $C_{i,[\mathrm{B}]}$ is the interface concentration of boron. The bulk of the melt is thus defined in terms of concentration and it is considered to be the part of the melt at approximately constant or maximum concentration. Correspondingly, there is no resistance and no driving force acting in what is considered as the bulk of the melt. In small-scale experiments, natural or forced convection is expected to cause a relatively narrow boundary layer so that almost the entire melt is considered as the bulk. Diffusion to the interface is driven by the difference between bulk and interface concentrations, which in Section 2.3.1 is used in expressions for the rate of diffusion at the interface. Boron reacts to HBO with concentration $C_{i,\mathrm{HBO}}$ at the interface, $C_{b,\mathrm{HBO}}$ in the bulk of the gas flow along the surface (above the gas boundary layer) and $C_{4,\mathrm{HBO}}$ in the gas flow leaving the system in step 4.

Step 4 is not a direct continuation of step 3 because boron accumulates in the gas while flowing horizontally over the surface before the flux continues upwards in step 4. The accumulation of HBO and silica fume in the gas flow along the surface is accounted for by the finally accumulated concentration C_4 in step 4 ($\frac{1}{Q}\frac{\mathrm{d}n_{\mathrm{SiO}_2}}{\mathrm{d}t}$ for silica fume in gas of flow rate Q). These products are accumulated as the reactions proceeds towards equilibrium while the gas flows along the surface, and steam is also consumed from the gas flow along the surface. Since step 4 does not take place near the interface, it does not relate to the interface area and continuity in Equation (2.20) only holds for the rate of removal (or average flux related to the interface area) when step 4 is included. Mass transfer through steps 1-3 may however be assumed unidirectional normal to the interface, so continuity and fluxes in these steps can be expressed for any location along the melt surface.

The rate expressions for steps 1-3 add together to a rate expression that describes boron removal across the surface (supply of boron to reactions and removal of HBO), while the total rate expression in Equation (2.21) includes step 4. These expressions are combined in Section 2.3.5 from models for each step in Sections 2.3.1-2.3.4. The total rate expression describes boron removal from the melt and out of the system (eventually to the environment with $C_{\mathrm{HBO}} = 0$). The total driving force thus equals the bulk concentration in the melt, which can be measured in experiments. The resistances in each step adds together to a total resistance ($\frac{1}{k_t}$) in Equation (2.22).

$$J_{\mathrm{B}} = -k_t C_{[\mathrm{B}]} \tag{2.21}$$

$$\frac{1}{k_t} = \frac{1}{k_1} + \frac{1}{k_2} + \frac{1}{k_3} + \frac{1}{k_4} \tag{2.22}$$

If the interface reactions are at equilibrium, the equilibrium constant can relate the interface concentration of HBO in the gas to that of boron in the melt without knowledge of the reaction kinetics. The resistance $\frac{1}{k_2}$ is then negligible (Section 2.3.2). In many cases, only one step dominates the total resistance, here exemplified by step 1, if its mass transfer coefficient is by far lower than that of any other step ($k_1 \ll k_{\mathrm{k} \neq 1}$). This step (1) is said to be rate determining and the other steps (2-4) are said to be fast. The resistances posed by the fast steps can be neglected ($\sum_{\mathrm{k} \neq 1} \frac{1}{k_{\mathrm{k}}} \ll \frac{1}{k_1}$) in Equation (2.22). The total mass transfer coefficient then equals that of the rate determining step and the total driving force $\Delta_t C = C_{[\mathrm{B}]}$ acts predominately over this step. The concentration differences necessary to drive the fast steps at the same rate are negligible. Each step has a rate limit, which is reached if the total driving force acts across this step only. Accordingly, the total mass transfer coefficient approximates the rate limit for the rate determining step.

Measurements of the boron removal rate only give information about the kinetics of steps that determine the total rate (i.e step 1 in the above example, since $k_t \approx k_1$). The rate determining step can thus be identified experimentally by comparing how the rate or the total mass transfer coefficient depends on variations of experimental parameters to the kinetic models for each step (described in Sections 2.3.1-2.3.4 and 2.3.6). If the resistance of more than one step contributes significantly to the total resistance, it is said to be mixed rate limitation. The total resistance over steps 1-4 becomes a sum of the steps that can not be neglected in Equation (2.22). The total mass transfer coefficient depends on the experimental parameters that determine the mass transfer coefficient for all of these steps, but not as strongly as expected from the rate limit of the step they take effect through. Mixed control can be evaluated from the total mass transfer expressions in Section 2.3.5.

The rates of consumption of reactants and production of products in each reaction at the interface are related through the stoichiometry of the reaction as exemplified for Reaction (2.23) in Equation (2.24). Consequently, the rate of supply of the reactive gases can also be rate determining for boron removal (Section 2.3.6).

$$[\mathrm{B}] + \mathrm{H_2O} \rightleftarrows \tfrac{1}{2}\,\mathrm{H_2} + \mathrm{HBO} \tag{2.23}$$

$$-\frac{\mathrm{d}n_{[\mathrm{B}]}}{\mathrm{d}t} = -\frac{\mathrm{d}n_{\mathrm{H_2O}}}{\mathrm{d}t} = 2\frac{\mathrm{d}n_{\mathrm{H_2}}}{\mathrm{d}t} = \frac{\mathrm{d}n_{\mathrm{HBO}}}{\mathrm{d}t} \tag{2.24}$$

2.3.1 Mass Transfer from Melt

Mass transfer in a fluid like the melt proceed through the mechanisms of diffusion and convection. At the interface, a concentration gradient drives diffusion of dilute impurities like boron from the melt. The concentration gradient at the interface depends on its distance from the bulk concentration of boron. Convection can move the surface itself and expose a body of melt with bulk concentration, but a diffusion layer would in principle start to grow immediately or in advance. Mass transfer of boron from the melt is thus presented in terms of diffusion to the interface. Convection within the melt greatly enhances the rate of diffusion to the interface. Convection distributes boron within the bulk and limits the growth of the diffusion layer by maintaining a front with bulk concentration of boron. Such a front is hypothetical and not necessarily constant over time and position. Additionally, convection can also contribute to transport boron towards the interface within the diffusion layer.

The rate of diffusion is at steady state proportional to the concentration gradient according to Fick's first law. Fick's first law is shown for diffusion of boron in the melt to the interface in Equation (2.25), where $D_{[B]}$ is the diffusion coefficient of boron in the silicon melt.

$$J_{\mathrm{B}} = -D_{[\mathrm{B}]}\nabla C_{i,[\mathrm{B}]} \tag{2.25}$$

The simplest model for mass transfer is the film theory [65], in which steady state diffusion according to Equation (2.25) transfer mass at a constant rate from the bulk to the interface through a stagnant boundary layer of thickness δ. Equation (2.26) expresses the film model for diffusion of boron from the melt.

$$J_{\mathrm{B}} = -\underbrace{\frac{D_{[\mathrm{B}]}}{\delta_{[\mathrm{B}]}}}_{k}\underbrace{\frac{\rho}{M}(x_{[\mathrm{B}]} - x_{i,[\mathrm{B}]})}_{\Delta_1 C} \tag{2.26}$$

The driving force for diffusion is the concentration difference between bulk and the interface, and the mass transfer coefficient depends on convection in the bulk through the boundary layer thickness. Increasing bulk fluid velocities qualitatively decreases the boundary layer thickness and increases the mass transfer coefficient.

Film theory gives wrong dependence on the diffusion coefficient, at least compared to experiments with turbulent liquid flow. Furthermore, the boundary layer thickness is hypothetical as there is not a sudden transition from the bulk to the boundary layer in reality, both regarding melt velocity and the concentration gradient. Models that agree with experimental measurements of mass transfer in turbulent liquids and produce actual concentration profiles are based on transient diffusion according to Fick's second law in Equation (2.27), where z is distance normal to the interface.

$$\frac{\partial C}{\partial t} = D\frac{\partial^2 C}{\partial z^2} \tag{2.27}$$

Penetration theory assumes eddy currents in turbulent liquids to extend through the boundary layer and expose liquid with bulk concentration directly to the surface. The liquid exposed to the surface is assumed to be stagnant, and transient diffusion immediately starts to build a concentration boundary layer. The boundary layer grows until the surface is renewed by a new eddy current after a constant exposure time. Surface renewal theory assumes a more realistic Gaussian distribution of the exposure time for different eddy currents. The variation in boundary layer thickness with time in one location at the interface is conceptualized in Figure 2.5. Equation (2.28) gives the average flux of boron to the interface for the surface renewal theory, where τ is the mean exposure time of the eddy currents and depends on melt convection.
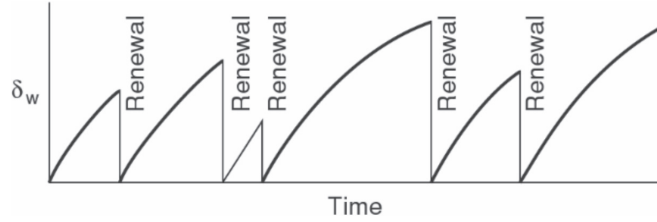
Figure 2.5: Schematic of boundary layer variation with time in surface renewal theory (Gulliver [65]).

$$J_{\text{B}} = -\underbrace{\sqrt{\frac{D_{[\text{B}]}}{\tau}}}_{k_1} \underbrace{\frac{\rho}{M}(x_{[\text{B}]} - x_{i,[\text{B}]})}_{\Delta_1 C} \tag{2.28}$$

If step 1 limits the removal rate ($k_1 \ll k_{\text{k} \neq 1}$), boron is consumed instantly as it reaches the interface ($x_{i,[\text{B}]} \approx 0$ in Equation (2.28)). The flux of boron out of the melt can then be calculated by Equation (2.29).

$$J_{\text{B}} = -\underbrace{\sqrt{\frac{D_{[\text{B}]}}{\tau}}}_{k_t \approx k_1} \underbrace{\frac{\rho}{M}x_{[\text{B}]}}_{C_{[\text{B}]}} \quad \text{if } k_1 \ll k_{\text{k} \neq 1} \tag{2.29}$$

For rate limitation by step 1, the total mass transfer coefficient increases strongly with melt convection. Additionally, diffusion coefficients in liquids increase with increasing temperature and decreases with increasing total pressure [66].

Suzuki et al. [25] assumed step 1 to be the rate determining step in plasma refining experiments with no device for stirring the melt. They calculated a mass transfer coefficient of $1.3 \cdot 10^{-5}$ m/s as an average over the melt surface. This was however deemed too slow compared to the expected rate limit of step 1, considering strong convection of the 5.5 g melt by

the impinging plasma jet. Consequently, they suggested that the reaction only occurred in the plasma impingement area and found the mass transfer coefficient of $1.4 \cdot 10^{-4}$ m/s calculated based on the plasma torch cross-section area to be more reasonable and thus suggested that boron is only removed by reactive plasma species. Another explanation could be that mass transfer from the melt is not rate determining.

Degoulange [67] observed a contribution of step 1 to the resistance for boron removal only without stirring, and thus saw the importance of stirring the melt. He reported a time constant for induction stirring of about 7 min, which is fast compared to reported half-lives of boron removal (Table 2.4). Altenberend [18] calculated that mass transfer by step 1 should not be rate determining for half-lives of boron removal much longer than 3 min for his experiments with an optimal induction frequency for stirring. The average mass transfer coefficient for step 1 over his crucible cross-section calculates to $k_1 = 5.3 \cdot 10^{-4}$ m/s with this half-life in Equation (2.18). Considering that stirring varies greatly with induction power and frequency, time constants by Degoulange [67] and Altenberend [18] are in relative good agreement. Both Altenberend [18] and Nakamura et al. [11] considered mass transfer from the melt to be fast as reducing melt convection by high frequency induction in plasma experiments did not reduce the rate of boron removal.

2.3.2   Interface Reaction

Heterogeneous reactions at the interface converts boron in the silicon melt to predominately HBO in the gas. Which reactions that actually occur is not readily known and Section 2.3.2 presents possible reaction schemes. The simplest global reaction for volatilization of boron by steam to form HBO at the interface is shown in Reaction (2.30). Reactions at an interface may be compared by the reaction rate per area, and thus represent a flux of boron atoms across the interface. The rate of reaction increases with increasing reactant concentrations at the interface. In the case that Reaction (2.30) is an elementary reaction (describes a single molecular collision), its rate can be expressed by Equation (2.31). The reaction order (α_j) is typically a positive integer, as it is deduced from stoichiometry of reactants in an elementary reaction [68]. If Reaction (2.30) is rate determining for boron removal, the HBO product is assumed to be immediately removed and the net rate of reaction is given by the rate of the forward reaction in Equation (2.31). Otherwise, HBO and hydrogen can also collide and reform steam and boron, and the rate of this back-reaction depend on the concentrations of HBO and hydrogen in a similar expression to Equation (2.31) and the net rate is the difference between that of the forward reaction and back-reaction. Equilibrium concentrations establish if the net rate of boron removal or steam supply is slow compared to the reaction kinetics, because the equilibrium concentrations provide equal rates of the forward reaction and back-reaction.

$$H_2O + [B] \rightarrow HBO + \tfrac{1}{2} H_2 \tag{2.30}$$

$$J_B = - \underbrace{k C_{i,H_2O}^{\alpha_{H_2O}} C_{i,[B]}^{\alpha_{[B]}}}_{k_2} \tag{2.31}$$

Reaction orders can be evaluated experimentally by comparing mass transfer coefficients for boron from experiments with different concentrations of a reactive gas according to the Ostwald isolation method [68]. By this method, the reactive gas composition is held constant throughout each experiment, and the concentration of one reactant is varied over a series of experiments. This method is also used to determine dependencies of other parameters on the reaction rate.

Reaction rates increase strongly with temperature as rate constants (k_2) typically follow Arrhenius relationships shown in Equation (2.32). E_a is the activation energy and represent an energy barrier the reactants must overcome in order to break bonds in the reaction, and k_0 is a frequency factor.

$$k = k_0 e^{-\frac{E_a}{RT}} \tag{2.32}$$

If the overall boron removal rate is only limited by interface reactions kinetics, fast mass transfer can be approximated to supply reactants at bulk concentrations and instantly remove HBO from the interface. Thus, bulk concentrations of reactants in rate expressions like (2.31) represent the reaction rate limit. If mass transfer is not sufficiently fast to instantly remove HBO from the interface, product concentrations build up at the interface. Products act as reactants for the reverse reaction and the rate of back-reaction increases with increasing product concentrations at the interface. Experimental investigations of reaction rates and mechanisms require fast mass transfer of products compared to the rate of reaction because the rate of back-reaction must be negligible in order to measure the rate of the forward reaction. If the chemical reactions are fast compared to mass transfer, the forward and reverse reaction will proceed at approximately equal rates and equilibrium is established.

Data for the reaction orders and the evaluations of whether the interface reaction is rate determining or fast varies considerably in the literature, as shown in Table 2.5. Nakamura et al. [11] found boron removal to be unaffected by melt agitation and plasma gas flow rate, and Nordstrand and Tangstad [17] consistently suggested that interface reactions determine the overall boron removal rate. Altenberend [18] explained the dependence on reactant concentrations and temperature in his own and previous works (not Nakamura et al. [11]) by equilibrium at the interface, and instead proposed the mass transfer of steam from the gas to be rate determining. The possibility of rate limitation by mass transfer of HBO to the gas has not been considered in previous works, although thermodynamics dictates that the partial

pressures of HBO at the interface is low for refining of MG-Si to SoG-Si ($10^{-5} - 10^{-7}$ bar), which represents a low limit to the driving force.

Steam is assumed to be disintegrated in monoatomic oxygen and hydrogen radicals (and minor amounts of OH) [18] in plasma refining experiments, so that introducing oxygen and hydrogen into the plasma can be considered equivalent to introducing steam. This is also the case for increasing oxygen contents with excess hydrogen in plasma refining by Alemany et al. [69]. In Table 2.5, α_{H_2O} thus include oxygen radicals for plasma refining experiments. The data might suggest that the reaction order for steam is $\alpha_{H_2O} = \frac{1}{2}$ in the reactive gas refining experiments differ from the reaction order of plasma radicals of 1 in plasma refining experiments, although Altenberend [18] suggested that steam is supplied to the surface also in plasma refining (the melt surface cools the plasma).

Table 2.5: Summary of experimental reaction orders and suggested rate determining step (RDS), compared to equilibrium.

Gas and method [Reference]	RDS	α_{H_2O}	α_{H_2}	$\alpha_{[B]}$
H_2O/H_2 zone refining [28]		$\frac{1}{2}$		1
H_2O/H_2 impinging jet [17]	2	$\frac{1}{2}$	$\frac{1}{2}$ [18]	1
H_2O/Ar plasma [25]		1 ($\leq 1.6\%$ H_2O)		1
$H_2O/H_2/Ar$ plasma [11]	2	1	3.2	1
$O_2/H_2/Ar$ plasma [69]		1 (40% H_2)		1
$O_2/H_2/Ar$ plasma [18]	Steam supply	> 0	$\frac{1}{2}$	1
$[B] + SiO + \frac{1}{2} H_2 \rightleftarrows HBO + [Si]$	Steam/3/4	1	$\frac{1}{2}$	1

Nakamura et al. [11] and Nordstrand and Tangstad [17] suggested that interface reactions determine the overall boron removal rate based on increasing reaction rates with increasing steam and hydrogen contents in the feed gas. However, Sections 2.3.3 and 2.3.4 reveal that reaction rate also depend on the content of reactive gases if steam supply, step 3 or 4 is rate determining. The observation that the boron removal rate increases with the content of hydrogen at least reveals that Reaction (2.30) can not alone represent the interface reactions. Nakamura et al. [11] presented the empirical mass transfer coefficient in Equation (2.33) for plasma refining experiments. Bulk concentrations, presented as volume percent [vol%] in Equation (2.33), are representative at the interface assuming fast mass transfer.

$$k_t \approx k_2 = [\text{vol\%}]_{H_2O} \cdot (2.5 \cdot 10^{-5} \text{ m/s} + 1.8 \cdot 10^{-10} \text{ m/s} \cdot [\text{vol\%}]_{H_2}^{3.2}) \qquad (2.33)$$

If interface reactions are not rate determining for boron removal, equilibrium is established at the interface. It is often reasonable to assume reactions to be fast and at equilibrium for the high temperatures of molten metal, due to the strong temperature dependence in Equation (2.32) [56]. Indication of equilibrium at the interface are the decreasing mass transfer coefficients Nordstrand and Tangstad [17] found with increasing temperature and the reaction

order for hydrogen of $\frac{1}{2}$ found in most experiments in Table 2.5. Altenberend [18] measured the same dependencies during plasma refining, and explained them by chemical equilibrium at the interface. He proposed the global Reactions (2.34) and (2.35) to be at equilibrium at the interface. Consequently, he concluded that boron volatilization by a reactive radicals in plasma is equivalent to volatilization by stable species in reactive gas refining.

$$[Si] + H_2O \rightleftarrows SiO + H_2 \tag{2.34}$$
$$[B] + H_2O \rightleftarrows HBO + \tfrac{1}{2} H_2 \tag{2.35}$$

The equilibrium reaction orders for steam and hydrogen are observed by a slight majority of the investigators in Table 2.5. Further kinetic analyzes in this chapter consider equilibrium at the interface in accordance with the temperature and hydrogen dependencies in experiments by Nordstrand and Tangstad [17] and the most recent developments.

Thermodynamic calculations in Section 2.1 provides a low distribution coefficient for boron ($\frac{x_{HBO}}{x_{[B]}} = 0.20$). Such a low distribution coefficient is a typical sign that mass transfer to the gas phase may be slow compared to mass transfer from the melt [70] and chemical reactions at the interface in case of equilibrium. The low partial pressure of HBO provides a low driving force for diffusion to the gas compared to diffusion of boron from the melt. It can be reasoned that diffusion of HBO to the gas might be slow also compared to supply of steam to the surface, and should thus be included in the consideration of rate determining steps for boron removal.

The maximum HBO content at the interface during refining is according to thermodynamic calculations roughly 10^{-5} bar for MG-Si with around 30 ppmw boron and 10^{-7} bar for the SoG-Si with 0.3 ppmw boron. The HBO concentration at the interface, which drives diffusion of HBO from the surface, is thus several orders of magnitude lower than the steam concentration in the reactive gas, which drives diffusion of steam to the interface. However, the reaction between steam and SiO above the interface (Section 2.3.6) can reduce the rate of steam that reaches the interface compared to simple diffusion. A comparison of mass transfer coefficients for steam supply and HBO removal thus relies on a model for the consumption of steam above the interface. Furthermore, only a small fraction of steam that reacts at the interface oxidizes boron at low concentrations in MG-Si and SoG-Si, while steam reacts almost exclusively to SiO.

The amount of boron removed compared to the amount of silicon lost as SiO is calculated from a representative experiment (Experiment 2) by Nordstrand and Tangstad [17] to 0.3% for an average boron content of 20 ppmw during the experiment. In comparison, the thermodynamic model in Section 2.1 calculates this ratio to $\frac{p_{HBO}}{p_{SiO}} = 0.03\%$ for 20 ppmw boron in the melt. The ratio of boron to silicon oxidation thus appears greater in the experiment than equilibrium calculations, which agrees with the higher enrichment ratios observed in experiments compared to thermodynamic calculations by Altenberend [18] presented in Table 2.3.

Silicon oxidation has been found to be determined by the rate of oxygen supply to the surface (Section 2.3.6), and any other rate limitations for boron oxidation can only reduce the ratio of boron to silicon oxidation compared to equilibrium. The higher boron to silicon oxidation ratios in experiments than calculated for equilibrium may thus suggest that steam supply is rate determining also for boron removal. There are however issues regarding the accuracy of measuring the ratio of silicon and boron [18] as well as the thermodynamic data.

The thermodynamic model used for Figure 2.2 is representative for equilibrium at the interface, and can relate the partial pressure of HBO to the boron content in the melt at the interface. The overall reaction between the dominant species presented at the interface (Reaction (2.3)) can be constructed for production of HBO by reversing Reaction (2.34) and eliminate steam in Reaction (2.35). The distribution coefficient for Reaction (2.37) (Equation (2.4)) is rearranged to show the partial pressure of HBO at the interface in Equation (2.38). The reactions will not change the partial pressure of hydrogen if it is present in large excess. Furthermore, high contents of hydrogen introduced in the reactive gas provides fast mass transfer to the interface so that the interface and bulk partial pressures are essentially equal ($p_{i,H_2} \approx p_{b,H_2}$ in Equation (2.38)).

$$[Si] + H_2O \rightleftharpoons SiO + H_2 \tag{2.36}$$

$$[B] + SiO + \tfrac{1}{2} H_2 \rightleftharpoons HBO + [Si] \tag{2.37}$$

$$p_{i,HBO} = \frac{K_{HBO/SiO}}{p^{\ominus \frac{1}{2}}} \gamma_{[B]} x_{i,[B]} p_{i,SiO} p_{i,H_2}^{\frac{1}{2}} \tag{2.38}$$

The reaction orders for equilibrium can be deduced from comparing exponents in Equation (2.31) and (2.38), as the flux of boron out in the gas is proportional to the concentration of HBO (Section 2.3.3 and 2.3.4). Additionally, concentrations are proportional to partial pressure of gases and mole fraction of boron in the silicon melt (Equation (2.9)). The reaction orders in Equation (2.31) equal the stoichiometric coefficients in Reaction (2.37) for HBO formation at equilibrium (Equation (2.38)).

HBO formation at equilibrium in Equation (2.38) provides a reaction order for hydrogen of $\tfrac{1}{2}$, as measured in most experiments in Table 2.5. The equilibrium reaction order of 1 for steam also agrees with the majority of experiments in Table 2.5. The partial pressure of HBO is also proportional to the boron concentration at the melt interface in Equation (2.38), which agrees with the reaction order of 1 observed in all experiments in Table 2.5. Steam is converted essentially stoichiometrically to SiO at equilibrium as Reaction (2.36) has a high equilibrium constant ($K_{SiO/H_2O} = 850$ at 1500 °C). The concentration of SiO is thus proportional to the supply of steam from which the interface equilibrium is established. Consequently, the reaction order for steam is expected to equal 1 like that of SiO in Equation (2.38) for equilibrium at the interface. Studies of plasma refining in Table 2.5 have found the same dependence of steam content on the rate of boron removal. However, studies of

42

reactive gas refining report a reaction order of $\frac{1}{2}$ for steam based on three [28] and two [17] experimental measurements.

The temperature dependence of the distribution coefficient follows the HBO partial pressure, which is shown to decrease with increasing temperature for a constant SiO partial pressure above $1500\,°C$ in Figure 2.2. However, an increasing temperature is found to allow higher partial pressures of SiO and thus higher steam supply for the threshold of passivation (below $1500\,°C$ in Figure 2.2), and the HBO removal rate may be increased by increasing temperature and steam partial pressure simultaneously. Altenberend [18] found the temperature dependence for the HBO partial pressure at equilibrium to agree with experiments, including plasma refining by Imler et al. [63] and Baba et al. [71] and reactive gas refining by Nordstrand and Tangstad [17].

Reaction Schemes

Reaction proceeds through series of collisions which each represent a reaction step. Reaction steps suggested in previous works are here summarized as possible reaction schemes. The heterogeneous reaction for boron volatilization must include adsorption of the reactive gases to the melt surface and desorption of gaseous products from the surface. The reaction can also proceed through dissolved species in a narrow layer near the surface of the melt, and Safarian et al. [41] also proposed dissolution of hydrogen and subsequent reaction with steam in the sequence of Reactions (2.39)-(2.40). Minor amounts of hydrogen react to HBO, and the hydrogen partial pressure in the feed gas may presumably also be maintained at the interface, and can thus dissolve into the melt. Safarian et al. [41] observed pores in solidified silicon after experiments with hydrogen atmosphere as a sign of significant dissolution of hydrogen into the melt. They calculated hydrogen content in liquid silicon to $25\ \mathrm{ppma}$ ($0.90\ \mathrm{ppmw}$) in equilibrium with $1\ \mathrm{bar}$ hydrogen at $1430\,°C$.

$$\tfrac{1}{2}\,\mathrm{H_2} = [\mathrm{H}] \tag{2.39}$$

$$[\mathrm{B}] + [\mathrm{H}] + \mathrm{H_2O} = \mathrm{HBO} + \mathrm{H_2} \tag{2.40}$$
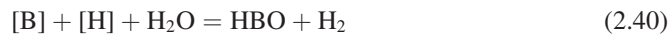
In 1987 Amouroux et al. [29] proposed a mechanism of oxidation to $\mathrm{B_2O_3}$ in the liquid silicon, evaporation of this specie at the liquid-plasma interface and subsequent decomposition to boron radicals in the plasma. This mechanism was found to directly depend on the oxygen content in a plasma. Degoulange [67] later considered possible mechanisms to include dissolution of oxygen and hydrogen into the melt and HBO formation to take place within a boundary layer of the melt. Figure 2.6 summarizes the possible mechanisms with plasma reactants.

Degoulange [67] proposed steps to first form stable intermediates of BO complexes in the melt and SiO gas at the interface, and argued that HBO formation proceeds from the BO

43
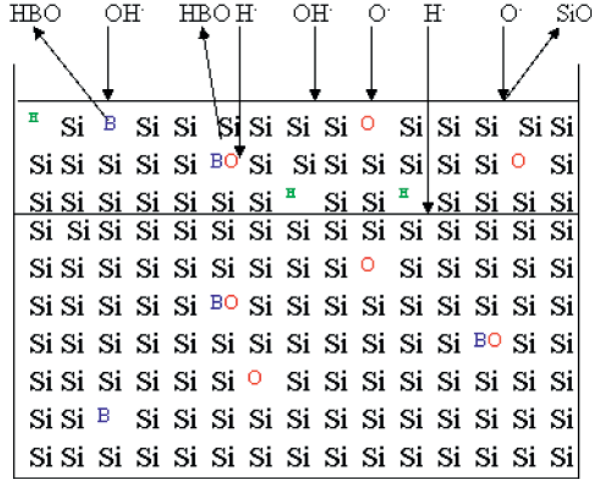
Figure 2.6: Schematic mechanism of boron volatilization by an $Ar/H_2/O_2$ plasma proposed by Degoulange [67]. The boundary layer is indicated in the upper section of the silicon melt.

complexes. Steps (2.41)-(2.43) show an extract of steps for formation of HBO through dissolution of oxygen and the BO complex. An analogy to reactive gas refining can be drawn by replacing $H^{\cdot} = \frac{1}{2} H_2$ and $OH^{\cdot} + \frac{1}{2} H_2 = H_2O$. $H^{\cdot}$ denotes a hydrogen radical with an unpaired valence electron.

$$OH^{\cdot} \rightarrow [O] + H^{\cdot} \tag{2.41}$$

$$[O] + [B] \rightarrow [BO] \tag{2.42}$$

$$[BO] + H^{\cdot} \rightarrow HBO \tag{2.43}$$

In the case that boron volatilization proceeds through BO complexes, oxygen can alternatively be supplied through the melt. Compared to an oxygen supply of $1 \text{ vol\%}$ O_2 in the argon plasma, Altenberend [18] observed a fourfold decrease in the silicon loss rate with oxygen supply by dissolution of silica plates. He reasoned that the dominant silicon specie in the gas was SiO in pure argon and SiO_2 when oxygen was introduced, and thus that the transport of oxygen to the interface was 7 times higher from the plasma than from dissolution of the silica plates.

An oxidizing agent like steam or $OH^{\cdot}$ adsorbed to the surface has much higher probability to react with silicon compared to boron since boron is highly diluted in the silicon melt. Oxidation of silicon in the parallel Step (2.44) can thus be assumed to occur at orders of magnitude higher rates than oxidation of boron. As a consequence, SiO may be readily available on the interface for oxidation of boron in Reaction (2.45). Degoulange [67] assumed

44

it more likely that OH˙ reacts directly with boron on the interface, due to the highly decreased probability of three species colliding in Step (2.45) compared to reactants in Step (2.46).

$$[Si] + OH^{˙} \rightarrow SiO + H^{˙} \tag{2.44}$$

$$[B] + SiO + H^{˙} \rightarrow HBO + [Si] \tag{2.45}$$

$$[B] + OH^{˙} \rightarrow BOH^{˙} \rightarrow HBO \tag{2.46}$$
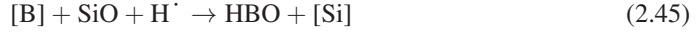
Degoulange [67] observed that oxygen initially dissolved in silicon reduced the rate of boron volatilization and concluded that Reaction (2.46) is faster than (2.43) due to the increased reactivity of oxygen radicals in the plasma. Altenberend [18] compared simultaneous and sequential supply of oxygen and hydrogen in plasma refining experiments. He reasoned that dissolved species are not important for boron removal to gas as significantly higher rates were obtained for simultaneous supply of reactants.

Kinetic limitations of specific steps does however only affect the rate of boron volatilization if they are rate determining in the reaction mechanism and at the same time the interface reaction is rate determining for the overall boron removal process. In the case of equilibrium at the interface, the rate of boron removal is independent of the reaction scheme and kinetics of any reaction step, in that back-reactions ensure that the concentrations at the interface are fixed at their equilibrium values.

2.3.3 Mass Transfer to Gas

HBO is removed from the surface into the bulk gas by diffusion through a boundary layer. The driving force for diffusion is the concentration difference between the surface and the bulk gas, which in Equation (2.47) is converted to partial pressure through the ideal gas law (Equation (2.9)).

$$J_{\mathrm{B}} = -k_{\mathrm{HBO}} \underbrace{\frac{1}{RT}(p_{i,\mathrm{HBO}} - p_{b,\mathrm{HBO}})}_{\Delta_3 C} \tag{2.47}$$

The boundary layer thickness and the mass transfer coefficient relies on fluid dynamics, like for diffusion in the melt. The fluid dynamic mass transfer coefficient for diffusion of HBO (k_{HBO}) and the boundary layer thickness may be calculated from the dimensionless Sherwood number (Sh) in Equation (2.48). Reynolds number (Re) in Equation (2.49) and the Schmidt number (Sc) in Equation (2.50) are the other dimensionless numbers for transport of mass. Re relates to the flow characteristics and its value indicate whether the flow is laminar (relatively low Re) or turbulent (high Re).

$$Sh = \frac{k_{\text{HBO}}L}{D_{\text{HBO}}} = \frac{L}{\delta_{\text{HBO}}} \tag{2.48}$$

$$Re = \frac{\rho v L}{\mu} \tag{2.49}$$

$$Sc = \frac{\mu}{\rho D_{\text{HBO}}} \tag{2.50}$$

In these equations, ρ is the density and μ is the dynamic viscosity of the fluid. L is a characteristic length related to the geometry and v is the bulk flow velocity. Correlations between the dimensionless numbers are fitted to experiments or derived from models for different of geometries and flow regimes.

A schematic of the impinging jet flow pattern from a nozzle that is perpendicular to the surface is shown in Figure 2.7. For a circular nozzle, the characteristic length is the diameter of the nozzle exit ($L = d$), and studies of impinging jets refer to the flow at this position. Re through the nozzle exit is calculated by Equation (2.51), and relates directly to the flow rate (Q) through the mean flow velocity $\bar{v} = \frac{4Q}{\pi d^2}$.

$$Re = \frac{\rho}{\mu}\bar{v}d = \frac{\rho}{\mu}\frac{4}{\pi d}Q \tag{2.51}$$

The flow is axisymmetric around the middle of the nozzle, and is stagnant in the stagnation point at the surface below. Figure 2.7 also identifies the stagnation region ($0 \leq r \leq r_s$) in which the flow is deflected by the impingement surface into the wall jet region ($r_s \leq r \leq r_w$), and it defines z as vertical distance and H as the height of the nozzle exit. Entrainment and shear from the ambient gas also start to slow down the free jet at the edges and cause it to broaden away from the nozzle. The gas slows down significantly in the wall jet region as it spreads over the surface and drags gas from the ambient. Computational fluid dynamic (CFD) modeling of a laminar impinging jet onto molten silicon by Næss [55] predicts the radial gas velocity along the surface to scale linearly with the gas velocity at the nozzle exit.

Like in most studies, the following theory is presented for a flat surface. The melt surface is however typically not flat. For instance, a dimple can form in the stagnation region [11], and induction can shape the surface as a dome. Fluid dynamic calculations by Nordstrand and Tangstad [17] did not indicate a dimple in their experiments, which are similar to experiments in this work, but ripples on the surface that is expected to increase the reaction area.
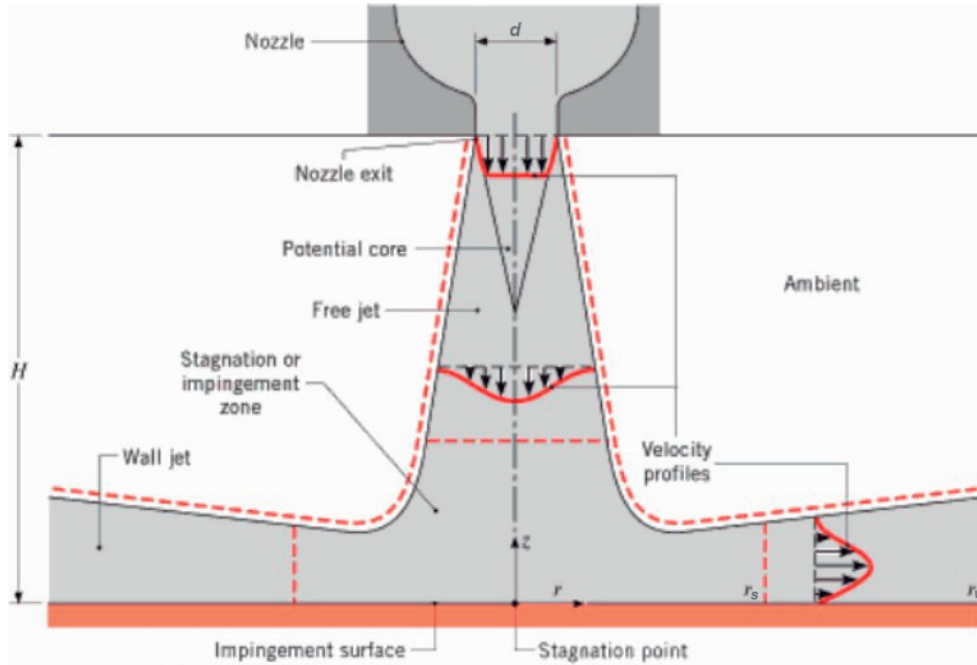
Figure 2.7: Schematic of impinging jet flow pattern (modified from Bergman et al. [72]).

Most studies consider uniform impinging jets, in which turbulence through a nozzle produce a uniform flow velocity at the nozzle exit (shown in Figure 2.7), while a tubular lance used by Nordstrand and Tangstad [17] for reactive gas refining has a nonuniform, parabolic velocity profile [73]. Re was also in the laminar region ($Re < 5000$ [74]). Scholtz and Trass [75] developed correlations for Sh for such a setup in the wall jet region in 1963 [74] and in the stagnation region in 1970 [75]. They found the mass transfer coefficient in the stagnation region to be higher for parabolic velocity profile compared to uniform flow by a factor of 2.2 at the stagnation point and 1.6 beneath the edge of the nozzle ($\frac{r}{d} = 0.5$). In Equations (2.52)-(2.53), expressions for Sh and Re in Equations (2.48) and (2.51) are inserted into their original equations to show the dependence of the mass transfer coefficient on gas flow rate and nozzle diameter separately. The conditions these correlations are verified within are given in Table 2.6.

Scholtz and Trass [75] found mass transfer to be independent of nozzle height for $0.25 \leq \frac{H}{d} \leq 6$ with nozzle diameters between 1.9 cm $\leq d \leq 5.2$ cm. In this range, the highest mass transfer coefficients are observed at the stagnation point (Equation (2.52)), and it decreases monotonically away from this point at $r = 0$. The radial variation is however not large within the stagnation region as shown in Figure 2.8, and Equation (2.52) agreed with exper-

47

Table 2.6: Conditions for Equations (2.52)-(2.53) and (2.56). *Assumptions in text.

Equation	Sc	Re	$\frac{r}{d}$	$\frac{H}{d}$
(2.52)	$[0, 10]$	$[500, 1960]$	$[0, 0.1]$	$[0.25, 6]$
(2.53) and (2.57)	> 1	$[1000, 3000]$	$[2.5, 25]$	
	> 1	300	$[0.6, 15]$	
(2.56)*	$[0, 10]$	300	$[0, 15]$	$[0.25, 6]$

iments at least for $\frac{r}{d} < 0.1$. Consistently, Altenberend [18] found the boron removal rate in plasma refining experiments to vary insignificantly with nozzle heights between $30 - 80$ mm ($0.74 \leq \frac{H}{d} \leq 1.98$).

$$k_{s,\text{HBO}} = 0.9300 D_{\text{HBO}} Sc^{0.361} \left(\frac{\rho}{\mu}\right)^{\frac{1}{2}} \frac{Q^{\frac{1}{2}}}{d^{\frac{3}{2}}} \quad \text{(stagnation point)} \tag{2.52}$$

For $\frac{H}{d} < 0.25$, mass transfer rates are increased away from the stagnation point to a maximum near the nozzle edge. Differences between jet impingement on a melt and on a solid plate can be expected, particularly for such low nozzle heights, as the gas jet impingement can make a dimple in the surface or penetrate into the liquid.

Scholtz and Trass [75] identified the stagnation region within $0 \leq \frac{r}{d} \leq 0.6$ and presented an approximate correlation for mass transfer of which Equation (2.52) is a special case. The correlation agreed with experiments with naphthalene-air ($Sc = 2.45$) within the entire experimental range of $500 \leq Re \leq 1960$ and $0.05 \leq \frac{H}{d} \leq 6$ as seen for the curve "Theoretical - stagnation region" in Figure 2.8.

In the wall jet region, Equation (2.53) [74] agrees with experimental data and the exact solution of momentum, continuity and mass conservation equations under the conditions given in Table 2.6. The radius in which Equation (2.53) applies decrease below $\frac{r}{d} < 25$ for decreasing $Re < 1000$ due to boundary layer separation. This was accompanied by vortex formation, which resulted in stagnant fluid and abrupt decrease in the mass transfer coefficient for $Re < 500$.

$$k_{w,\text{HBO}} = 0.1906 D_{\text{HBO}} Sc^{\frac{1}{3}} \left(\frac{\rho}{\mu}\right)^{\frac{3}{4}} \frac{Q^{\frac{3}{4}}}{d^{\frac{1}{2}} r^{\frac{5}{4}}} \quad \text{(wall jet region)} \tag{2.53}$$

The fluid dynamic mass transfer coefficient can be obtained over both stagnation and wall jet regions for low Re (375). Scholtz and Trass [75] found Equation (2.53) to intersect with the correlation for the stagnation region at $\frac{r}{d} = 0.6$ as shown in Figure 2.8. This consistency was not obtained for higher Re (1970).
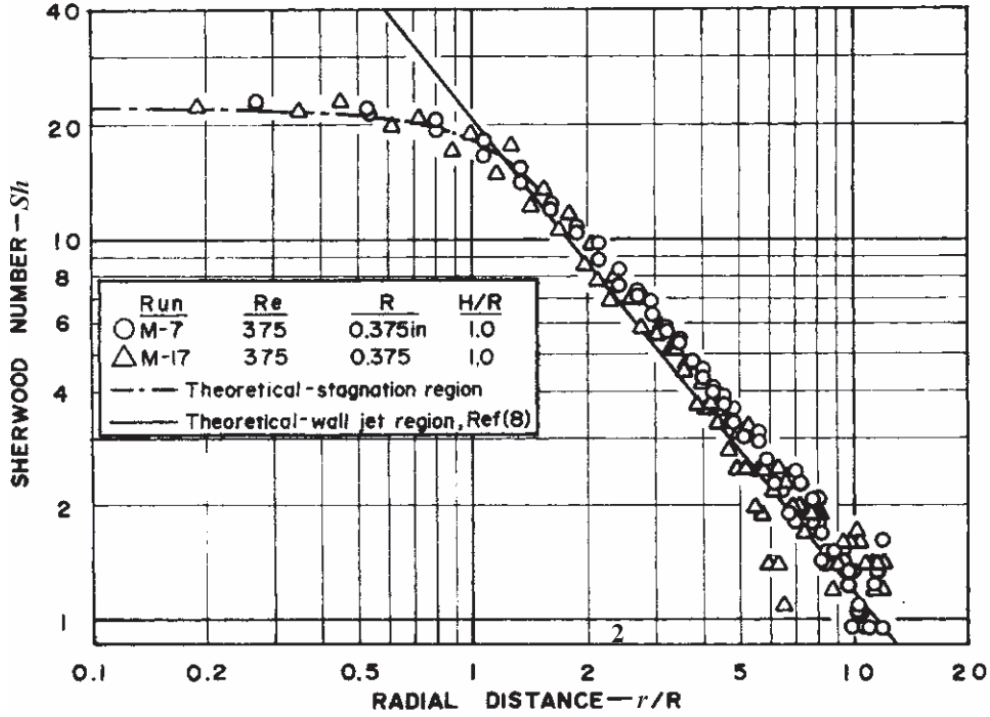
Figure 2.8: Mass transfer in stagnation and wall jet regions for $Re = 375$, $Sc = 2.45$, $0.25 \leq \frac{H}{d} \leq 6$ (modified from Scholtz and Trass [75]). R $= \frac{1}{2}d$ is the radius of the nozzle exit.

It is seen from Equation (2.52) that the mass transfer coefficient increases with gas flow rate as $k_{s,\text{HBO}} \propto Q^{\frac{1}{2}}$ in the stagnation region directly beneath the lance. This is found for the whole stagnation region. In the wall jet region, $k_{w,\text{HBO}} \propto Q^{\frac{3}{4}}$ and the mass transfer coefficient decreases with radial distance as $k_{w,\text{HBO}} \propto r^{-\frac{5}{4}}$. The mass transfer coefficient decreases with nozzle diameter as $k_{\text{HBO}} \propto d^{-1}$ at the stagnation point and $k_{\text{HBO}} \propto d^{-\frac{1}{2}}$ in the wall jet region due to decreased flow velocity.

The mass transfer coefficient also depends on the viscosity of the gas. The effect of viscosity for mass transfer to the gas can be studied by comparing removal rates in atmospheres with different inert gases. Boron removal do not appear sensitive to the atmosphere gas as in gas blowing experiments with steam in argon and nitrogen by Safarian et al. [41], for which they reported total mass transfer coefficients of $k_t = 7$ μm/s and $k_t = 6$ μm/s, respectively. Nakamura et al. [11] added helium to argon as plasma gas, but no effect on boron removal was observed. Furthermore, they did not observe an increasing flow rate to directly affect boron removal. Consequently, mass transfer to the gas was not considered to be rate determining.

Finally, diffusion coefficient of gases increases with increasing temperature and decreases (inversely proportional) with total pressure, but is almost independent of composition for a given binary gas pair [66]. The temperature dependence of diffusion rates can however be masked by chemical equilibrium, which typically scales exponentially with temperature as an Arrhenius relation.

Since the mass transfer coefficient and thus the flux is not constant over the reaction area, it must be averaged over the crucible cross-section area (a flat surface is assumed) in order to relate it to the removal rate according to Equation (2.54). Due to the axisymmetric geometry of the impinging jet flow, cylindrical coordinates are used for integration over the crucible cross-section area $A_c = \int_0^{2\pi} \int_0^{r_c} r\mathrm{d}r\mathrm{d}\Theta$, where r_c is the radius of the crucible and Θ is the angle of integration. The average mass transfer coefficient also explicitly shows the dependence on crucible radius.

$$\frac{\mathrm{d}n_\mathrm{B}}{\mathrm{d}t} = \int_0^{2\pi} \int_0^{r_c} J_{[\mathrm{B}]} r\mathrm{d}r\mathrm{d}\Theta = A_c \bar{J}_{[\mathrm{B}]} \tag{2.54}$$

Integration of the mass transfer coefficient in Equation (2.55) is possible if k_HBO in the stagnation region is assumed constant to Equation (2.52) and that it intersects with (2.53) for the wall jet region at $r_s \approx 0.6d$ for $Re = 300$ like for $Re = 375$ in Figure 2.8, so that the integral is valid for $\frac{r}{d} \leq 15$ like Equation (2.53). The radial integration limit is the lower of the crucible radius (r_c) and the radius of the wall jet region (r_w) used in Equation (2.56). Equation (2.56) shows the dependence of the average mass transfer coefficient on the ratio of nozzle diameter to crucible radius and the gas flow rate.

$$\bar{k}_\mathrm{HBO} = \frac{1}{A_c} \left(\int_0^{2\pi} \int_0^{r_s} k_{s,\mathrm{HBO}} r\mathrm{d}r\mathrm{d}\Theta + \int_0^{2\pi} \int_{r_s}^{r_w} k_{w,\mathrm{HBO}} r\mathrm{d}r\mathrm{d}\Theta \right) \tag{2.55}$$

$$= D_\mathrm{HBO} \left(0.3348 Sc^{0.361} \left(\frac{\rho}{\mu}\right)^{\frac{1}{2}} Q^{\frac{1}{2}} \frac{d^{\frac{1}{2}}}{r_c^2} + 0.5082 Sc^{\frac{1}{3}} \left(\frac{\rho}{\mu}\right)^{\frac{3}{4}} Q^{\frac{3}{4}} \frac{r_w^{\frac{3}{4}} - 0.6817 d^{\frac{3}{4}}}{r_c^2 d^{\frac{1}{2}}} \right) \tag{2.56}$$

The wall jet was found dominating for the average mass transfer in impinging jet experiments by Næss [55], which can also be expected for typical setups with crucible cross-section areas orders of magnitude larger than the stagnation area. Næss [55] found $J_\mathrm{Si} \propto Q^{\frac{3}{4}}$ for oxidation of silicon in a setup similar to that of Nordstrand and Tangstad [17], although at a slightly larger scale. Thus, a dependence close to $\bar{k}_\mathrm{HBO} \propto Q^{\frac{3}{4}}$ can be expected. Equation (2.56) reduces to Equation (2.57) when the contribution of the stagnation region is assumed negligible, and this equation is valid for a larger range of Sc as shown in Table 2.6.

$$\bar{k}_\mathrm{HBO} \approx 0.5082 D_\mathrm{HBO} Sc^{\frac{1}{3}} \left(\frac{\rho}{\mu}\right)^{\frac{3}{4}} Q^{\frac{3}{4}} \frac{r_w^{\frac{3}{4}} - 0.6817 d^{\frac{3}{4}}}{r_c^2 d^{\frac{1}{2}}} \tag{2.57}$$

50

The nozzle diameter has two contributions to mass transfer in the wall jet region. The decreased gas velocity through a wider lance decreases $\bar{k}_{\text{HBO}} \propto d^{-\frac{1}{2}}$. A thicker lance also increases the area that is not included in the wall jet (the stagnation area), which gives an offset from proportionality as the second term of the fraction in Equation (2.57) decreases decreases proportionally to $-d^{\frac{1}{4}}$.

If the crucible radius is longer than the wall jet region ($r_w > r_c$ in Equation (2.56)), the maximum area of the impinging jet is utilized. The total rate of boron removal is then expected to be independent of crucible radius, and the average mass transfer coefficient decreases as $\bar{k}_{\text{HBO}} \propto r_c^{-2}$. If the crucible radius is shorter than the wall jet radius, the crucible radius becomes the upper integration limit for the wall jet region and $r_w = r_c$. The dependence on crucible radius in the first term in the fraction of the wall jet integral becomes $\frac{r_c^{3/4}}{r_c^2} = r_c^{-\frac{5}{4}}$. The effect of a second stagnation region along the crucible wall, which deflects the wall jet if $r_w > r_c$, is not accounted for by Equations (2.56) and (2.57).

Boron removal through step 3 proceeds at its maximum rate when the bulk concentration of HBO equals zero in Equation (2.47). If all other steps are fast in comparison, there is equilibrium at the interface with the bulk content of boron in the melt. Insertion of Equation (2.38) into (2.47) with $p_{i,\text{H}_2} \approx p_{b,\text{H}_2}$ for fast supply of hydrogen to the surface provides Equation (2.58).

$$J_{\text{B}} = - \underbrace{k_{\text{HBO}}(Q,d,r) p_{i,\text{SiO}} p_{b,\text{H}_2}^{\frac{1}{2}} \frac{K_{\text{HBO/SiO}} \gamma_{[\text{B}]} M}{p^{\ominus \frac{1}{2}} RT \rho}}_{k_t \approx k_3} \underbrace{\frac{\rho}{M} x_{[\text{B}]}}_{C_{[\text{B}]}} \quad \text{if } k_3 \ll k_{\text{k} \neq 3} \tag{2.58}$$

The mass transfer coefficient in Equation (2.58) shows the same dependence on reactant concentrations as the equilibrium distribution of boron at the interface (Equation (2.4)). The partial pressure of SiO at the interface can not be simplified to the bulk concentration of steam because steam reacts with SiO above the surface as explained in Section 2.3.6, and only a fraction of the supplied steam reaches the surface.

Furthermore, the SiO partial pressure at the interface is expected to show a radial dependence for impinging jets, because it found that the partial pressure of SiO on the surface is determined by the flux of oxygen to the surface [55]. The partial pressure of SiO on the surface can thus be expected to decrease outwards in the wall jet region, not only because of its fluid dynamic mass transfer coefficient, but also the fact that the bulk content of steam decreases as it is consumed while it flows over the surface in the wall jet region. This suggests the flux of boron to decrease faster with radial distance compared to k_{HBO}. Additionally, the assumption of negligible partial pressure of HBO in the bulk may not hold in the entire wall jet region even if step 3 is rate determining, due to accumulation of HBO in the bulk gas flow. An expression for the rate of boron removal if step 3 is rate determining (integration of Equation (2.58)) is not complete without a model for active oxidation by steam, which is

not fully developed (Section 2.3.6), and fluid dynamic modeling for accumulation of HBO (Section 2.3.5).

2.3.4   Mass Transfer in Bulk Gas

In step 4, the flux of boron in the gas flow is the product of gas velocity (v) and concentration ($C_j = \frac{p_j}{RT}$). The gas velocity can thus represent a mass transfer coefficient. For a constant or averaged gas velocity, the mass transfer coefficient is proportional to the gas flow rate (Q) as $v = \frac{Q}{A}$. As shown in Figure 2.4, step 4 is not a direct continuation of step 3 as the gas does not flow away from the surface (in the direction of $-J$) until the end of the wall jet. Accordingly, $p_{4,\text{HBO}}$ is the fully accumulated partial pressure of HBO in the gas leaving the system. In Equation (2.59), T_Q refers to the temperature of the gas flow.

$$J_\text{B} = -v\frac{p_{4,\text{HBO}}}{RT} = -\underbrace{\frac{Q}{A_c}}_{k}\underbrace{\frac{p_{4,\text{HBO}}}{RT_Q}}_{\Delta_4 C} \tag{2.59}$$

Step 4 becomes rate determining if the bulk partial pressure of HBO accumulates sufficiently in the wall jet to establish equilibrium with the boron content in the bulk of the melt and the gaseous reactants. The rate limit can be represented by the highest HBO partial pressure that is thermodynamically possible ($p_{4,\text{HBO}} = p_{eq,\text{HBO}}$ in Equation (2.60)) for the supply of reactants to the interface.

$$J_\text{B} = -\frac{Q}{A_c}\frac{p_{eq,\text{HBO}}}{RT_Q} \tag{2.60}$$

Equation (2.60) shows that equilibrium calculations can estimate the highest possible boron removal rate for a reactant supply. Tang et al. [30] have made a model that simulates boron removal at equilibrium between melt and gas. Using Equation (2.4), $p_{eq,\text{HBO}}$ is calculated from equilibrium between boron in the bulk melt and the partial pressure of SiO and hydrogen at the interface in Equation (2.61). Hydrogen may however be supplied to the interface with no loss (assuming fast diffusion for bulk gas rate limitation). The partial pressure of SiO at the interface is used to represents the supply of steam because steam reacts essentially stoichiometrically to SiO at the silicon melt surface (Section 2.1). As summarized at the start of Section 2.3, formation of silica fume consumes 50% of the steam for equilibrium. Insertion of Equation (2.61) into Equation (2.60) provides the mass transfer coefficient for step 4 in Equation (2.62).

$$p_{eq,\text{HBO}} = p_{i\text{SiO}}p_{i,\text{H}_2}^{\frac{1}{2}}\frac{K_{\text{HBO/SiO}}}{p^{\ominus\frac{1}{2}}}\gamma_{[\text{B}]}x_{[\text{B}]} \tag{2.61}$$

$$J_{\text{B}} = -\frac{Q}{A_c} p_{i\text{SiO}} p_{i,\text{H}_2}^{\frac{1}{2}} \frac{K_{\text{HBO/SiO}}\gamma_{[\text{B}]}M}{p^{\ominus\frac{1}{2}}RT_Q\rho} \underbrace{\frac{\rho}{M}x_{[\text{B}]}}_{C_{[\text{B}]}} \quad \text{if } k_4 \ll k_{\text{k}\neq 4} \tag{2.62}$$

$k_t \approx k_4$

2.3.5 Total Mass Transfer of Boron

The driving force for the flux of boron in step 3 (Equation (2.47)) can be related to the boron content in the melt in the case of equilibrium at the interface (suggested in Section 2.3.2). The resulting Equation (2.63) contains a hypothetical bulk equilibrium content for boron in the melt ($x_{hyp,[\text{B}]}$). Equation (2.64) calculates the content of boron in the melt $x_{hyp,[\text{B}]}$ for equilibrium if bulk concentrations of gases are present at the interface and with no concentration gradient in the melt.

$$J_{\text{B}} = -\underbrace{k_{\text{HBO}}(Q,d,r)p_{i,\text{SiO}}p_{i,\text{H}_2}^{\frac{1}{2}}\frac{K_{\text{HBO/SiO}}\gamma_{[\text{B}]}M}{p^{\ominus\frac{1}{2}}RT\rho}}_{k_3}\underbrace{\frac{\rho}{M}\left(x_{i,[\text{B}]} - \frac{p_{b,\text{H}_2\text{O}}p_{b,\text{H}_2}}{p_{i,\text{SiO}}p_{i,\text{H}_2}}x_{hyp,[\text{B}]}\right)}_{\Delta_3 C} \tag{2.63}$$

$$x_{hyp,[\text{B}]} = \frac{p_{b,\text{HBO}}\,p^{\ominus\frac{1}{2}}}{p_{b,\text{H}_2\text{O}}p_{b,\text{H}_2}^{\frac{1}{2}}K_{\text{HBO/SiO}}\gamma_{[\text{B}]}} \tag{2.64}$$

The driving force ($\Delta_3 C$) for transport to the gas depend on the difference in concentrations of species at the interface and the bulk gas, which is represented by the ratio of bulk to interface concentrations of reactants in the second term of Equation (2.63). For a large excess of hydrogen, the bulk and interface concentrations are essentially equal ($p_{i,\text{H}_2} \approx p_{b\text{H}_2}$) as discussed for interface equilibrium in Equation (2.38).

Equation (2.28) combines with Equation (2.63) to Equation (2.65), which shows the local resistances ($\frac{1}{k}$) to mass transfer at any position on the surface. Figure 2.9 shows a schematic concentration profile for boron if step 1 and 3 are both rate determining ($k_1 \sim k_3$) and visualizes the meaning of $x_{hyp[\text{B}]}$.

$$-J_{\text{B}}\underbrace{\left(\frac{1}{\sqrt{\frac{D_{[\text{B}]}}{\tau}}} + \frac{\frac{p^{\ominus\frac{1}{2}}RT\rho}{K_{\text{HBO/SiO}}\gamma_{[\text{B}]}M}}{k_{\text{HBO}}(Q,d,r)p_{i,\text{SiO}}p_{i,\text{H}_2}^{\frac{1}{2}}}\right)}_{\frac{1}{k_{1\text{-}3}}=\frac{1}{k_1}+\frac{1}{k_3}\text{ for }k_2\gg k_{\text{k}\neq 2}} = \underbrace{\frac{\rho}{M}\left(x_{[\text{B}]} - \frac{p_{b,\text{H}_2\text{O}}p_{b,\text{H}_2}}{p_{i,\text{SiO}}p_{i,\text{H}_2}}x_{hyp,[\text{B}]}\right)}_{\Delta_{1\text{-}3}C} \tag{2.65}$$
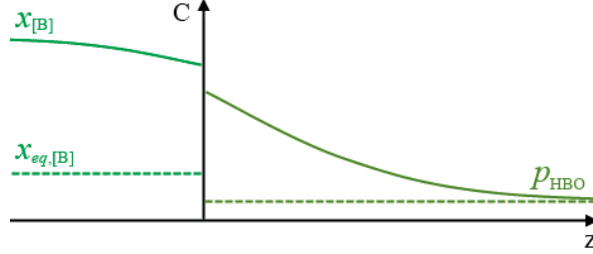
Figure 2.9: Schematic concentration profile for boron removal across the surface (vertical axis). The hypothetical bulk equilibrium content for boron in the melt ($x_{hyp,[B]}$) relates to the actual partial pressure of HBO in order to express the driving force as a concentration difference in the melt.

The mass transfer in bulk gas (Equation (2.62)) is included in the total mass transfer expression in Equation (2.66) for equilibrium interface reactions. The concentration that is transported away by step 4 ($\frac{1}{RT}p_{4,\text{HBO}}$) is the final accumulated concentration of HBO, and does not relate to a position along the interface like $p_{b,\text{HBO}}$ in Equation (2.65). The accumulation of $p_{b,\text{HBO}}$ to $p_{4,\text{HBO}}$ may be accounted for by integrating the fluxes in steps 1 through 3 over the crucible radius to provide average fluxes from which averaged parameters can be calculated for Equation (2.66). The importance of each of steps 1-4 to the overall mass transfer resistance can be evaluated by comparison to measured dependencies between removal rates and parameters varied in experiments. Since all mass transfer resistances included in Equation (2.66) depend on convection in either the melt or the gas, rate limitation by the interface reaction in step 2 can be identified if variation of convection in both phases does not change the reaction rate.

$$-J_{\text{B}} \underbrace{\left(\frac{1}{\sqrt{\frac{D_{[B]}}{\bar{\tau}}}} + \frac{\frac{p^{\ominus \frac{1}{2}} RT\rho}{K_{\text{HBO/SiO}}\gamma_{[B]}M}}{\bar{k}_{\text{HBO}}(Q,d,r_c)p_{i,\text{SiO}}p_{i,\text{H}_2}^{\frac{1}{2}}} + \frac{\frac{p^{\ominus \frac{1}{2}} RT_Q\rho}{K_{\text{HBO/SiO}}\gamma_{[B]}M}}{\frac{Q}{A_c}p_{i,\text{SiO}}p_{i,\text{H}_2}^{\frac{1}{2}}} \right)}_{\frac{1}{k_t}=\frac{1}{k_1}+\frac{1}{k_3}+\frac{1}{k_4} \text{ for } k_2 \gg k_{\text{k}\neq 2}} = \underbrace{\frac{\rho}{M}x_{[B]}}_{\Delta_t C} \qquad (2.66)$$

Accumulation of HBO can be modeled by implementing reactions in CFD modeling of the impinging jet flow pattern, including deflection of the wall jet at the crucible wall. Figure 2.10 visualizes the flow of gases at the end of the wall jet region over a melt with uniform boron concentration in the bulk. In addition to the radial flow along the surface, entrainment/loss of gases from/to the ambient gas above the wall jet can dilute reactants and affect HBO accumulation.

Bulk concentrations within a volume element of the wall jet are along with the bulk boron concentration in the melt input to the micromodel, in which Equation (2.65) calculates the
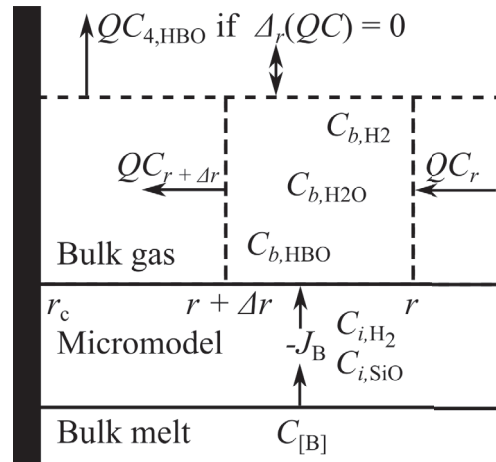
Figure 2.10: Conceptual macromodel for accumulation of HBO, with integration of reactions in a micromodel for mass transfer through boundary layers along the interface.

flux of boron into the volume element. The concentration of hydrogen at the interface can be simplified to the bulk concentration for a large surplus of hydrogen in the reactive gas. Estimation of the interface concentration of SiO in Equation (2.65) and the amount of steam consumed does however require additional modeling of active oxidation. The concentration of SiO at the interface also determines the threshold at which passive oxidation stops boron removal.

2.3.6 Steam Supply

The supply of steam to the interface reactions can be low, and even rate determining for boron removal as proposed by Altenberend [18]. Part of the steam may be consumed above the interface in production of silica fume particles observed in experiments with silicon oxidation [55] and as an aerosol in plasma experiments [18]. Removal of boron directly from melt to gas requires that the silicon surface remains exposed and HBO can only form at the surface in parallel to active oxidation of silicon, which is considered here. The flux of steam to the interface also has a threshold where silica formation occurs at the interface and forms a passivating layer, which is considered in Section 2.3.7. According to thermodynamic calculations for ppmw levels of boron in the melt (Section 2.3.2), most of the steam oxidizes silicon at the interface and only a small fraction produce HBO in parallel.

Studies of active oxidation have mainly been concerned with oxygen and not steam in the gas. Fluxes and concentration profiles in the gas boundary layer have been investigated in theoretical studies of active oxidation of silicon and metals with high vapor pressures [76–

78]. Experimental work on active oxidation is also relevant as Hinze and Graham [79] and Næss [55] found oxygen supply to the interface to be rate determining for active oxidation of a silicon melt.

Wagner [76] formulated equations for fluxes of oxygen to the interface and SiO from the interface based on the partial pressure of oxygen in bulk gas, for the case of pure diffusion through the gas boundary layer. Turkdogan et al. [77] included formation of a thermodynamic stable metal oxide within the gas boundary layer, as presented in Figure 2.11. Metal oxide formation in the general Equation (2.67) is modeled as a sink for oxygen and metal vapor, and its position in the gas boundary layer is shifted towards the metal surface with increasing oxygen partial pressures in the gas. Unit activity of the metal is assumed between the metal surface and the position where metal oxide form. With unit activity of silicon, oxygen may be consumed essentially completely (towards $< 3 \cdot 10^{-13}$ bar at $< 1800\ ^\circ$C), which agree with observations of silica fume in all experiments with active oxidation by oxygen in the gas.

$$2\,\mathrm{Me} + \mathrm{O_2} \rightleftarrows 2\mathrm{MeO}\ (\mathrm{s/l}) \qquad\qquad (2.67)$$
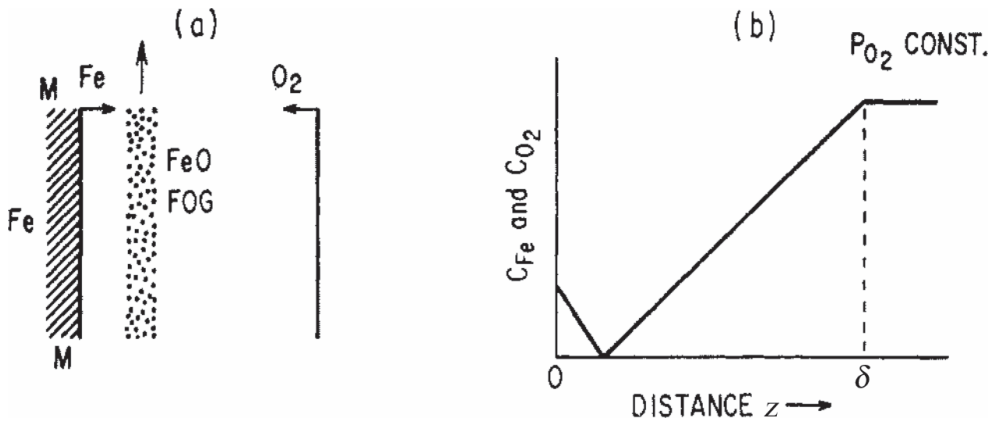
Figure 2.11: Concept (a) of counterflux of metal vapor and oxygen to form metal oxide within the boundary layer, and concentration profiles (b) for diffusion of metal vapor from the surface (left) and oxygen from bulk gas (right), modified from Turkdogan et al. [77] with iron as example metal. The fume (fog) is assumed to be removed by the gas flow.

Ratto et al. [78] developed an extended theory for active oxidation and presented the limits of instantaneous reaction for silica formation and no reaction in the boundary layer, the latter corresponding to the original theory by Wagner [76]. Instantaneous reaction was modeled with local equilibrium for silica fume formation within the boundary layer. Silica was modeled to form within a heterogeneous zone in the gas boundary layer, as compared to a single point in the model by Turkdogan et al. [77] (Figure 2.11). The heterogeneous zone can be
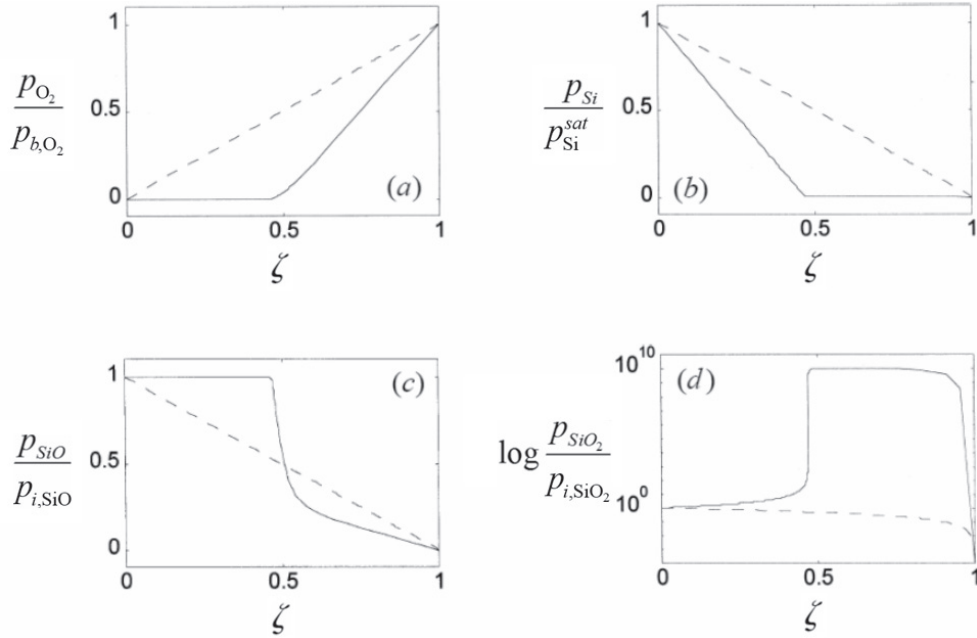
Figure 2.12: Concentration profiles in terms of relative pressure for (a) oxygen, (b) silicon vapor, (c) SiO and (d) SiO_2 across the boundary layer, for the kinetic extremes of nil reactivity (dashed lines) and instantaneous formation of silica fume (solid lines) at 0.1 Pa and 1750 °C (modified from Ratto et al. [78]). ζ is the distance from the interface relative to the gas boundary layer ($z = \delta$ at $\zeta = 1$). Three sub-layers are possible for instantaneous reaction, an inner homogeneous zone with metal vapor diffusion, a heterogeneous zone ($\zeta \in [0.49, 0.63]$) where fume is produced and an outer homogeneous zone with oxygen diffusion.

surrounded by an inner and outer homogeneous zone, where no reaction occurs in either side in the gas boundary layer. Figure 2.12 shows calculated concentration profiles through the gas boundary layer in the limits of nil reactivity (dashed lines) and instantaneous reaction (solid lines), for which silica form in the heterogeneous zone between $\zeta = \frac{z}{\delta} \in [0.49, 0.63]$. Like for the model by Turkdogan et al. [77] in Figure 2.11, the concentration profile for oxygen show essentially complete consumption above the interface so that it does not diffuse further in the inner homogeneous zone towards the interface. Ratto et al. [78] expected an intermediate reactivity in reality and that actual concentration profiles would lie within the limits of nil reactivity and instantaneous reaction. As representative for an intermediate reactivity, Næss et al. [31] included reaction kinetics with nucleation and growth of silica particles in CFD modeling for active oxidation of silicon by oxygen.

Næss et al. [31] used CFD modeling with kinetic expressions for Reactions (2.68)-(2.71) to

calculate concentration profiles in the boundary layer of impinging jet experiments of active oxidation of liquid silicon by oxygen in air. In Equation (2.70), M denotes a third-body molecule acting as a catalyst. The model was calibrated to experiment for fixing kinetic parameters of Reaction (2.68).

$$[Si] + \tfrac{1}{2} O_2 \rightarrow SiO \qquad (2.68)$$

$$SiO + O_2 \leftrightarrow SiO_2 + O \qquad (2.69)$$

$$SiO + O + M \leftrightarrow SiO_2 + M \qquad (2.70)$$

$$SiO_2 \rightarrow SiO_2 \text{ (s)} \qquad (2.71)$$
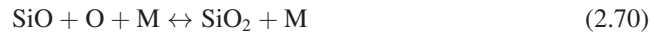
Above the melting point of silicon, SiO may form at orders of magnitude higher pressure at the interface than silicon vapor as shown in Figure 2.2, and the maximum flux of silicon by SiO diffusion could accordingly be higher than that of silicon vapor evaporation. As the flux of oxygen increases beyond the maximum for silicon evaporation, SiO would start to form at the interface and not immediately silica as in the model by Turkdogan et al. [77]. Active oxidation could be maintained with further increasing oxygen supply until the SiO partial pressure at the interface reaches saturation for silica formation, which instead determines the maximum flux of silicon/oxygen from/to the interface. Correspondingly, Næss et al. [31] did not consider metal evaporation and counterflux.

Oxygen and SiO concentration profiles modeled by Næss et al. [31] for an experiment with the highest gas velocity in the lance (26 m/s) and an experiment with the lowest gas velocity (5 m/s) are shown in Figure 2.13. Oxygen appears in Figure 2.13 to diffuse directly to the interface. Also, Hinze and Graham [79] concluded that oxygen is directly supplied to the gas-melt interface in experiments and that SiO is the dominant specie desorbing from the interface. Næss et al. [31] found SiO to react relatively close to the interface and the concentration boundary layer for SiO was found to be an order of magnitude shorter than the oxygen concentration boundary layer and less than 0.5 mm. Only the oxygen boundary layer was found to change thickness with changing gas velocity, like the fluid dynamic boundary layer.

Consumption of oxygen as it reacts through the SiO boundary layer would be expected to reduce the remaining oxygen flux towards the interface, but this is not pronounced in the concentration profiles of oxygen. The slope of the concentration profiles and the diffusive flux of oxygen appears to be constant like in the case of nil reactivity due to the difference in the scales for the oxygen and SiO mole fractions in Figure 2.13. In terms of the model by Ratto et al. [78], the SiO boundary layer (enlarged to the right in Figure 2.13) include the inner homogeneous zone and heterogeneous zone with practically complete consumption of SiO, leaving the majority of the boundary layer for oxygen as the outer homogeneous zone. As oxygen and SiO are also expected to diffuse in the inner homogeneous zone, the thickness of the inner homogeneous zone (if any) is not clearly seen from the concentration profiles in

Figure 2.13. Since the diffusive flux start to decrease when SiO starts to react, the transition between the inner homogeneous and the heterogeneous zone would be at a distance from the interface where the concentration profile for SiO start to curve, assuming negligible effect of convection within the SiO boundary layer.

Næss [55] estimated the partial pressure of SiO at the interface using the hydrodynamic mass transfer coefficient (Section 2.3.3) and rates of silica fume formation in impinging jet experiments. She found the partial pressure of SiO to be practically constant at $3.7 \cdot 10^{-3} - 6.9 \cdot 10^{-3}$ bar with variation of gas velocity at the nozzle exit within $5 - 26$ m/s. As SiO did not accumulate at the interface, she concluded that SiO is removed faster from the interface than oxygen is supplied. This agrees with expectations that oxidation of SiO above the interface enhances removal of SiO and impairs supply of oxygen compared to pure diffusion (for impinging jets in Section 2.3.3). This led to her conclusion that supply of oxygen to the interface is the only rate determining step for active oxidation of silicon.
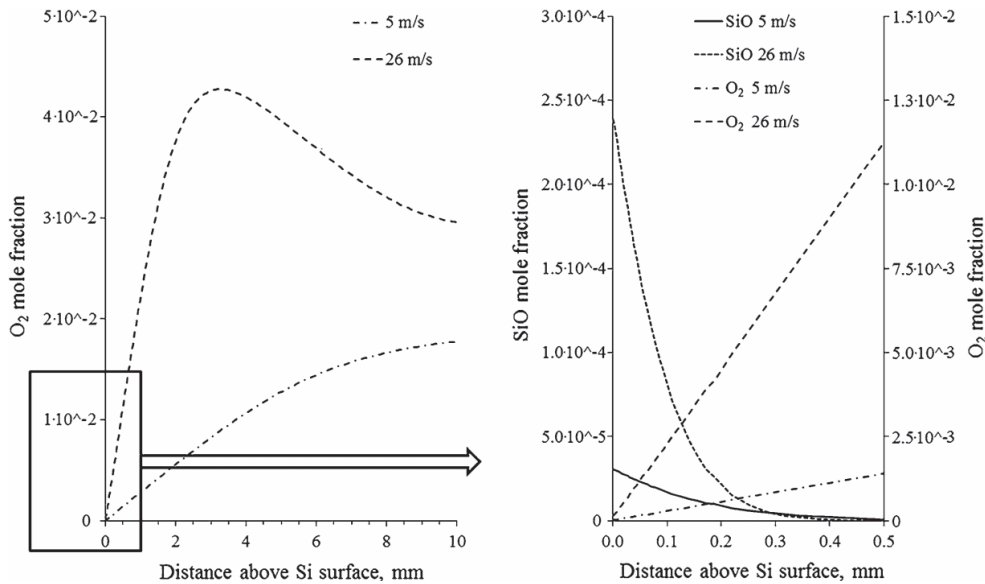
Figure 2.13: Concentration profiles for oxygen and SiO from CFD and kinetic modeling of impinging jet experiments with highest (26 m/s) and lowest (5 m/s) gas velocities in the lance in experiments by Næss et al. [31]. The SiO boundary is an order of magnitude shorter than the oxygen boundary layer and is enlarged in the graph to the right, with different scales for SiO and oxygen concentrations.

While the oxidizing agent used in most studies is oxygen, Hildal [80] found silica to form in a similar manner from steam. He proposed Reaction (2.72) to occur above the interface, where steam directly replaces oxygen as the oxidizing agent.

59

$$H_2O + SiO = SiO_2 \text{ (s)} + H_2 \tag{2.72}$$

Concentration profiles for active oxidation by steam may possibly assimilate those for oxygen supply and SiO production at the interface in Figure 2.13. For the limit of instantaneous reactivity in models by Turkdogan et al. [77] and Ratto et al. [78] however, there is an important difference in that the inner homogeneous zone may not be characterized by counter-diffusion of metal vapor, but instead continued diffusion of steam to the interface. The saturation pressure of steam with respect to silica ($p_{H_2O}^{sat} = 4.0 \cdot 10^{-5}$ bar in 1 bar hydrogen at 1500 °C in Figure 2.2) is higher than the vapor pressure of elemental silicon ($p_{Si}^{sat} = 1.5 \cdot 10^{-6}$ bar) and the oxygen saturation pressure ($p_{O_2}^{sat} = 2.8 \cdot 10^{-18}$ bar). A higher partial pressure of steam would remain at $\zeta = 0.49$ than that of oxygen in Figure 2.12 and steam could have a steeper concentration gradient and higher flux towards the interface than silicon vapor from the interface. Steam may thus diffuse in the inner homogeneous zone at a higher rate than silicon vapor also after consumption by fuming, and the supply of oxygen to the interface would presumably be balanced by diffusion of SiO directly from the interface.

Næss [55] studied the mechanism of active oxidation, including the position of the reaction steps. Based on a test developed by Arato et al. [81], she calculated that both thermodynamics and gas-phase kinetics of Reaction (2.71) favors formation of SiO_2 gas within the boundary layer. SiO_2 does however have a low vapor pressure ($p_{SiO_2}^{sat} = 9 \cdot 10^{-9}$ bar at 1500 °C in Figure 2.2) and finally condenses. Næss [55] calculated condensation times with a method presented by Kamfjord et al. [82] based on equations by Ulrich [83]. Coupled with theoretically calculated mass transfer coefficient for SiO_2, she calculated the distance traveled during condensation to be shorter than the oxygen boundary layer thickness extracted from CFD modeling (Figure 2.13), but longer than the SiO boundary layer thickness [31]. Accordingly, SiO was first oxidized to SiO_2 gas (in the SiO boundary layer) and the SiO_2 gas condensed to form silica fume mainly outside the SiO boundary layer, after most SiO was reacted to SiO_2 gas. Condensation of SiO_2 gas is shown above the SiO boundary layer in the mechanisms in Figure 2.14.

Considering local equilibrium between gas species in Reaction (2.73) without condensation of silica, SiO_2 gas would tend to form directly above the interface as the product $p_{SiO}\sqrt{p_{O_2}}$ in Equation (2.74) increases above the interface. The product $p_{SiO}\sqrt{p_{O_2}}/p^{\ominus 1.5} \leq 1$ for each 0.01 bar SiO_2 gas at equilibrium. Altenberend [18] estimated SiO_2 gas to form closer to the interface than its mean free path in plasma refining in which case the inner homogeneous zone is effectively diminished.

$$SiO + \tfrac{1}{2} O_2 = SiO_2 \tag{2.73}$$
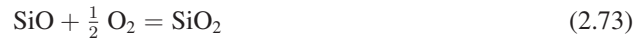
$$\frac{K_{O_2 + SiO}}{\sqrt{p^{\ominus}}} = \frac{p_{SiO_2}}{p_{SiO}\sqrt{p_{O_2}}} \tag{2.74}$$
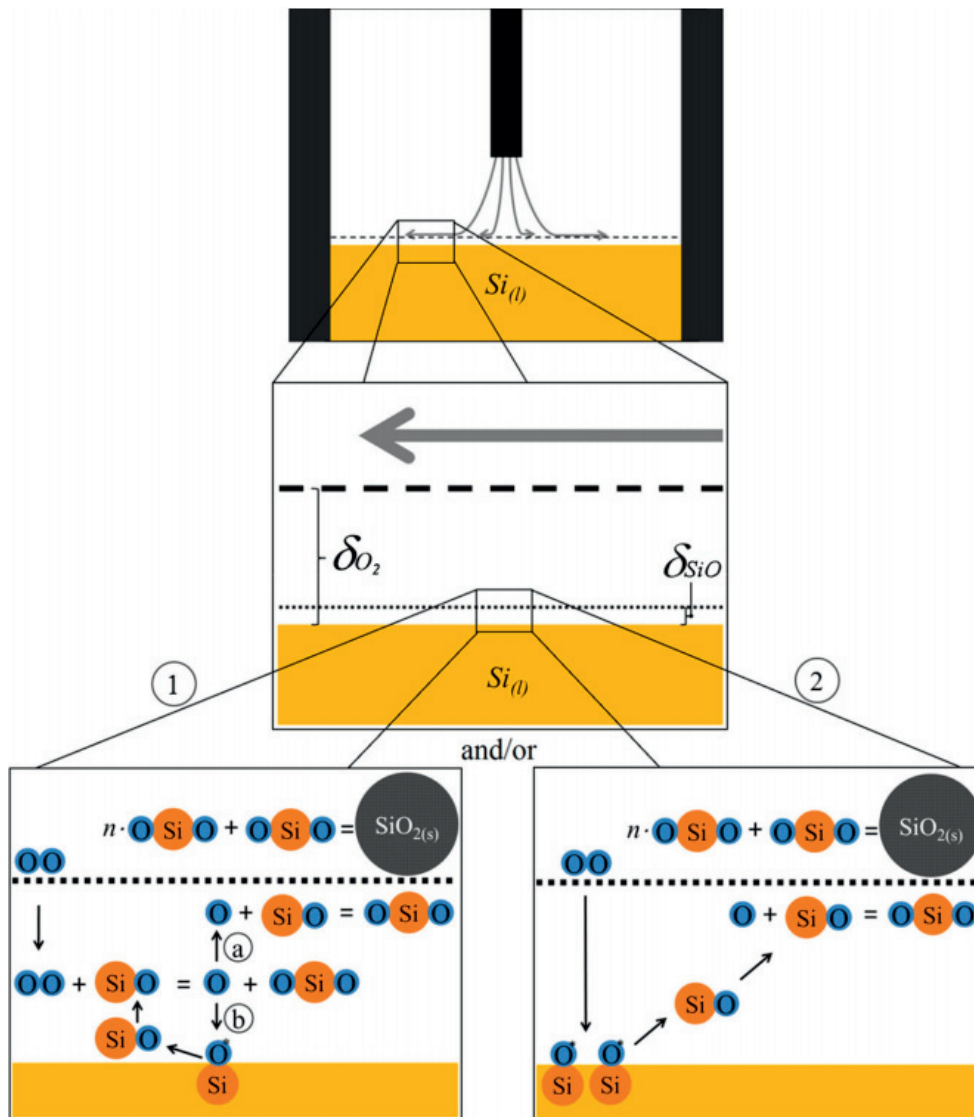
Figure 2.14: Schematic by Næss et al. [31] of the mechanism for active silicon oxidation by oxygen, showing the impinging jet gas flow (top), the relative thicknesses of oxygen and SiO boundary layers (middle) and two possible mechanisms to SiO$_2$ gas within the SiO boundary layer (bottom). Mechanism 1 is not available for steam A second steam molecule is required in the reaction with SiO in mechanism 2, and it would release hydrogen. Steam would also release hydrogen instead of a second SiO molecule in reaction with the silicon surface.

With steam however, equilibrium modeling of the gas without SiO_2 condensation does not predict SiO_2 to form a dominant gas specie, and SiO is not predicted to react with steam until condensed silica fume forms. As an upper limit, 0.5 bar SiO and hydrogen was input for the interface together with 1 bar steam for the bulk gas, and SiO_2 gas contained less than 2.1% of the silicon in the equilibrated gas at less than $1800\,°C$. As oxidation of SiO may be delayed by nucleation and growth of silica fume, the SiO boundary layer may be thicker with steam than with oxygen (in Figure 2.13). Based on the active oxidation mechanism with oxygen (Mechanism 2 in Figure 2.14) and expected differences, Reactions (2.75)-(2.77) are considered possible for active oxidation with steam. Stoichiometry in Reactions (2.75) and (2.76) represent a maximum limit to the extent of fuming, assuming negligible rate of silicon evaporation. The steam molecule in both reactions must be supplied from the bulk gas, so up to 50% of the influx steam to the hydrodynamic boundary layer may be consumed by SiO (Reaction (2.76)) and the remaining 50% may be supplied to the interface (Reaction (2.75)) to produce the SiO reacting with steam to fume (Reaction (2.76)).

$$[\text{Si}] + \text{H}_2\text{O} \rightleftharpoons \text{SiO} + \text{H}_2 \quad \Delta H^{\ominus}(1500\,°C) = 85.5 \text{ kJ/mol} \tag{2.75}$$

$$\text{H}_2\text{O} + \text{SiO} = \text{SiO}_2 \text{ (l)} + \text{H}_2 \quad \Delta H^{\ominus}(1500\,°C) = -524.3 \text{ kJ/mol} \tag{2.76}$$

$$\text{SiO}_2 \text{ (l)} \rightarrow \text{SiO}_2 \text{ (s)} \quad \Delta_{trs}H^{\ominus}(1500\,°C) = -6.7 \text{ kJ/mol} \tag{2.77}$$

Altenberend [18] suggested that the spherical shape of the fume particles was due to solidification from liquid state as opposed to direct condensation of the gas to solid. He supported this with the high heat of condensation of SiO_2 ($\Delta_{trs}H^{\ominus} = -562.7$ kJ/mol) which gives a highly negative enthalpy ($\Delta H^{\ominus}$) of Reaction (2.76). Additionally, Kamfjord et al. [82] suggested condensation of SiO_2 to produce local temperatures sufficient to form radicals. A stoichiometric combustion model could reproduce NO concentrations in the off-gas of industrial silicon production furnaces, where SiO gas from the furnace is oxidized by air, with a local temperature of $4390\,°C$. Altenberend [18] found that reactions or gas flow (without preheating to plasma) did not change the temperature at the surface by measuring the temperature with a two color pyrometer before and after blowing oxygen in argon onto the surface. The heat of Reaction (2.75) may be effectively supplied to the interface by conduction and convection in the melt.

During plasma refining, Suzuki et al. [25] observed a linear increase in the silicon loss rate due to formation of SiO gas with increasing contents of steam, oxygen or CO_2 in argon plasmas. Næss [55] also observed that the flux of silicon increased proportionally to the partial pressure of oxygen in the feed for laminar flow of up to $2 \cdot 10^{-3}$ bar oxygen in Ar through a horizontal tube furnace. In an impinging jet setup at a larger scale however, the rate of oxidation did not increase for 25%-100% air in Ar ($p_{O_2} = 0.05 - 0.21$ bar), but instead found utilization of oxygen to decrease with increasing oxygen content. As the rate of oxidation did not increase, a larger fraction of oxygen remained unreacted in the gas flow after passing over the silicon surface. The rate of silicon oxidation was however observed to

increased with increasing flow rate of dry air, with a similar dependence as expected for mass transfer in impinging jets in Section 2.3.3.

The rate of silicon loss by oxidation to SiO was found by Nakamura et al. [11] to be constant over time and solely controlled by the oxygen content of the plasma. Ikeda and Maeda [62] observed 6% silicon loss after 45 min of plasma treatment with 0.39 vol% steam in the plasma, which represented a similar silicon loss rate as in experiments by Nakamura et al. [11]. The silicon loss for 0.39 vol% steam was found to represent a three times higher loss rate compared to evaporation of elemental silicon in a pure argon plasma. The mechanism of silicon loss was explained by Ikeda and Maeda [62] as a sequence of Reactions (2.78) and (2.79), for which they calculated a SiO pressure of $4 \cdot 10^{-3}$ bar. After experiments with Ar/O$_2$ and Ar/H$_2$O plasmas, a white powder was deposited in the reaction chamber. Lee et al. [33] found the silicon loss to amount to about 8% of the initial mass after 5 min of Ar/H$_2$/H$_2$O plasma treatments.

$$Si\ (l) + 2\ H_2O \rightleftarrows SiO_2\ (l) + 2\ H_2 \tag{2.78}$$
$$SiO_2\ (l) + [Si] \rightleftarrows 2\ SiO \tag{2.79}$$

The silicon loss appeared random and averaged $10.73\% \pm 2.85\%$ for 4.5 h reactive gas refining experiments by Nordstrand and Tangstad [17]. The silicon loss correlates to a flux of 0.037 g/h/cm^2 across the crucible cross-section area. Oxidation to SiO gas appeared not to be the only reason for silicon loss as about 5% also was lost in an experiment with a pure argon atmosphere. An experiment with 7.4 vol% steam was terminated after 2 h due to extensive crystal growth from the crucible wall over the melt surface.

2.3.7 Passivation

The melt surface becomes passivated by formation of silica at the interface. Silica floats on silicon and can build up a layer that blocks oxygen supply to the melt, so that boron and silicon volatilization stops. Alemany et al. [13] found the silicon content of the gas to drop dramatically as a silica surface layer was formed. However, this layer was removed by stopping the flow of oxygen in argon plasma.

Figure 2.15 shows a drop in the silicon volatilization rate as the bulk oxygen partial pressure is increased beyond the threshold for passivation $p_{b,O_2}(\max)$. The drop in the volatilization rate accompanies the transition from active to passive oxidation, at which silica start to form at the interface (Reaction (2.80)). The rate of oxidation and volatilization of both silicon and boron has a maximum value at which the SiO partial pressure at the silicon interface is just below saturation at which silica start to form on the surface.

$$2\,H_2O + [Si] = SiO_2\ (s/l) + 2\,H_2 \qquad\qquad (2.80)$$
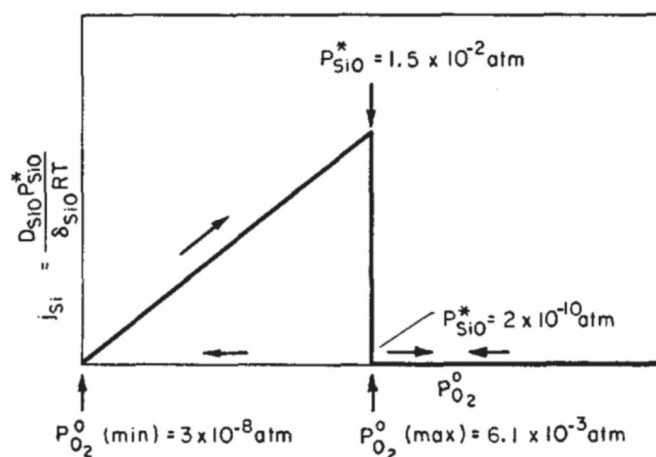
Figure 2.15: Flux of silicon oxidation with increasing bulk oxygen partial pressure ($p^0 = p_b$) calculated by Wagner [76] for nil reaction above the surface at $1410\ ^\circ$C, including hysteresis effect for formation of silica above $p^0_{O_2}$(max) and removal of silica below $p^0_{O_2}$(min). In the figure, $p^*_{SiO} = p_{i,SiO}$ denotes the partial pressure of SiO at the interface.

There is a hysteresis in the volatilization rate as Wagner [76] calculated a minimum value (p_{b,O_2} (min)) of the bulk oxygen partial pressure at which an already formed silica layer is stable. The hysteresis is due to the absence of a concentration gradient as diffusion of the oxidizing agent stops upon passivation, and additionally consumption of the oxidizing agent by reaction with SiO above the interface is absent.

In the plot of SiO partial pressures at the surface compared to bulk oxygen partial pressures in Figure 2.16, Ratto et al. [78] have plotted the steady state line for active oxidation in the case of nil reaction above the surface (solid line) and instantaneous reaction (dotted line). These cases are identical for low bulk oxygen contents at which silica is not stable at any point above the surface. The case of nil reaction gives the lower threshold to the bulk partial pressure at which SiO reaches saturation at the interface and passivation occurs. For instantaneous reaction, silica can not form on the surface for any bulk oxygen contents, because oxygen is consumed to equilibrium with metal vapor already above the interface, in the inner homogeneous layer. Ratto et al. [78] pointed out that the limit for instantaneous reaction is conceptual, and that a reality would lie between the limits of instantaneous and nil reactivity. The instantaneous reaction model in Figure 2.16 deviates from the model by Turkdogan et al. [77] in this respect, as Turkdogan et al. [77] considered passivation to occur if the oxygen flux to the surface exceeds the flux at which silicon can evaporate from the surface. The bulk

64

oxygen threshold in the approach by Turkdogan et al. [77] is shown in Figure 2.17 to be lower that of the nil reactivity model by Wagner [76]. The fuming reaction may also be expected to increase the passivation threshold for the partial pressure of oxygen in bulk gas considering supply of oxygen directly to the interface in the mechanism by Næss et al. [31], as the reaction consumes part of the oxygen diffusing towards the interface, reducing concentrations and the remaining flux of oxygen supply to the interface.
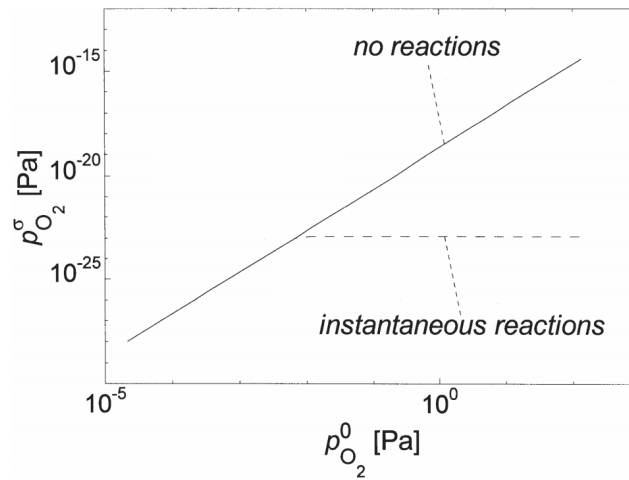
Figure 2.16: Oxygen partial pressure at interface ($p^\sigma = p_i$) compared to bulk ($p^0 = p_b$) at $1477\,°\mathrm{C}$ (modified from Ratto et al. [78]), with threshold for passivation at the SiO saturation pressure at the top end of the solid line.

Experiments reveal that the bulk oxygen partial pressure threshold for passivation is not a constant value even at constant temperature. Næss [55] investigated the threshold for passivation experimentally and found it to vary significantly depending on the experimental setup. The transition from active to passive oxidation occurred between $2 - 5 \cdot 10^{-3}$ bar bulk oxygen partial pressure at $1500\,°\mathrm{C}$ in small scale horizontal tube experiments, while active oxidation could be maintained in air ($p_{b,O_2} = 0.21$ bar) in impinging jet experiments and industrial ladle refining.

Næss [55] related the difference in the threshold for passivation between the experimental setups to accumulation of adsorbed oxygen on a still surface in the horizontal tube experiments compared to rapidly renewed surface due to stirring in impinging jet experiments and in industry. Desorption of SiO is the kinetically favorable path compared to silica formation for low coverage of adsorbed oxygen on the surface [84–86]. The time available for accumulation of the oxygen coverage at the surface is significantly shorter for a rapidly renewed surface compared to a still surface. Thus, in order to reach high oxygen coverages at which silica formation is kinetically favorable, a higher supply rate of oxygen is required for

the rapidly renewed surface, which can explain the higher bulk oxygen content passivation threshold for experiments with stirred compared to still melts.

When comparing boron removal from EG-Si to MG-Si in plasma refining, Altenberend [18] observed an oxide layer over part of the MG-Si melt. No oxide was observed on EG-Si in an otherwise identical experiment. Passivation on the MG-Si melt was considered either to be a random effect or form due to impurities. Impurities in MG-Si that form more stable oxides than silica can narrow the operational window in which a clean surface can be maintained.

In a reactive gas refining experiments by Sulentic [54] at $1500\,^{\circ}\mathrm{C}$, a high steam content of roughly $11\,\mathrm{vol\%}$ in $44.5\,\mathrm{vol\%}$ hydrogen and argon resulted in a viscous byproduct that prevented melt sampling after $1\,\mathrm{h}$. The final boron content achieved was also higher than with $3.2\,\mathrm{vol\%}$ steam in $48.4\,\mathrm{vol\%}$ hydrogen and argon. However, an image of the crucible after the experiment shows a reflective silicon melt with a white ring along the crucible wall above the melt, which indicate active rather than passive oxidation.

The steam contents found to cause passivation vary greatly in plasma refining experiments. Yuge et al. [10] reported inhibition of boron removal due to silica formation for $7.2\,\mathrm{vol\%}$ and higher steam contents in argon plasma. Ikeda and Maeda [62] found boron removal to stop after a few hundred seconds of plasma refining when using $2.6\,\mathrm{vol\%}$ oxygen in argon, but not with $0.66\,\mathrm{vol\%}$ oxygen. Nakamura et al. [11] successfully removed boron with up to $14.2\,\mathrm{vol\%}$ steam in an argon plasma with $39.8 - 51.3\,\mathrm{vol\%}$ hydrogen blown onto the melt at $2220\,\mathrm{l_N/min}$. A $650\,\mathrm{kW}$ non-transfer plasma torch and induction heating held the melt at $1550 - 1600\,^{\circ}\mathrm{C}$, while the surface was estimated to be several hundred degrees warmer. Thermodynamics in Section 2.1 suggests the threshold steam content for silica formation to increase with temperature. They actually observed silica coverage on the melt surface outside the dimple area formed by the impinging jet. The melt surface in the dimple area was held clean possibly due to the local high temperature of the plasma or convection by the impinging jet gas flow.

The temperature dependence of the bulk oxygen partial pressure threshold for passivation for both models by Wagner [76] (nil reaction) and Turkdogan et al. [77] (instantaneous reaction) is compared to experiments by Hinze and Graham [79] in Figure 2.17. The experiments were conducted on solid silicon, which experienced two regimes of active oxidation. A clean silicon surface was maintained for $p_{b,O_2} < p_{b,O_2}(\mathrm{max})_\mathrm{I}$ and silicon whiskers formed on the surface for $p_{b,O_2}(\mathrm{max})_\mathrm{I} < p_{b,O_2} < p_{b,O_2}(\mathrm{max})_\mathrm{II}$. Næss [55] and Altenberend [18] did not observe silicon whiskers on liquid silicon so that complete passivation represented by $p_{b,O_2}(\mathrm{max})_\mathrm{II}$ in Figure 2.17 is presumably most relevant for liquid silicon. The transition from a clean surface to complete passivation occurred within a narrow oxygen concentration range in reactive gas refining experiments by Altenberend [18], and only one value is reported for the oxygen concentration threshold (Table 2.7).
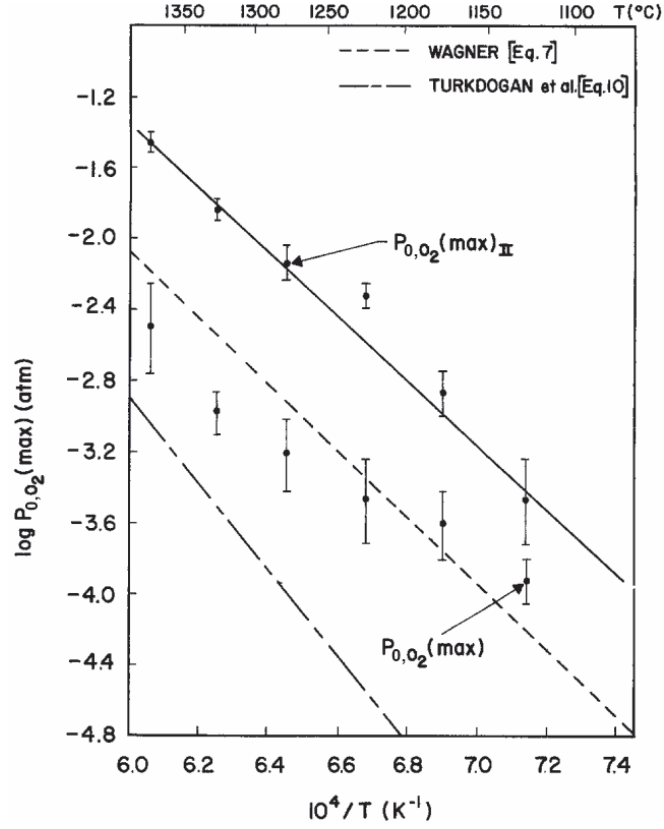
Figure 2.17: Temperature dependence of passivation threshold for the oxygen partial pressure in bulk gas ($p_{0,O_2}(\text{max}) = p_{b,O_2}(\text{max})$) in experiments with solid silicon by Hinze and Graham [79].

Figure 2.17 constitutes an Arrhenius plot for which the slope of lines represents an activation energy (E_a in Equation (2.32)). The activation energy found from the slope of the lines for the models of Wagner [76] and Turkdogan et al. [77] is the formation enthalpy of SiO ($\Delta_f H_{\text{SiO}} = -83$ kJ/mol) and sublimation enthalpy of Si, respectively. The experimental threshold for complete passivation ($p_{b,O_2}(\text{max})_{\text{II}}$) shows the same slope as the model by Wagner [76], although shifted to almost an order of magnitude higher values. The bulk oxygen threshold for passivation at different temperatures T_1 and T_2 can nevertheless be related through Equation (2.81).

$$\frac{p_{b,O_2}(\text{max})(T_2)}{p_{b,O_2}(\text{max})(T_1)} = e^{\frac{\Delta_f H_{\text{SiO}}}{R}\left(\frac{1}{T_2} - \frac{1}{T_1}\right)} \tag{2.81}$$

67

Fourmond et al. [53] found p_{O_2}(max) to increase from $0.008 - 0.018$ bar in a plasma with 3.2 vol% hydrogen in argon blown at $7 - 78$ l$_N$/min onto the melt when the temperature was increased by 150 ± 20 °C. Table 2.7 summarizes an an experiment by Altenberend [18] on the temperature dependence of p_{O_2}(max). Oxygen and argon gas was blown at 16.7 l$_N$/min through a 7 mm diameter vertical nozzle 55 mm above the melt surface. The threshold for passivation was not reach with the maximum oxygen flow represented by 19 vol% oxygen at 1680 °C. The significantly higher passivation thresholds in experiments compared to theoretical calculations with the model by Wagner [76] led Altenberend [18] to conclude that the model can not predict oxidation in the impinging jet setup used. The deviation can relate to an intermediate reactivity, which according to Figure 2.16 and the model by Ratto et al. [78] increases the threshold bulk oxygen partial pressure. Altenberend [18] also found the oxygen concentration threshold in experiments to increase less with temperature compared to the model by Wagner [76].

Table 2.7: Temperature dependence of the passivation threshold for feed oxygen partial pressure in gas blowing experiments, compared to Wagner [76] model (modified from Altenberend [18]).

Melt temperature	1410 °C	1560 °C	1680 °C
p_{O_2}(max) [bar] in experiment (Altenberend [18])	0.036	0.071	>0.19
p_{b,O_2}(max) [bar] in Wagner [76] model	0.0055	0.035	0.15

Altenberend [18] investigated the dependence of gas flow rate on the threshold for passivation in an experiment with gas blowing, and results are summarized in Table 2.8. The threshold oxygen concentration for passivation decreased as the total flow rate increased, but the flow rate of oxygen could be increased. Altenberend [18] also found significantly higher oxygen concentration thresholds for the inclined nozzle compared to the vertical nozzle, which can be related to thinner boundary layers and increased mass transfer coefficients in the stagnation region of vertical nozzles.

Table 2.8: Flow rate dependence of the passivation threshold for oxygen in argon during reactive gas refining by Altenberend [18].

Nozzle inclination	Vertical				15° from horizontal		
Nozzle diameter (d)	7 mm				3.9 mm		
H from center of surface	55 mm ($\frac{H}{d} = 7.9$)				70 mm ($\frac{H}{d} = 18$)		
Total flow rate [l$_N$/min]	22	38	63	100	20	37	58
Oxygen flow rate [l$_N$/min]	1.5	2.3	3.0	3.8	2.7	3.3	3.8
p_{O_2}(max) [10^{-2} bar]	7.1	6.2	4.9	3.9	13	9.1	6.6

For laminar flow through a horizontal tube with a gas velocity of 0.047 m/s, Næss [55] found the transition from active to passive oxidation to occur between $2 - 5 \cdot 10^{-3}$ bar bulk oxygen partial pressure at $1500\,°C$. A similar theoretical threshold of $p_{b,O_2}(\text{max}) \approx 3 \cdot 10^{-3}$ bar was obtained by using mass transfer coefficients calculated from CFD modeling in a similar approach to Wagner [76], with nil reaction above the surface.

Chapter 3

Experiments and Analyzes

The main focus of the project is an experimental study of process kinetics of boron removal by gas refining of silicon melts. The experimental setup in Section 3.1 and procedures in Section 3.2 were developed throughout the experimental work. Experimental control was thus improved, particularly as the melt could be observed for passivation during experiments. Furthermore, estimation of the weight lost during experiments allowed for comparison between the parallel processes of silicon loss and boron removal, and proved valuable for understanding the process kinetics and particularly the rate determining step. The parameters of all experiments are presented in Section 3.3, which also shows the progression of experimental studies. Series of two or more experiments with variation of one main parameter were conducted to study its effect on mass transfer of boron, for comparison to theory for individual mass transfer steps. A set of experiments was also conducted exclusively to observe the threshold for passivation.

ICP-MS analyzes presented in Section 3.4 were used to estimate boron concentrations in samples taken periodically during each experiment, and the total mass transfer coefficient was calculated as outlined in Section 3.5 with uncertainties (at approximately 95% confidence level) typically around 17%. Both the weightloss and the total mass transfer coefficients were compared to models (Section 3.6) for equilibrium at the melt surface. The comparison first provided an estimate for the actual supply of steam to the interface reactions in experiments, and secondly the supply of steam could be correlated to the rate of boron removal. Simple models for the flow of gas and for convection and diffusion in the melt were also used to rationalize the experimental results.

3.1 Equipment

The main equipment used for the gas blowing experiments were a furnace, flowmeters and a humidifier. Section 3.1.1 describes the flowmeters and humidifiers used in setups for feeding the reactive gas to the furnace, and Sections 3.1.2-3.1.4 describe the three different furnaces used (Resistance, Induction 1 and -2) and accessories like vacuum and sampling systems. The experimental setup was upgraded incrementally throughout the experimental work, particularly when the furnace was changed. References are provided to specifications of different equipment, materials or software used.

3.1.1 Gas System

Gases of CO, steam, hydrogen and argon were continuously fed through a lance to molten silicon in the furnaces during experiments. The gas flasks shown in Figure 3.1 were used with the Resistance furnace. Hydrogen 5.0 and argon 4.6 was typically used for the induction furnaces. Argon was was also connected directly to the furnace chamber for filling inert atmosphere in the furnaces before experiments. The lances were tubes going through the top of the furnaces. $4\,\mathrm{mm}$ inner diameter tubes of alumina ("Alsint 99.7" by W. Haldenwanger Technische Keramik [87]) were typically used. Quartz ("Quartz Glass" by OGT Bad Harzburg [88]) was used for other diameters.

Steam was added by evaporation of water to the gas flow through the humidifier. The partial pressure of steam was controlled by the water temperature and was calculated by the Antoine Equation (rearranged in Equation (3.1) to express T in K) with parameters by NIST [89] in Table 3.1. The composition and flow of each of the other gases in the feed was controlled by flowmeters. The setpoint flows were adjusted for the added flow of steam to achieve the desired total gas flow rate.

$$\frac{T}{\mathrm{K}} = \frac{B}{A - \log \frac{p_{\mathrm{H_2O}}}{\mathrm{bar}}} - C \tag{3.1}$$

Table 3.1: Antoine Equation parameters [89] used in the Equation (3.1) to calculate the saturation temperatures for the humidifier.

Temperature range	A	B	C
0-30 °C = 273-303 K	5.40221	1838.675	-31.737
31-60 °C = 304-333 K	5.20389	1733.926	-39.485
61-90 °C = 334-363 K	5.07680	1659.793	-45.622
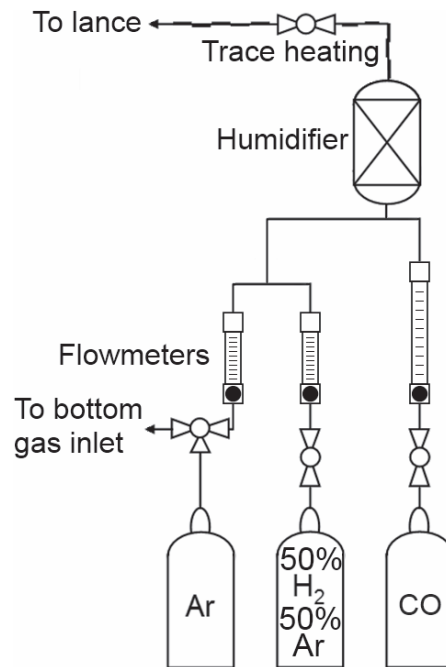
Figure 3.1: Schematic of gas feeding setup, modified from Nordstrand and Tangstad [17].

Two different humidifiers were used for experiments with steam feeding. The first was an assembly of three consecutive bubble flasks of which the last two were submerged in a water bath. The middle bubble flask contained water and a dispersion stone for bubbling of the gas through the water in the flask. The water temperature was measured by a K-type thermocouple in side the bubble flask and controlled by manually adjusting heating of the surrounding water bath. The temperature responded slowly to heating adjustments and the temperature drifted to cause up to $0.005\,\mathrm{bar}$ off-set in the steam saturation pressure during experiments. This humidifier was used with the Resistance furnace, and for part of the experiments in the Induction 1 furnace. It was replaced by a LS-HS Gas Humidification System from Fuel Cell Technologies, Inc. containing two LF-HBA Humidification Bottles [90] with $4\,\mathrm{m}$ Nafion membrane tubing each. The flow through each bottle was restricted to $8\,\mathrm{l_N/min}$ to ensure close to complete steam saturation. The controller adjusted the temperature typically within $0.3\,^\circ\mathrm{C}$ from the setpoint, and the corresponding accuracy of the steam saturation pressure was typically within $4\,\mathrm{mbar}$ for experiments set to $32\,\mathrm{mbar}$ steam. Deionized water was used in the humidification bottles.

The gas flow from the humidifier to the furnace was heated 5-20 $^\circ\mathrm{C}$ above the water temperature of the humidifier to avoid condensation of steam. A resistance heated wire spiraled around a silicone hose and several layers of aluminum foil was wrapped around the heated

wire and silicon hose for distribution of the heat across the hose. A valve was also installed in this gas line to allow evacuation of the furnace chamber without evaporating the water bath and to avoid unintentional water feeding. A K-type thermocouple was positioned along the outside of the silicone hose, in between coils of the heating wire, and the temperature was controlled by a variable power supply.

Variable area flowmeters were used with the Resistance and Induction 1 furnaces, while mass flow controllers were used with the Induction 2 furnace. The variable area flowmeters were Purgemaster "SNAP-IN" Small Flowmeters by ABB [91] with interchangeable tubes and floats. The flowmeters were configured for 0.115-1.15 l_N/min and 0.366-3.66 l_N/min hydrogen, 0.133-1.33 l_N/min 50:50 H_2:Ar, 0.105-1.05 l_N/min and 1.02-10.2 l_N/min argon and 1.1-45 ml_N/min CO. The flowmeters were used at atmospheric pressure in room temperature, which correspond to the normal condition of 1 atm and 20 °C for which the flow capacity was calculated by the AP-Calc software by ABB [92]. The flow was manually controlled by a needle valve and an accuracy of 3% of the maximum flow capacity is assumed from variations during experiments. Alicat MC Mass Flow Controllers [93] with 5 SLPM (4.92 l_N/min) and 10 SLPM (9.83 l_N/min) flow capacity of relevant gases were used with the Induction 2 furnace. Two controllers were used in parallel for achieving higher gas flow rates. The accuracy of the controllers are 0.2% of the maximum capacity plus 0.8% of the setpoint [93].

3.1.2   Resistance Furnace

The first experiments were conducted in a vertical alumina tube furnace ("Green furnace"), here called the Resistance furnace. The furnace was constructed by Fenstad [94] and the configuration for current experiments is included in Figure 3.2. The furnace was equipped with a vacuum pump connected to the outlet and the furnace pressure could be reduced below 0.1 mbar, but the furnace was not sufficiently sealed to hold vacuum after the pump was stopped. The inner diameter of the alumina tube was 50 mm and crucibles of 35-38 mm inner diameter were used. The crucible could not be consistently aligned concentric to the alumina tube, and the lance was also slightly off center, both in relation to the alumina tube and the crucible. The lance and sample tube were inserted through holes in the upper radiation shields. The alumina tube was surrounded by a 25 cm high $MoSi_2$ heating spiral with 80 mm inner diameter. The power was regulated by a controller connected to the furnace thermocouple positioned at the vertical middle of the heating spiral, outside the alumina tube. The setpoint of the controller was adjusted to the experimental temperature measured with an S-type thermocouple under the crucible. In order to protect the alumina tube from thermal shock, the heating rate was restricted to 5 °C/min in the first hour and more than 3 h was used to stabilize the temperature under the crucible at 1500 °C. The cooling rate was also restricted to 5 °C/min.

74

sampling tube (quartz glass)

lance (quartz glass)

inlets for gas, lances, sampling,
thermocouples, EMF sensors et c.

brass top lid

brass head
(upper end piece)

O-ring seal

upper insulation collar
(porous alumina)
(ceramic fiber)

copper tubing
(for water cooling)

alternative gas outlet
overpressure security valve
vacuum-meter
vacuum valve
vacuum pump

steel clamp

**FURNACE
ENCLOSURE :**
upper brass plate
+
cylindrical jacket

main insulation body
(porous alumina)

thermocouple for
temperature control

heating element
(MoSi$_2$ spiral)

furnace tube
(dense Al$_2$O$_3$)

radiation shields
/ convection retarders

support tube

lower insulation collar
(porous alumina)
(ceramic fiber)

bottom gas inlet

40

30

20   scale
        (cm)

10

0

crucible support
(graphite)

thermocouple
in alumina sheath

distance tubes
(dense Al$_2$O$_3$)

Figure 3.2: Cross-section schematic of Resistance furnace, modified from Fenstad [94].

75

Figure 3.3 shows temperature profiles recorded with argon atmosphere. The thermocouple was moved up and down over the same distance. At each height, the temperature was stabilized and measurements continued for at least 5 min to ensure a standard error below $0.5\,°C$ (vertical error bars in Figure 3.3). The height of the crucible support was adjusted by stacking distance tubes and radiation shields around the alumina support tube surrounding the bottom thermocouple. For the temperature profiles in Figure 3.3, the support was near the bottom of the furnace insulation (0 cm on the scale in Figure 3.2). A crucible support height of 9.6 cm was finally used for experiments and the temperature profile in Figure 3.4.
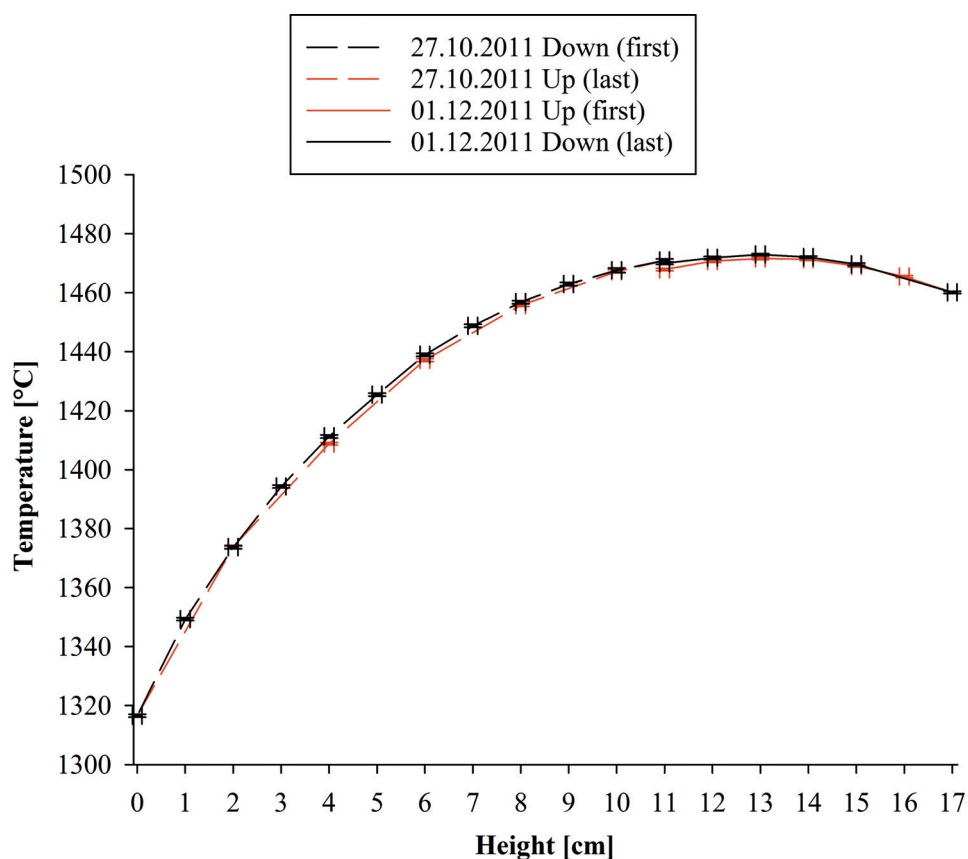
Figure 3.3: Temperature profiles in empty Resistance Furnace with argon atmosphere, recorded October 27, 2011 and December 1, 2011. The furnace temperature was controlled to $1500\,°C$. The height scale refers to Figure 3.2.

Figure 3.4 shows temperature profiles recorded with silicon melt in a quartz crucible and alumina retainer while blowing $0.045 \, \text{bar}$ steam in 50:50 H_2:Ar at $1 \, l_N/\text{min}$ total gas flow rate through the sample tube, while a thermocouple in an alumina thermowell was inserted through the lance port (in Figure 3.2). The temperature profile was recorded from the bottom of the melt to shortly above the exit of the sample tube lance, which was positioned $10 \, \text{mm}$ above the melt surface as indicated by the vertical reference lines in Figure 3.4.

A sample chamber was used to be able to keep the furnace sealed during sampling. In Figure 3.2, the sample chamber is included as it was mounted on top of the furnace. It consisted of a tube with a ball valve below and a detachable stuffing box on the upper end with o-rings sealing around the sample tube. The volume and length of the sample extracted into the sample tube were controlled to reduce damage by heating of the o-rings in the stuffing box while the ball valve was closed under the sample. The stuffing box and sample tube was disconnected after the ball valve was closed, and reconnected before the valve was opened for extraction of the next sample.
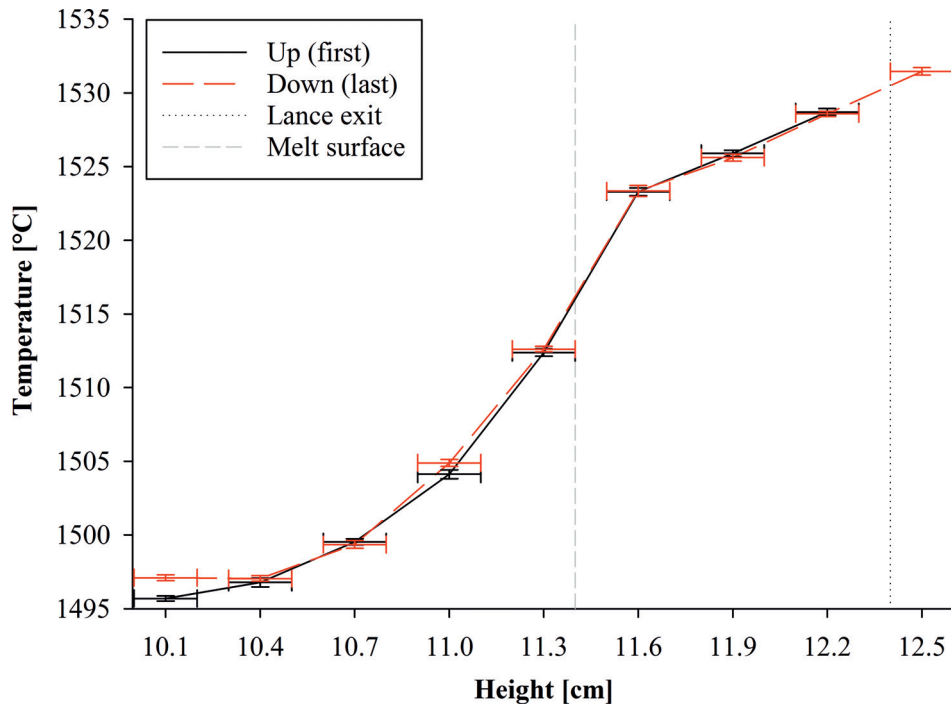
Figure 3.4: Temperature profiles from bottom of the silicon melt to the height of the lance exit during gas blowing of $0.045 \, \text{bar}$ steam in 50:50 H_2:Ar at $1 \, l_N/\text{min}$ total gas flow rate. The furnace temperature was controlled to $1494 \, °C$ and the temperature directly under the quartz crucible and alumina retainer was $1396 \, °C$. The height scale refers to Figure 3.2.

3.1.3 Induction 1 Furnace

The experimental setup was moved to the Induction 1 furnace after repeated cracking of the alumina tube in the Resistance furnace. The induction furnace was also considered better suited for the process due to forced convection. Furthermore, the melt surface could be observed in the part close to the crucible wall towards the back of the furnace through a viewport in front of the lance. The temperature could be accurately measured inside the melt, as a graphite thermowell was fastened along the inside of the crucible wall. The graphite thermowell rested on the bottom of the crucible. A second alumina thermowell was positioned inside the graphite thermowell to further protect the thermocouple (included in Figure 3.9). B-type thermocouples were used in the Induction 1 furnace.

A schematic of the Induction 1 furnace (Balzers VSG 10) is shown as part of the experimental setup in Figure 3.5. The furnace was equipped with a vacuum pump connected to the outlet (not shown in Figure 3.5). The furnace could typically be evacuated to 0.1-0.2 mbar before experiments, but the furnace sealing could not hold such vacuum without the pump running. A continuous flow of argon was introduced through the furnace chamber from re-filling of the furnace until final evacuation after cooling, except during feeding of reactive gas, in order to minimize oxygen contamination from the outside air. Crucibles of 70 mm inner diameter were inserted into concentric sheets of graphite felt with a sheet of mica as the outer insulation inside the coil. The sample chamber used for the Induction 1 furnace is the same as that described for the Resistance furnace in Section 3.1.2.

The main source of error in the temperature reported for experiments in the induction furnaces is fluctuations of the temperature over time. The temperature was controlled by manually adjusting the power supply. The average temperature and its uncertainty is assumed from the variations during the experiments. Although spikes of up to 30 °C offsets from the desired temperature could occur, the temperature was rarely more than 10 °C off and this is used to cover the typical uncertainty of the mean.

Temperature profiles in Figure 3.6 were recorded after experiment $Q(\mathrm{Ind\_1})\_3$. A S-type thermocouple inside an alumina thermowell was lowered through the sample chamber while a 3.0 $\mathrm{l_N/min}$ total gas flow rate of 50:50 H_2:Ar with 0.032 bar steam was continued out of the lance 50 mm above the melt surface. The thermowell was off-center and at an 18.5° angle from vertical. The temperature profile across the melt surface is assumed to be smoothed out in Figure 3.6 by the cold-finger effect of the thermowell, so the actual gradient during experiments could be greater, particularly directly beneath the lance where fresh gas is supplied. A second temperature profile was recorded without gas flow as the thermowell was raised after gas feeding was stopped.
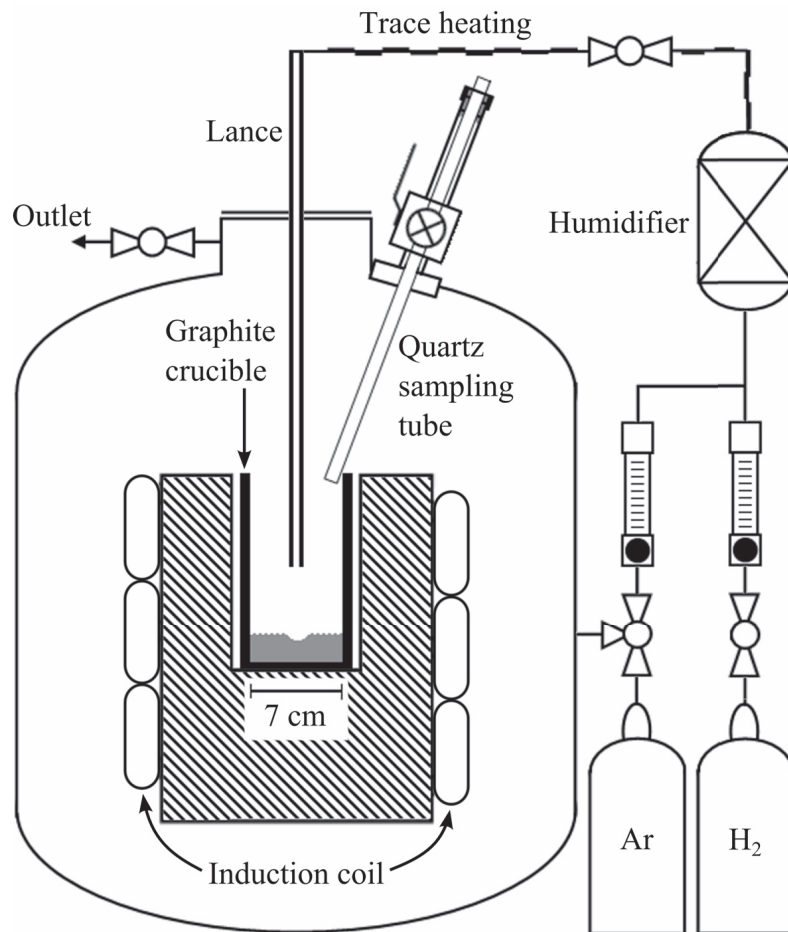
Figure 3.5: Experimental setup with cross-section schematic of Induction 1 furnace "Balzers", modified from Nordstrand and Tangstad [17]. Only the inside of the crucible is drawn to scale with the scalebar, for 200 g melt.
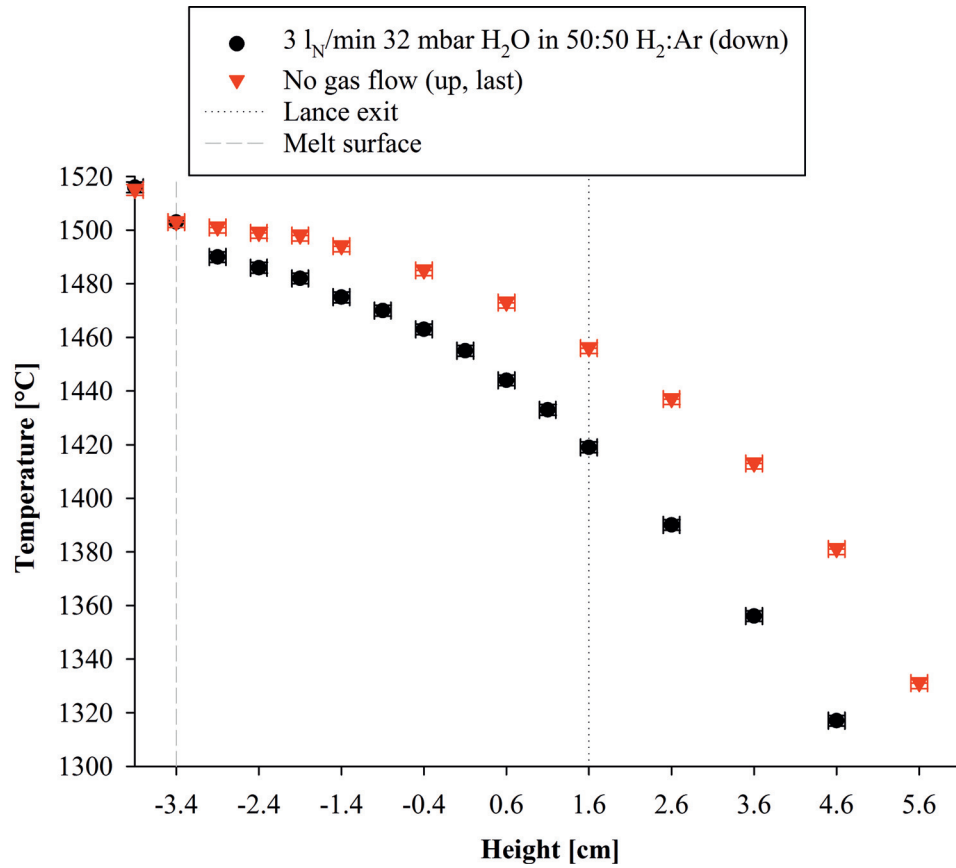
Figure 3.6: Temperature profiles in the Induction 1 furnace recorded through sample chamber with continued gas flow after experiment $Q(\text{Ind\_1})\_3$ and after stopping the gas flow. The height scale refers to the middle of the coil height at 0 cm. The temperature dropped to 373 °C at the top of the coil at 12.6 cm and was 82 °C directly beneath the wall of the furnace chamber lid. The reading at -3.9 cm (0.5 cm below the surface) indicate a melt temperature of 1516 °C.

3.1.4 Induction 2 Furnace

The experimental setup was again moved to the Induction 2 furnace ("Blue furnace") after a final break-down of the power supply to the Induction 1 furnace. The Induction 2 furnace also had manual temperature control and used the same crucibles as the Induction 1 furnace, but the coil was smaller as shown in Figures 3.7 and 3.8 compared to Figure 3.5. The weight of the crucible was held by the coil and it had crept to a 5-7° angle off vertical (Figure 3.7). Almost all of the melt surface could be observed through the viewport labeled in Figure 3.7, and a camera ("D3200" by Nikon [95]) was mounted over the viewport for imaging of the melt surface and potentially build-up of surface coverage during experiments. Different optical filters were attempted for promoting contrast between silica and silicon, and a glass with thin gold coating was selected.

The Induction 2 furnace could be evacuated to less than $1.3 \cdot 10^{-3}$ mbar, and could typically hold such vacuum without the pump running. The vapor pressure of the vacuum oil was rated to $1 \cdot 10^{-4}$ mbar, and the actual furnace pressure could not be measured because the pressure sensor stopped at $1.3 \cdot 10^{-3}$ mbar as the lower limit of its operation range. The furnace was evacuated from the bottom of the chamber. Due to dust formation in the experiments, the vacuum pump required frequent flushing and oil replacement.

An one-way valve was installed at the outlet in order to protect against accidental surging of air from the ventilation into the furnace. There was a pressure drop across the valve which caused over-pressure in the furnace during the gas blowing experiments. The furnace pressure was indirectly adjusted by adjusting a flow of auxiliary argon through the furnace. The auxiliary argon was introduced at the top of the furnace to the left and behind the crucible, and was not supplied to the melt surface. Up to around 24 l_N/min was used in "H_2O" experiments (Table 3.15), and such high flow rates of argon also reduced the risk of condensation of steam inside the furnace in the case it remained unreacted.

The bottom of the sample chamber and its valve is shown in Figure 3.7. The sample chamber was large compared to that for the Resistance and Induction 1 furnaces. It was connected to vacuum and argon, so that air could be evacuated and replaced by argon while keeping the ball valve to the furnace closed. The top lid of the sample chamber was a stuffing box through which a stainless steel tube was inserted. The stuffing box and tube could be disconnected from the top of the sample chamber. The stainless steel tube was connected to a syringe in the top end and had a connection in the lower end for fitting 30 cm long quartz tubes with 6 mm outer and 2 mm inner diameter to hold the samples. PTFE (Teflon) ferrules were used in the connection to prevent cracking of the quartz tubes.
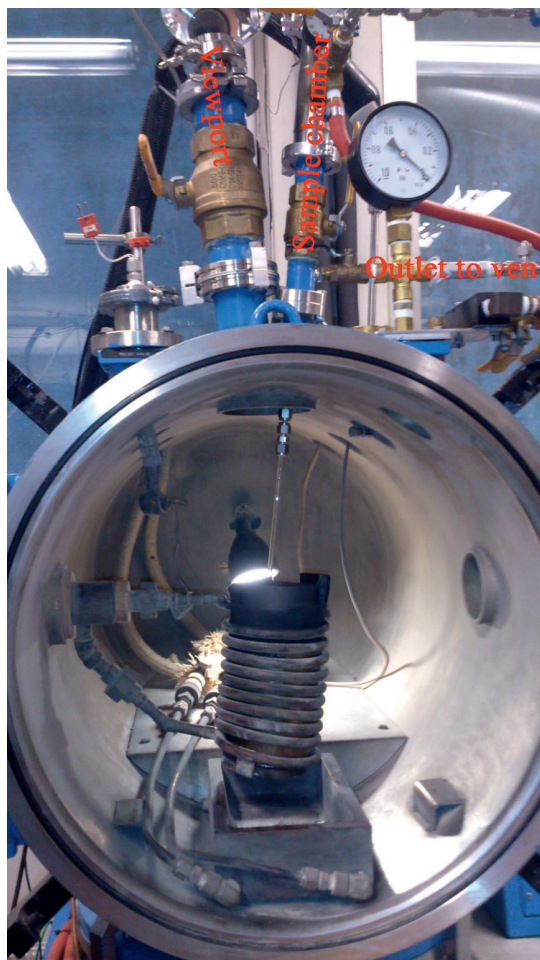
Figure 3.7: Picture of Induction 2 furnace with sample tube extending from the sample chamber. The lance is pictured in Figure 3.8. For reference, the inner diameter of the chamber is $51\,\mathrm{cm}$.

The lance is pictured in Figure 3.8 together with the C-type thermocouple mounted in the crucible after experiment H_2O_30. Most experiments used an alumina lance with $4\,\mathrm{mm}$ inner diameter. The lance could be rotated around a tube coming down to the connection at the upper right in Figure 3.8 through a stuffing box on top of the furnace. This stuffing box and tube could also be tilted in all directions. The lance was aligned to track the center of the tilted crucible when raised and lowered to different positions.
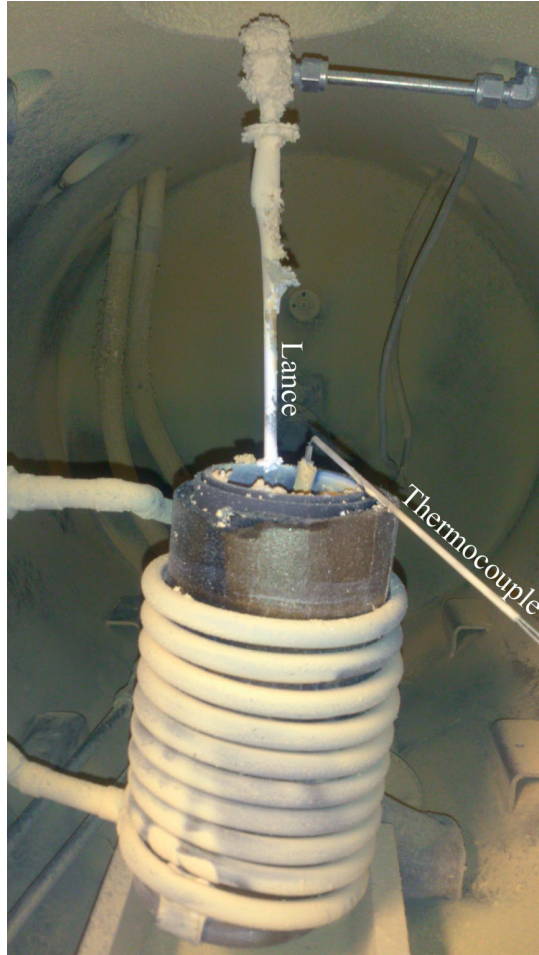
Figure 3.8: Picture inside Induction 2 furnace with lance raised above crucible top after experiment H_2O_30. The crucible was positioned 4 cm above the support by a stack of graphite felt discs. The lance was lowered inside the crucible during experiments.

The temperature at the top of the crucible wall was measured with an additional thermocouple in experiments Pass_H_2a and Pass_Ar,H_2 (Table 3.18). A thermocouple was placed in the alumina thermowell fastened over the crucible wall in Figure 3.9. At a melt temperature of $1498\,°C$, the temperature at the crucible top was stabilized to $873.4 − 875\,°C$ over 5 min before starting gas blowing in Pass_Ar,H_2. In Pass_H_2a, the temperature gradually decreased to $833\,°C$ over $71 − 81$ min gas blowing of $0.060 − 0.065$ bar steam in hydrogen at 2.01 l_N/min total gas flow rate.
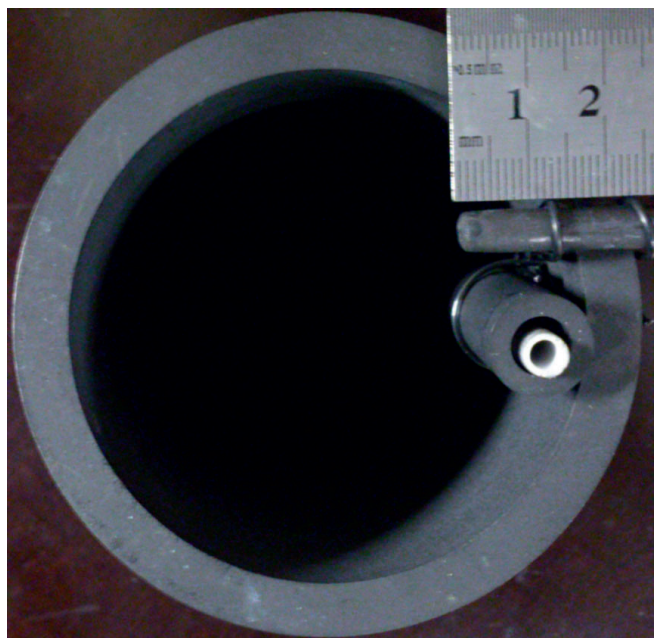
Figure 3.9: Thermowells in 70 mm crucibles for the induction furnaces. The image is taken from above. The graphite and alumina thermowell (lower in picture) extend to the bottom of the crucible and was used for measurement of the melt temperature in all experiments in induction furnaces. The alumina thermowell mounted over the crucible wall (upper in picture) was added in Pass_H_2a and Pass_Ar,H_2 to measure the temperature at the top of the crucible.

3.2 Procedure

In preparations to experiments, the silicon feedstock and boron powder (99.6%, "B 006012" by Goodfellow Corporation [96]) was weighted and added to the crucible. The boron powder was weighted to a mass fraction of $150 \cdot 10^{-6}$ of the mass of silicon in experiments with EG-Si, FBR-, or UMG-Si, but was not added in experiments with MG-Si. Analysis of the MG-Si purity is reported in Table 4.21. UMG-Si was also analyzed for the same 19 impurity elements. The concentrations of all impurity elements were below 1 ppmw and the measurements were not considered accurate for such low concentrations. FBR-Si and EG-Si has even higher purities of 5N and 9N, respectively. The charged crucible was weighted before experiments. The crucible material was isotropic graphite ("IG-15" by Toyo Tanso [97] of regular purity) with 3 ppmw boron contamination or high-purity "Quartz Glass".

84

For experiments in induction furnaces, a thermowell was first fitted along the inside wall of the crucible. Two holes were drilled with horizontal spacing of the thermowell diameter a few centimeters below the top of the graphite crucible. A molybdenum wire was bent in a U-shape around the thermowell and threaded through the holes in the crucible. The ends of the molybdenum wire were bent tightly to the outside crucible wall for secure attachment of the thermowell. The graphite thermowell rested on the bottom of the crucible. An alumina thermowell was positioned inside the graphite thermowell for further protection of the thermocouple (see Figure 3.9).

The charged crucibles were mounted in the furnace and the furnace was evacuated and re-filled with argon (grade 4.6) before heating. More than 3 h were used to heat the Resistance furnace. The silicon feedstock started melting up to 1.5 h before the experiment started. Three consecutive samples were extracted from different depths in the melt before reactive gas blowing in the first experiment (CO_Quartz in Table 3.2) to test for boron dissolution and homogeneity. The first sample was extracted from near the bottom of the melt and contained 127 ± 3 ppmw boron, the second sample from the middle of the 2 cm deep melt was analyzed to 131 ± 9 ppmw and the last sample from near the top contained 126 ± 3 ppmw boron. The variation of the measurements is within the uncertainty of the boron analysis, suggesting that boron was homogeneously distributed in the melt before experiments and completely dissolved. Analysis of boron contents in samples taken after melting in argon were lower than the 150 ppmw expected from weighing of the boron addition. Boron is not expected to evaporate significantly fast in argon due to its high boiling point, but could potentially react with impurities in the atmosphere. Boron powder may potentially be carried at the melt surface by surface tension. Analysis of the first sample was used for reference to assess boron removal during experiments.

The induction furnaces were heated for more than 30 min with step-wise increasing the power during heating. After melting, adjustments continued for more than 15 min before starting reactive gas blowing. Boron dissolution and homogenization was tested three times in the Induction 2 furnace. Boron was added to 800 ppmw in two of the tests and 4920 ppmw in one (green squares in Figure 3.10). The first sample in each test was extraction directly after melting. Figure 3.10 shows that 800 ppmw boron dissolved quickly as the silicon melted and no further increase is shown after the silicon melted. Furthermore, the variations between samples are within the uncertainty of the analyzes, which can be taken as a sign of homogeneous boron distribution in the melt. Due to convection by induction, samples were not extracted from the same body of melt and inhomogeneities in the melt would likely cause different concentrations between samples. Lower boron contents was added in gas blowing experiments and boron may also be assumed to be completely dissolved and homogenized in the melt before gas blowing was started. A slightly increasing trend is shown in Figure 3.10 for the test in which boron was added to 4920 ppmw, suggesting that dissolution continued after melting of silicon completed. After 65 min with argon flow, the boron content was reduced to 3680 ± 156 ppmw.
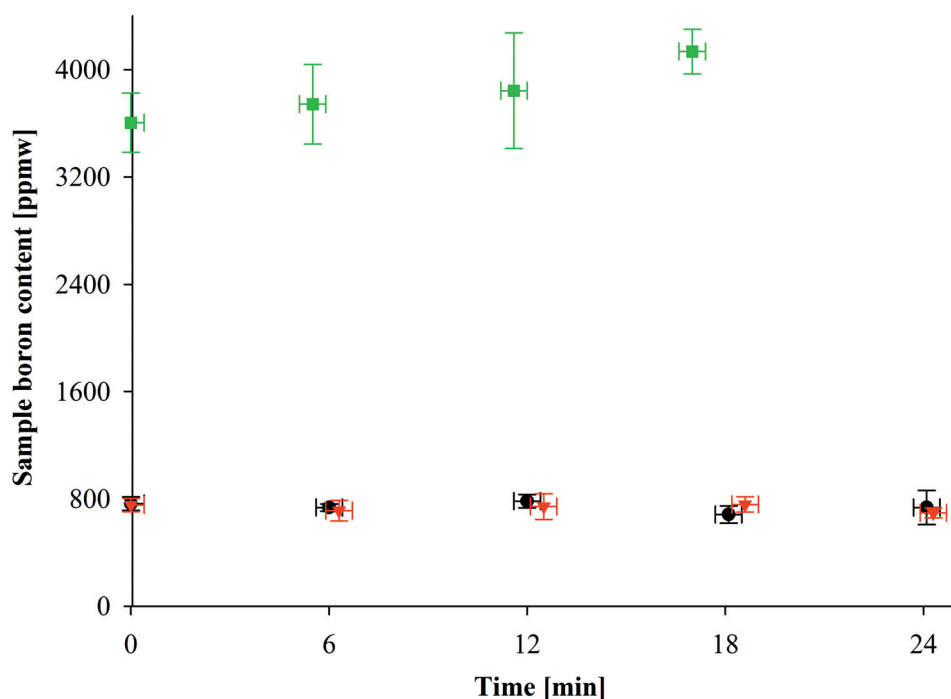
Figure 3.10: Evolution of boron content in samples extracted directly after melting (at ≈ 0 min) under argon atmosphere. Each series is a different test. 800 ppmw dissolved quickly and the variations between samples are within the uncertainty of analysis, which suggests homogeneous boron distribution. Addition of boron to 4920 ppmw caused an increasing trend as a sign of on-going dissolution.

In the Resistance furnace, the first sample was extracted after stabilization of the furnace, but before starting reactive gas blowing. Timing of the experiment was started when the reactive gas was introduced through the lance. The temperature of the humidifier typically fluctuated within 0.5 °C around setpoint in the first minutes of steam feeding. After switching to induction furnaces, also the gas flow and humidifier was stabilized before the initial sample was extracted, so the blow time started typically a few minutes before timing of the samples.

At time of sampling, a quartz tube was inserted into the melt and a syringe on the top end was used to extract melt into the quartz tube. The samples were typically 0.5-1.5 g. Six samples were typically extracted during the experiment, unless excessive surface coverage or technical problems prematurely prevented further sampling. The quartz tubes tended to soften in the melts at 1500 °C and higher temperature. Care was taken to minimize the time that the quartz tubes were exposed to the high temperatures inside and shortly above the melt. Quartz tubes of 1 mm thickness tended to curl up and break off in the melt in the earliest experiments.

86

Reliable sampling was achieved with tubes of 2 mm wall thickness.

In the Resistance and Induction 1 furnaces, a long (up to 150 cm) quartz tube went through a stuffing box which made the top lid of the sample chamber. The tube was mounted by attaching the stuffing box on top of the sample chamber and a ball valve between the furnace and sample chamber was opened during sampling and closed again before the tube was disconnected. The small quantity of air in the sample chamber was not observed to be detrimental for the experiments. The part of the tube that contained the sample was cut off and the tube was marked at the height between the middle of the melt and top of the stuffing box when assembled on the sample chamber, in preparation for extracting the next sample. For experiments in the Induction 2 furnace, the larger sample chamber was evacuated and filled with argon before and after sampling. A steel tube was connected to the syringe and glided through the stuffing box. 30 cm quartz tubes were changed between each sample extraction.

The melt was observed for passivation and surface coverage during experiments in the induction furnaces. Due to the angle of the viewport over the melt, only one side of the melt surface could be observed in the Induction 1 furnace, while most of the surface could be observed in the Induction 2 furnace. The melt surface was observed and imaged before and/or after sampling to assess surface coverage and whether it could have affected the rate of boron removal. There was an increased risk of surface coverage from falling deposits during sampling because the sample tube was moved and could loosen fume deposits from the lance crucible and also radiation shields in the Resistance furnace. In the Induction 2 furnace, also the lance was moved towards the crucible wall to make space for sampling. The trend of boron concentration reduction between samples was also later cross-referenced to images. After gas blowing was completed, the lance was lifted out of the crucible and the final melt surface was imaged, including the center part that was hidden by the lance and its fume deposits during the experiment. The silicon surface was also inspected visually and imaged in the crucible after cooling to assess surface coverage, which was most important for experiments in Resistance and Induction 1 furnaces.

The crucibles tended to crack during solidification due to expansion of silicon. Remaining melt could then flow through the cracks. During furnace cooling, the melt tended to solidify inside or directly outside the crack and minor amounts of melt occasionally spilled into the graphite wool insulation. Care was taken to avoid premature solidification as the silicon could not be re-melted due to the risk of cracks in the crucible. With experience, cracking of graphite crucibles with 200 g silicon was avoided for several of the later experiments in the Induction 2 furnace, mainly by maintaining induction at low power during solidification.

After cooling, remains of reactive gases were removed by evacuation of the furnace before it could be opened and the crucible was taken out. The crucible was cleaned from fume deposits by pressurized air blowing and weighted. Fume also deposited in the furnace chamber, which was cleaned after each experiment using dust protection. Figure 3.11 show fumes inside Induction 2 furnace after experiment H$_2$O_60.

Figure 3.11: Fume deposits in Induction 2 furnace after experiment H_2O_60.

3.3 Parameters and Series

Series of experiments were conducted to study the effects of individual experimental parameters on boron removal, silicon oxidation and passivation. Tables in this section list the experiments in each series and their experimental parameters. In these tables, p is the total pressure, m is the melt mass, $d_c = 2r_c$ is the inner crucible diameter and t_r is the duration of reactive gas blowing. The values are reported to their significant figure unless the uncertainty (at approximately 95% confidence level) is explicitly stated, so that the last digit is uncertain or vary between experiments in the series.

3.3.1 Reactive Gases

The initial vision of the project was to use natural gas or its derivatives in metallurgical purification of silicon for solar cell applications, and boron removal was attempted with CO for oxidation. HBO was not established as the principal product responsible for gas refining at that time. Different parameters was varied in initial experiments with CO as shown in Table 3.2, including the partial pressure of CO in argon, total gas flow rate and flow patterns (impinging jet for $H = 10$ mm and bubbling for $H = -10$ mm). The experiments turned out to be most important for the study of CO decomposition and SiC formation at the melt surface.

Table 3.2: Parameters for "CO" experiments. Common parameters: argon atmosphere, $p = 1.00$ bar, $d = $ 2-4 mm, $m = 40$ g, EG-Si feedstock, $T \sim 1550 \pm {<}50\,°\mathrm{C}$ ($T = 1500\,°\mathrm{C}$ under crucible), Resistance furnace.

"CO" experiments	p_{CO} [bar]	Q [l$_\mathrm{N}$/min]	H [mm]	Crucible material	d_c [mm]	A_c [cm^2]	t_r [min]	Date [dd.mm.yyyy]
CO_Quartz	0.001	1.00	10	Quartz	31.5	7.8	150	03.01.2012
CO_0.1	0.001	1.00	10	Graphite	38.0	11.3	250	10.01.2012
CO_1.1	0.011	1.00	10	Graphite	38.0	11.3	183	17.01.2012
Q(CO)_0.1	0.009	0.11	10	Graphite	38.0	11.3	183	20.01.2012
Q(CO)_Sub	0.009	0.11	-10	Graphite	38.0	11.3	202	24.01.2012
CO_4.8	0.048	1.00	10	Graphite	38.0	11.3	169	13.01.2012

CO was compared to steam as the oxidizing agent in "H$_2$O/CO" experiments in Table 3.3, in which the same amount of oxygen atoms were introduced in both experiments together with equal or higher amounts of hydrogen atoms in steam.

Table 3.3: Parameters for "H_2O/CO" experiments. Common parameters: $p = 1.00$ bar, $Q = 1.00$ l_N/min, $d = 4.0$ mm, $H = 10$ mm, $m = 40$ g, EG-Si feedstock, $T \sim 1550 \pm <50\,°C$ ($T = 1500\,°C$ under crucible), Resistance furnace, $d_c = 38$ mm, graphite crucible, $A_c = 11.3$ cm^2.

"H_2O/CO" experiments	p_{H_2O} [bar]	p_{CO} [bar]	t_r [min]	Date [dd.mm.yyyy]
H_2O/CO_2.2/2.4	0.022	0.024	206	
H_2O/CO_4.5/0	0.045	0	198	03.02.2012

The necessity for supplying hydrogen in addition with oxygen for removal of boron to the gas was revealed in experiments where both CO and hydrogen was used as reactive gases, with partial pressures in Table 3.4. Steam was selected as the oxidizing agent in further experiments based on results in Section 4.1.1.

Table 3.4: Parameters for "CO/H_2" experiments. Common parameters: $p = 1.04$ bar, $Q = 1.07$ l_N/min, $d = 4.0$ mm, $H = 10$ mm, $m = 40$ g, EG-Si feedstock, $T \sim 1550 \pm <50\,°C$ ($T = 1500\,°C$ under crucible), Resistance furnace, $d_c = 38$ mm, graphite crucible, $A_c = 11.3$ cm^2.

"CO/H_2" experiments	p_{CO} [bar]	p_{H_2} [bar]	t_r [min]	Date [dd.mm.yyyy]
CO/H_2_2.3/6.3	0.023	0.063	182	23.03.2012
CO/H_2_2.4/9.9	0.024	0.099	184	26.03.2012

3.3.2 Gas Flow Rate

The effect of gas flow rate on the rate of boron removal was important for investigating mass transfer in the gas phase. After an initial test of the importance of the total gas flow rate in "Q(Res)" experiments (Table 3.5) in the Resistance furnace, the number of experiments were increased in "Q(Ind_1)" (Table 3.6) after switching to the Induction 1 furnace. More controlled experiments were finally conducted in the "Q" series (Table 3.7) in the Induction 2 furnace after optimizing the lance height, and extracted samples were weighted for complete accounting of the weightloss.

Table 3.5: Parameters for "Q(Res)" experiments. Common parameters: $p_{H_2O} = 0.023$ bar, $p_{H_2} = 0.49$ bar, argon atmosphere, $p = 1.00$ bar, $d = 4.0$ mm, $H = 10$ mm, $m = 40$ g, EG-Si feedstock, $T \sim 1500 \pm {<}30$ °C ($T = 1426$ °C under crucible and alumina retainer), Resistance furnace, $d_c = 35$ mm, quartz crucible, $A_c = 9.6$ cm^2.

"Q(Res)" experiments	Q [l$_N$/min]	t_r [min]	Date [dd.mm.yyyy]
Q(Res)_0.14	0.14	182	23.08.2012
Q(Res)_1	1.01	215	21.08.2012

Table 3.6: Parameters for "Q(Ind_1)" experiments. Common parameters: $p_{H_2O} = 0.032$ bar, $p_{H_2} = 0.49$ bar, argon atmosphere, $p = 1.00$ bar, $d = 4.0$ mm, $m = 200$ g, EG-Si feedstock, $T = 1500$ °C, $d_c = 70$ mm, graphite crucible, $A_c = 36.9$ cm^2.

"Q(Ind_1)" experiments	Q [l$_N$/min]	H [mm]	t_r [min]	Date [dd.mm.yyyy]
Q(Ind_1)_0.5	0.50	50	161	28.11.2012
Q(Ind_1)_1	1.00	50	>150	19.10.2012
Q(Ind_1)_2	2.00	50	>150	26.11.2012
Q(Ind_1)_3	3.0	50	315	19.12.2012
Q(Ind_1)_3.5	3.5	46	153	24.07.2013
Q(Ind_1)_4	4.1	50	156	19.07.2013
Q(Ind_1)_6	5.9	50	157	23.07.2013

Table 3.7: Parameters for "Q" experiments. Common parameters: $p_{H_2O} = 0.032$ bar, hydrogen atmosphere, $p = 1.12$ bar, $d = 4.0$ mm, $H = 20$ mm, $m = 200$ g, EG-Si feedstock, $T = 1500$ °C, Induction 2 furnace, $d_c = 70$ mm, graphite crucible, $A_c = 36.9$ cm^2.

"Q" experiments	Q [l$_N$/min]	t_r [min]	Date [dd.mm.yyyy]
Q_2	1.99 ± 0.03	69.2	19.11.2013
Q_4	4.00 ± 0.06	63.0	18.12.2013a
Q_6	6.00 ± 0.06	73.2	10.12.2013
Q_8a	8.00 ± 0.08	67.0	16.12.2013b
Q_8b	7.99 ± 0.09	62.0	17.12.2013b
Q_10	10.00 ± 0.09	67.0	11.12.2013
Q_12	12.00 ± 0.11	64.0	16.12.2013a
Q_14	14.00 ± 0.13	65.0	18.12.2013b
Q_16a	16.00 ± 0.15	69.0	17.12.2013a
Q_16b	16.00 ± 0.15	69.1	19.12.2013a

3.3.3 Crucible Diameter

The effect of gas-melt interface area on the rate of boron removal by an impinging gas jet was studied by comparing crucibles of different sizes in the Induction 1 furnace, with parameters in Table 3.8. Figure 3.12 shows the crucible assembly used to fit a 38 mm diameter crucible inside a 70 mm crucible used in the Induction 1 furnace. In preliminary attempts, the melt ended up in the porous graphite spacer ring. The melt was held inside the crucible by adding an alumina crucible around the graphite crucible 38 mm for separation from the porous graphite spacer.

Table 3.8: Parameters for "d_c" experiments. Common parameters: $p_{H_2O} = 0.032$ bar, $p_{H_2} = 0.49$ bar, argon atmosphere, $p = 1.01$ bar, $Q = 3.0$ l$_N$/min, $d = 4.0$ mm, $H = 50$ mm, EG-Si feedstock, $T = 1500$ °C, Induction 1 furnace, graphite crucible.

"d_c" experiments	"d_c" [mm]	A_c [cm^2]	m [g]	t_r [min]	Date [dd.mm.yyyy]
d_c_38	38.0	9.8	39.99	182	22.11.2012
$Q(Ind\_1)\_3$	70.0	36.9	199.94	315	19.12.2012
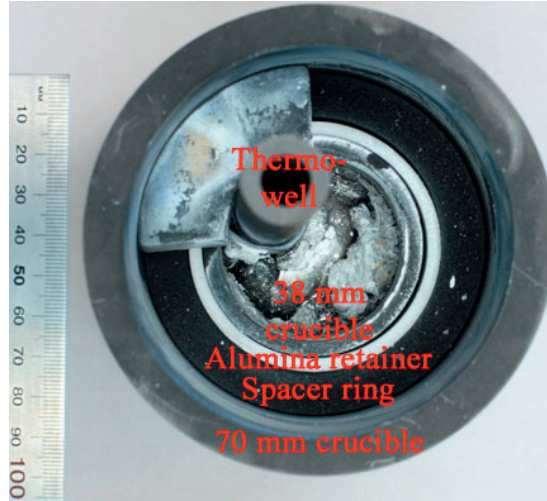
Figure 3.12: Crucible assembly in experiment d_c_38, with 38 mm diameter graphite crucible in the Induction 1 furnace. An alumina retainer around the graphite crucible prevented leakage of the melt into the porous graphite spacer ring which held the 38 mm crucible in the middle of the 70 mm crucible fitting in the Induction 1 furnace. A B-type thermocouple inside an alumina thermowell was positioned inside the graphite thermowell mounted along the inside crucible wall, like in 70 mm diameter crucibles. The image was taken after experiment d_c_38.

3.3.4 Melt Mass

Boron removal from different melt masses were compared in identical crucibles in order to confirm that it does not affect the total mass transfer coefficient for boron removal in which case mass transfer in the bulk melt is not rate determining. The parameters of these "m" experiments are listed in Table 3.9.

Table 3.9: Parameters for "m" experiments. Common parameters: $p_{H_2O} = 0.032$ bar, $p_{H_2} = 0.50$ bar, argon atmosphere, $p = 1.01$ bar, $Q = 3.0$ l_N/min, $d = 4.0$ mm, $H = 50$ mm, EG-Si feedstock, $T = 1500$ °C, Induction 1 furnace, $d_c = 70$ mm, graphite crucible, $A_c = 36.9$ cm^2.

"m" experiments	m [g]	t_r [min]	Date [dd.mm.yyyy]
$Q(\text{Ind}\_1)\_3$	199.91	182	19.12.2012
m_400	399.99	181	14.12.2012

3.3.5 Melt Convection

Similar experiments in the Resistance and Induction 1 furnaces were compared in order to assess whether mass transfer in the melt was rate determining for boron removal in the experiments. Forced convection by induction consistently caused ripples on the melt surface in the Induction 1 furnace, both with and without impinging jet gas flow. Velocities and the mass transfer coefficient in the melt is assumed to be significantly lower for natural convection in the Resistance furnace, as drag from the gas flow did not show an observable contribution to convection of the melt surface in the induction furnaces.

The "Conv" experiments in Table 3.10 used quartz crucibles spray coated with silicon nitride, which in Conv_Ind was inserted in the alumina crucible in the assembly in Figure 3.12. The crucible and lance geometry was identical to minimize geometrical effects like the surface area. However, Conv_Ind used a 9 mm outer diameter quartz thermowell inside the crucible, which is thinner than the graphite thermowell in Figure 3.12 of 14 mm outer diameter. The thermowell was put inside the crucible for most accurate temperature measurements, while this was not practical for Q(Res)_1 in the Resistance furnace. In initial experiments where the thermocouple was positioned along the outside crucible wall, 1490 °C was measured near the end of silicon melting while 1417 °C in the thermowell inside the melt in Conv_Ind agrees with the melting point of silicon of 1414 °C. The temperature and its uncertainty in Q(Res)_1 is assumed for the melt based on a calibration test in which the temperature was measured both under a quartz crucible and alumina retainer and inside the melt under 1 l_N/min total gas flow rate of 0.045 bar steam in 50:50 H_2:Ar, which assimilate conditions of Q(Res)_1.

Table 3.10: Parameters for "Conv" experiments. Common parameters: $p_{H_2O} = 0.023$ bar, $p_{H_2} = 0.49$ bar, argon atmosphere, $p = 1.01$ bar, $Q = 1.01$ l_N/min, $d = 4.0$ mm, $H = 10$ mm, $m = 40$ g, EG-Si feedstock, $d_c = 35$ mm, quartz crucible.

"Conv" experiments	Furnace	T [°C]	A_c [cm^2]	t_r [min]	Date [dd.mm.yyyy]
Q(Res)_1	Resistance	$\sim$1500 $\pm$ <30	9.6	215	21.08.2012
Conv_Ind	Induction 1	1496 $\pm$ 10	9.0	>155	10.01.2013

3.3.6 Lance Diameter

After effects of total gas flow rate on the boron removal rate was observed in "Q(Res)" and "Q(Ind_1)" experiments, "d" experiments with different lance diameters were compared to determine if the effect of the total gas flow rate was due to the gas velocity and diffusion in the gas boundary layer. Mass transfer coefficients for diffusion through the gas boundary layer is expected to increase with increasing gas velocity and reducing lance diameter (Equation (2.53)) when only the lance diameter is changed as in the "d" series in Table 3.11. Experiments d_1-3 used quartz lances with 6 mm outer diameter. The 1.5 mm thick wall in the lance in d_3 was not sufficient for mechanical rigidity when exposed to the high temperature 10 mm above the $1500\ ^\circ$C melt, as the tip of this lance softened and bent.

A 35 mm diameter wide lance was acquired after moving to the Induction 2 furnace, in which the gas flow produced a slight overpressure. Such a wide lance was attempted in order to feed fresh gas over a large area of the melt surface. The effect of gas flow rate could be due to an increasing amount of reactive gases supplied per time for increasing total gas flow rates, and not necessary due to the gas velocity and its effect on gas boundary layer diffusion.

Table 3.11: Parameters for "d" experiments. Common parameters: $p_{H_2O} = 0.032$ bar, hydrogen atmosphere, $Q = 2.0\ l_N/min$, $H = 10$ mm, $m = 200$ g, EG-Si feedstock, $T = 1500\ ^\circ$C, $d_c = 70$ mm, graphite crucible, $A_c = 36.9\ cm^2$.

"d" experiments	d [mm]	p [bar]	Furnace	t_r [min]	Date [dd.mm.yyyy]
$H(d\_35)\_10$	35.0	1.13	Induction 2	61.4	20.11.2013
Ind_1	3.9	0.99	Induction 1	167.0	25.07.2013
d_3	3.0	0.98	Induction 1	159.0	29.07.2013
d_2	2.0	0.99	Induction 1	153.0	26.07.2013
d_1	1.05	0.99	Induction 1	154.0	30.07.2013

3.3.7 Lance Height and Bubbling

The lance height was varied in "H" experiments (Table 3.12) in order to see if boron removal follows the dependence of constant mass transfer in a range of lance heights near the surface as expected from impinging jet theory in Section 2.3.3, and to find this range for current experiments. The 35 mm diameter lance was also moved 5 mm close to the melt surface as shown in Table 3.13, with hope of minimizing loss of gas.

Table 3.12: Parameters for "H" experiments. Common parameters: $p_{H_2O} = 0.032$ bar, hydrogen atmosphere, $p = 1.2$ bar, $Q = 1.99$ l$_N$/min, $d = 4.0$ mm, $m = 200$ g, EG-Si feedstock, $T = 1500\,°C$, Induction 2 furnace, $d_c = 70$ mm, graphite crucible, $A_c = 36.9$ cm^2.

"H" experiments	H [mm]	t_r [min]	Date [dd.mm.yyyy]
H_45	40-50	63.2	13.11.2013
H_30	30	68	14.11.2013
H_24	24	65.5	15.11.2013
Q_2	20	69.2	19.11.2013
H_15	8-20	68	22.11.2013
Ind_2a	10	73	08.11.2013
Ind_2b	10	67	11.11.2013

Table 3.13: Parameters for "$H(d\_35)$" experiments. Common parameters: $p_{H_2O} = 0.032$ bar, hydrogen atmosphere, $p = 1.12$ bar, $Q = 1.99$ l$_N$/min, $d = 35.0$ mm, $m = 200$ g, EG-Si feedstock, $T = 1495\,°C$, Induction 2 furnace, $d_c = 70$ mm, graphite crucible, $A_c = 36.9$ cm^2.

"$H(d\_35)$" experiments	H [mm]	t_r [min]	Date [dd.mm.yyyy]
$H(d\_35)\_10$	10	61.4	20.11.2013
$H(d\_35)\_5$	5	55.5	21.11.2013

The lance was submerged to $H = -32$ mm below the melt surface (10 mm above the bottom) in experiment Bubble_Lance, in order to compare bubbling to impinging jet gas flow. A relatively low gas flow rate of 0.50 l$_N$/min was selected after splashing tests in water, to prevent splashing of the melt over out of the crucible. All parameters are listed in Table 3.14. The submerged part of the quartz lance of 2 mm wall thickness bent $45°$.

Table 3.14: Parameters for experiment Bubble_Lance: $p_{H_2O} = 0.032$ bar, hydrogen atmosphere, $p = 0.99$ bar, $d = 2.0$ mm, $m = 400$ g, EG-Si feedstock, $T = 1500\,°C$, Induction 1 furnace, $d_c = 70$ mm, graphite crucible, $A_c = 36.9$ cm^2.

"Bubble" experiment	H [mm]	Q [l$_N$/min]	t_r [min]	Date [dd.mm.yyyy]
Bubble_Lance	-32	0.50	157	17.12.2012

3.3.8 Steam Content and Temperature

Experiments with different steam partial pressures were compared in the "H_2O" series with parameters in Table 3.15. An elevated melt temperature of 1700 °C was used to allow a wide range of steam partial pressures without passivation. The duration of the experiment was originally selected based on expected boron removal rates from equilibrium modeling with 12 l_N/min total gas flow rate, but excessive fuming and deposition inside the crucible caused surface coverage in the first attempts and the gas flow rate was reduced to 2 l_N/min. Different UMG- and FBR-Si feedstock were compared in H_2O_03a-b with expectation of negligible effect on boron removal like in the comparison of materials by Altenberend [18]. Argon atmosphere was used because the reaction order for steam was predicted from equilibrium equations to be 1.5 in argon, which is not previously observed as shown in Section 5.4.1.

Table 3.15: Parameters for "H_2O" experiments. Common parameters: argon atmosphere, $p = 1.36$ bar, $Q = 2.00$ l_N/min, $d = 4.0$ mm, $H = 20$ mm, $m = 200$ g, $T = 1700$ °C, Induction 2 furnace, $d_c = 70$ mm, graphite crucible, $A_c = 36.9$ cm^2.

"H_2O" experiments	p_{H_2O} [bar]	Feedstock material	t_r [min]	Date [dd.mm.yyyy]
H_2O_03a	0.0317 ± 0.0002	UMG-Si	40.0	27.06.2014a
H_2O_03b	0.0317 ± 0.0002	FBR-Si	40.0	25.08.2014a
H_2O_09	0.0901 ± 0.0005	UGM-Si	40.1	26.06.2014
H_2O_15	0.1501 ± 0.0011	FBR-Si	41.0	19.08.2014
H_2O_20	0.1974 ± 0.0023	EG-Si	37.0	23.06.2014
H_2O_25	0.2506 ± 0.0011	FBR-Si	35.3	29.08.2014b
H_2O_30	0.3003 ± 0.0013	FBR-Si	38.0	21.08.2014
H_2O_35	0.3505 ± 0.0007	FBR-Si	38.0	28.08.2014b
H_2O_40	0.3993 ± 0.0050	EG-Si	39.3	24.06.2014
H_2O_50	0.4998 ± 0.0050	EG-Si	37.2	25.06.2014b
H_2O_60	0.5995 ± 0.0035	EG-Si	40.3	25.06.2014

Atmospheric steam partial pressures were attempted in "$H_2O(T$_1800)_100" experiments at around 1800 °C melt temperature according to Table 3.16, with the hypothesis that the passivation threshold was increased higher at this temperature. $H_2O(T$_1800)_100a used MG-Si for comparison to UMG-Si of relatively high purity in $H_2O(T$_1800)_100b. The humidifier appeared to have malfunctioned in $H_2O(T$_1800)_100b as excessive consumption of steam was observed in the water reservoir. The H_2O content in the feed was above the setpoint and excess water was collected in the bottom of the furnace after the experiments. Excessive dust formation and deposition in the crucible above the melt presumably caused surface coverage by falling deposits, which illustrates the importance of handling the fumes and directing gas flow with fumes out over the side of the melt surface.

Table 3.16: Parameters for $H_2O(T\_1800)\_100$ experiments. Common parameters: argon atmosphere, $d = 4.0$ mm, $H = 20$ mm, $m = 600$ g, Induction 2 furnace, $d_c = 70$ mm, graphite crucible, $A_c = 36.9$ cm^2.

"$H_2O(T\_1800)$" experiments	p_{H_2O} [bar]	p [bar]	Q [l_N/min]	Feedstock	T [°C]	t_r [min]	Date [dd.mm.yyyy]
$H_2O(T\_1800)\_100a$	1.03	1.36	2.02	MG-Si	1799 ± 4	41.5	20.08.2014
$H_2O(T\_1800)\_100b$	> 1.02	1.47	> 1.92	UMG-Si	1785 ± 15	42.6	05.09.2014

3.3.9 Surface Coverage

The effect of surface coverage on boron removal and its reproducibility was observed in the first experiments in the Induction_1 furnace (A/A_c_27 and A/A_c_75), which attempted to reproduce experiment "12" by Nordstrand and Tangstad [17] in the same furnace. Experiment "12"[17] was reproduced without surface coverage in $Q(Ind\_1)\_3$. The crucible was lowered so that the melt surface was 34 mm below the middle of the induction coil in $Q(Ind\_1)\_3$ and later experiments in the Induction 1 furnace. The melt surface was 3 mm above the middle of the induction coil in A/A_c_27 and A/A_c_75. Experiment A/A_c_00 is included in the study of the effect of surface coverage on boron removal in Table 3.17 in spite of its higher total gas flow rate because the surface was completely passivated. A humidifier malfunction caused increased water consumption and steam feeding. The steam was not consumed over the completely passivated melt and severely oxidized the graphite crucible instead, making a hole above the melt in one side.

Table 3.17: Parameters for "A/A_c" experiments. Common parameters: $p_{H_2} = 0.49$ bar, argon atmosphere, $p = 1.02$ bar, $d = 4.0$ mm, $H = 50$ mm, $m = 200$ g, EG-Si feedstock, $T = 1500$ °C, Induction 1 furnace, $d_c = 70$ mm, graphite crucible, $A_c = 36.9$ cm^2.

"A/A_c" experiments	Q [l_N/min]	p_{H_2O} [bar]	t_r [min]	Date [dd.mm.yyyy]
A/A_c_00	4.9	>0.032	≥ 151	18.10.2012
A/A_c_27	3.1	0.032	235	15.10.2012
A/A_c_75	3.0	0.032	160	25.10.2012
$Q(Ind\_1)\_3$	3.0	0.032	315	19.12.2012

3.3.10 Passivation Threshold

Dedicated experiments in the "Pass" series were conducted to observe the threshold steam partial pressure for passivation at $1500\,°C$ melt temperature. The steam partial pressure set in the feed was increased in typically $0.005\,bar$ increments until a secondary phase of silica was observed to form on the melt surface. The passivation threshold could be observed under different conditions in a single experiment, by bypassing the humidifier and heating the melt above $1700\,°C$ for evaporation of the surface coverage within several minutes. Table 3.18 lists the "Pass" experiments and the range of variation for the different parameters. Boron was not added in these experiments.

After evaporation and resetting the steam partial pressure closely below the passivation threshold for $2\,l_N/min$ total gas flow rate in Pass_H_2b and Pass_Ar,H_2, the gas flow rate was increased to observe its effect on the passivation threshold. At high gas flow rates like $10\,l_N/min$, observations of the passivation threshold was increasingly difficult because excessive fuming blurred vision to the melt surface and increased the risk of fume deposits falling onto the melt and cause surface coverage without passivation. These effects were also observed in "$H_2O(T\_1800)$" experiments and H_2O_40-60 with higher steam partial pressures and increased melt temperature at $2\,l_N/min$ gas flow rate, so direct observation of the passivation threshold was not attempted in experiments similar to "Pass" above $1500\,°C$.

Table 3.18: Parameters for "Pass" experiments. Common parameters: $p = 1.09$-1.36 bar, $d = 4.0$ mm, $H = 20$ mm, $m = 200$ g, $T = 1500\,°C$, Induction 2 furnace, $d_c = 70$ mm, graphite crucible, $A_c = 36.9$ cm^2.

"Pass" experiments	p_{H_2O} [bar]	Q [l_N/min]	Atmosphere	Feedstock	Date [dd.mm.yyyy]
Pass_Ar	0.038-0.075	2.01	Argon	FBR-Si	22.08.2014
Pass_Ar,H_2	0.059-0.095	1.99-10.2	Argon	FBR-Si	27.08.2014
	0.065	10.0	Hydrogen	FBR-Si	
Pass_H_2a	0.060-0.065	2.01	Hydrogen	EG-Si	26.08.2014
Pass_H_2b	0.050-0.085	2.00-5.01	Hydrogen	FBR-Si	29.08.2014a

3.4 Analyzes and Sample Preparation

Samples extracted from the melt during experiments were analyzed for boron content by inductively coupled plasma mass spectroscopy (ICP-MS). Samples were prepared in-house with the aid of Torild Krogstad (DMSE, NTNU) for use of hydrofluoric acid and analyzed by Syvering Lierhagen at Department of Chemistry, NTNU. After experiments in the Resistance furnace, formation and distribution of byproducts were assessed by scanning electron microscopy (SEM), energy dispersive X-ray spectroscopy (EDS) and wavelength-dispersive X-ray spectroscopy (WDS) mapping in vertical cut cross-sections of the crucibles with solidified melt. The microprobe analyzes were conducted in-house in collaboration with Morten Peder Raanes (DMSE, NTNU).

3.4.1 ICP-MS

After experiments, the samples from the melt were encapsulated inside a quartz tube. For experiments in the Resistance and Induction 1 furnaces, the samples were released by dissolving in concentrated hydrofluoric acid over two days. The samples were inspected for complete dissolution of the quartz tube before proceeding. Etching of the quartz tubes proved unnecessary as pieces of silicon was released by hammering the quartz tube. Silicon pieces were collected directly from hammering of the quartz tubes for experiments in the Induction 2 furnace.

Samples with or without quartz tube were hammered to pieces with a WC hammer on a silicon top cut plate from directional solidification for simplicity and in order to minimize contamination. This method was compared to crushing the pieces to powder in a WC disk mill for samples of experiments Ind_2a and -b. Tungsten contamination varied between $3\text{-}47\,\mathrm{ppmw}$ for crushing to pieces with WC hammer and was over $1300\,\mathrm{ppmw}$ for crushing to powder in the disk mill. The equipment were cleaned with deionized water and wiped with cleenroom wipes ("Amplitude EcoCloth" by Contec [98]) before and after crushing each sample. As the wipe absorbed remaining washing water, it effectively removed small chips and particles formed upon cracking of silicon.

Inhomogeneities in the samples were not observed to cause error in the boron analyzes, as the boron concentration in samples with $\sim 800\,\mathrm{ppmw}$ boron in Figure 3.10 did not vary more than the uncertainty of the ICP-MS analysis even though the analyzed pieces were taken from different lengths along the extracted rods. Pieces collected for ICP-MS analysis typically contained the entire radius of the rod of sample in the quartz tube. The samples likely solidified from the cold wall of the quartz tube towards the center and presumably too fast for a plane solidification front, so that segregation is not expected to have occurred over significantly large distances and not along the length of the rod. Segregation is of particularly low concern for boron due to its near unity segregation coefficient of 0.8.

Each silicon piece was visually inspected to be clean from quartz before collected for weighing. $10 - 45$ mg of the samples were collected for ICP-MS analysis and the weight was determined to 0.1 mg precision. For each day of sample preparation, three samples of standard reference material NIST-57b [99] of metallurgical grade silicon with boron content certified to 14.43 ± 0.27 ppmw were weighted out for control analyzes. Analyzes of fumes used USGS "Diabase, W-2" [100] as standard reference material. Electrostatic noise was frequent during weighing. It did not affect the reported boron concentrations because the boron analysis was normalized to the silicon analysis in the same sample.

The weighted samples and standard references were dissolved and analyzed following the procedure of Jakobsson [19]. For each day of sample preparation, three blanks followed the same procedure from empty containers. 1.5 ml concentrated nitric acid (HNO_3) and 0.5 ml concentrated hydrofluoric acid was added for dissolution of the materials. Most samples dissolved at room temperature, but many were set in ultrasonic bath at $80\,^\circ$C for more than one hour, and still some could not be completely dissolved. Again, normalization of the boron analysis to the analysis of the silicon host material in each sample mitigated errors in the amount of sample that was analyzed. The solutions were diluted to 216 ml with deionized water. A portion of the diluted solution was stored with lid, typically less than a month until analysis.

Sample solutions were analyzed in a double focusing magnetic sector field ICP-MS ("Element 2" by Thermo Scientific [101]). Its high resolution allows for eliminating most interferences. Each sample solution was analyzed three times from which the average and relative standard deviation was calculated for each element. The sample analyzes were corrected for baseline analyzes of the blanks in each run, and the standard reference materials were used to assess accuracy and repeatability or drift between runs. The accuracy reduces towards the detection limit at which the measured value is mainly artificial, and artificially high boron contents were measured in samples where boron was removed below $0.5 - 1$ ppmw.

No loss of boron or silicon was found during dissolution and storage of samples for ICP-MS, as analyzes of the standard reference material NIST-57b [99] provided close to 100% recovery of both boron and silicon. The average recovery of boron when normalized to the silicon concentration is $103\% \pm 12\%$ for all analyzes of NIST-57b and the measurements was not observed to drift over time. The accuracy may be assumed more consistent between samples within each experiment, as they were analyzed in the same run and the samples were treated and stored together.

3.4.2 Microprobe

Vertical cross-sections of the crucibles were used for microprobe analyzes as it allow imaging of phase distributions both at the surface and in the bulk of silicon. Half of the cross-section of the smaller crucibles used in the Resistance furnace could be fitted in sample holders, so the solidified melt could be investigated along the radius and height in the face exposed in Figure 3.13. The radius cut for analysis was selected in an area of the surface that looked representable and included characteristic features originating from the refining process, like the trapped bubble in Figure 3.13 after bubbling in experiment $Q(CO)\_Sub$.

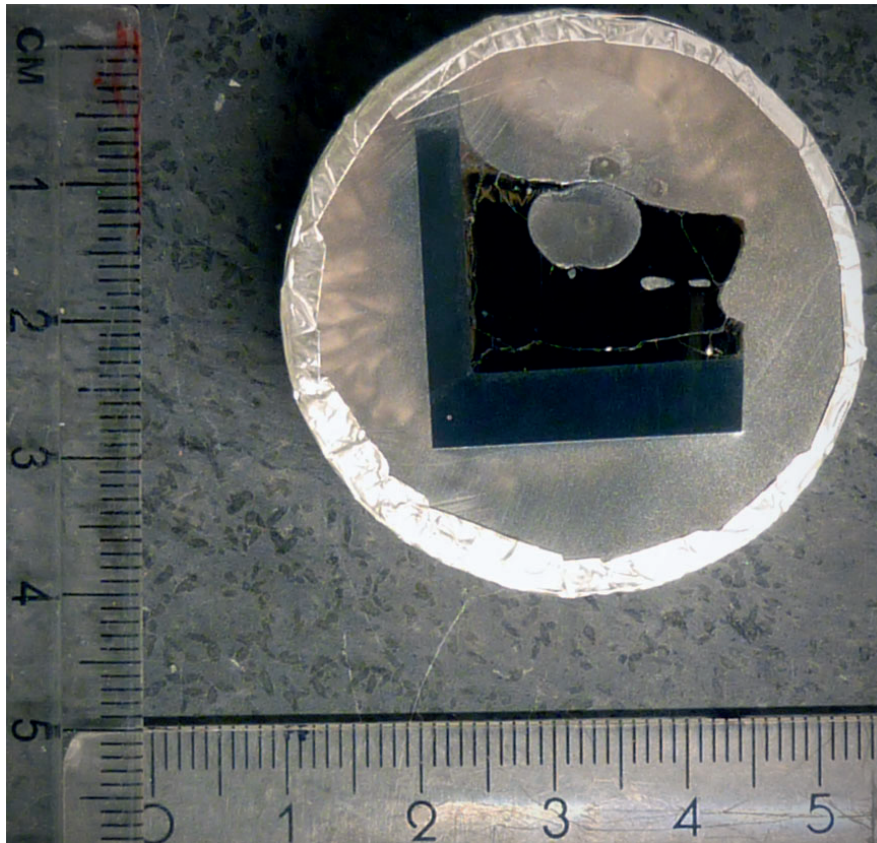Figure 3.13: Microprobe sample prepared from crucible with solidified melt after experiment $Q(CO)\_Sub$. The crucible was cut in form of a cake slice which was molded in epoxy to expose a cross-section spanning the radius and height of the solidified melt. The cross-section was ground, polished washed and dried before analysis. Aluminum foil is wrapped around the side edge and bottom of the epoxy in the image.

The crucibles were cut in the shape of a cake slice which could be fitted in the sample holders. First, the crucible above the melt surface was cut away. A vertical cut was made along a diameter of the crucible and melt, and one of the resulting half cylinders was cut along the radius to reveal a cake slice form. Cut-off wheels with diamond crystals were used for sawing through silicon. The cake slice piece was positioned in a mold with the cross-section selected for analysis facing down before the mold was filled with liquid and powder which hardened into epoxy. The cross-section selected for analysis was exposed in the surface of the epoxy after removing the mold, as shown in Figure 3.13. This surface was ground manually with four increasingly finer silicon carbide papers with grit sizes from about 200 μm (FEPA P-80) to 5 μm (EFPA P-4000) rotated at 250 rpm, and polished manually using diamond spray with 3 μm monocrystalline diamonds in suspension on a rotating cloth disk. Finally, the polished cross-section was visually inspected, washed with ethanol and deionized water and dried in a heating cabinet at 100 °C for at least 2 h.

The microprobe analyzes were conducted in a JEOL JXA-8500F [102] electron probe micro analyzer (EPMA). During the analyzes, the cross-section at the top surface were searched for surface coverage at minimum magnification of 40x, and a representative area was imaged. The samples were also scanned vertically to assess bulk cleanliness, and settling of particles was documented by imaging the interphase to the crucible bottom and wall along with any characteristic features observed. WDS an EDS were used to identify phases by the ratio of elements. The identified silicon, silica and SiC phases could later be recognize by atomic number contrast in BSE imaging and by their visual appearance on the surface. Microprobe analyzes was thus not continued for experiments in induction furnaces.

3.5   Calculations and Uncertainty

Uncertainties are calculated according to the Guide to the Expression of Uncertainty in Measurement [103] for representation at approximately 95% confidence interval. Uncertainty from regression of samples in each experiment wascombined with the uncertainty from repeated experiments. Uncertainty of repeatability is assumed normally distributed with standard uncertainty equal to the standard error (not of mean). Accuracies and tolerances reported in equipment specifications are assumed uniformly distributed. Effective degrees of freedom were used in propagation of standard error for measurements and student t-statistics were used to represent uncertainty of regression or averages of measurements due to small sample sizes. Regressions were performed for linearized equations with corresponding propagated standard uncertainties, with a MATLAB script [104] using the method by York et al. [105]. Each point is weighted according to its uncertainties, so that measurements with highest uncertainties are less influential to the regression line than measurements with lower uncertainties. The weight is also applied to the deviation of each point from the fitted line in calculations of the standard error of slope and intercept parameters.

3.5.1 Total Mass Transfer Coefficient for Boron Removal

The total mass transfer coefficient (k_t in Equation (3.2)) for boron removal was calculated by linear regression of $\ln \frac{C_{[B]}}{C_{[B]}(t=0)}$ as function of $\frac{A_c}{V}t$.

$$\ln \frac{C_{[B]}}{C_{[B]}(t=0)} = -k_t \frac{A_c}{V} t \tag{3.2}$$

The concentration of boron in each sample ($C_{[B]}$) and its uncertainty are calculated from ICP-MS analysis of the sample. The boron concentration in all samples in each experiment is normalized to that in the first sample of the experiment ($C_{[B]}(t=0)$). The total mass transfer coefficient for boron removal represents an average for the rate of boron removal over the available cross-section area in the crucible (subtracting that of any thermowell inside the crucible).

Calculations and uncertainty of the total mass transfer coefficient for boron removal in each experiment were based on three repeated ICP-MS scans for each of up to six samples in regression. The measurement of boron concentration was normalized to the measured concentration of silicon as the host material in each sample, and its uncertainty was typically within 10%. Variations between samples contribute to the spread of measurements which is the basis for the standard error of the total mass transfer coefficient from regression of samples, while a constant relative inaccuracy in concentration measurements does not affect the total mass transfer coefficient, due to normalization by the initial sample in the calculations. Regression of samples typically contributes 5-10% uncertainty to the total mass transfer coefficient for most representative experiments.

Uncertainties in $\frac{A_c}{V}t$ are propagated from all its factors. A_c and its uncertainty are calculated from crucible and thermowell dimensions and their tolerances. The melt volume is calculated from the weighted mass of silicon feedstock added to the crucible with correction for weight reduction by silicon oxidation and extraction of samples. Silicon oxidation is assumed to proceed at constant rate during experiments as the concentration in the silicon melts is constant like the experimental parameters. The melt mass at the time of sample extraction is estimated by subtracting the weightloss multiplied by the fraction of time since the oxidizing gas was introduced compared to the total blow time (of oxidizing gas). Also the weights of previously extracted samples were subtracted. The mass of each sample was measured for experiments in the Induction 2 furnace by weighing the sample tube before and after sampling. The weight of samples in experiments in the Induction 1 and Resistance furnaces were assumed from the average of 12 samples. The uncertainty of melt mass was propagated from accuracy of the weights, the time and the weightloss estimates, and it was combined with the uncertainty of silicon density by Mukai and Yuan [106] in calculations of the melt volume. From experience, the standard uncertainty in time is assumed to be 0.3 min for experiments in the Resistance and Induction 1 furnaces and 0.2 min for experiments in the Induction 2 furnace. For a normal probability distribution, it expands to respectively 0.6 min and 0.4 min at

presumably 95% confidence level. Timing is typically the most important contribution to the uncertainty of $\frac{A_c}{V}t$ together with the uncertainty in A_c, while the uncertainty in melt volume has a minor contribution.

Boron Removal Repeatability

In order to assess experimental uncertainty in mass transfer coefficients, the repeatability of experiments were investigated for comparison to the uncertainty calculated from samples within each experiment. Repeatability is presented as the relative uncertainty in mass transfer coefficients base on variations between repeated experiments with identical target parameters and procedures. The relative uncertainty was selected for representation instead of absolute uncertainty because the absolute uncertainty was typically found to increase with the absolute value of the mass transfer coefficient, both for the uncertainty calculated from samples within each experiment and the uncertainty from spread of repeated experiments. No clear relation is observed between the relative uncertainty and the absolute value, providing the absolute value is well above the lower limit of measurement.

Table 3.19 lists the experiments used to evaluate repeatability. Experiments with different target parameters and procedures were repeated, and in order to exclude the effect of changes between each set of repetitions, each set of repeated experiments are grouped into repetition sets. The R&P and Hammer sets use the same experiments (Ind_2a-b), but differ in crushing of the samples. The Hammer set follow the normal procedure while the R&P set used a tungsten carbide disk mill following the method by Jakobsson [19]. The relative error (e_r) of an experiment is calculated from the mean of its set ($\overline{k_t}$) with Equation (3.3).

$$e_r = \frac{k_t - \overline{k_t}}{\overline{k_t}} \tag{3.3}$$

Repeatability is calculated as the standard deviation of the relative errors of all experiments in Table 3.19. The mass transfer coefficient from a single experiment is assumed to have a normal probability distribution and the expansion factor 2 is used to calculate the uncertainty at approximately 95% confidence level to $U_r = 2\sigma_r$. The uncertainty of repeatability of 14% is for most experiments greater than the uncertainty calculated from regression of samples and the uncertainties typically combines to around 17% for representative experiments.

105

Table 3.19: Repeated experiments and repeatability of total mass transfer coefficients.

Set	Experiments		$\overline{k_t}$ [μm/s]	$|e_r|$
Hammer	Ind_2a	Ind_2b	8.4	4.5%
R&P	Ind(R&P)_2a	Ind(R&P)_2b	9.4	0.5%
Q_8	*Q*_8a	*Q*_8b	27	3.4%
Q_16	*Q*_16a	*Q*_16b	46	11%
Repeatability of k_t	$\sigma_r = 6.7\%$	$U_r = 14\%$		

3.5.2 Weightloss by Silicon Oxidation

Active oxidation of silicon causes a weightloss ($-\Delta m$) as silicon at the melt surface reacts to SiO gas. The amount of silicon oxidation was estimated from the difference in weight of the crucible with charge before and after the experiment, subtracted by the weight of samples extracted. The weight of each samples was measured for experiments in the Induction 2 furnace. Fumes were removed from the crucible by pressurized air before the final weighing. The following two systematic errors are introduced by estimating the weightloss of silicon from the weightloss of the entire crucible. A hard layer of sintered fumes remained along the crucible wall (Figure 3.14), and contributed to underestimate the silicon weightloss. Also the graphite crucible may be oxidized, particularly if steam remains in the gas flow leaving the silicon surface, which contributes to overestimate the weightloss of silicon. For experiments with clean silicon surfaces the crucibles appeared mostly intact, with barely visible pits in the upper part. The layer of sintered fumes further down in the crucible appeared dense and may have protected the crucible from oxidation. Silica surface coverage represents a weight gain as oxygen from the gas is bound to the silicon surface, and experiments with significant amounts of silica on the surface was not used for estimation of silicon oxidation. A correction factor of 3.3% (increase) from estimation of the systematic error in experiment H$_2$O_30 was applied to the weightloss estimates. The correction for the systematic error is less than the random uncertainty of the weightloss. The uncertainty of weightloss estimates is taken from the repeatability assessment, as the inaccuracies of weight measurements are negligible in comparison.

Attempts were also made to eliminate the systematic errors. Concentrated hydrofluoric acid was used in order to etch remaining fume deposits from the graphite crucible after H$_2$O_30, but not all of it could be dissolved (after two days). A crucible after a failed experiment was also burnt away in a muffle furnace at 900 °C over 2 days in order to weigh the silicon separately after the experiment. All of the silicon was however not easily separated as a mixed powder remained after burning the crucible. The powder consisted of pieces of silicon and silicon carbide witch according to X-ray diffraction (XRD) also contained silica and its amount was significant compared to the weightloss.

Weightloss Repeatability

Weightloss measurements of repeated experiments in Table 3.20 are the basis for estimating the uncertainty in the weightloss of individual experiments. The repeatability is estimated from the standard deviation of relative errors for repeated experiments. The relative error of an experiment is calculated using weightloss in Equation (3.3) with $\overline{-\Delta m}$ as the average of its set. The relative error is selected to assess repeatability of the weightloss because experiments with the high weithlosses were observed to have larger amounts of fume deposits that could not be removed by pressurized air compared to experiments with lower weightloss. The weightloss in a single experiment is assumed to have a normal probability distribution and the weightloss uncertainty is reported at approximately 95% confidence level as $U_r = 2\sigma_r$.

Table 3.20: Repeated experiments and repeatability of weightloss measurements.

Set	Experiments		$\overline{-\Delta m}$ [g]	$|e_r|$
H$_2$O_03	H$_2$O_03a	H$_2$O_03b	1.41	3.6%
Q_16	*Q*_16a	*Q*_16b	13.2	3.2%
Repeatability of $-\Delta m$	$\sigma_r = 3.9\%$	$U_r = 7.9\%$		

Systematic Error for Silicon Weightloss

The systematic error in weightloss, from silicon deposits and oxidation of graphite above the melt surface, was estimated in experiment H$_2$O_30. The inner crucible wall above the level of the melt was cut loose as a cylinder (depicted after the experiment in Figure 3.14(a)). Alumina spacers were used to keep this cylinder apart from the rest of the crucible since preliminary experiments found that the graphite pieces bonded at contact points as silicon wetting both parts solidified. The inner cylinder was weighted separately before and after the experiment and pressurized air treatment. The inner cylinder gained 0.78 g so that fume deposits was the main systematic error source. The fumes were found to be relatively pure silica (Table 4.20) and the weight gain is assumed to contain 0.36 g silicon form the melt. The amount of silicon in the remaining fume deposit amounted to 3.3% of the weightloss measured for the silicon in the crucible (without fume deposits), and all weightloss measurements were increased by this correction factor. Figure 3.14(a) show deposits of fume agglomerates and the layer of sintered fume along the inner crucible wall after experiment H$_2$O_30. A similar layer typically formed on part of the crucible wall and a cross-section of the layer after experiment H$_2$O_35 was studied by secondary electron microscopy (Figure 3.14(b)) and EDS. At the graphite wall, the structure resembles sintered fume particles.

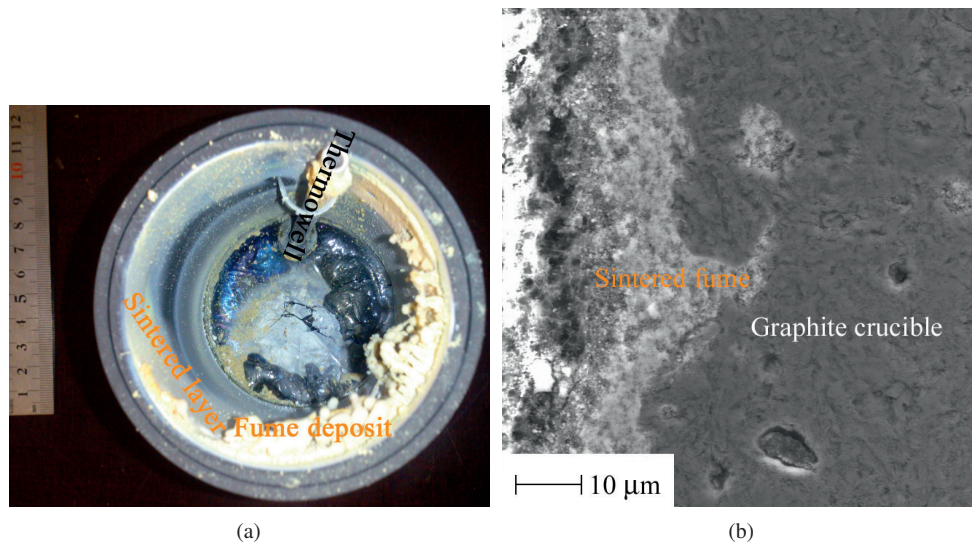Figure 3.14: Crucible for systematic weightloss measurement depicted after H_2O_30 (a). The inner crucible wall above the silicon is a separate cylinder. Part of the fume fused to the graphite wall also in H_2O_35 and its cross-sectional topography appear sintered from fume particles in the SEM micrograph (b). EDS of the sintered fume identified silicon and oxygen with a minor signal of carbon.

3.6 Modeling

Each experiment was simulated and compared to an equilibrium model developed by Tang et al. [30], to assess how much of the feed gas is utilized in reactions and resistances to boron removal in experiments. Melt convection in the Induction 2 furnace was modeled in a magnetohydrodynamic (MHD) model made by Mark William Kennedy (DMSE, NTNU). This model was expanded to include diffusion of boron in silicon in order to provide a rough estimate of the mass transfer coefficient for boron in the melt for comparison to experiments in order to assess whether melt mass transfer could be rate determining. A CFD model of the gas flow was made in order to assess the impinging jet flow pattern, particularly to verify that the gas velocity is expected to increase along the surface when the lance diameter is decreased. The gas flow model was also used to qualitatively rationalize effects of varying experimental parameters, particularly in the "d", "d_c" and "Q" experiments. Collaboration was initiated with PhD candidate Mathieu Vadon at the EPM group of the SiMaP laboratory in Grenoble for comprehensive modeling of plasma and current gas refining experiments.

3.6.1 Equilibrium Simulation

Each experiment was simulated in an equilibrium model developed by Tang et al. [30], using the ChemSheet (GTT-Technologies [107]) add-on in Microsoft Excel [108]. The model uses ChemSheet to calculate equilibrium phases and compositions at minimum Gibbs free energy based on thermodynamic properties of phases and compounds in a database. The model includes equilibrium reactions at the interface and not the gas-phase reaction (Equation (3.4)), nor convection and diffusion.

$$H_2O + SiO = SiO_2 \text{ (s)} + H_2 \qquad (3.4)$$

An extract of the database for thermodynamic properties of solar grade silicon materials by Tang et al. [39] is used for the melt, with Redlich-Kister polynomials for boron, oxygen and hydrogen impurities. The activity coefficient for boron corresponds to that in COST 507 [40] Thermochemical Database for Light Metal Alloys. Intermediate compounds, oxides and other solids in the H-B-O-Si system are included as pure phases. A liquid slag of silica and B_2O_3 is modeled with the quasi-chemical model for oxide solutions. The gas phase is an ideal mixture of gases in the H-B-O-Si system with data from JANAF [44] Thermochemical Tables, except the standard enthalpy of formation of HBO is modified to $\Delta_f H_{HBO}^{\ominus}(298 \text{ K}) = -251 \text{ kJ/mol}$ as recommended by Page [51]. The Gibbs free energy at standard state for selected compounds in the equilibrium model are in Figure 3.15 plotted over a relevant temperature for the melt surface. The enthalpy is referenced to the most stable state of elements at 1 bar and 298 K. The standard state is pure compound at 1 bar. The

values plotted in Figure 3.15 are calculated from modeling results of molar Gibbs free energy (G_j) and the activity (a_j) of the compounds as $G_j = G_j^\ominus + RT ln(a_j)$.
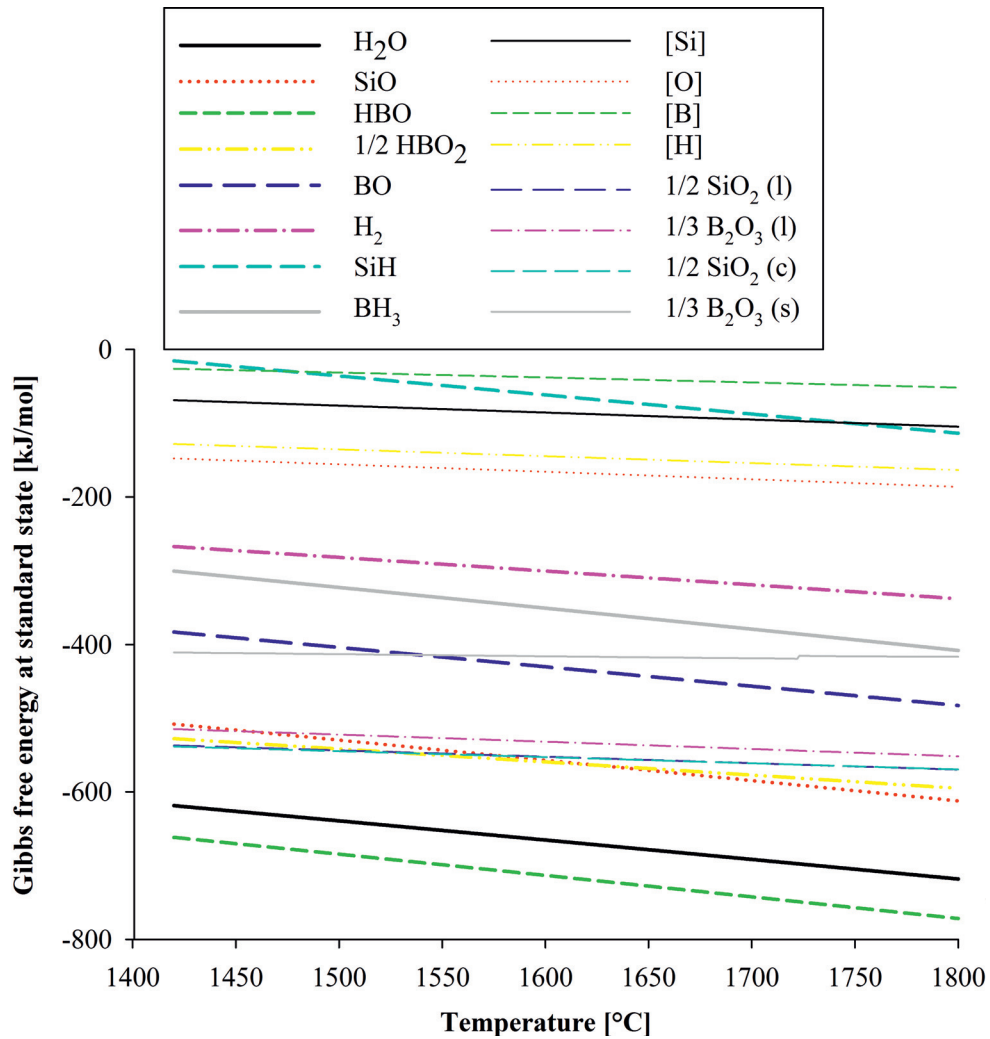
Figure 3.15: Gibbs free energy at standard state for selected compounds in the equilibrium model. SiO_2 (c) is cristobalite and both SiO_2 (l) and B_2O_3 (l) are components of a slag.

Inputs to the model are the initial boron concentration, temperature, pressure, gas composition and flow rate, which were taken from experimental data in Section 3.3. ChemSheet uses the amount of substance for the equilibrium calculations, which was calculated from

ideal gas law according to Equation (3.5) for each input gas compound "j". The gas flow rate (Q) is input in [l_N/min] with the gas constant $R = 0.082\ l_N \cdot atm/mol/K$ and temperature $T_Q = 293$ K.

$$\Delta n_j = \frac{p_j}{p} \frac{Q \Delta t \cdot 1\ \text{atm}}{RT_Q} \tag{3.5}$$

The equilibrium simulates the course of refining by iterative equilibrium calculations for every minute of gas blowing with steam. The input mass of silicon is the mass weighted into the crucible and that of boron is calculated from ICP-MS analysis of the boron content in the first sample. The input mass of oxygen in the melt is set close to saturation for silica formation. The amount of gas calculated by Equation (3.5) with $\Delta t = 1$ min and the whole of the melt are input to ChemSheet for calculating the resulting equilibrium compositions. Remaining amounts in the melt is transferred to the next minute iteration and re-equilibrated with the next minute of gas supply, while the equilibrated gas amounts output from ChemSheet are discarded. Table 3.21 presents an excerpt from equilibrium simulation of experiment Q_16b.

Table 3.21: Excerpt from iterative equilibrium simulation of experiment Q_16b. The amount of gases in line Input is used for every iteration ($\Delta t = 1$ min), together with $T = 1500\ °C$ for the melt and $p = 1.12$ bar measured in the furnace. Input masses in the melt are used in the first equilibrium calculation and the second iteration uses the masses in condensed phases (m_j) from the first output, while the output gas amounts (Δn_j) are discarded. Selected simulation outputs are listed for the first, second and 69th equilibrium calculation ($t_r = 69.1$ min for Q_16b), from which silicon weightloss compares to the weightloss of the crucible during the experiment. Additional parameters for calculating inputs: 79 ppmw boron in first sample, $m_{[O]} = 20.8 \cdot 10^{-6} m_{[Si]}$, $p_{H_2O} = 0.011$ bar, $p_{H_2} = 1.11$ bar, $Q = 16.00\ l_N$/min.

t [min]	$m_{[Si]}$ [g]	$m_{[B]}$ [g]	$m_{[H]}$ [g]	$m_{[O]}$ [g]	$m_{SiO_2 (c)}$ [g]	Δn_{H_2} [mmol]	$\Delta n_{H_2O}^s$ [mmol]	Δn_{SiO} [mmol]	Δn_{HBO} [mmol]
Input	200.23	14.8	0.000	4.16	0	658	6.8		
1	200.05	12.6	0.265	4.49	0	665	0.011	6.58	0.201
2	199.86	10.8	0.264	4.52	0	665	0.011	6.63	0.173
69	187.05	$1.31 \cdot 10^{-4}$	0.247	4.34	0	665	0.011	6.80	$2.30 \cdot 10^{-6}$

Regression of $\ln \frac{C_{[B]}}{C_{[B](t=0)}}$ to $\frac{t}{V}$ provides $A_c k_{eq}$, called the equilibrium rate coefficient. Loss of the silicon melt by oxidation is taken into account by adding $\frac{\Delta t}{V}$ successively for each iteration to calculate $\frac{t}{V}$ used for regression. The reaction area does not take part in equilibrium modeling and does not affect the equilibrium rate of refining. The mass transfer coefficient for equilibrium simulation of experiments (k_{eq}) is found by dividing the equilibrium rate coefficient over the available crucible cross-section area like in regression for k_t from boron contents in samples. If the boron content in simulations become too low, like for $t = 69$ min

in Table 3.21, it start to deviate from the first order rate law used for regression. Concentrations far below the detection limit for ICP-MS measurements (~ 1 ppmw boron) are not included in regressions of mass transfer coefficients for comparison to experiment.

Boron removal in experiments is compared to the equilibrium simulations in order to estimate the fraction of equilibrium that is achieved in the experiments. The ratio $\frac{k_t}{k_{eq}}$ is called gas utilization when the feed gas is input to the equilibrium model, as it estimates the fraction of the feed gas that is utilized completely to equilibrium in the interface reactions (see Section 5.2). Almost all of the utilized gas reacts with silicon for equilibrium at the interface and a minor fraction reacts with boron impurities in the melt as shown in Section 2.1. The gas utilization thus approximates the fraction of the feed gas that reacts with the melt in order to reproduce the experimental removal rate of boron for equilibrium at the interface. The fraction of the feed gas that reacts with boron is orders of magnitude less than the gas utilization of experiments.

Also the weightloss in experiments is compared to the weightloss of silicon due to SiO formation in the equilibrium model ($-\Delta m_{eq}$) for the experimental time of blowing steam in the feed gas. The comparison estimates the fraction of steam in the feed gas that has reacted at the melt interphase in the experiments. In accordance with considerations by Ratto et al. [78] and the conclusion by Næss et al. [31] that oxygen supply to the interface is the sole rate determining step for active oxidation of silicon, local equilibrium is assumed at the high-temperature melt surface. Equilibrium modeling predicts that essentially all of the supplied oxygen is consumed (see discussion above Reaction (5.34)). The weightloss comparison is thus used to estimate the fraction of steam in the feed gas (with partial pressure $p_{\mathrm{H_2O}}$) that is supplied to the interface ($p_{\mathrm{H_2O}}^s$), which is called the steam supply fraction ($\frac{p_{\mathrm{H_2O}}^s}{p_{\mathrm{H_2O}}}$ in Equation (3.6).) Since the partial pressures relates to the mole fraction through the total pressure, which may be assumed constant in the open system, the steam supply fraction also expresses the fraction of steam supply on a molar basis. The steam supply fraction accounts for loss of steam by fuming Reaction (2.72) and diffusion resistance through the gas boundary layer, which are not included in the equilibrium model.

$$\frac{p_{\mathrm{H_2O}}^s}{p_{\mathrm{H_2O}}} = \frac{-\Delta m}{-\Delta m_{eq}} \qquad (3.6)$$

Equation (3.6) is used to estimate actual supply of steam to the interface reactions in experiments and the equilibrium model was run a second time for each experiment with $p_{\mathrm{H_2O}}^s = \frac{-\Delta m}{-\Delta m_{eq}} p_{\mathrm{H_2O}}$ as input for steam ($p_{\mathrm{H_2O}}$ is in tables in Section 3.3). The resulting simulation estimates the equilibrium rate limit for boron removal for the actual supply of steam to the interface reactions ($k_{eq}(p_{\mathrm{H_2O}}^s)$), which is used as a measure of the equilibrium rate limit for boron removal (Equation (2.60)). A new comparison to the experimental mass transfer coefficient ($\frac{k_t}{k_{eq}(p_{\mathrm{H_2O}}^s)}$) estimates resistances to transfer of boron in Section 5.2, as separate from the resistances to steam supply.

3.6.2 Gas Flow Pattern

The gas flow pattern in the crucibles used in the induction furnaces was modeled by the finite element method in COMSOL Multiphysics 4.4 [109], using Nonisothermal Flow physics in the CFD Module. Laminar flow was used and produced low Reynolds numbers ($Re < 10$) as expected from Næss et al. [31] with similar gas flow. The model was solved for the steady-state solution.

Figure 3.16 shows the axisymmetric geometry and meshing of the model with labels for the materials used. The height spans from the surface of a 200 g melt to the top of the 70 mm diameter crucibles (the geometry in Figure 3.16 continues up to 145 mm). The melt surface is simplified to a flat, no-slip wall (lower boundary inside the crucible in Figure 3.16) at the melt temperature in experiments. No-slip walls are also used for the lance and crucible. The horizontal length includes the inner radius of the crucible, the crucible wall and graphite felt cross-section. Hydrogen enters at a specified mass flow in the inlet through the top boundary inside the lance, with an assumed temperature of 100 °C at the height of the crucible top. The hydrogen flow leaves at 1 atm through an outlet at the top of the crucible outside the lance.

In addition to heat transfer in solids and in the hydrogen flow, Surface-to-surface radiation is included for heat transfer with ambient temperature of 70 °C assumed on the inside furnace wall. Also the temperature outside the graphite felt was assumed to 70 °C. The emissivity of the silicon melt was set to 0.23 [110], and 0.85 was used for the graphite crucible an alumina. In experiments there was an additional insulating shield of mica insulation between the graphite felt and the water-cooled coil. The gas flow pattern was not significantly changed by these heat transfer contributions. 3 kW heat was applied to the graphite crucible wall to provide a seemingly realistic vertical temperature profile. Around 1100 °C at the top of the crucible in the model compares to around 850 °C measured inside an alumina thermowell on top of the crucibles in experiments Pass_Ar,H_2 and Pass_H_2a.
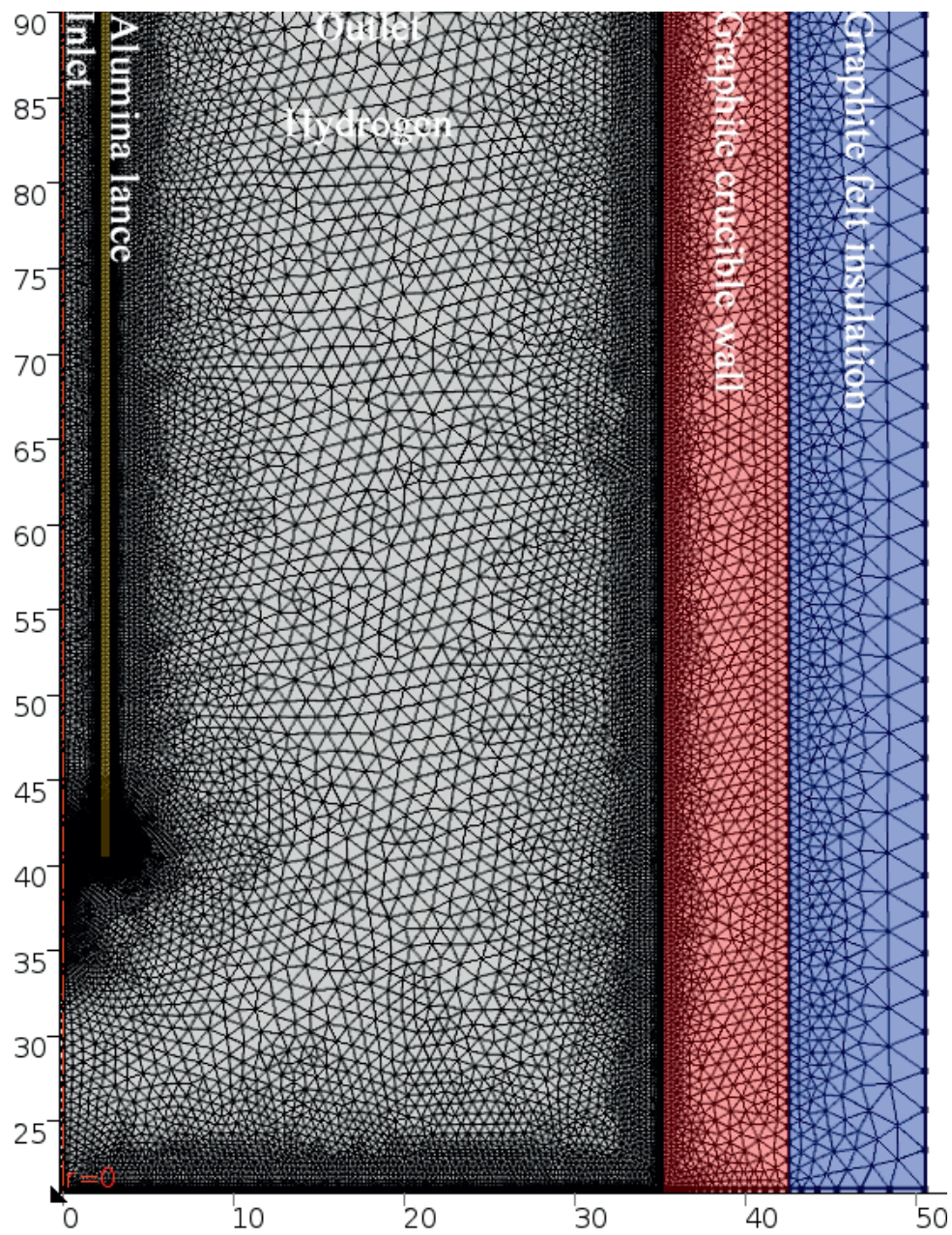
113

Figure 3.16: Geometry and mesh of gas flow model. The axes show height and radius [mm].

3.6.3 Melt Convection by Induction

Convection and diffusion in the melt as a result of induction forces in the Induction 2 furnace is modeled in the MHD model, using the finite element method in COMSOL Multiphysics 4.4 [109]. The model solves in two steps. First, a Frequency Domain study calculates Magnetic Field physics in the geometry and mesh of Figure 3.17. Resulting time-averaged Lorentz forces are input as volume forces in Turbulent Flow (k-ϵ) physics, which is coupled with physics for Transport of Diluted Species in the "Si melt" domain of Figure 3.17, using the mesh in Figure 3.18. Stationary solvers are used to estimate time-averaged velocities and diffusion fluxes from the time-averaged Lorentz forces.

Due to the axisymmetric simplification of the model, the coil is represented by a vertical stack of Single-Turn Coil Domains shown as the copper rings in Figure 3.17 (dark green overlay). The model thus neglects the vertical component of the current in the real spiral coil (imaged in Figures 3.7 and 3.8). Based on electrical measurements by Mark William Kennedy, correlated to typical powers of the Induction 2 furnace for experiments at 1500 °C, the coil current is set to 286.24 A.

Parameters used for the silicon melt at 1500 °C are electrical conductivity of $1.39 \cdot 10^6$ S/m [111], dynamic viscosity of $5.43 \cdot 10^{-4}$ kg/s/m [112] and density of 2490 kg/m^3 [106]. An experimental value for the diffusion coefficient for boron in liquid silicon is reported by Garandet [113] to $1.2 \cdot 10^{-8}$ m^2/s at the melting point (1687 K), for which Mukai and Yuan [106] provides a viscosity of $5.73 \cdot 10^{-4}$ kg/s/m for liquid silicon. The diffusion coefficient is shown by Engh [56] to scale proportionally with temperature and inversely with the melt viscosity. Following calculations by Safarian and Tangstad [114], Equation (3.7) estimates the diffusion coefficient for boron in liquid silicon to $1.3 \cdot 10^{-8}$ m^2/s at 1500 °C, which is used in the MHD model.

$$D_{[B]}(T) = 1.2 \cdot 10^{-8} \text{ m}^2/\text{s} \cdot \frac{T}{\mu(T)} \frac{5.73 \cdot 10^{-4} \text{ kg/s/m}}{1687 \text{ K}} \qquad (3.7)$$

The top surface of the melt is simplified to be horizontal and is set to slip in contact with the gas (air in the model at atmospheric pressure), so the velocity at the surface is determined from CFD modeling of the melt. A constant concentration of 30 ppmw boron was set at the bottom boundary of the melt and the concentration at the top surface was set to 0 ppmw in order to provide time averaged mass transfer of boron from the melt at the rate limit for melt mass transfer ($C_{i,[B]} = 0$ in Equation (2.20)). The mass transfer coefficient in the melt was estimated by dividing the vertical diffusive flux averaged across the top surface by the melt concentration averaged in the melt volume.
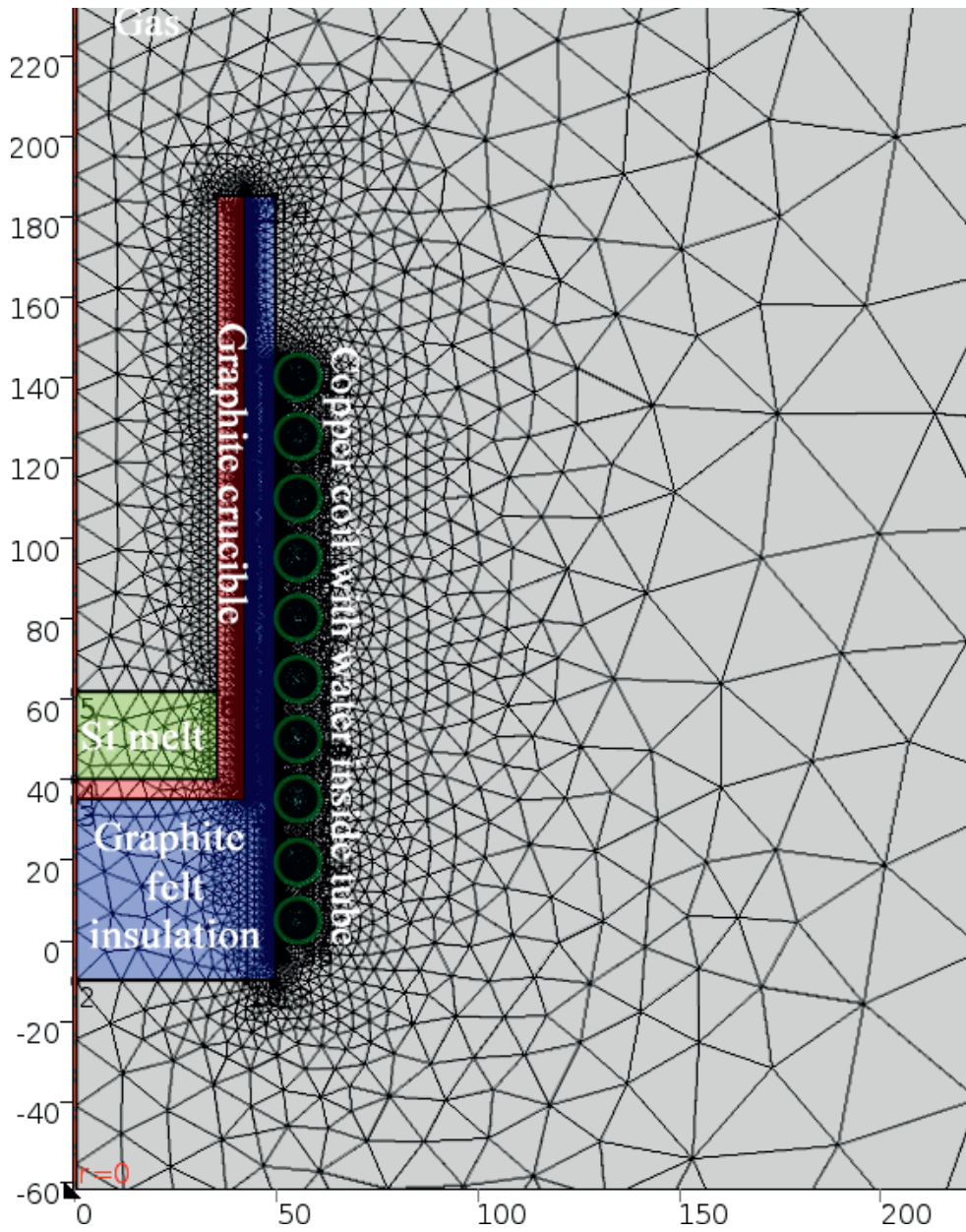
Figure 3.17: Geometry and mesh around for magnetic field in MHD model, showing the middle of the gas domain of 2 m height 1 m radius. The axes show height and radius [mm].
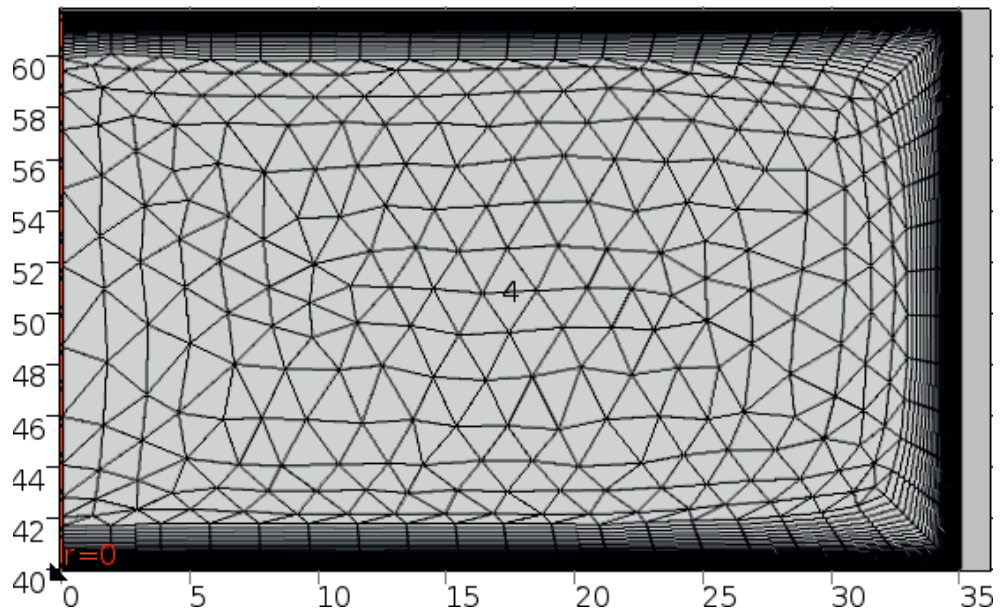
Figure 3.18: Mesh in MHD model for convection and diffusion in the "Si melt" domain in Figure 3.17. The axes show height and radius [mm].

Chapter 4

Results

Experimental results are in this chapter reported with main focus on the rates of boron removal and mass transfer coefficients in Section 4.1. Comparison to equilibrium simulation is also reported in the form of the gas utilization fraction of the feed gas. Weightloss results are reported in Section 4.2 for further comparison to equilibrium simulation in Chapter 5. The results in Sections 4.1-4.2 are considered representative for refining across melt surfaces that are essentially clean from silica, and analyzes that are considered to be significantly affected by silica surface coverage are excluded as outliers. The detrimental effect of silica surface coverage on the rate of boron removal is qualitatively shown in Section 4.3, as complete surface coverage may completely inhibit boron removal. Observations of the threshold steam supply for formation of silica passivation on the melt surface are reported in Section 4.4. Silica and SiC at the surface of silicon is characterized in Section 4.5 together with silica fume as the principal byproduct of oxidizing gas refining. Firstly, boron removal and gas consumption is introduced for the experiment with the highest refining rate.

The fastest boron removal rate was achieved with the highest gas flow rate, and fastest supply of reactants, in experiment Q_16b. This experiment also had the highest weightloss among the experiments with clean melt surfaces and hence the lowest silicon recovery. The silicon recovery was 93% of the initial melt mass after approximately 69 min of steam supply. The total gas flow rate was 16 l_N/min of 0.032 bar steam in hydrogen and the melt was held at 1500 °C. The melt mass was 200 g and the gas flow rates converts to 79.8 l_N/min/kg of which 2.26 l_N/min/kg steam or 3.740 g/min/kg water per melt mass.

Figure 4.1 shows the concentration reduction of boron in samples from 80 ppmw to 0.59 ppmw in 37.4 min. The sample concentration at 37.4 min is close to the detection limit of the ICP-MS analyzer and further boron removal could not be measured. Subsequent samples are thus outliers and were not included for regression. The gas consumption was 598 l_N of which 16.9 l_N steam (28.0 g water) in the 37.4 min refining could be measured. Regression of the first order rate law to the representative samples gives a 100-fold reduction in boron content in 32 min (from 60 ppmw to 0.6 ppmw in Figure 4.1), and compared to the melt mass, this was

achieved with 2.54 m^3_N/kg gas of which 71.8 l$_N$/kg steam (119 g/kg water/silicon mass). Equilibrium simulation for the interface reactions reproduces the experimental refining rate with a gas utilization of 36% of the gas feed rate used in the experiment. Reasons for the loss are discussed in Chapter 5. Particularly Sections 5.3 and 5.4.1 give a foundation for reducing the total gas consumption (not only losses). A higher melt temperature allows for using a higher fraction of steam in the feed without causing passivation, which reduces the need for dilution with additional gases, and higher steam fractions also increases the rate and extent of boron removal by supplying more oxygen (in addition to hydrogen) to the melt surface.
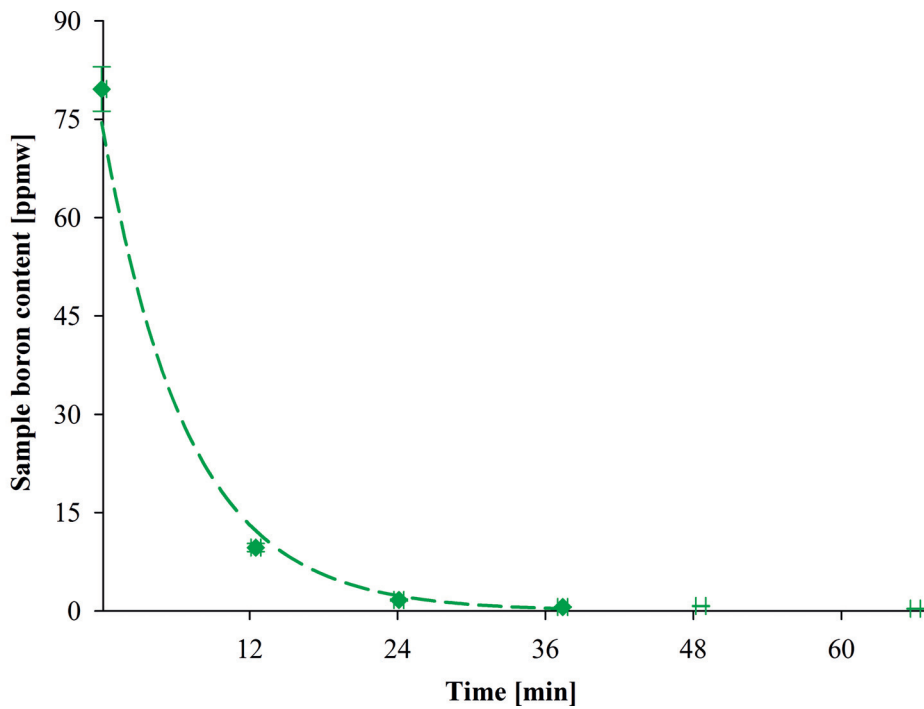

Figure 4.1: Boron content in samples as function of sampling time in experiment Q_16b, with regression curve. Samples without symbols are outliers. Parameters: $p_{H_2O} = 0.032$ bar, hydrogen atmosphere, $p = 1.12$ bar, $Q = 16.0$ l$_N$/min, $d = 4.0$ mm, $H = 20$ mm, $m = 200$ g, EG-Si feedstock, $T = 1500$ °C, Induction 2 furnace, $d_c = 70$ mm, graphite crucible, $A_c = 36.9$ cm^2.

4.1 Boron Removal Dependencies

Experimental series in subsections show the effect of separate parameters on the rate of boron removal. The rates in this section represent boron removal from an essentially clean silicon surface unless otherwise noted. Passivated experiments are outliers because surface coverage influences the rate of boron removal. In experiments where surface coverage developed after several samples were extracted, the rate of removal and the total mass transfer coefficient are calculated from samples taken while the melt surface was essentially clean.

Two main plots are included in this section for each experimental series of boron removal. First, the boron content from ICP-MS analyzes of samples is plotted as function of time of sampling for each experiment together with a fitting curve using the parameters from regression of $\ln \frac{C_{[B]}}{C_{[B]}(t=0)}$ to $\frac{A_c}{V} \cdot t$ and the average $\frac{A_c}{V}$ ratio in the experiment. Second, $\ln \frac{C_{[B]}}{C_{[B]}(t=0)}$ is plotted as function of $\frac{A_c}{V} \cdot t$, for which regression provides the total mass transfer coefficient as the negative slope. The $\frac{A_c}{V}$ ratio is factored out in the unit for series with identical crucibles and initial silicon mass target, so that the value on the horizontal axis corresponds approximately to the time of sampling. The values for samples in these plots are slightly shifted from the sampling time because the volume reduction during experiments is accounted for. Volume reduction between sampling is due to the extraction of the previous sample and loss of Si by SiO formation. A constant rate of Si loss was assumed in calculations. Error bars represent uncertainty at approximately 95% confidence level.

The results of boron removal are summarized in tables with the total mass transfer coefficient from experiments and from simulation of the experiments in the equilibrium model. The gas utilization k_t/k_{eq} is reported as an estimate of the fraction of the feed gas that is utilized for removal of boron. Uncertainties are given at approximately 95% confidence level.

4.1.1 Reactive Gases

Different reactive gases tested for the process of boron removal are CO, hydrogen and steam. Experiments with CO as the only reactive gas in argon is presented first and then CO together with hydrogen. Finally, the oxidizing agents CO and steam are compared. The effect of using hydrogen-containing atmosphere for diluted oxidizing agents is also pointed out.

Experiments using CO in argon is presented in Figure 4.2. The experiments used different CO contents, compared quartz to graphite crucible and submerged lance to $10\ \mathrm{mm}$ lance height. The boron content did not decrease in any of the experiments and regression was not performed. The inability of CO to remove boron from silicon is consistent with thermodynamic calculations (Section 2.1), which does not indicate any enrichment of boron in the gas, as the ratio between the partial pressures of B-O gases and SiO is lower than the fraction of boron in the melt.
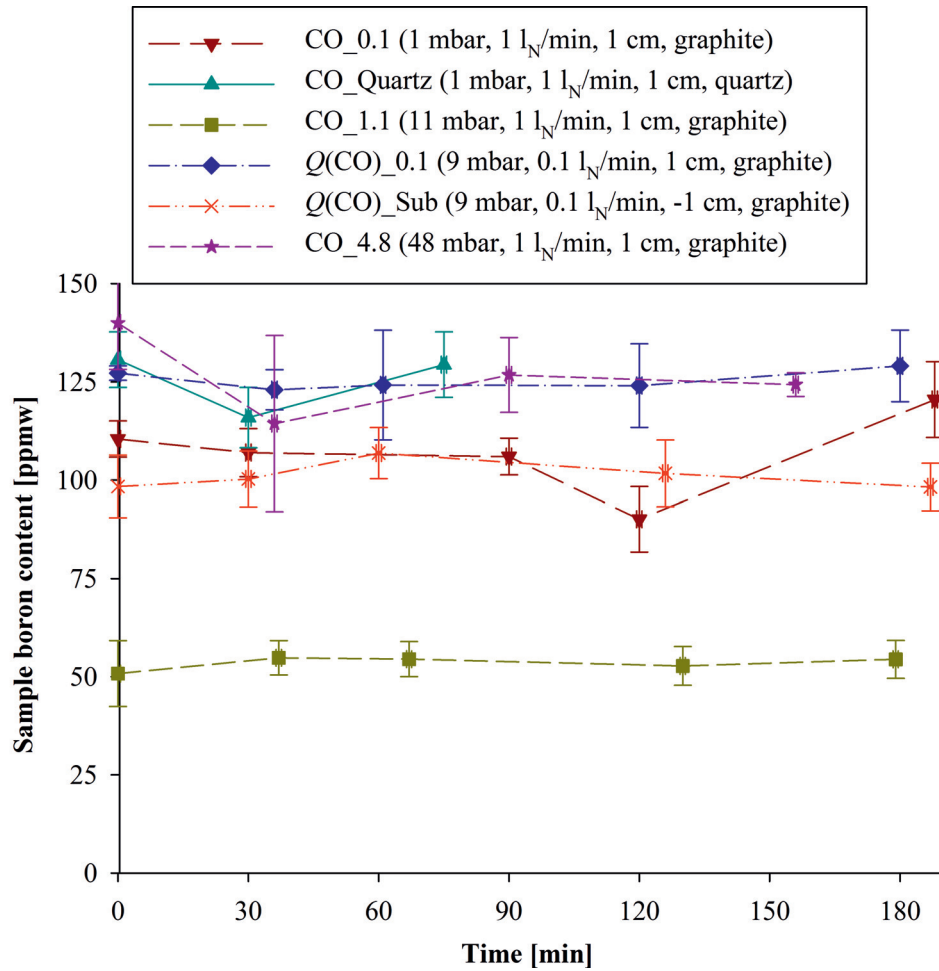
Figure 4.2: Boron content in samples as function of sampling time in experiments in the "CO" series. Lines are added for visual aid. Varied parameters are listed in the legend (CO partial pressure in feed gas, total gas flow rate, lance height above/below surface, crucible material). Common parameters: argon atmosphere, $p = 1.00$ bar, $d = 2\text{-}4$ mm, $m = 40$ g, EG-Si feedstock, $T \sim 1550 \pm {<}50\,°\text{C}$ ($T = 1500\,°\text{C}$ under crucible), Resistance furnace.

Figure 4.3 show a reduction in boron content during experiments with CO and hydrogen in argon. 0.023 bar CO and 0.063 bar hydrogen was used in argon atmosphere in CO/H$_2$_2.3/6.3 and experiment CO/H$_2$_2.4/9.9 used 0.024 bar CO and 0.099 bar hydrogen in argon. The addition of hydrogen allows formation of HBO, which at $1500\,°C$ is stable enough compared to SiO to enrich boron in the gas and facilitate removal of boron from the melt. Differences of mass transfer between the experiments are expressed in the slope of regression lines in Figure 4.4.

Figure 4.3: Boron content in samples as function of sampling time in experiments with CO and hydrogen in argon, with regression curves. Samples without symbols are outliers. Common parameters: $p = 1.04$ bar, $Q = 1.07\,\mathrm{l_N/min}$, $d = 4.0$ mm, $H = 10$ mm, $m = 40$ g, EG-Si feedstock, $T \sim 1550 \pm {<}50\,°C$ ($T = 1500\,°C$ under crucible), Resistance furnace, $d_c = 38$ mm, graphite crucible, $A_c = 11.3$ cm^2.

There was a temporary stop of CO flow in CO/H$_2$_2.3/6.3 between sampling at 65 and 89 min. The stop in oxygen supply is expected to reduce the rate of boron removal. Consistently, analyzes of these samples do not show a decrease in boron content in this time interval. Random scatter between samples analyzes also appear large enough to explain this effect. The event was excluded from regression to find the mass transfer coefficient by only

including samples taken after the CO flow was reset, using the sample at 89 min as the initial sample in Figure 4.4. Similarly, the CO flow dropped temporarily 30% between 62 and 120 min in CO/H$_2$_2.4/9.9, but the analyzes of these samples give a faster drop in boron content in this time interval than for the average of the experiment. Consequently, the drop in CO flow has no distinguishable effect in this experiment, and all samples are included in the regression. Table 4.1 summarizes the results of boron removal in terms of the total mass transfer coefficients obtained in the experiment compared to equilibrium modeling. Gases with carbon was not included in the equilibrium model, and k_{eq} was estimated by using SiO instead of CO, as CO is expected to decompose to SiO at the interphase.

Figure 4.4: Linearized plot for regression of samples (lines have slope $-k_t$) for experiments with CO and hydrogen in argon. Common parameters: $p = 1.04$ bar, $Q = 1.07$ l$_N$/min, $d = 4.0$ mm, $H = 10$ mm, $m = 40$ g, EG-Si feedstock, $T \sim 1550 \pm {<}50$ °C ($T = 1500$ °C under crucible), Resistance furnace, $d_c = 38$ mm, graphite crucible, $A_c = 11.3$ cm^2.

Table 4.1: Total mass transfer coefficients for experiments with CO and hydrogen in argon compared to equilibrium modeling. CO and hydrogen partial pressures are given in the name of each experiment (CO/H$_2$_[$\frac{1}{100}$ bar CO]/[$\frac{1}{100}$ bar H$_2$]). Common parameters: $p = 1.04$ bar, $Q = 1.07$ l$_N$/min, $d = 4.0$ mm, $H = 10$ mm, $m = 40$ g, EG-Si feedstock, $T \sim 1550 \pm {<}50$ °C ($T = 1500$ °C under crucible), Resistance furnace, $d_c = 38$ mm, graphite crucible, $A_c = 11.3$ cm^2.

Experiment	k_t [μm/s]	k_{eq} [μm/s]	k_t/k_{eq} [%]
CO/H$_2$_2.3/6.3	0.35 ± 0.42	7.50	4.7 ± 5.6
CO/H$_2$_2.4/9.9	0.67 ± 0.18	9.36	7.1 ± 2.5

Boron removal during experiments with steam and CO in argon ("H$_2$O/CO" series) is shown in Figures 4.5 and 4.6. Mass transfer coefficients are listed in Table 4.2. The equilibrium limit k_{eq} was estimated for H$_2$O/CO_2.2/2.4 by using SiO instead of CO. Steam appears to be a more efficient oxidation agent than CO as the gas utilization is estimated to be higher for H$_2$O/CO_4.5/0 than for H$_2$O/CO_2.2/2.4 in Table 4.2 and other experiments with CO in Table 4.1. Furthermore, the mass transfer coefficient was significantly higher in experiment H$_2$O/CO_4.5/0 than in CO/H$_2$_2.4/9.9 (Table 4.1) in spite of a higher content of hydrogen atoms in the feed in experiment CO/H$_2$_2.4/9.9. The reduced efficiency of CO may relate to its decomposition to SiC particles that are observed after experiments to passivate the surface locally and thus reduce the effective reaction area, and steam was selected as the oxidizing agent for further studies.
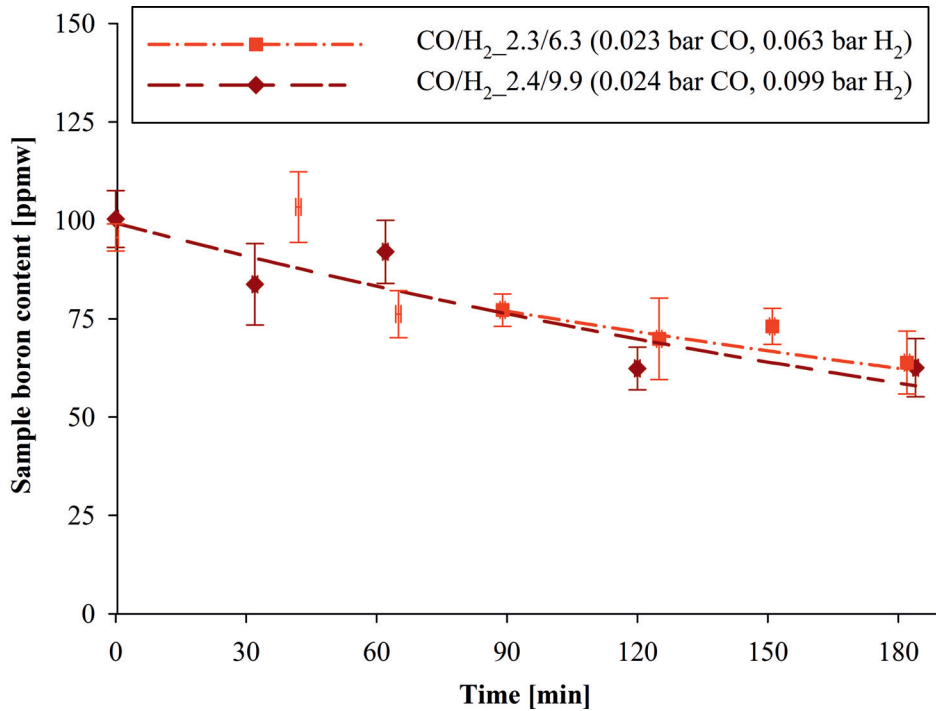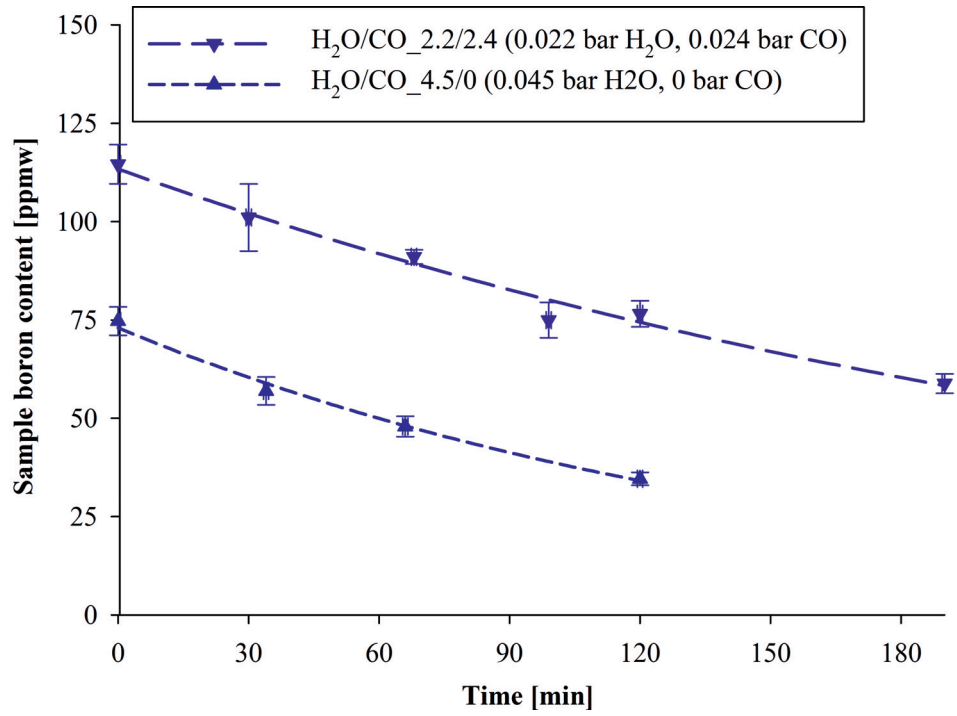
Figure 4.5: Boron content in samples as function of sampling time in experiments with steam and CO in argon, with regression curves. Common parameters: $p = 1.00$ bar, $Q = 1.00$ l$_N$/min, $d = 4.0$ mm, $H = 10$ mm, $m = 40$ g, EG-Si feedstock, $T \sim 1550 \pm {<}50$ °C ($T = 1500$ °C under crucible), Resistance furnace, $d_c = 38$ mm, graphite crucible, $A_c = 11.3$ cm^2.

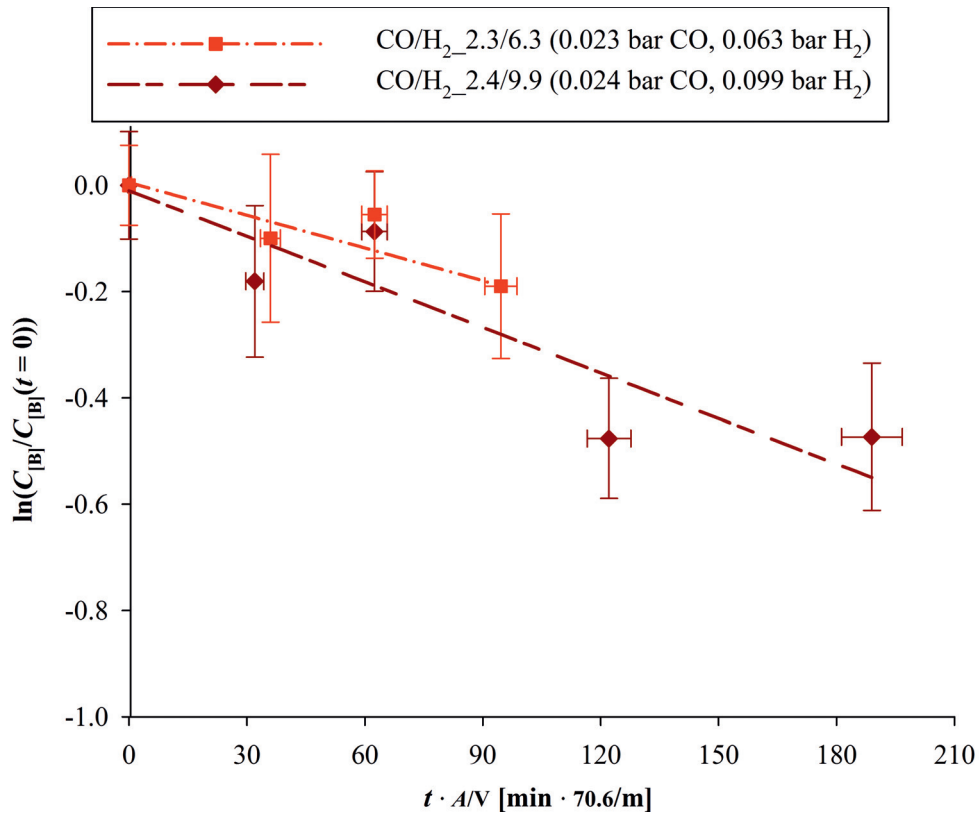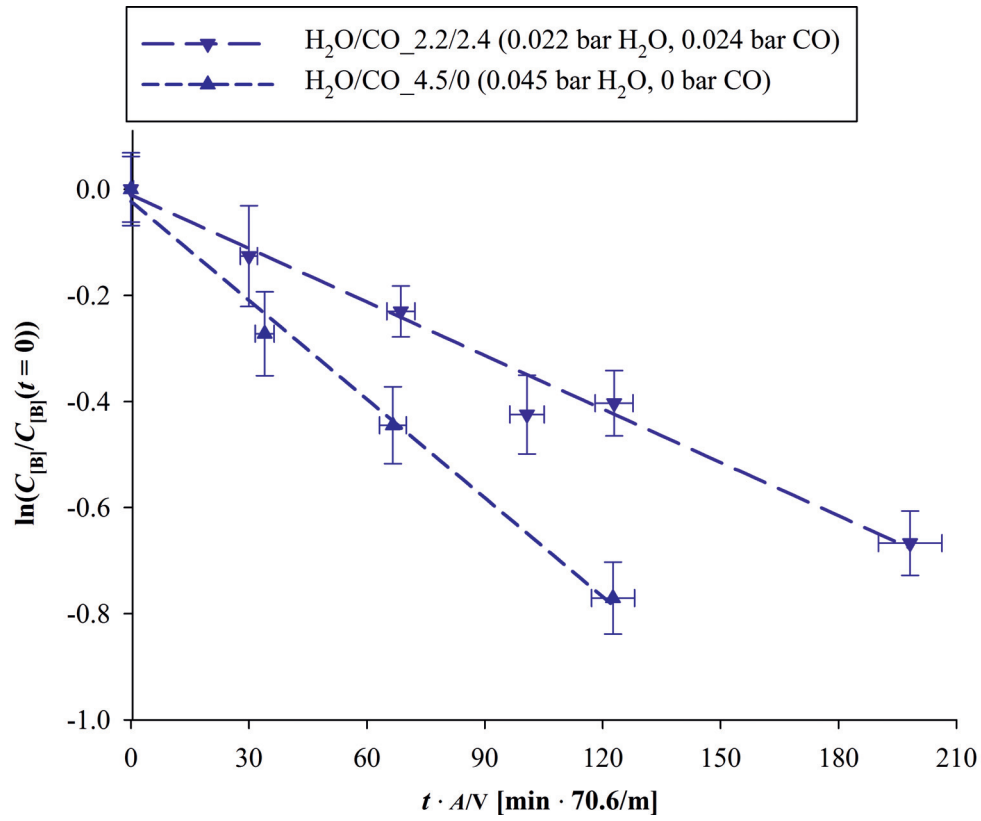Figure 4.6: Linearized plot for regression of samples (lines have slope $-k_t$) for experiments with steam and CO in argon. Common parameters: $p = 1.00$ bar, $Q = 1.00$ l_N/min, $d = 4.0$ mm, $H = 10$ mm, $m = 40$ g, EG-Si feedstock, $T \sim 1550 \pm <50$ °C ($T = 1500$ °C under crucible), Resistance furnace, $d_c = 38$ mm, graphite crucible, $A_c = 11.3$ cm^2.

Table 4.2: Total mass transfer coefficients for experiments with steam and CO in argon compared to equilibrium modeling. Steam and CO partial pressures are given in the name of each experiment ($H_2O/CO\_[\frac{1}{100}$ bar $H_2O]/[\frac{1}{100}$ bar CO]). Common parameters: $p = 1.00$ bar, $Q = 1.00$ l_N/min, $d = 4.0$ mm, $H = 10$ mm, $m = 40$ g, EG-Si feedstock, $T \sim 1550 \pm {<}50$ °C ($T = 1500$ °C under crucible), Resistance furnace, $d_c = 38$ mm, graphite crucible, $A_c = 11.3$ cm^2.

Experiment	k_t [μm/s]	k_{eq} [μm/s]	k_t/k_{eq} [%]
$H_2O/CO\_2.2/2.4$	0.78 ± 0.14	4.85	16.1 ± 2.8
$H_2O/CO\_4.5/0$	1.44 ± 0.26	6.78	21.3 ± 3.8

4.1.2 Steam Content

Series "H_2O" was conducted to investigate how boron removal depends on the partial pressure of steam in an argon atmosphere. The experiments was initially designed for 12 l_N/min total gas flow rate, but the large amount of fumes caused practical problems in an initial experiment and the gas flow rate was reduced to 2 l_N/min. The large amount of fume formation at 12 l_N/min gas flow rate built large deposits on the crucible and lance, which easily broke lose and fell onto the melt surface during sampling. The large amount of fumes also blocked vision to the melt surface so that the surface coverage could not be assessed during experiments.

Figure 4.7 shows the boron concentration in samples from unpassivated experiments in the "H_2O" series. Passivation occurred in experiments at 0.500 and 0.600 bar steam in the feed gas, and H_2O_50 and -60 are not included here. The duration of the experiments was not sufficient to measure boron removal in experiments with a partial pressure of steam of 0.090 bar and below (H_2O_03 and -09) in argon at 2 l_N/min total gas flow rate. These experiments are not included in Figure 4.8, and their mass transfer coefficients are lower than the uncertainty and they are reported to 0 μm/s in Table 4.3.
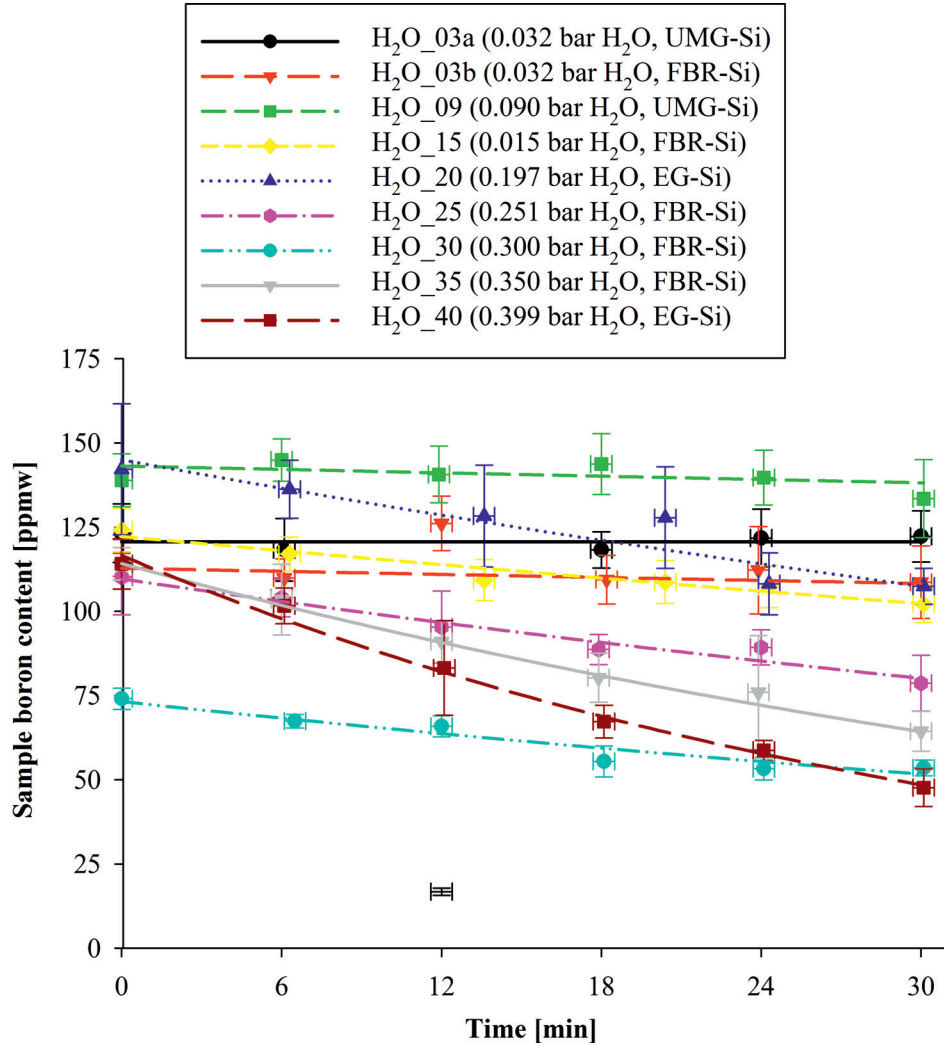
Figure 4.7: Boron content in samples as function of sampling time in "H$_2$O" experiments, with regression (thick curves). The sample without a symbol is an outlier. Common parameters: argon atmosphere, $p = 1.36$ bar, $Q = 2.00$ l$_N$/min, $d = 4.0$ mm, $H = 20$ mm, $m = 200$ g, $T = 1700$ °C, Induction 2 furnace, $d_c = 70$ mm, graphite crucible, $A_c = 36.9$ cm^2.

129

Figure 4.8: Linearized plots for regression of samples (thick lines) for H_2O_15-40 experiments, compared to equilibrium modeling (thin lines). Lines have slope $-k$. Common parameters: argon atmosphere, $p = 1.36$ bar, $Q = 2.00\,l_N/min$, $d = 4.0$ mm, $H = 20$ mm, $m = 200$ g, $T = 1700\,°C$, Induction 2 furnace, $d_c = 70$ mm, graphite crucible, $A_c = 36.9$ cm^2.

Table 4.3: Total mass transfer coefficients compared to equilibrium modeling for H_2O_03-40 experiments. Steam partial pressure is given in the name of each experiment (H_2O_$[\frac{1}{100}$ bar]). Common parameters: argon atmosphere, $p = 1.36$ bar, $Q = 2.00$ l_N/min, $d = 4.0$ mm, $H = 20$ mm, $m = 200$ g, high-purity silicon feedstock, $T = 1700$ °C, Induction 2 furnace, $d_c = 70$ mm, graphite crucible, $A_c = 36.9$ cm^2.

Experiment	k_t [μm/s]	k_{eq} [μm/s]	k_t/k_{eq} [%]
H_2O_03a	0	0.83	
H_2O_03b	0	0.83	
H_2O_09	0	4.04	
H_2O_15	2.07 ± 0.90	8.59	24.1 ± 9.8
H_2O_20	3.3 ± 2.0	12.4	27 ± 16
H_2O_25	3.6 ± 1.7	17.9	20.3 ± 9.1
H_2O_30	4.0 ± 1.0	22.7	17.4 ± 4.0
H_2O_35	6.5 ± 1.4	28.7	22.8 ± 4.6
H_2O_40	9.9 ± 1.8	33.4	29.6 ± 5.2

4.1.3 Gas Flow Rate

The effect of gas flow rate was studied in three different experimental series. First a preliminary series ("Q(Res)") in the Resistance furnace, second in the Induction 1 furnace with 0.48 bar hydrogen and a high lance height (50 mm) in series "Q(Ind_1)" and finally in the Induction 2 furnace with 1.08 bar hydrogen atmosphere and optimized lance height in series "Q".

The rate of boron removal for experiments with 0.14 l_N/min and 1.01 l_N/min total gas flow rate in the "Q(Res)" series is indicated in Figure 4.9 and mass transfer coefficients are the slope of regression lines in Figure 4.10. Total mass transfer coefficients are listed in Table 4.4 and compared to equilibrium modeling to estimate the gas utilization. The figures and mass transfer coefficients clearly show that the mass transfer of boron and the refining rate is enhanced at increased gas flow rates, as it represents an increased supply of reactants. This is also the general trend for the "Q(Ind_1)" and the "Q" series. However, a larger fraction of the feed gas escapes unreacted at the higher gas flow rate as seen from the lower gas utilization, and the effect of increasing the gas flow rate is less for experiments than for equilibrium modeling.

131

Figure 4.9: Boron content in samples as function of sampling time in "Q(Res)" experiments, with regression (thick curve). Common parameters: $p_{H_2O} = 0.023$ bar, $p_{H_2} = 0.49$ bar, argon atmosphere, $p = 1.00$ bar, $d = 4.0$ mm, $H = 10$ mm, $m = 40$ g, EG-Si feedstock, $T \sim 1500 \pm {<}30$ °C ($T = 1426$ °C under crucible and alumina retainer), Resistance furnace, $d_c = 35$ mm, quartz crucible, $A_c = 9.6$ cm^2.
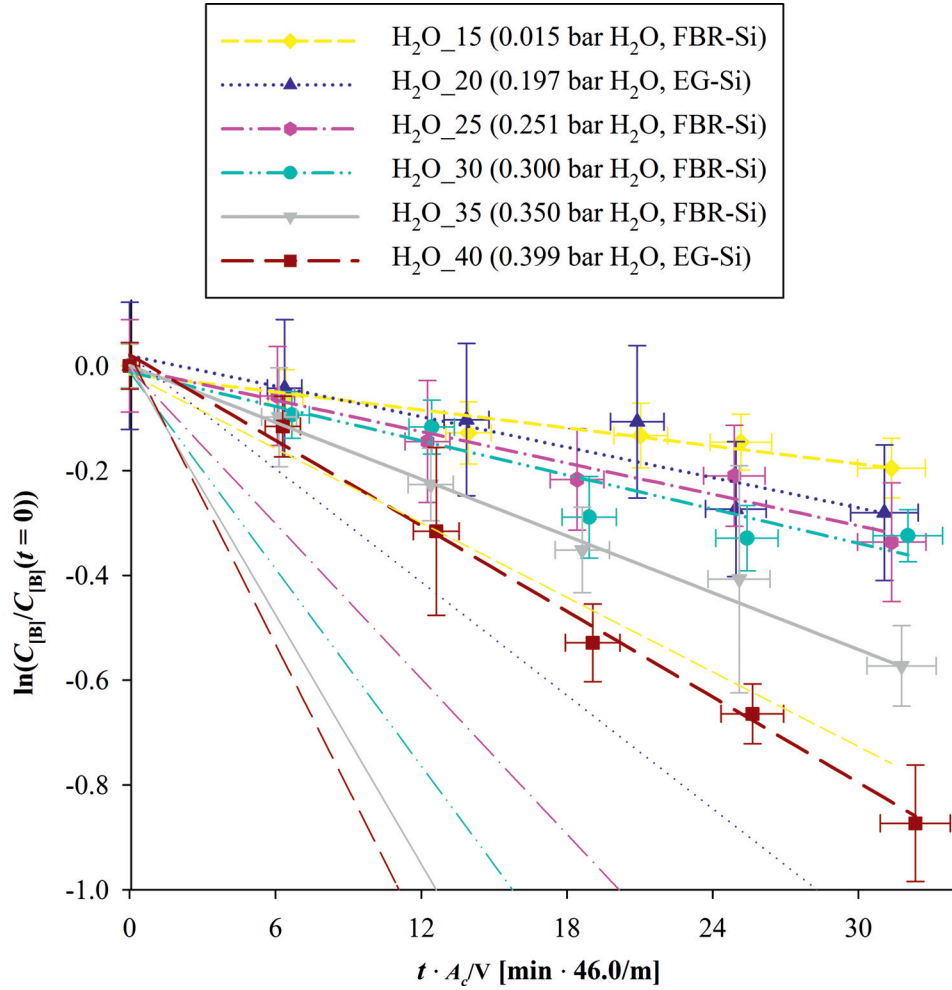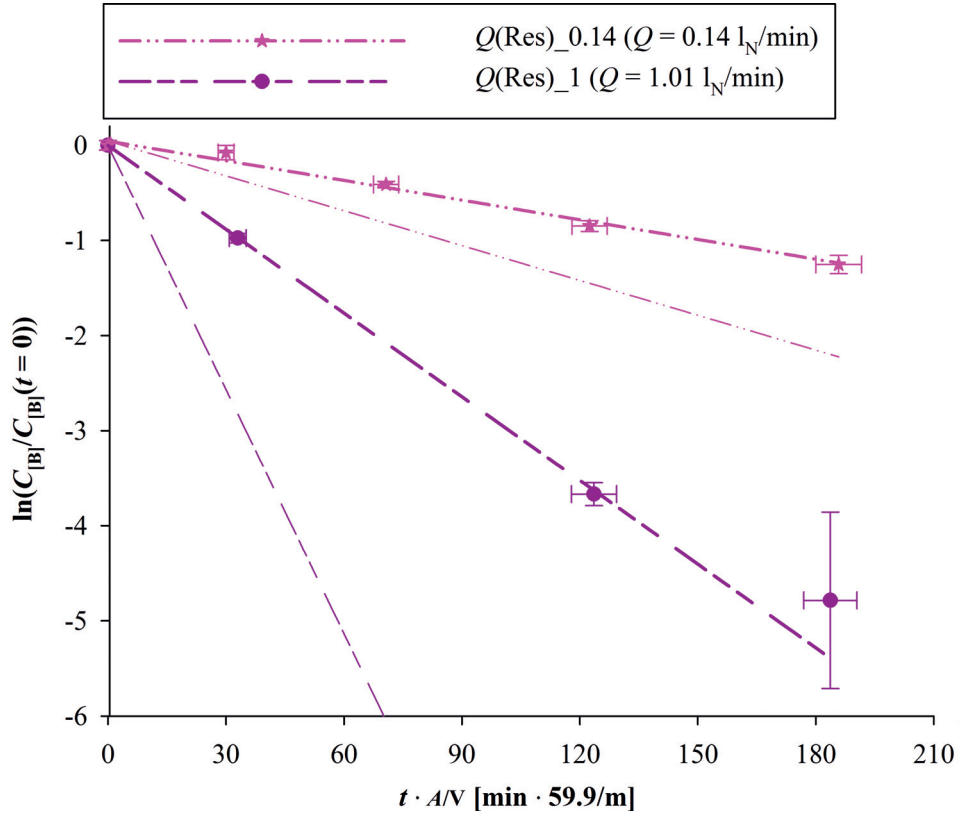
Figure 4.10: Linearized plots for regression of samples (thick lines) for "Q(Res)" experiments, compared to equilibrium modeling (thin lines). Lines have slope $-k$. Common parameters: $p_{H_2O} = 0.023$ bar, $p_{H_2} = 0.49$ bar, argon atmosphere, $p = 1.00$ bar, $d = 4.0$ mm, $H = 10$ mm, $m = 40$ g, EG-Si feedstock, $T \sim 1500 \pm {<}30\,°C$ ($T = 1426\,°C$ under crucible and alumina retainer), Resistance furnace, $d_c = 35$ mm, quartz crucible, $A_c = 9.6$ cm^2.

Table 4.4: Total mass transfer coefficients compared to equilibrium modeling for experiments with total gas flow rates of 0.14-1 l_N/min in Resistance furnace. Total gas flow rate is given in the name of each experiment (Q(Res)_[l_N/min]). Common parameters: $p_{H_2O} = 0.023$ bar, $p_{H_2} = 0.49$ bar, argon atmosphere, $p = 1.00$ bar, $d = 4.0$ mm, $H = 10$ mm, $m = 40$ g, EG-Si feedstock, $T \sim 1500 \pm {<}30$ °C ($T = 1426$ °C under crucible and alumina retainer), Resistance furnace, $d_c = 35$ mm, quartz crucible, $A_c = 9.6$ cm^2.

Experiment	k_t [μm/s]	k_{eq} [μm/s]	k_t/k_{eq} [%]
Q(Res)_0.14	1.88 ± 0.31	3.44	54.7 ± 8.9
Q(Res)_1	8.0 ± 1.4	23.7	33.8 ± 5.6

The evolution of the boron content during experiments in the "Q(Ind_1)" series is shown in Figure 4.11 and regressions to estimate mass transfer coefficients are shown in Figure 4.12. The boron content in Q(Ind_1)_6 reached below 1 ppmw and the detection limit for the ICP-MS analyzes before 120 min, and subsequent samples are outliers.

Table 4.5 lists the mass transfer coefficients from experiments and equilibrium modeling together with the gas utilization in the experiments. The gas utilization in this series does not decrease with increasing total gas flow rate because the lance was positioned higher than optimal. The reactants were not successfully supplied to the interphase at 0.5 l_N/min gas flow rate in experiment Q(Ind_1)_0.5. In Q(Ind_1)_3.5, the lance was positioned 46 mm above the melt surface and not 50 mm, which contributed to increase the total mass transfer coefficient and the gas utilization.

Experiments in the "Q" series shows the effect of total gas flow rate in Figures 4.13 and 4.14 without any influence of lance height, which was optimized after "H" experiments. The detection limit of the ICP-MS analyzes was reached after 36 min in experiments Q_10-16 and consecutive samples in these experiments are outliers. The mass transfer coefficients in Table 4.6 increases with increasing gas flow rate.
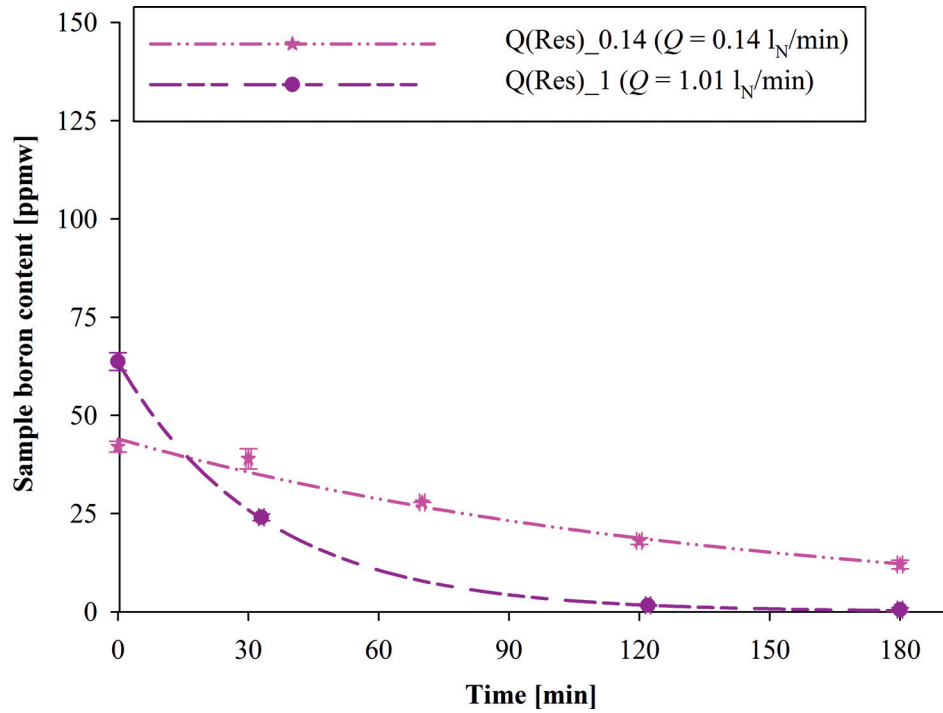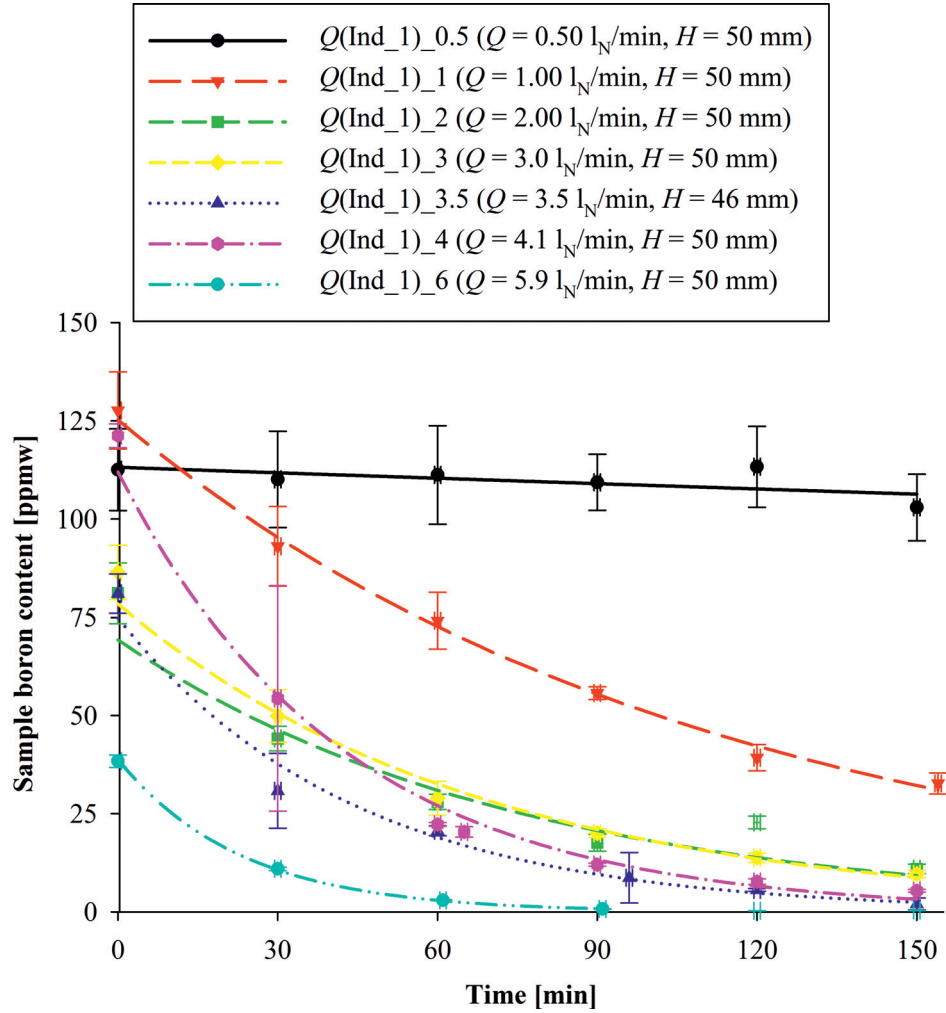
Figure 4.11: Boron content in samples as function of sampling time in "Q(Ind_1)" experiments, with regression (thick curve). Samples without symbols are outliers. Common parameters: $p_{H_2O} = 0.032$ bar, $p_{H_2} = 0.49$ bar, argon atmosphere, $p = 1.00$ bar, $d = 4.0$ mm, $m = 200$ g, EG-Si feedstock, $T = 1500\,^\circ$C, Induction 1 furnace, $d_c = 70$ mm, graphite crucible, $A_c = 36.9$ cm^2.
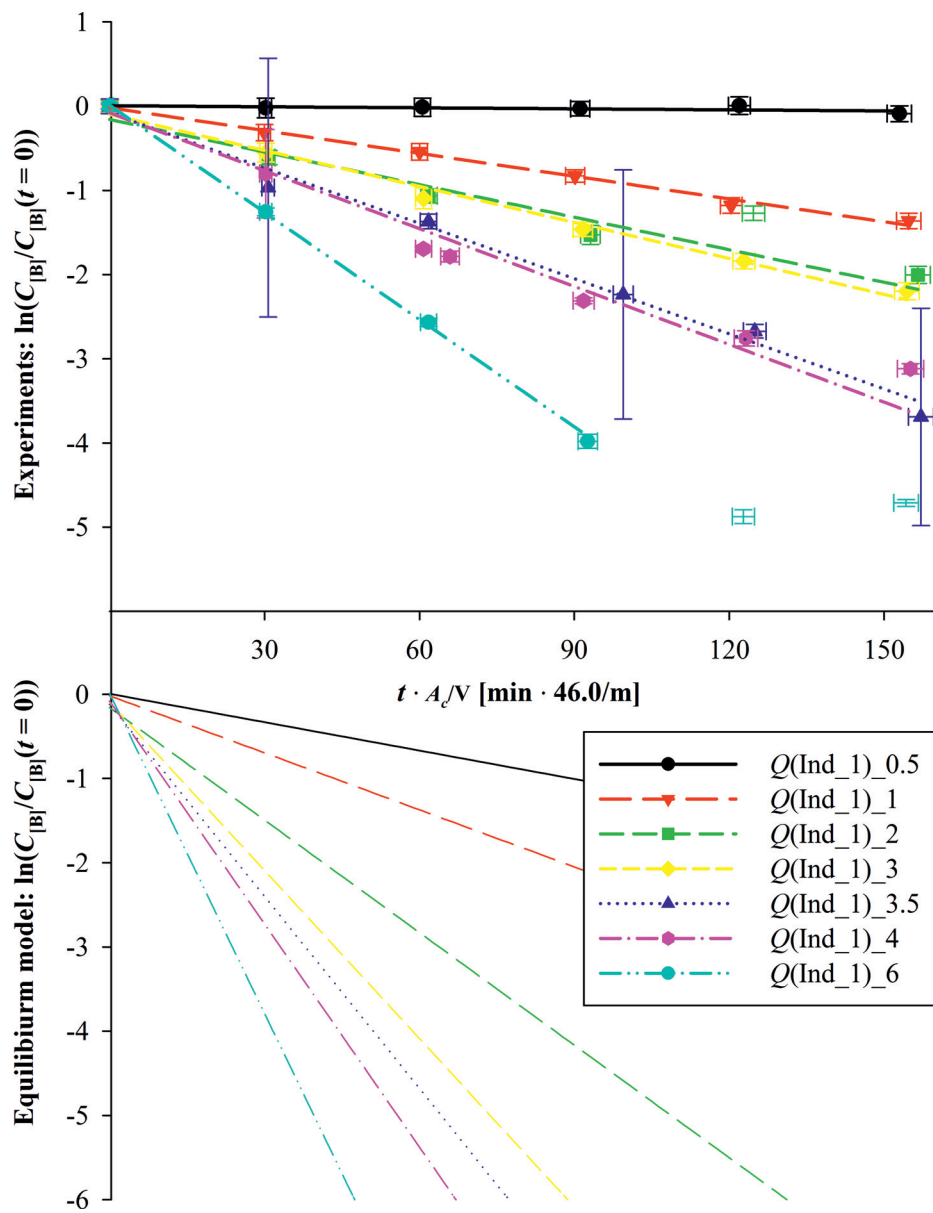
Figure 4.12: Linearized plots for regression of samples (thick lines in upper plot) for "$Q(\text{Ind\_1})$" experiments, compared to equilibrium modeling (thin lines in lower plot). Lines have slope $-k$. Samples without symbols are outliers. See Figure 4.11 for parameters.

Table 4.5: Total mass transfer coefficients compared to equilibrium modeling for experiments in Induction 1 furnace with total gas flow rates in the range 0.5-6 l_N/min. Total gas flow rate is given in the name of each experiment (Q(Ind_1)_[l_N/min]). Common parameters: $p_{H_2O} = 0.032$ bar, $p_{H_2} = 0.49$ bar, argon atmosphere, $p = 1.00$ bar, $d = 4.0$ mm, $H = 50$ mm ($H = 46$ mm for Q(Ind_1)_3.5), $m = 200$ g, EG-Si feedstock, $T = 1500\,°C$, $d_c = 70$ mm, graphite crucible, $A_c = 36.9$ cm^2.

Experiment	k_t [μm/s]	k_{eq} [μm/s]	k_t/k_{eq} [%]
Q(Ind_1)_0.5	0.15 ± 0.32	4.07	3.6 ± 7.7
Q(Ind_1)_1	3.27 ± 0.55	8.17	40.0 ± 6.7
Q(Ind_1)_2	4.66 ± 0.77	16.1	28.9 ± 4.8
Q(Ind_1)_3	5.16 ± 0.85	24.1	21.4 ± 3.6
Q(Ind_1)_3.5	7.9 ± 1.3	27.5	28.7 ± 4.7
Q(Ind_1)_4	8.3 ± 1.4	32.0	25.9 ± 4.2
Q(Ind_1)_6	15.4 ± 2.5	45.9	33.5 ± 5.4
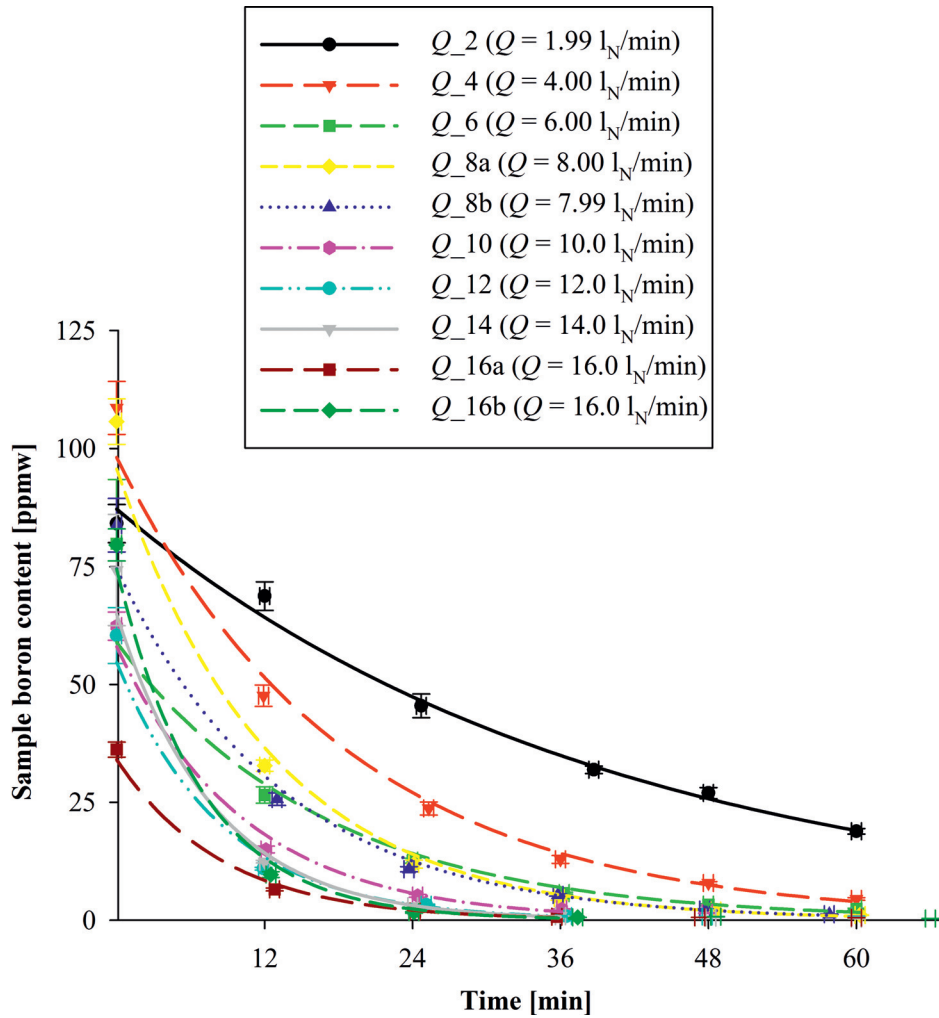
Figure 4.13: Boron content in samples as function of sampling time in "Q" experiments, with regression (thick curve). Samples without symbols are outliers. Common parameters: $p_{H_2O} = 0.032$ bar, hydrogen atmosphere, $p = 1.12$ bar, $d = 4.0$ mm, $H = 20$ mm, $m = 200$ g, EG-Si feedstock, $T = 1500\ °C$, Induction 2 furnace, $d_c = 70$ mm, graphite crucible, $A_c = 36.9\ cm^2$.
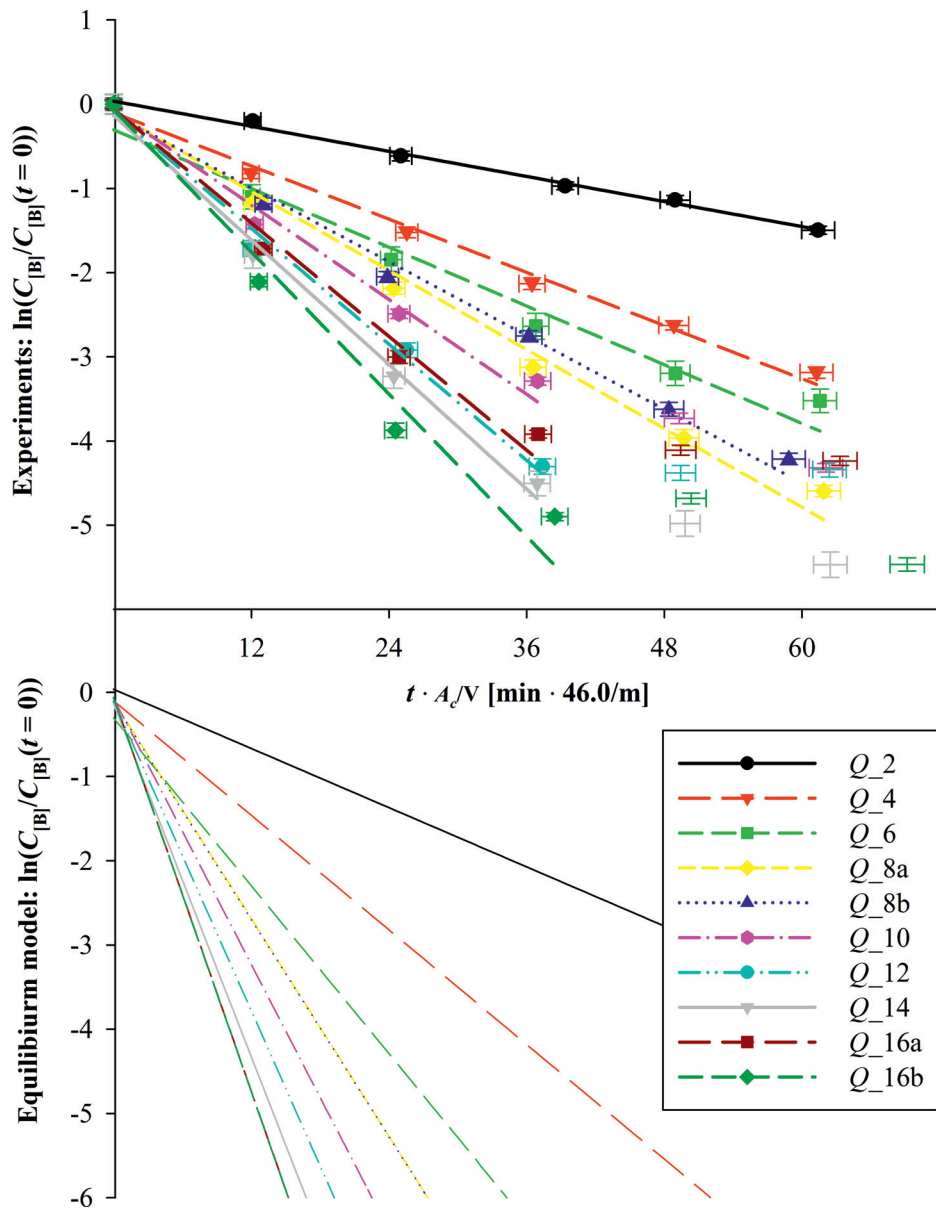
Figure 4.14: Linearized plots for regression of samples (thick lines in upper plot) for "Q" experiments, compared to equilibrium modeling (thin lines in lower plot). Lines have slope $-k$. Samples without symbols are outliers. See Figure 4.13 for parameters.

Table 4.6: Total mass transfer coefficients compared to equilibrium modeling for experiments with total gas flow rates in the range 2-16 l_N/min in Induction 2 furnace. Total gas flow rate is given in the name of each experiment ($Q\_[l_N/min]$). Common parameters: $p_{H_2O} = 0.032$ bar, hydrogen atmosphere, $p = 1.12$ bar, $d = 4.0$ mm, $H = 20$ mm, $m = 200$ g, EG-Si feedstock, $T = 1500\,°C$, Induction 2 furnace, $d_c = 70$ mm, graphite crucible, $A_c = 36.9$ cm^2.

Experiment	k_t [μm/s]	k_{eq} [μm/s]	k_t/k_{eq} [%]
Q_2	9.0 ± 1.5	21.2	42.4 ± 6.9
Q_4	19.1 ± 3.1	41.0	46.4 ± 7.6
Q_6	21.0 ± 3.4	60.2	35.0 ± 5.7
Q_8a	28.3 ± 4.6	78.0	36.3 ± 5.9
Q_8b	26.4 ± 4.3	77.9	34.0 ± 5.5
Q_10	33.9 ± 5.6	95.3	35.6 ± 5.9
Q_12	41.5 ± 6.9	111.1	37.4 ± 6.2
Q_14	44.6 ± 7.3	126.6	35.3 ± 5.8
Q_16a	40.7 ± 6.7	141.1	28.8 ± 4.7
Q_16b	51.0 ± 8.3	141.1	36.1 ± 5.9

4.1.4 Crucible Diameter

In series "d_c" , experiment d_c_38 with 38 mm inner crucible diameter is compared to experiment $Q(Ind\_1)\_3$ to investigate how the interphase area affects boron removal to an impinging jet. When comparing the concentration profiles at equal concentrations (horizontal translation in Figure 4.15), the boron concentration reduces faster in experiment d_38, partially because the $\frac{A_c}{V}$ ratio was higher in experiment d_c_38 ($\frac{A_c}{V} = 70$ m^{-1}) than in $Q(Ind\_1)\_3$ ($\frac{A_c}{V} = 47$ m^{-1}). This difference is taken into account in Figure 4.16. Samples d_c_38 are considered outliers because a deposit built up over the melt surface in d_c_38 and it appears to have obstructed the gas flow after 60 min as the boron concentration is not reduced in consecutive samples.
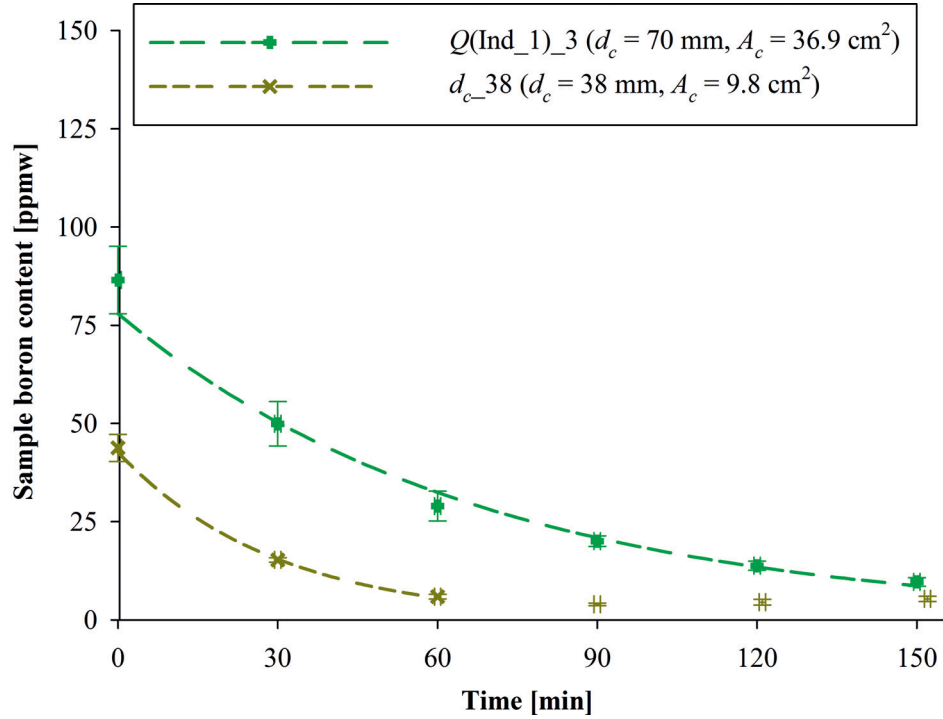
Figure 4.15: Boron content in samples as function of sampling time in "d_c" experiments. Common parameters: $p_{H_2O} = 0.032$ bar, $p_{H_2} = 0.49$ bar, argon atmosphere, $p = 1.01$ bar, $Q = 3.0$ l_N/min, $d = 4.0$ mm, $H = 50$ mm, $m = 200$ g, EG-Si feedstock, $T = 1500$ °C, Induction 1 furnace, graphite crucible.

The actual rate of the amount of boron removed across the interface at equal concentrations of boron in the melt is comparable through the rate coefficient $A_c k_t$ in Table 4.7. The removal rate is increased for the larger surface area, and the increased distance over which the gas flows in contact with the melt surface allow reactions to proceed further towards equilibrium as indicated by the increased gas utilization in the 70 mm diameter crucible. The total mass transfer coefficient is averaged over the available crucible cross-section area, and the higher value in the smaller crucible indicates that the local mass transfer coefficients are larger towards the center of the crucible and decreases away from the stagnation region of the impinging jet, so the total mass transfer coefficient follow the dependence expected for mass transfer in the gas phase.
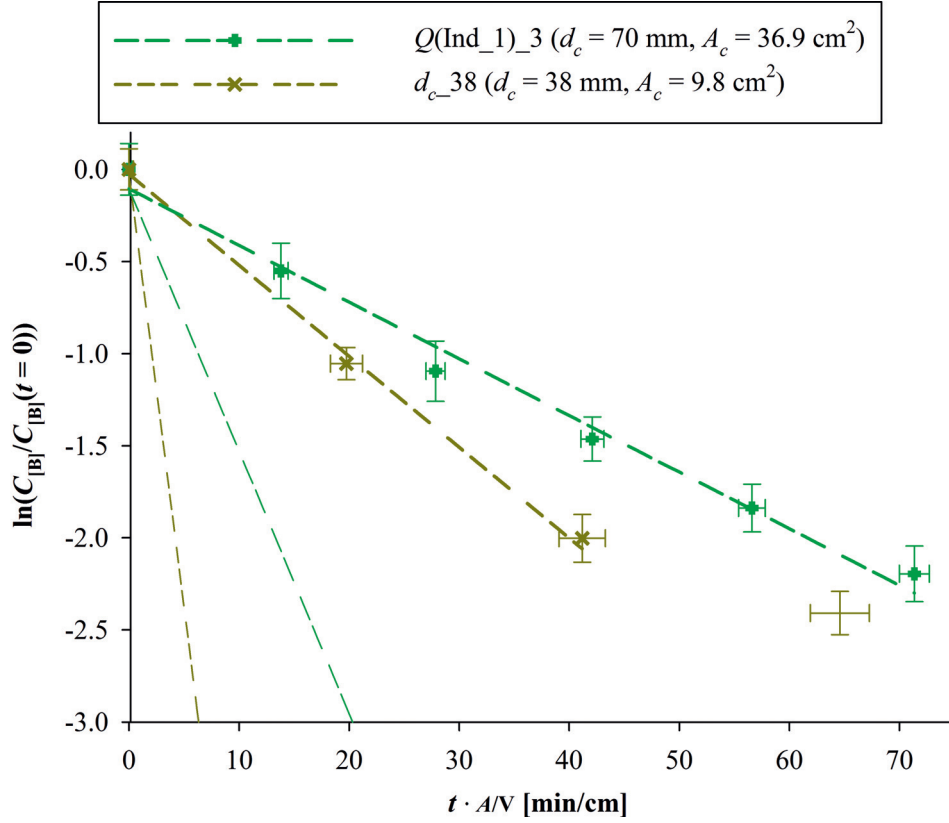
Figure 4.16: Linearized plot for regression of samples (lines have slope $-k$) for "d_c" experiments. Common parameters: $p_{H_2O} = 0.032$ bar, $p_{H_2} = 0.49$ bar, argon atmosphere, $p = 1.01$ bar, $Q = 3.0 \, l_N/\text{min}$, $d = 4.0$ mm, $H = 50$ mm, $m = 200$ g, EG-Si feedstock, $T = 1500\,°\text{C}$, Induction 1 furnace, graphite crucible.

Table 4.7: Total mass transfer coefficients compared to equilibrium modeling for "d_c" experiments with crucible diameters of 38 mm (d_c_38 had $A_c = 9.8$ cm^2 and $m = 40$ g) and 70 mm ($Q(\text{Ind}\_1)\_3$ had $A_c = 9.8$ cm^2 and $m = 200$ g). Common parameters: $p_{H_2O} = 0.032$ bar, $p_{H_2} = 0.49$ bar, argon atmosphere, $p = 1.01$ bar, $Q = 3.0 \, l_N/\text{min}$, $d = 4.0$ mm, $H = 50$ mm, EG-Si feedstock, $T = 1500\,°\text{C}$, Induction 1 furnace, graphite crucible.

Experiment	$A_c k_t$ [10^{-9} m^3/s]	k_t [μm/s]	k_{eq} [μm/s]	k_t/k_{eq} [%]
d_c_38	7.9 ± 1.5	8.1 ± 1.4	76.2	10.6 ± 1.9
$Q(\text{Ind}\_1)\_3$	19.1 ± 3.2	5.16 ± 0.85	24.1	21.4 ± 3.6

4.1.5 Lance Diameter

The lance diameter was varied between 1-4 mm with a total gas flow rate of $2\,l_N/min$ in the "d" series in the Induction 1 furnace (Ind_1 used $4\,mm$ lance diameter). A wide lance of $35\,mm$ inner diameter at the exit was tested in the "$H(d\_35)$" series in the Induction 2 furnace, and $H(d\_35)\_10$ is included here since it used the same height and other parameters as experiments in the "d" series.

The rate of boron removal is similar for most experiments as indicated in Figures 4.17 and 4.18. The removal rate and mass transfer coefficient in experiment d_3 is slightly reduced, which is because the tip of the lance softened and bent. Bending of the lance provides two effects that is expected to have negative effects on mass transfer in the gas. Firstly, the gas jet was inclined. Secondly, the jet did not impinge onto the center of the melt, but closer to the crucible wall so that most of the gas contacts the melt over a shorter distance and time. Judging from the boron content in samples in Figure 4.17, the lance likely bent in the first $30\,min$ as the concentration of the initial sample is high compared to the regression curve, and is consistent with faster mass transfer in this period than the remainder of the experiment.

The total mass transfer coefficients for all experiments in Table 4.8 are all within the 95% confidence interval of each other. The different gas velocities of the impinging jets do not effectively influence the total mass transfer coefficient in these experiments with $2\,l_N/min$ total gas flow rate.
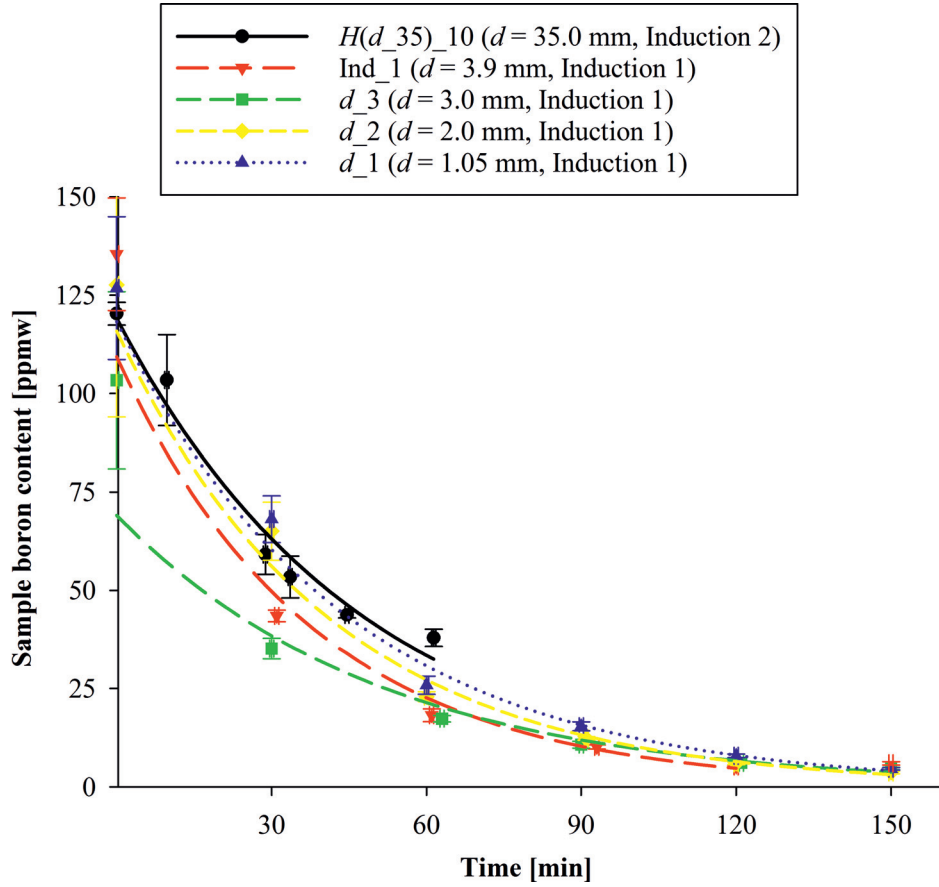
Figure 4.17: Boron content in samples as function of sampling time in "*d*" experiments and $H(d\_35)\_10$, with regression (thick curves). Samples without symbols are outliers. Common parameters: $p_{H_2O} = 0.032$ bar, hydrogen atmosphere, $p = 0.99$ bar ($p = 1.13$ bar for $H(d\_35)\_10$), $Q = 2.0$ l_N/min, $H = 10$ mm, $m = 200$ g, EG-Si feedstock, $T = 1500$ °C, $d_c = 70$ mm, graphite crucible, $A_c = 36.9$ cm^2.
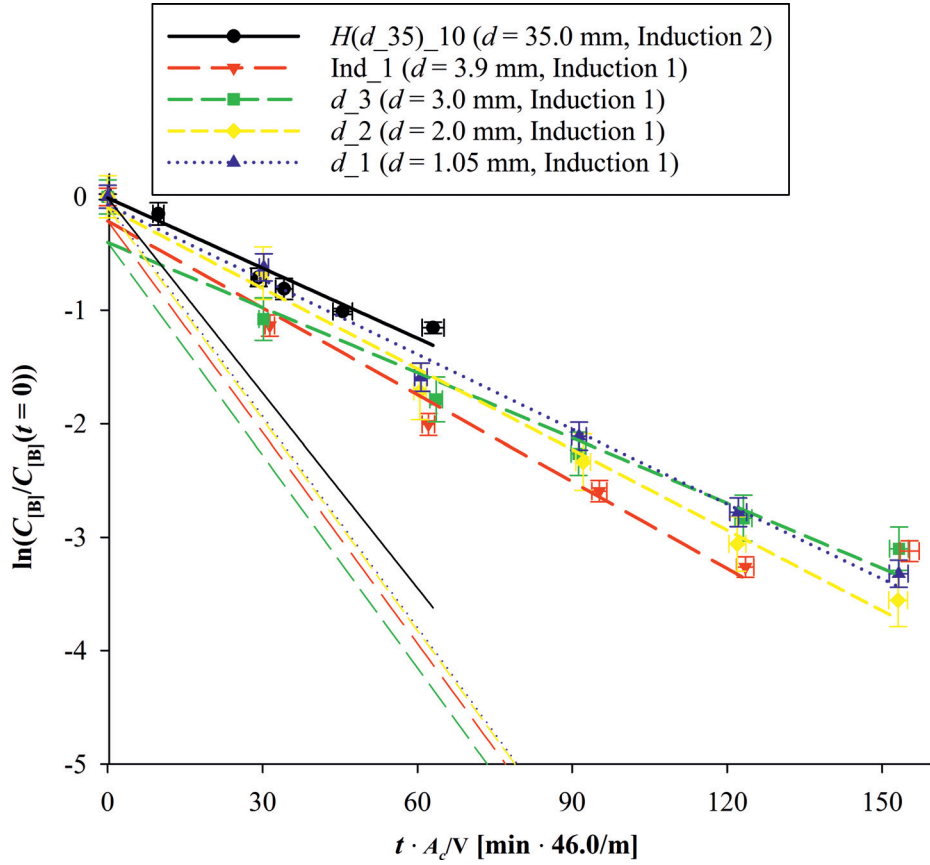
Figure 4.18: Linearized plots for regression of samples (thick lines) for "d" experiments and $H(d\_35)\_10$, compared to equilibrium modeling (thin lines). Lines have slope $-k$. Samples without symbols are outliers. Common parameters: $p_{H_2O} = 0.032$ bar, hydrogen atmosphere, $p = 0.99$ bar ($p = 1.13$ bar for $H(d\_35)\_10$), $Q = 2.0$ l_N/min, $H = 10$ mm, $m = 200$ g, EG-Si feedstock, $T = 1500$ °C, $d_c = 70$ mm, graphite crucible, $A_c = 36.9$ cm^2.

Table 4.8: Total mass transfer coefficients compared to equilibrium modeling for "d" experiments with lance diameters in the range 1-4 mm in Induction 1 furnace and $H(d\_35)\_10$ with 35 mm lance diameter in Induction 2 furnace. Lance diameter is given in the name of each experiment ($d\_$[mm]), except $d = 3.9$ mm for Ind_1. Common parameters: $p_{H_2O} = 0.032$ bar, hydrogen atmosphere, $p = 0.99$ bar ($p = 1.13$ bar for $H(d\_35)\_10$), $Q = 2.0$ l_N/min, $H = 10$ mm, $m = 200$ g, EG-Si feedstock, $T = 1500$ °C, induction furnaces, $d_c = 70$ mm, graphite crucible, $A_c = 36.9$ cm^2.

Experiment	k_t [μm/s]	k_{eq} [μm/s]	k_t/k_{eq} [%]
$H(d\_35)\_10$	7.5 ± 1.3	20.7	36.0 ± 5.8
Ind_1	9.2 ± 1.6	22.5	41.1 ± 6.7
d_3	6.9 ± 1.2	22.7	30.6 ± 5.1
d_2	8.6 ± 1.5	22.5	38.1 ± 6.4
d_1	8.0 ± 1.4	22.5	35.4 ± 5.8

4.1.6 Lance Height

The lance height was varied in two different series, first in the "H" series with 4 mm lance diameter in the Induction 1 furnace and second in the "$H(d\_35)$" series with 35 mm lance diameter in the Induction 2 furnace. Both series are included in Figures 4.19-4.20 and in Table 4.9. Experiment H_45 provided at remarkably lower total mass transfer coefficient and gas utilization than experiments with lance heights of 30 mm and below. The 95% confidence intervals overlap slightly with the 95% confidence intervals for the other experiments. Increasing the lance height to 45 mm may however be identified to reduce the mass transfer of boron and gas utilization at confidence level slightly lower than 95%. The "$H(d\_35)$" experiments provided a slightly lower total mass transfer coefficient and gas utilization compared to experiments with up to 30 mm lance height in the "H" series, but a difference can not be verified at a high confidence level as the 95% confidence intervals overlap comfortably.
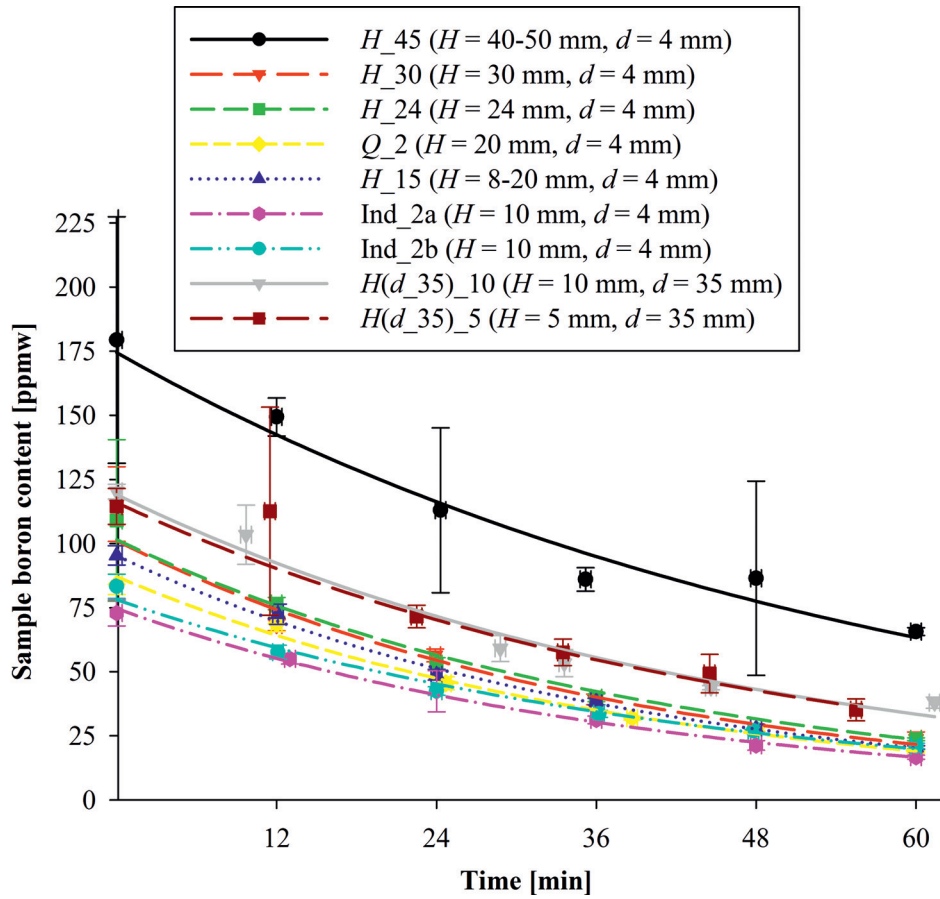
Figure 4.19: Boron content in samples as function of sampling time in "*H*" and "*H*(*d*_35)" experiments, with regression (thick curves). Common parameters: $p_{H_2O} = 0.032$ bar, hydrogen atmosphere, $p = 1.2$ bar, $Q = 1.99$ l$_N$/min, $m = 200$ g, EG-Si feedstock, $T = 1500$ °C, Induction 2 furnace, $d_c = 70$ mm, graphite crucible, $A_c = 36.9$ cm^2.
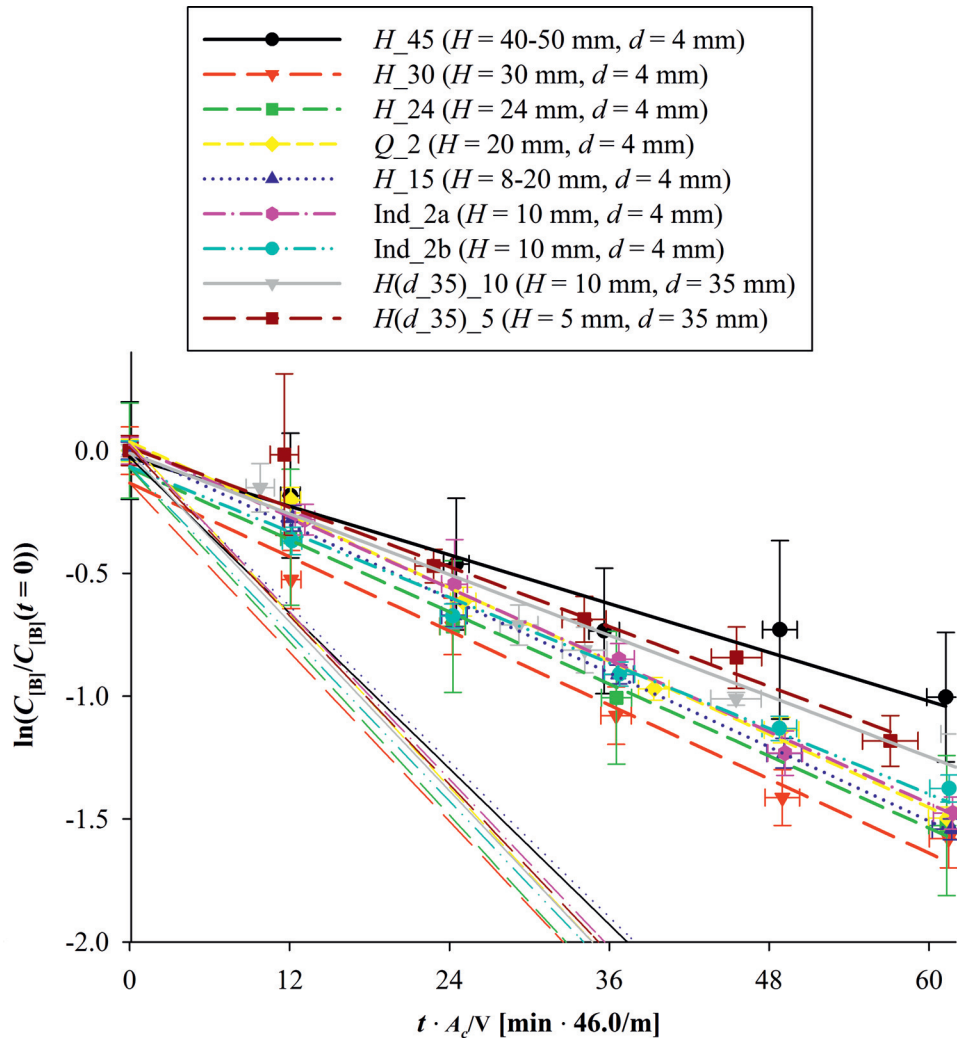
Figure 4.20: Linearized plots for regression of samples (thick lines) for "H" and "$H(d\_35)$" experiments, compared to equilibrium modeling (thin lines). Lines have slope $-k$. Common parameters: $p_{H_2O} = 0.032$ bar, hydrogen atmosphere, $p = 1.2$ bar, $Q = 1.99$ l_N/min, $m = 200$ g, EG-Si feedstock, $T = 1500\,°\text{C}$, Induction 2 furnace, $d_c = 70$ mm, graphite crucible, $A_c = 36.9$ cm^2.

Table 4.9: Total mass transfer coefficients compared to equilibrium modeling for "H" and "$H(d\_35)$" experiments. Lance height is given in the name of each experiment ($H(d\_35)$_[mm]), except $H = 10$ mm for Ind_2a-b and $H = 20$ mm for Q_2. Common parameters: $p_{H_2O} = 0.032$ bar, hydrogen atmosphere, $p = 1.2$ bar, $Q = 1.99$ l_N/min, $d = 4.0$ mm ($d = 35.0$ mm for "$H(d\_35)$" experiments), $m = 200$ g, EG-Si feedstock, $T = 1500\,°\text{C}$, Induction 2 furnace, $d_c = 70$ mm, graphite crucible, $A_c = 36.9$ cm^2.

Experiment	k_t [μm/s]	k_{eq} [μm/s]	k_t/k_{eq} [%]
H_45	6.0 ± 1.7	19.1	31.3 ± 7.5
H_30	9.1 ± 1.6	20.8	43.8 ± 7.4
H_24	8.8 ± 2.0	21.3	41.5 ± 9.1
Q_2	9.0 ± 1.5	21.2	42.4 ± 6.9
H_15	9.1 ± 1.5	19.1	47.7 ± 7.8
Ind_2a	8.8 ± 1.5	20.5	42.9 ± 7.1
Ind_2b	8.1 ± 1.3	20.6	39.2 ± 6.4
$H(d\_35)\_10$	7.5 ± 1.3	20.7	36.0 ± 5.8
$H(d\_35)\_5$	7.3 ± 1.3	20.7	35.5 ± 6.2

4.1.7 Melt Mass

The effect of melt volume was investigated separately by comparing experiment m_400 with 400 g melt to $Q(\text{Ind\_1})\_3$ with 200 g melt in identical crucibles. The concentration profile is less steep in the experiment with higher melt mass in Figure 4.21, because the concentration in the larger volume is less reduced for the same amount of boron removed from the melt. This relation is expected when the boron is removed in reactions at the surface, and Figure 4.22 and Table 4.10 show no significant difference in the mass transfer across the interface.
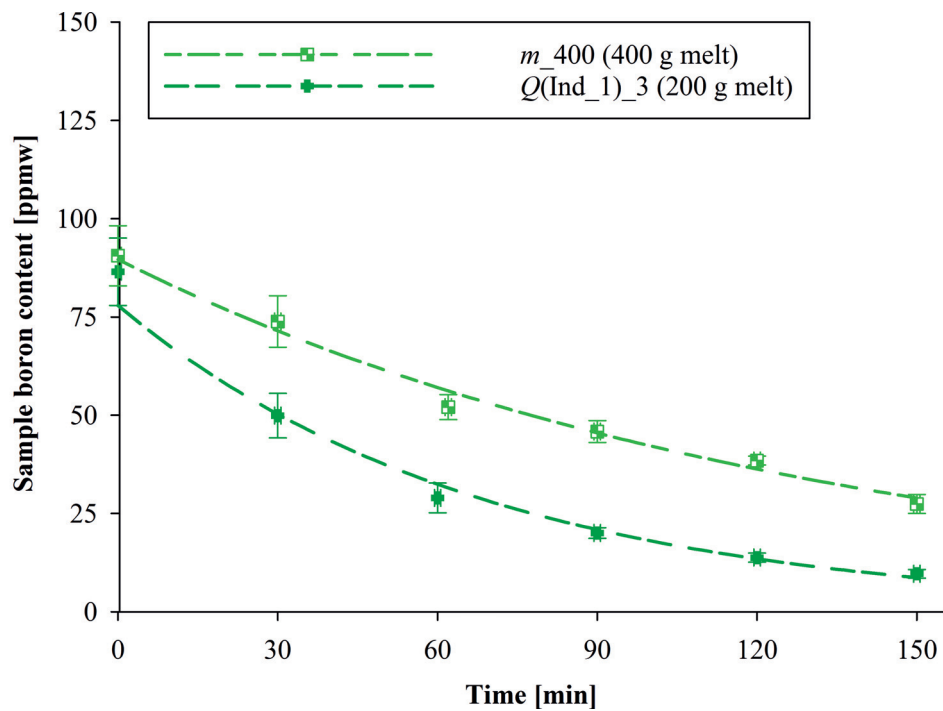
Figure 4.21: Boron content in samples as function of sampling time in "m" experiments. Common parameters: $p_{\text{H}_2\text{O}} = 0.032$ bar, $p_{\text{H}_2} = 0.50$ bar, argon atmosphere, $p = 1.01$ bar, $Q = 3.0 \, \text{l}_\text{N}/\text{min}$, $d = 4.0$ mm, $H = 50$ mm, EG-Si feedstock, $T = 1500\,°\text{C}$, Induction 1 furnace, $d_c = 70$ mm, graphite crucible, $A_c = 36.9 \, \text{cm}^2$.
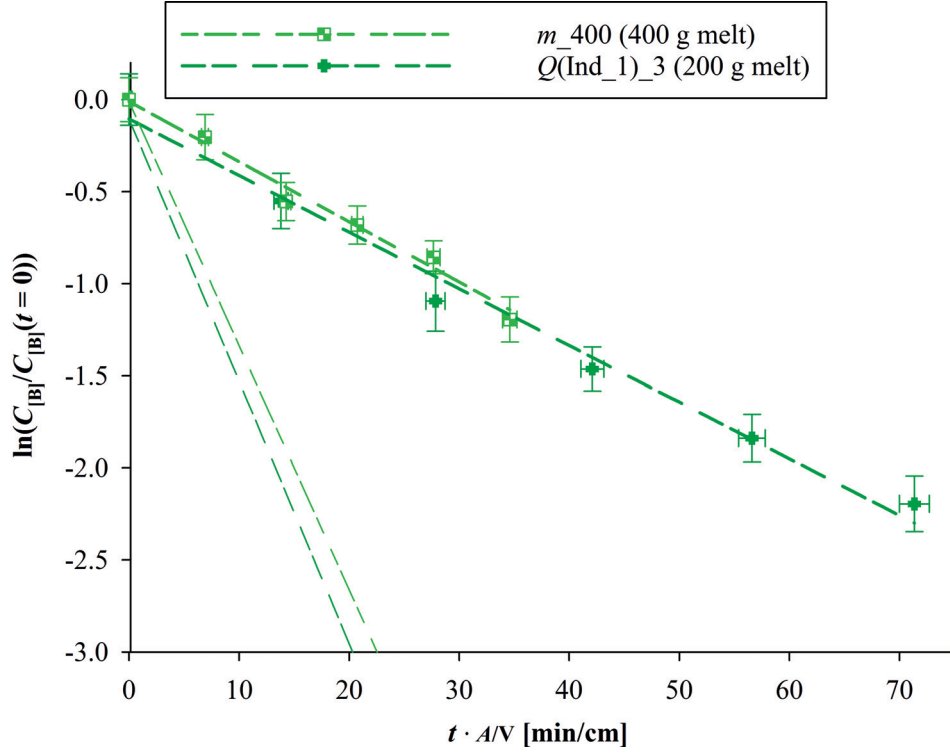
Figure 4.22: Linearized plot for regression of samples (lines have slope $-k$) for "m" experiments. Common parameters: $p_{H_2O} = 0.032$ bar, $p_{H_2} = 0.50$ bar, argon atmosphere, $p = 1.01$ bar, $Q = 3.0$ l_N/min, $d = 4.0$ mm, $H = 50$ mm, EG-Si feedstock, $T = 1500$ °C, Induction 1 furnace, $d_c = 70$ mm, graphite crucible, $A_c = 36.9$ cm^2.

Table 4.10: Total mass transfer coefficients compared to equilibrium modeling for "m" experiments with melt masses of 200 g (Q(Ind_1)_3) and 400 g (m_400). Common parameters: $p_{H_2O} = 0.032$ bar, $p_{H_2} = 0.50$ bar, argon atmosphere, $p = 1.01$ bar, $Q = 3.0$ l_N/min, $d = 4.0$ mm, $H = 50$ mm, EG-Si feedstock, $T = 1500$ °C, Induction 1 furnace, $d_c = 70$ mm, graphite crucible, $A_c = 36.9$ cm^2.

| Experiment	k_t [μm/s]	k_{eq} [μm/s]	k_t/k_{eq} [%]
Q(Ind_1)_3	5.16 ± 0.85	24.1	21.4 ± 3.6
m_400	5.70 ± 0.93	23.9	23.8 ± 4.3

4.1.8 Bubbling

Boron removal in an experiment with bubbling of 3.2 bar steam in hydrogen from a submerged lance in experiment Bubble_Lance is shown in Figure 4.23. No attempt was made to estimate the surface area of the bubbles. Linear regression was performed on $\ln \frac{C_{[B]}}{C_{[B]}(t=0)}$ as function of $\frac{t}{V}$ (accounted for weightloss) in Figure 4.24, giving $-Ak_t$ as the slope. The samples taken at 60 min and 120 min were excluded as outliers due to contamination. 60 mg boron powder was added to 400 g EG-Si in the crucible and it represents 150 ppmw as a maximum boron content in the melt, while the boron content in the sample at 60 min was measured to 206 ppmw and is contaminated by additional boron.
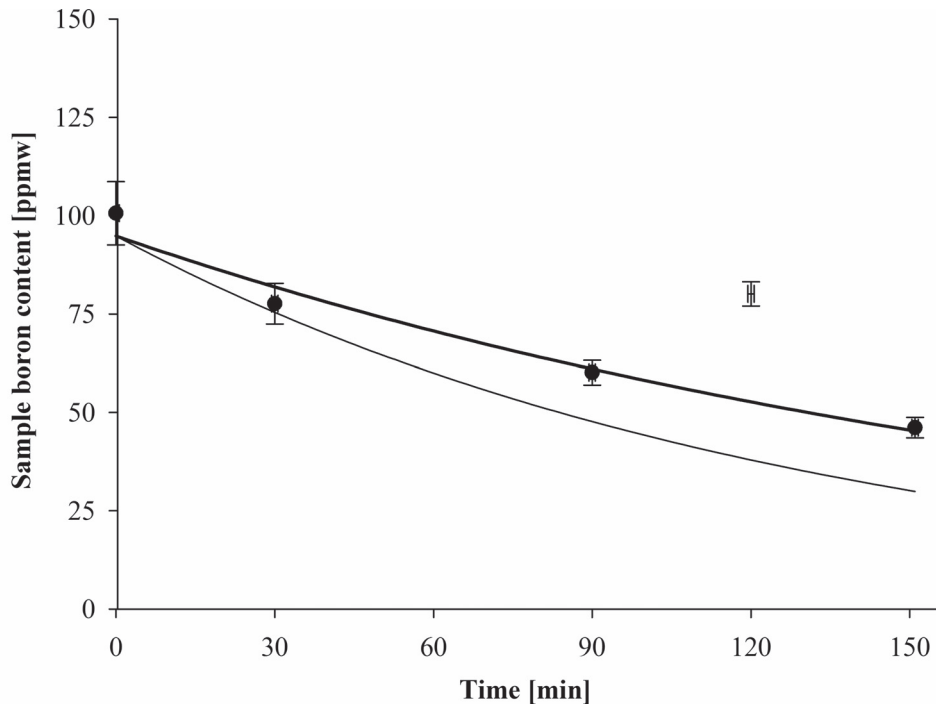
Figure 4.23: Boron content in samples as function of sampling time in experiment Bubble_Lance, with regression (thick curve) compared to equilibrium model (thin curve). The sample without symbol is an outlier. Parameters: $p_{H_2O} = 0.032$ bar, hydrogen atmosphere, $p = 0.99$ bar, $Q = 0.50$ l$_N$/min, $d = 2.0$ mm, $H = -32$ mm, $m = 400$ g, EG-Si feedstock, $T = 1500\,°C$, Induction 1 furnace, $d_c = 70$ mm, graphite crucible, $A_c = 36.9$ cm^2.
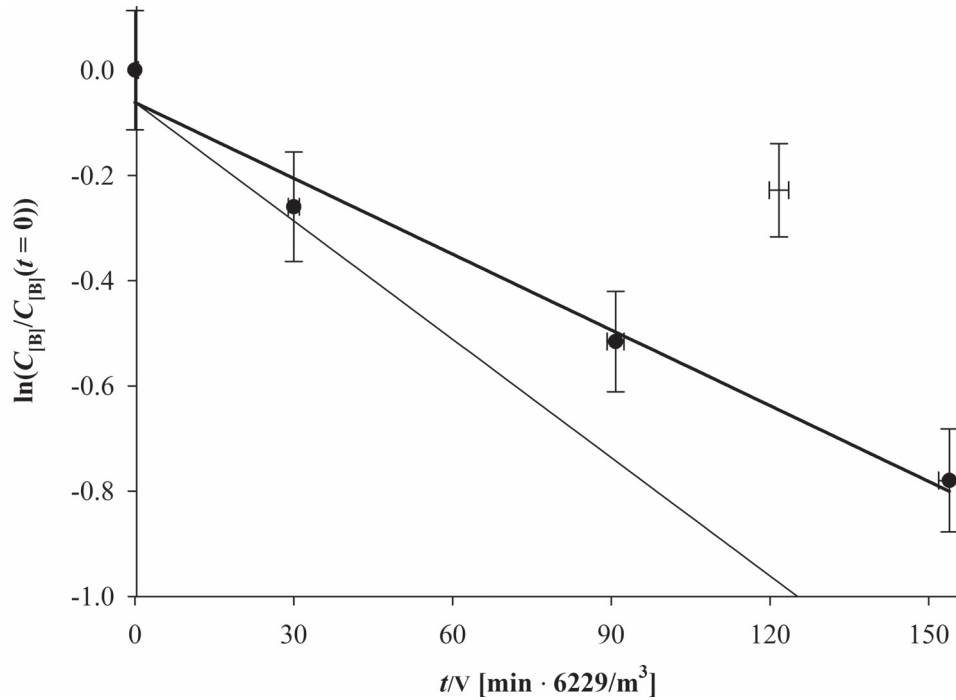
Figure 4.24: Linearized plot for regression of samples (thick line) for experiment Bubble_Lance, compared to equilibrium model (thin line). Lines have slope $-Ak$. The sample without symbol is an outlier. Parameters: $p_{H_2O} = 0.032$ bar, hydrogen atmosphere, $p = 0.99$ bar, $Q = 0.50$ l_N/min, $d = 2.0$ mm, $H = -32$ mm, $m = 400$ g, EG-Si feedstock, $T = 1500$ °C, Induction 1 furnace, $d_c = 70$ mm, graphite crucible, $A_c = 36.9$ cm^2.

In addition to the weightloss, the amount of liquid silicon was further reduced by solidification of droplets that splashed several centimeters up onto the crucible wall. A structure of solid silicon was observed to form gradually and was depicted 50-90 mm below the top of the crucible wall after the experiment (see Figure 4.25). The flow rate of 0.5 l_N/min hydrogen was above the limit for splashing with a 4 mm diameter submerged lance, and bubbling at higher gas flow rates was not attempted.

Below the solid structure of splashed silica in Figure 4.25, the temperature of the crucible wall appears high enough for the splashed droplets to be liquid and flow back into the bulk melt. The droplets that solidified on the wall after the experiment are not passivated like the solid structure above.

Silica fumes presumably form inside gas bubbles, and do not appear to be entrained into the melt, leaving the silicon surface and the cross-section of the melt after solidification visually

153

free from silica (Figure 4.25). It may be assumed that significant amounts of entrained fume particles in the melt would be visible at the melt surface, as they would agglomerate due to induction stirring and float to the surface where it could be seen as sintered particles or a layer.
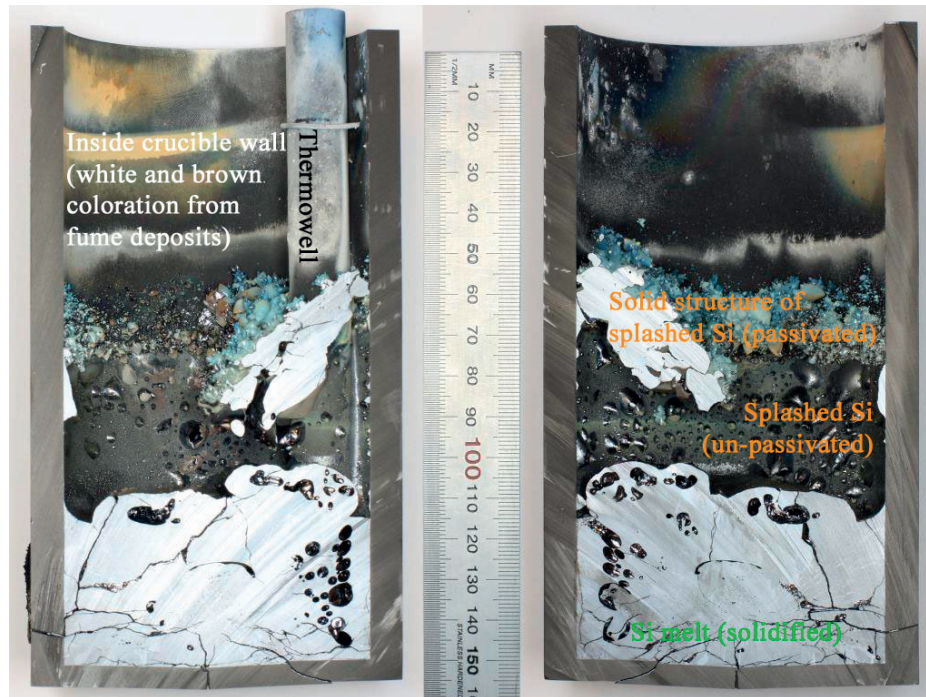
Figure 4.25: Pictures of cross-sections of the crucible after experiment Bubble_Lance.

Coefficients for the removal rate in the experiment and the equilibrium model are listed in Table 4.11. In order to be able to compare the values to impinging jet experiments, the crucible area is factored out in the unit of the rate coefficients Ak. Compared to Bubble_Lance, the fastest impinging jet experiment (Q_16b in Table 4.6) used a 32-fold higher flow rate of gas with the same composition, and the melt did not splash. The gas utilization was approximately halved and the rate coefficient was a factor 15 higher in Q_16b compared to Bubble_Lance. A similar gas utilization to that in Bubble_Lance was achieved only in the impinging jet experiment with the lowest total gas flow rate of $0.14 \, \mathrm{l_N/min}$ ($Q(\mathrm{Res})\_0.14$ in Table 4.4). It should also be noted that the volume reduction due to solidification of silicon splashing onto the crucible wall in Bubble_Lance is expected to cause an error in the estimation of the rate coefficient so that the actual rate coefficient and gas utilization was slightly lower than the estimates.

Table 4.11: Rate coefficients and gas utilization for experiment Bubble_Lance. $A_c = 3.69 \cdot 10^{-3}$ m² is factored out in the unit of rate coefficients and listed values are effectively $\frac{A}{A_c} k$ to allow comparisons to values of k for other experiments. Parameters: $p_{H_2O} = 0.032$ bar, hydrogen atmosphere, $p = 0.99$ bar, $Q = 0.50$ l$_N$/min, $d = 2.0$ mm, $H = -32$ mm, $m = 400$ g, EG-Si feedstock, $T = 1500$ °C, Induction 1 furnace, $d_c = 70$ mm, graphite crucible, $A_c = 36.9$ cm².

Experiment	Ak_t [$3.69 \cdot 10^{-3}$ m² · μm/s]	Ak_{eq} [$3.69 \cdot 10^{-3}$ m² · μm/s]	k_t/k_{eq} [%]
Bubble_Lance	3.44 ± 0.59	5.50	63 ± 13

4.1.9 Melt Convection

The effect of mass transfer in the melt on the rate of boron removal was investigated experimentally by comparing experiments with similar parameters and geometry in induction and resistance heated furnaces. Different convection regimes are expected in the melt in these furnaces as electromagnetic forces provides forced convection in the induction furnace, as compared to natural convection in the resistance furnace.

The refining rates are similar in Q(Res)_1 in the Resistance furnace and Conv_Ind in the Induction 1 furnace (Figures 4.26 and 4.27), and the total mass transfer coefficients in Table 4.12 are not significantly different (the 95% confidence intervals overlap). Thus, melt convection is not found to be determining for the total mass transfer coefficient at least up to 10^{-5} m/s.

The effect of melt convection on removal of boron is also studied in "Ind" experiments by comparing experiments Ind_1 in series "d" in Induction 1 to Ind_2a and -b in series "H" in the Induction 2 furnace, as the furnaces have different induction frequencies (3895 Hz for Induction 1 and 10750 Hz for Induction 2). The difference in concentration profiles in Ind_1 and Ind_2 experiments in Figure 4.28 is mainly due to the difference in initial concentration. The mass transfer (Figure 4.29) in the Induction 1 and -2 furnaces is not significantly different as the 95% confidence intervals as all of the total mass transfer coefficients in Table 4.13 overlap.
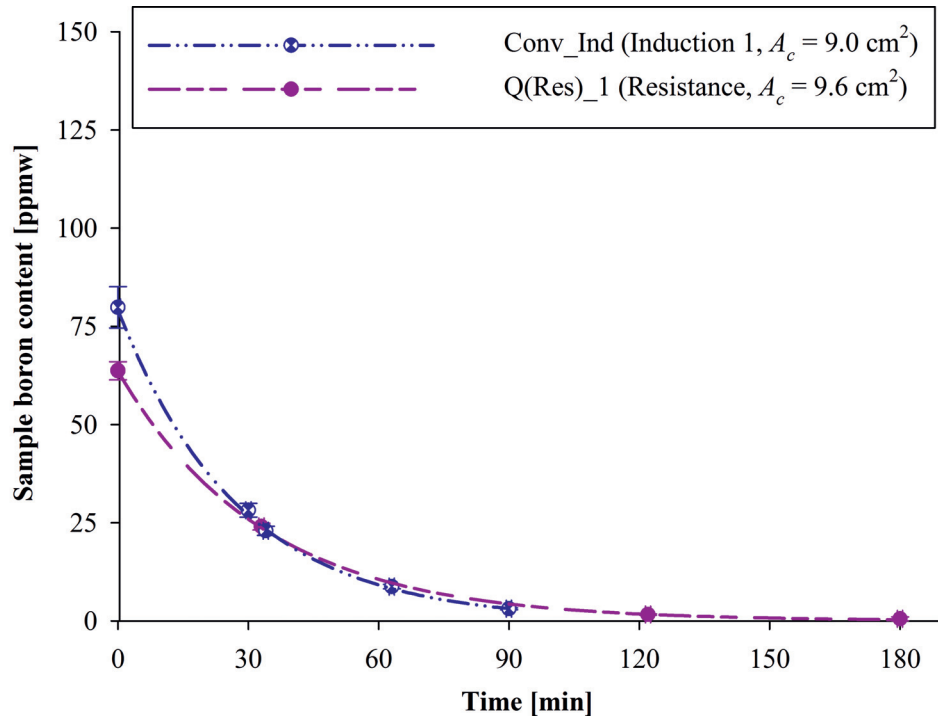
Figure 4.26: Boron content in samples as function of sampling time in "Conv" experiments, with regression (thick curve). The melt temperature in $Q(Res)\_1$ is assumed to $T \sim 1500 \pm {<}30$ °C ($T = 1422$ °C under crucible and alumina retainer), while Conv_Ind had $T = 1496 \pm 10$ °C inside the melt. Common parameters: $p_{H_2O} = 0.023$ bar, $p_{H_2} = 0.49$ bar, argon atmosphere, $p = 1.01$ bar, $Q = 1.01$ l_N/min, $d = 4.0$ mm, $H = 10$ mm, $m = 40$ g, EG-Si feedstock, $d_c = 35$ mm, quartz crucible.
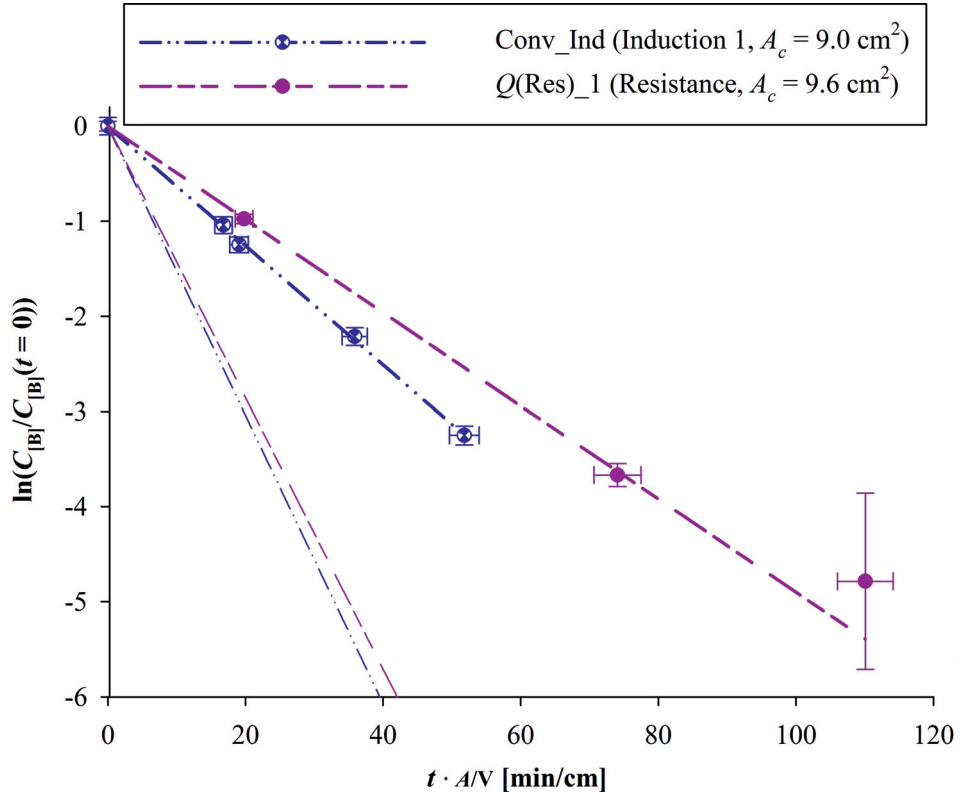
Figure 4.27: Linearized plots for regression of samples (thick lines) for "Conv" experiments, compared to equilibrium modeling (thin lines). Lines have slope $-k$. The melt temperature in $Q(\text{Res})\_1$ is assumed to $T \sim 1500 \pm {<}30\ °\text{C}$ ($T = 1422\ °\text{C}$ under crucible and alumina retainer), while Conv_Ind had $T = 1496 \pm 10\ °\text{C}$ inside the melt. Common parameters: $p_{\text{H}_2\text{O}} = 0.023$ bar, $p_{\text{H}_2} = 0.49$ bar, argon atmosphere, $p = 1.01$ bar, $Q = 1.01\ \text{l}_\text{N}/\text{min}$, $d = 4.0$ mm, $H = 10$ mm, $m = 40$ g, EG-Si feedstock, $d_c = 35$ mm, quartz crucible.

Table 4.12: Total mass transfer coefficients compared to equilibrium modeling for "Conv" experiments. Q(Res)_1 used Resistance furnace and $T \sim 1500 \pm {<}30\,°C$ ($T = 1422\,°C$ under crucible and alumina retainer), while Conv_Ind used Induction 1 furnace and $T = 1496 \pm 10\,°C$ inside the melt. Common parameters: $p_{H_2O} = 0.023$ bar, $p_{H_2} = 0.49$ bar, argon atmosphere, $p = 1.01$ bar, $Q = 1.01\,l_N/min$, $d = 4.0$ mm, $H = 10$ mm, $m = 40$ g, EG-Si feedstock, $d_c = 35$ mm, quartz crucible, $A_c = 9.0\text{-}9.6\ cm^2$.

Experiment	k_t [μm/s]	k_{eq} [μm/s]	k_t/k_{eq} [%]
Q(Res)_1	8.0 ± 1.4	23.7	33.8 ± 5.6
Conv_Ind	10.2 ± 1.7	23.7	40.3 ± 6.6
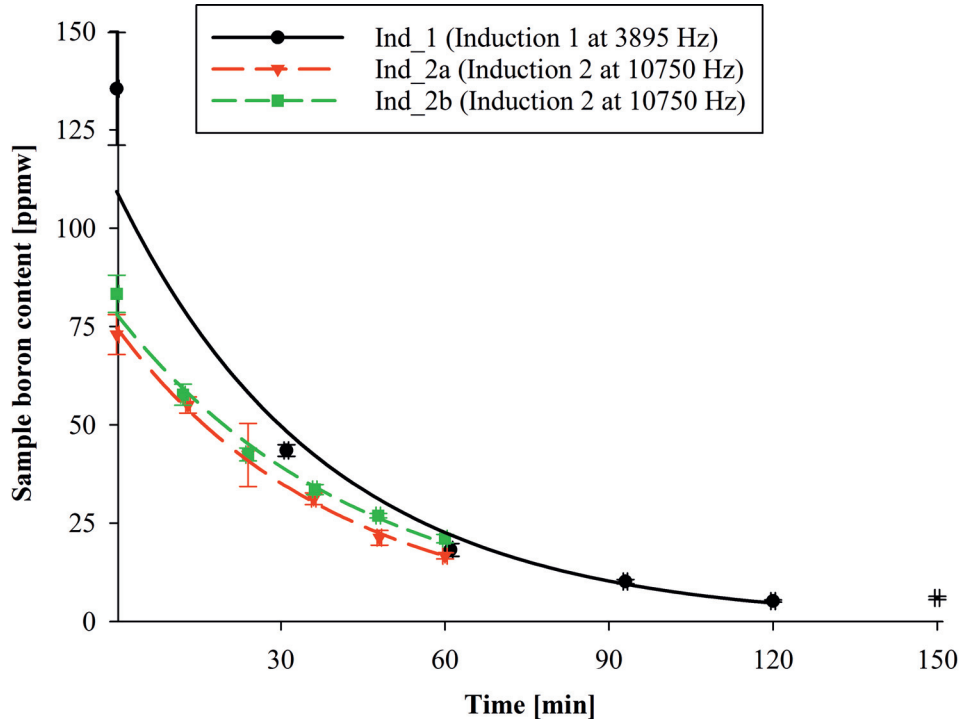
Figure 4.28: Boron content in samples as function of sampling time in "Ind" experiments, with regression (thick curve). The sample without symbol is an outlier. Common parameters: $p_{H_2O} = 0.032$ bar, hydrogen atmosphere, $p = 1.13$ bar ($p = 0.99$ bar for Ind_1), $Q = 2.00\,l_N/min$, $d = 4.0$ mm, $H = 10$ mm, $m = 200$ g, $T = 1500\,°C$, EG-Si feedstock, $d_c = 70$ mm, graphite crucible, $A_c = 36.9\ cm^2$.
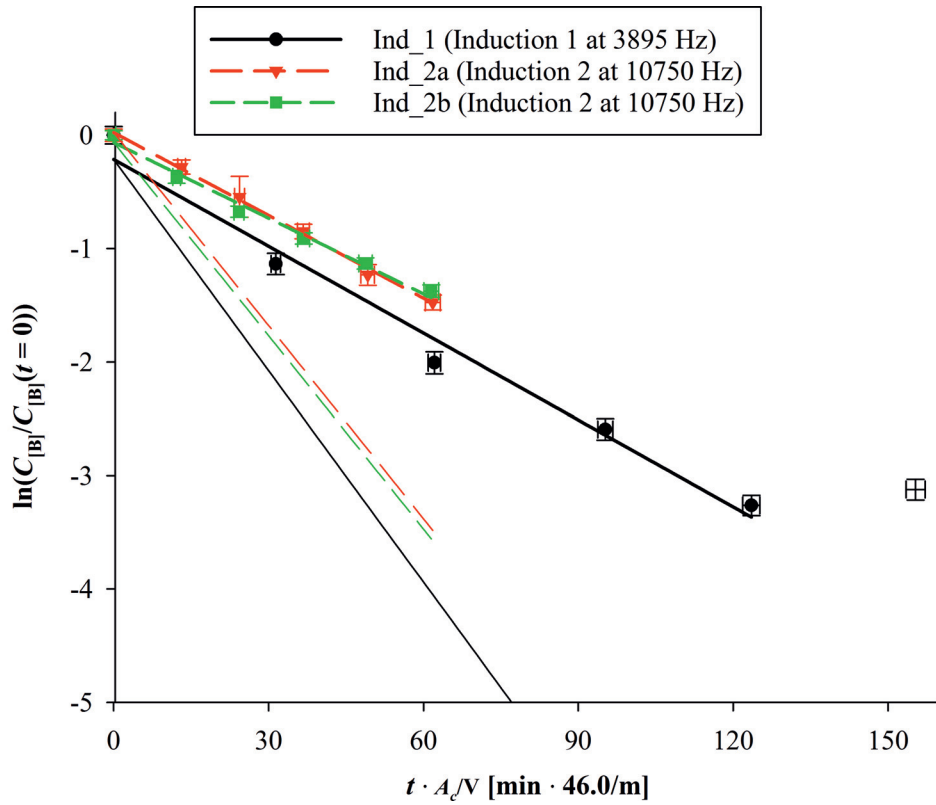
Figure 4.29: Linearized plots for regression of samples (thick lines) for "Ind" experiments, compared to equilibrium modeling (thin lines). Lines have slope $-k$. The sample without symbol is an outlier. Common parameters: $p_{H_2O} = 0.032$ bar, hydrogen atmosphere, $p = 1.13$ bar ($p = 0.99$ bar for Ind_1), $Q = 2.00$ l_N/min, $d = 4.0$ mm, $H = 10$ mm, $m = 200$ g, $T = 1500$ °C, EG-Si feedstock, $d_c = 70$ mm, graphite crucible, $A_c = 36.9$ cm^2.

Table 4.13: Total mass transfer coefficients compared to equilibrium modeling for "Ind" experiments in the Induction 1 furnace at 3895 Hz (Ind_1) and the Induction 2 furnaces at 10750 Hz (Ind_2). Common parameters: $p_{H_2O} = 0.032$ bar, hydrogen atmosphere, $p = 1.13$ bar ($p = 0.99$ bar for Ind_1), $Q = 2.00$ l_N/min, $d = 4.0$ mm, $H = 10$ mm, $m = 200$ g, $T = 1500$ °C, EG-Si feedstock, $d_c = 70$ mm, graphite crucible, $A_c = 36.9$ cm^2.

Experiment	k_t [μm/s]	k_{eq} [μm/s]	k_t/k_{eq} [%]
Ind_1	9.2 ± 1.6	22.5	41.1 ± 6.7
Ind_2a	8.8 ± 1.5	20.5	42.9 ± 7.1
Ind_2b	8.1 ± 1.3	20.6	39.2 ± 6.4

4.2 Weightloss Dependencies for SiO Formation

This section reports the weightloss in experiments where it could be fully accounted for. The weightloss is considered to be fully accounted for in experiments where the initially weighted crucible assembly could be fully recovered after solidification and the weight of the samples was taken into account. Full account of the weightloss was first obtained for experiments using the Induction 2 furnace, and these experiments are divided according to their experimental series in the following subsections. Experimental series in other furnaces are not considered for weightloss measurements. Weightloss is used as a measure for the extent of silicon oxidation, as SiO gas is produced at the melt surface during active oxidation, providing the surface is not passivated.

4.2.1 Steam Content

The weightloss during experiments in the "H_2O" series are shown in Figure 4.30 as a function of the partial pressure of steam set in the feed gas in each experiment. The weightloss for H_2O_20 was not fully accounted for and this experiment is not included in Figure 4.30. Experiments H_2O_50 and H_2O_60 (with 0.50 and 0.60 bar steam) were passivated and considered to be outliers as the weight of the passivation layer reduces the measured weightloss. For the representative experiments, the weightloss clearly increases with an increasing amount of the steam reactant in the feed gas, as expected from complete decomposition of the steam at the interphase.
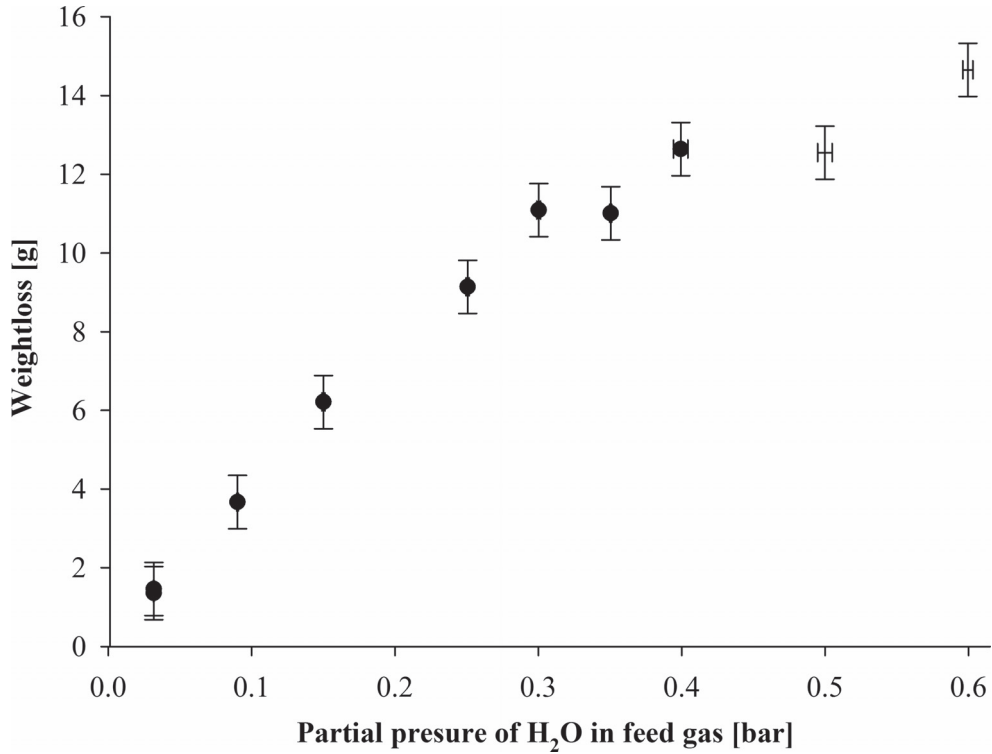
Figure 4.30: Weightloss in experiments in the "H₂O" series as a function of $p_{H_2O}^{feed}$. Experiments without symbols are outliers. Common parameters: argon atmosphere, $p = 1.36$ bar, $Q = 2.00$ l$_N$/min, $d = 4.0$ mm, $H = 20$ mm, $m = 200$ g, high-purity silicon feedstock, $T = 1700$ °C, Induction 2 furnace, $d_c = 70$ mm, graphite crucible, $A_c = 36.9$ cm².

4.2.2   Gas Flow Rate

Figure 4.31 plots the weightloss during experiments with varying total gas flow rates in the "Q" series. The weightloss of representative experiments increases with the total gas flow rate, which again can be related to an increasing supply of steam that decomposes and forms SiO gas at the interphase. The measurements obtained for experiments Q_8a and -b appear too low to be representative for the series, particularly because the supply of steam calculated from the weightloss provides a lower mass transfer coefficient for boron removal in equilibrium modeling than the total mass transfer coefficient in the experiments.
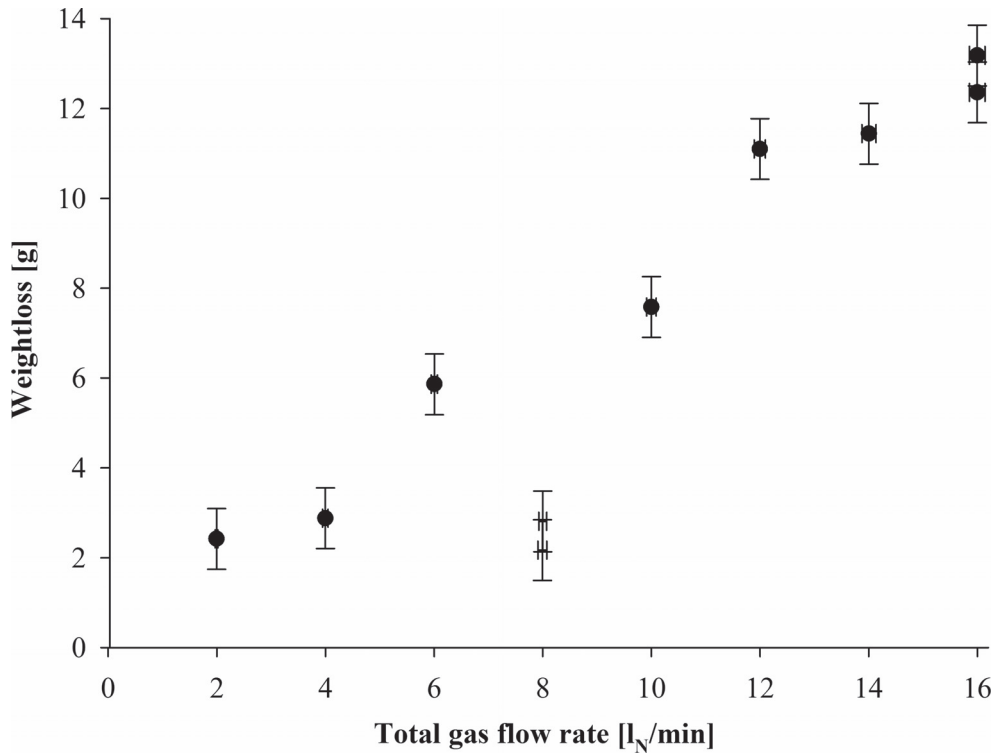
Figure 4.31: Weightloss in experiments in the "Q" series as a function of total gas flow rate. Experiments without symbols are outliers. Common parameters: $p_{H_2O} = 0.032$ bar, hydrogen atmosphere, $p = 1.12$ bar, $d = 4.0$ mm, $H = 20$ mm, $m = 200$ g, EG-Si feedstock, $T = 1500$ °C, Induction 2 furnace, $d_c = 70$ mm, graphite crucible, $A_c = 36.9$ cm^2.

4.2.3 Lance Height and Diameter

Experiments in the "H" and "$H(d\_35)$" series for which the weightloss could be fully accounted for is included in Figure 4.32. The weightloss measurement for experiment Ind_2a is considered to be an outlier. The weightloss during the experiments are plotted as function of the lance height above the melt surface. The variation between representative experiments is within the estimated uncertainty of the measurements. Like for boron removal, the weightloss does not clearly depend on lance diameter and lance height below 30 mm with 2 l$_N$/min gas flow rate.

162
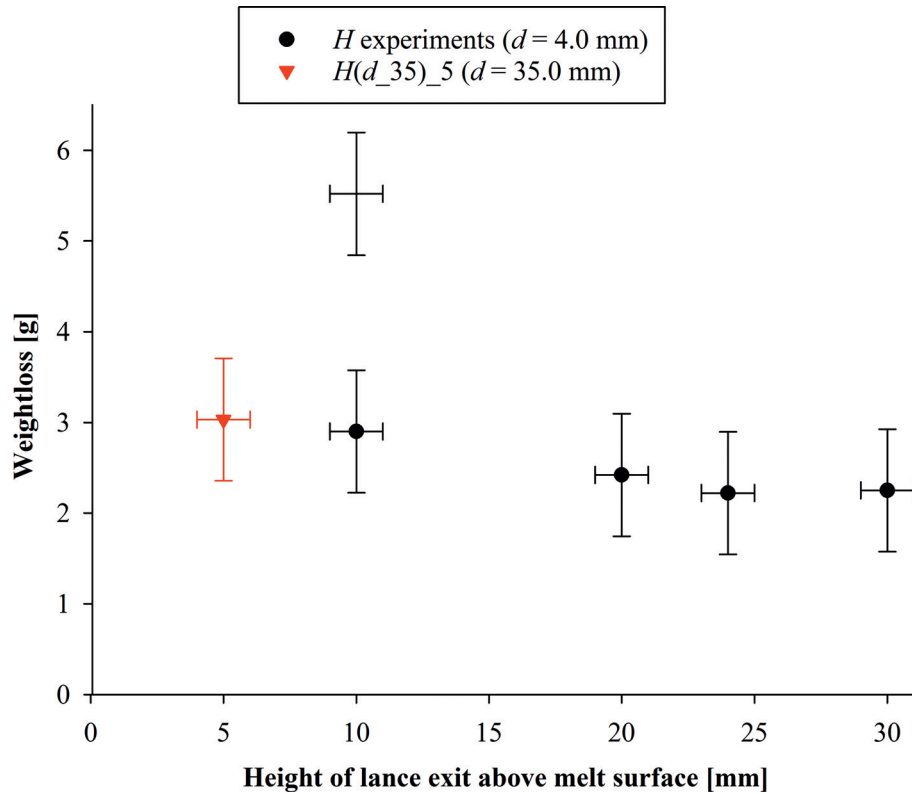
Figure 4.32: Weightloss in experiments in the "H" series and $H(d\_35)\_5$ as a function of lance height above the melt surface. Experiments without symbols are outliers. Common parameters: $p_{H_2O} = 0.032$ bar, hydrogen atmosphere, $p = 1.2$ bar, $Q = 1.99$ l_N/min, $m = 200$ g, EG-Si feedstock, $T = 1500$ °C, Induction 2 furnace, $d_c = 70$ mm, graphite crucible, $A_c = 36.9$ cm^2.

The weightloss appears to be higher in hydrogen at 1500 °C melt temperature (experiments in Figure 4.32) than in argon at 1700 °C melt temperature (H_2O_03a and -b at 0.032 bar steam in Figure 4.30). However, this comparison is not conclusive as the 95% confidence intervals H_2O_03a and -b at 0.032 bar steam in Figure 4.30 do overlap with the confidence intervals for the experiments in Figure 4.32.

163

4.3   Boron Removal with Silica Surface Coverage

In most experiments deemed unsuccessful for investigation of the mass transfer of boron, silica covered the whole or part of the melt surface and reduced the effective area for boron removal. Silica surface coverage formed either from passivation or from deposits of silica fumes falling onto the melt surface from the lance or crucible wall. Falling deposits was occasionally observed during sampling to form islands along the crucible wall.

Experiments in the "A/A_c" series qualitatively shows the detrimental effect of surface coverage on boron removal. Experiment $Q(\text{Ind\_1})\_3$ was attempted twice (A/A_c_27 and -75) before a clean surface was obtained after solidification. Experiment A/A_c_00 was intended for the "$Q(\text{Ind\_1})$" series with a higher total gas flow rate of $5 \, \text{l}_N/\text{min}$, but since the surface was completely covered and boron was not removed the difference in gas flow rate has no impact on the boron removal, and A/A_c_00 illustrates the effect of complete surface coverage rather than gas flow rate.

Pictures of the surface after the experiments are shown in Figure 4.33. The relative area of silica on the surface in these pictures is used as an estimate for silica surface coverage. Figure 4.33(c) also shows an area of SiC particles with green coloration and Figure 4.33(d) show brown coloration of the surface due to SiC particles. SiC particles are not assumed to cover the surface during experiments in the induction furnaces because Kadkhodageigi et al. [60] found them to be removed to the crucible wall by a pressure gradient in the melt caused by electromagnetic forces. Consistently, solid particles are not observed on the melt surface during experiments, but a negligibly thin ring was observed along the crucible wall. The ring is recognizable in pictures after solidification in Figure 4.33, but the SiC particles appear to have been pushed away from the crucible wall during solidification, which is observed to start at the crucible wall and proceed towards the center.

The impact of silica surface coverage on boron removal is not only expected to depend linearly on the fraction of the melt surface area that is blocked by silica, but also depend on the position of the silica surface coverage due to the inhomogeneous gas flow pattern for impinging jets. Surface coverage is expected to be most detrimental directly beneath the lance where mass transfer to the impinging jet flow is fastest. The gas stagnates in the corner formed by the melt surface and the crucible wall, so mass transfer to the gas is expected to be significantly lower close to the crucible wall than beneath the lance even for a clean surface. Thus, the effect of surface coverage along the crucible wall has a lower impact on the boron removal rate and mass transfer (averaged over A_c) compared to surface coverage closer to the center. Formation of small islands or thin layers of silica along the crucible wall or thermowell, like in the picture after solidification of $Q(\text{Ind\_1})\_3$ in Figure 4.33(d), was assumed to have insignificant impact on boron removal.

164

(a) A/A_c_00: $\frac{A_{\text{SiO}_2}}{A_c} = 100\%$

(b) A/A_c_27: $\frac{A_{\text{SiO}_2}}{A_c} \sim 73\%$

(c) A/A_c_75: $\frac{A_{\text{SiO}_2}}{A_c} \sim 25\%$

(d) $Q(\text{Ind\_1})\_3$: $\frac{A_{\text{SiO}_2}}{A_c} = 0\%$
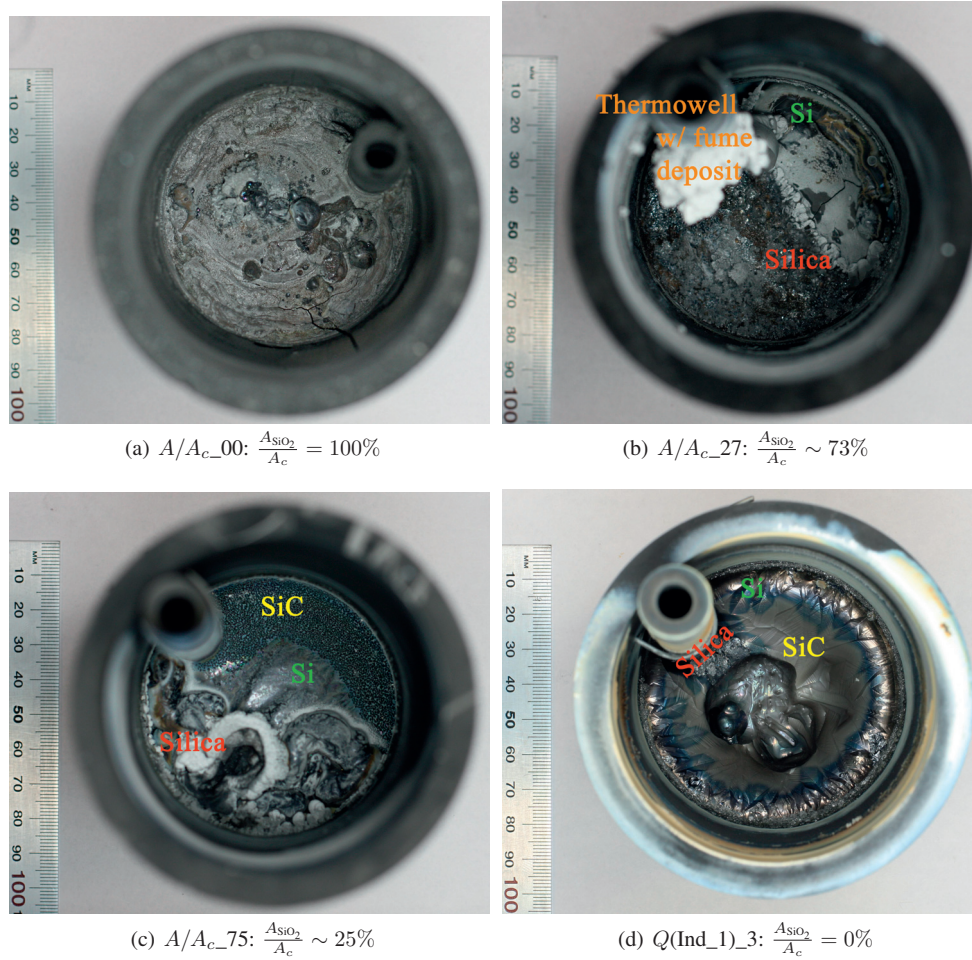
Figure 4.33: Pictures of the surface of silicon in crucibles after "A/A_c" experiments, with labels for identifying silica surface coverage, clean silicon and SiC particles at the surface. Silica surface coverage ($\frac{A_{\text{SiO}_2}}{A_c}$) is estimated from the area of silica in the surface of the images. The fume deposit depicted on the thermowell after A/A_c_27 (b) is near the top of the crucible. It was not removed by pressurized air. White fume particles appear to have settled on the melt after experiment A/A_c_27, and this area is assumed to expose silicon during gas blowing. For reference, the inner crucible diameter is 70 mm.

Figure 4.34 reveals that boron was not removed in experiment A/A_c_00, because a solid silica layer covered the entire melt surface as shown in Figure 4.33(a). As the steam was not

consumed over the silicon melt, it remained in the gas flow towards the crucible wall and instead oxidized the graphite crucible, which was severely damaged over the silica layer. The total mass transfer coefficient was not calculated by regression, and A/A_c_00 is not included in Figure 4.35. The samples follow a continuous trend in all of the experiments, which suggests that the silica surface coverage in A/A_c_00-75 either formed entirely before the experiment started or developed gradually. The silica layer was frequently noticed to cause resistance when the sample tube was moved into and out the melt. In experiment A/A_c_00, the silica layer was first noticed during sampling at 30 min, and the layer developed to a hard crust within 94 min. In experiment A/A_c_27, the silica layer was noticed already for the initial sample. The silica layer was not noticed during A/A_c_75. Presumably, silica surface coverage did not develop in the area of the surface from which samples were extracted.
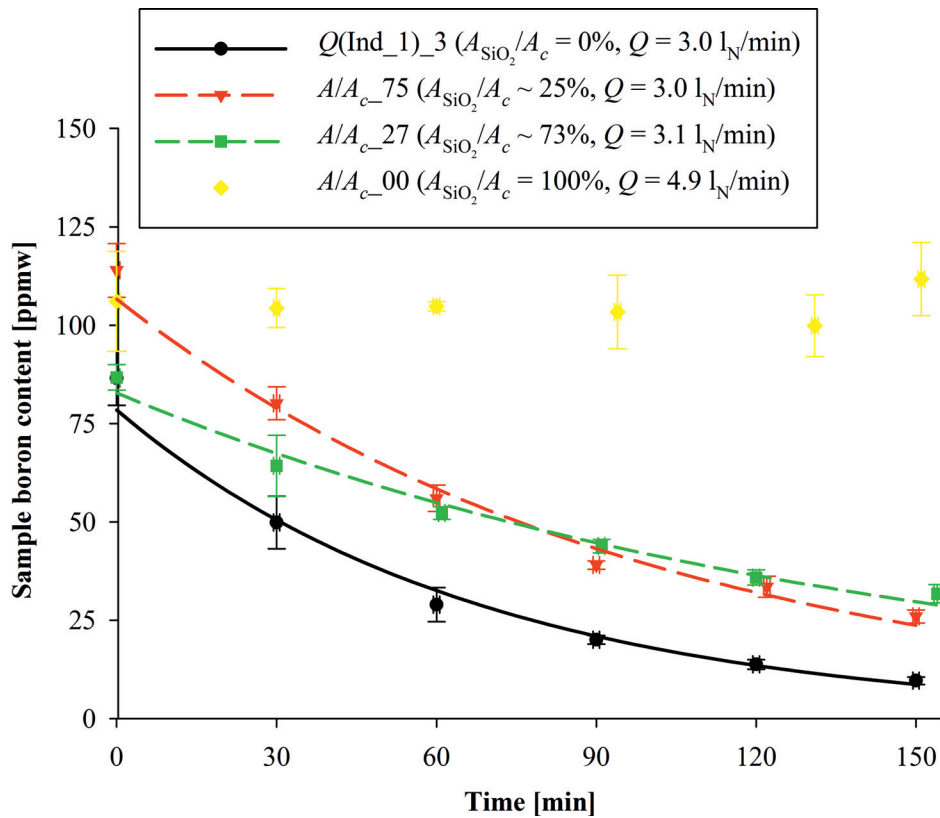
Figure 4.34: Boron content in samples as function of sampling time in "A/A_c" experiments, with regression (thick curve). Common parameters: $p_{H_2O} = 0.032$ bar, $p_{H_2} = 0.49$ bar, argon atmosphere, $p = 1.02$ bar, $d = 4.0$ mm, $H = 50$ mm, $m = 200$ g, EG-Si feedstock, $T = 1500$ °C, Induction 1 furnace, $d_c = 70$ mm, graphite crucible, $A_c = 36.9$ cm^2.
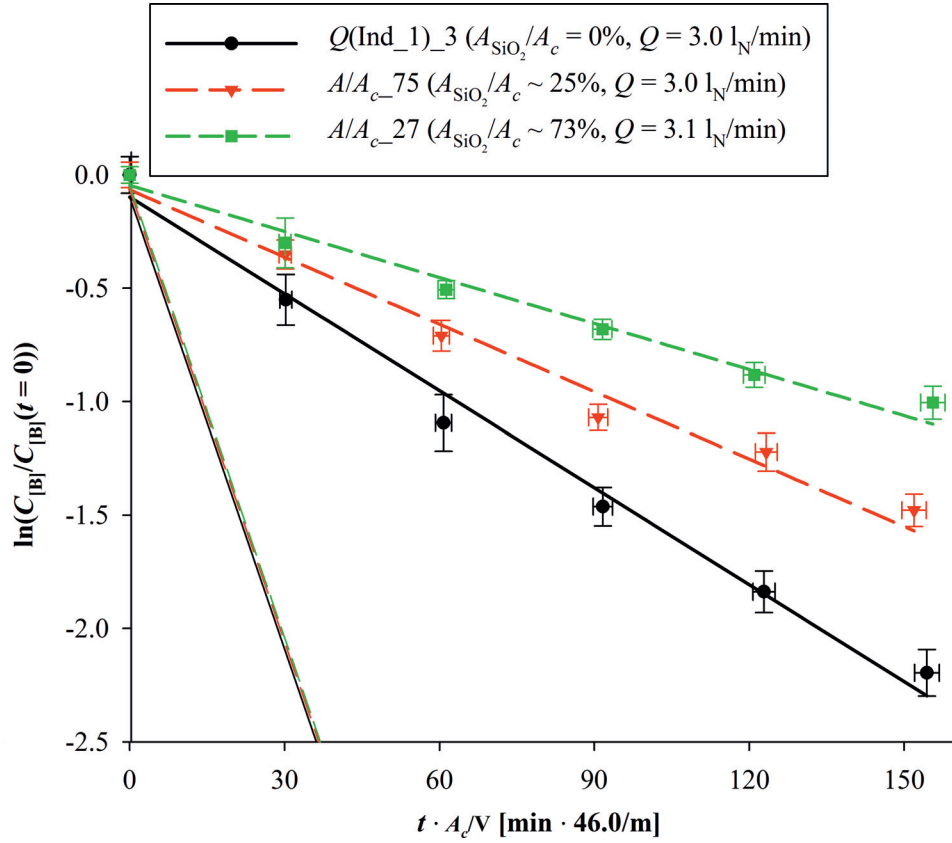
Figure 4.35: Linearized plots for regression of samples (thick lines) for "A/A_c" experiments, compared to equilibrium modeling (thin lines). Lines have slope $-k$. Common parameters: $p_{H_2O} = 0.032$ bar, $p_{H_2} = 0.49$ bar, argon atmosphere, $p = 1.02$ bar, $d = 4.0$ mm, $H = 50$ mm, $m = 200$ g, EG-Si feedstock, $T = 1500\,°C$, Induction 1 furnace, $d_c = 70$ mm, graphite crucible, $A_c = 36.9$ cm^2.

Table 4.14 reports rate coefficients (Ak) because the area of clean silicon during the A/A_c_27 and -75 experiments are not accurately known and mass transfer is expected to depend on the position of the exposed surface area. However, as A_c is factored out in the unit, the values for each experiment are effectively averaged over the available crucible cross-section area and compares directly to mass transfer coefficients of other experiments. The rate coefficient and gas utilization is reduced for experiments with increasing silica surface coverage, as the effective area for boron removal is reduced.

Table 4.14: Rate coefficients and gas utilization for "A/A_c" experiments. $A_c = 3.69 \cdot 10^{-3}$ m^2 is factored out in the unit of rate coefficients and listed values are effectively $\frac{A}{A_c}k$ to allow comparisons to values of k for other experiments. Approximate fraction of exposed silicon surface area after each experiment is given in the name ($A/A_c\_[\%]$), except $A/A_c = 100\%$ after $Q(Ind\_1)\_3$. Common parameters: $p_{H_2O} = 0.032$ bar, $p_{H_2} = 0.49$ bar, argon atmosphere, $p = 1.02$ bar, $Q = 3.0$ l$_N$/min ($Q = 4.9$ l$_N$/min for A/A_c_00), $d = 4.0$ mm, $H = 50$ mm, $m = 200$ g, EG-Si feedstock, $T = 1500$ °C, Induction 1 furnace, $d_c = 70$ mm, graphite crucible, $A_c = 36.9$ cm^2.

Experiment	Ak_t [$3.69 \cdot 10^{-3}$ m$^2 \cdot \mu$m/s]	Ak_{eq} [$3.69 \cdot 10^{-3}$ m$^2 \cdot \mu$m/s]	k_t/k_{eq} [%]
A/A_c_00	0	36.8	0
A/A_c_27	2.45 ± 0.41	24.1	10.2 ± 1.7
A/A_c_75	3.58 ± 0.59	24.1	14.9 ± 2.5
$Q(Ind\_1)\_3$	5.16 ± 0.85	24.1	21.4 ± 3.6

4.3.1 Steam at Atmospheric Pressure

Two experiments were attempted with atmospheric steam partial pressure at 1800 °C melt temperature. The $H_2O(T\_1800)\_100$ experiments used 600 g melts 2 l$_N$/min total gas flow rate of 1 bar steam in argon at 1.4 bar total pressure. The over-pressure was caused by obstruction of the flow through a one-way valve at the furnace outlet. $H_2O(T\_1800)\_100a$ used MG-Si and $H_2O(T\_1800)\_100b$ used UMG-Si. It was noticed after $H_2O(T\_1800)\_100b$ that the humidifier had consumed an excessive amount of water and the steam feed rate was presumably higher than intended.

Figure 4.36 shows pictures of the melt surface taken at the start and end of experiment $H_2O(T\_1800)\_100a$. Figure 4.36(a) shows a clean melt surface seconds after steam was introduced into the gas flow. Silica was not observed to form on the melt surface, as expected from equilibrium modeling. However, the large amount of fumes blocked vision to the melt surface, and development of silica surface coverage could not be observed. Silica surface coverage could form completely from fume deposits falling onto the melt.

Figure 4.36(b) show again the top view of the crucible after vision was restored minutes after finishing gas blowing. There were large amounts of silica fume deposits near the top of the crucible, except at the upper left position in Figure 4.36(b). Deposits here presumably broke off and onto the melt during sampling, as the lance was removed to the side to give space for the sample tube. A clean melt surface only remained in the position where samples had been extracted. Fumes also deposited onto the lance and part of it presumably also fell onto the melt.

There were technical problems with the silica sample tubes in the experiments at $1800\,°C$ because the temperature of the melt was above the melting point of the quartz tubes used for sampling. The risk of softening/melting of the sample tubes was reduced by minimizing the time of exposure to the high temperature in and shortly above the melt. A material with higher melting point could be ideal for the sample tubes. In a few sampling attempts, the sample tube were shut in the end, and a body of silica mixed with silicon was occasionally attached to the end of the sample tube. During sampling at $18\,min$, a viscous drag was felt when the sample tube was removed, and it shortly changed to a hard resistance. The sample tube was still intact after it was broken free and taken out of the furnace. As silica surface coverage was expected to be molten on the melt surface, it may have stuck to the colder sample tube and been stretched up as the tube was removed, and solidify as the temperature decreases upwards from the melt. This could form a tube-like structure that was observed to rise up from the silicon surface in the crucible after the experiment.
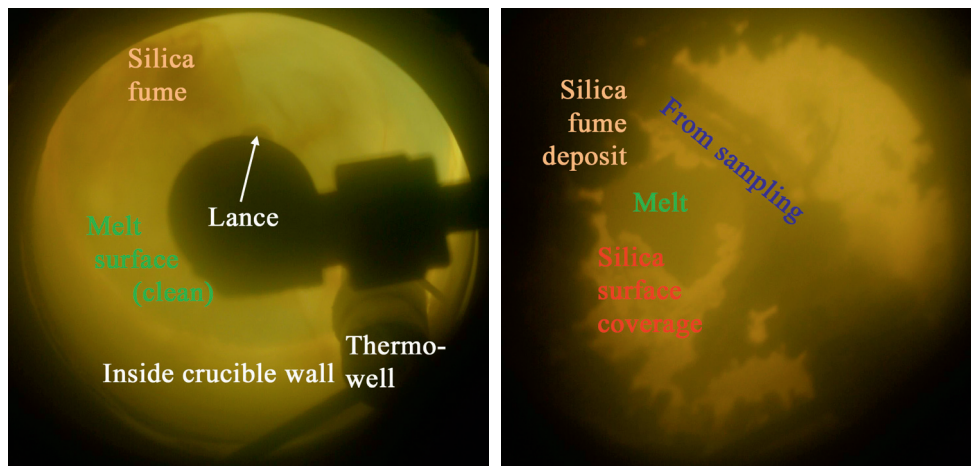
(a) Seconds after gas blowing with steam started   (b) Minutes after gas blowing ended (lance removed)

Figure 4.36: Pictures into the crucible during $H_2O(T\_1800)\_100a$, with labels for identifying silica surface coverage, clean silicon melt, silica fume and fume deposits. Molten silica may have stuck to a sample tube and been stretched up before it solidified and broke off while the sample tube was removed, making a tube-shaped structure labeled "From sampling" (b). A tube-shaped silica structure rising up from the melt was recognized in the crucible after the experiment. For reference, the inner crucible diameter is $70\,mm$.

169

Boron was removed in both $H_2O(T\_1800)\_100$ experiments as shown in Figures 4.37 and 4.38, but at a relatively slow rate judging by the low gas utilizations in Table 4.15. The difference in removal rates are mainly due to surface coverage, which presumably was different during $H_2O(T\_1800)\_100a$ and -b experiments, and due to excessive steam feeding in $H_2O(T\_1800)\_100b$.
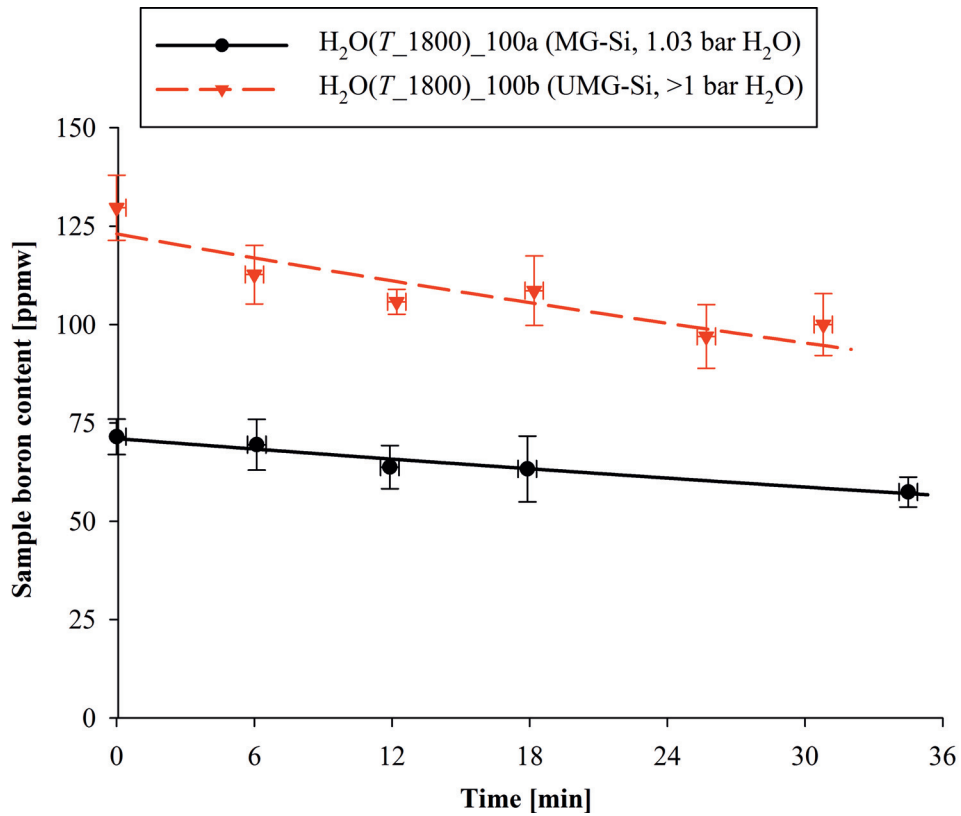
Figure 4.37: Boron content in samples as function of sampling time in $H_2O(T\_1800)\_100$ experiments, with regression (thick curve). Additional parameters for $H_2O(T\_1800)\_100a$ (-b if divergent): argon atmosphere, $p = 1.36$ bar ($p = 1.47$ bar), $Q = 2.02$ l_N/min ($Q > 1.92$ l_N/min), $d = 4.0$ mm, $H = 20$ mm, $m = 600$ g, $T = 1799$ °C ($T = 1785$ °C), Induction 2 furnace, $d_c = 70$ mm, graphite crucible, $A_c = 36.9$ cm^2.

170
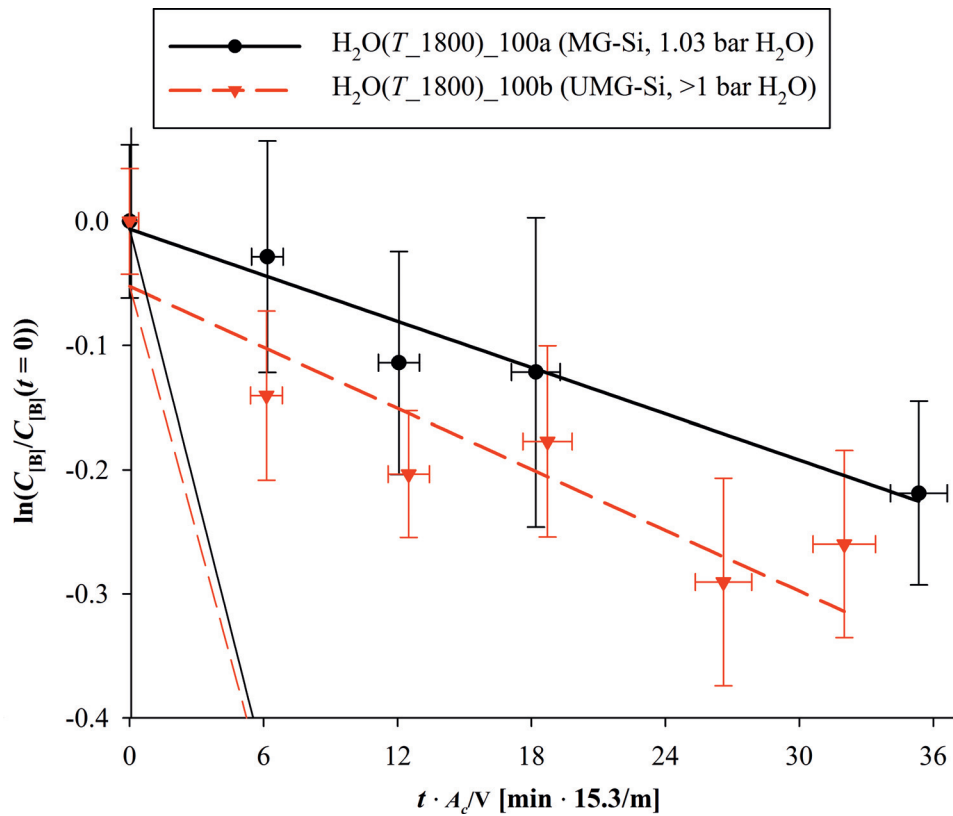
Figure 4.38: Linearized plots for regression of samples (thick lines) for $H_2O(T\_1800)\_100$ experiments, compared to equilibrium modeling (thin lines). Lines have slope $-k$. Additional parameters for $H_2O(T\_1800)\_100a$ (-b if divergent): argon atmosphere, $p = 1.36$ bar ($p = 1.47$ bar), $Q = 2.02\,l_N/min$ ($Q > 1.92\,l_N/min$), $d = 4.0$ mm, $H = 20$ mm, $m = 600$ g, $T = 1799\,°C$ ($T = 1785\,°C$), Induction 2 furnace, $d_c = 70$ mm, graphite crucible, $A_c = 36.9$ cm^2.

Table 4.15: Rate coefficients and gas utilization for $H_2O(T\_1800)\_100$ experiments. $A_c = 3.69 \cdot 10^{-3}$ m^2 is factored out in the unit of rate coefficients and listed values are effectively $\frac{A}{A_c}k$ to allow comparisons to values of k for other experiments. Parameters for $H_2O(T\_1800)\_100a$ (-b): $p_{H_2O} = 1.03$ bar ($p_{H_2O} > 1.02$ bar), argon atmosphere, $p = 1.36$ bar ($p = 1.47$ bar), $Q = 2.02$ l$_N$/min ($Q > 1.92$ l$_N$/min), $d = 4.0$ mm, $H = 20$ mm, $m = 600$ g, MG-Si (UMG-Si) feedstock, $T = 1799$ °C ($T = 1785$ °C), Induction 2 furnace, $d_c = 70$ mm, graphite crucible, $A_c = 36.9$ cm^2.

Experiment	Ak_t [$3.69 \cdot 10^{-3}$ m$^2 \cdot \mu$m/s]	Ak_{eq} [$3.69 \cdot 10^{-3}$ m$^2 \cdot \mu$m/s]	k_t/k_{eq} [%]
$H_2O(T\_1800)\_100a$	6.7 ± 4.4	77.4	8.7 ± 5.7
$H_2O(T\_1800)\_100b$	8.9 ± 3.0	72.1	12.3 ± 4.2

4.3.2 Partial Passivation

0.500 bar and 0.600 bar steam in the feed gas was used in experiments H_2O_50 and -60, respectively, with 1700 °C melt temperature. These experiments developed a silica passivation layer at the melt surface shown in Figure 4.39. The passivation layer formed as a disk roughly centered beneath the lance.

(a) H_2O_50 (b) H_2O_60
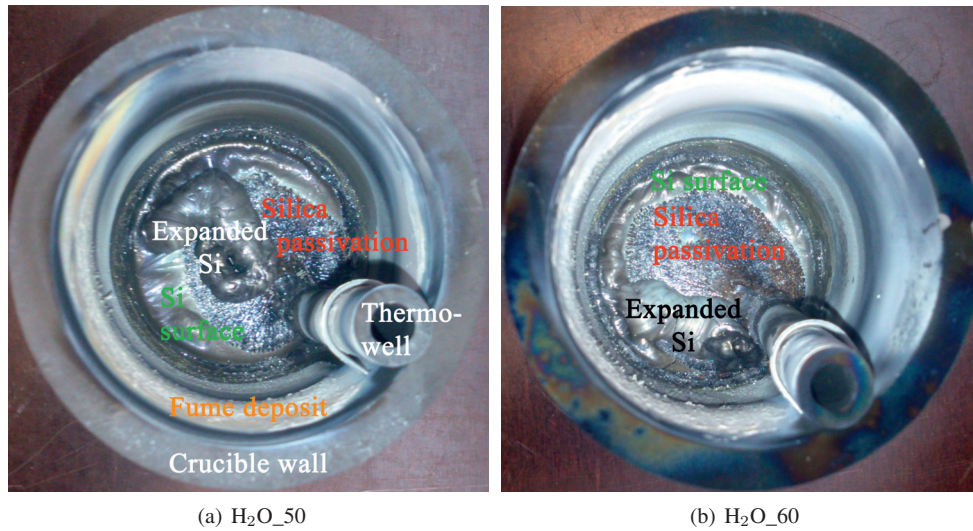
Figure 4.39: Pictures of the partially passivated surface of silicon after experiments H_2O_50-60. For reference, the inner diameter of the crucibles is 70 mm.

Silica passivation developed faster in H_2O_60 with a higher steam content above the passivation threshold than in H_2O_50, and the silica disk almost covered the entire silicon surface after experiment H_2O_60 (Figure 4.39(b)). The melt surface was observed to be clean at the start of the experiment and continuous trend of boron removal in Figures 4.40 and 4.41 reveal that the passivation layer developed gradually during the experiments. The melt surface could not be observed during the experiment because a large amount of fumes blocked vision to the melt surface.
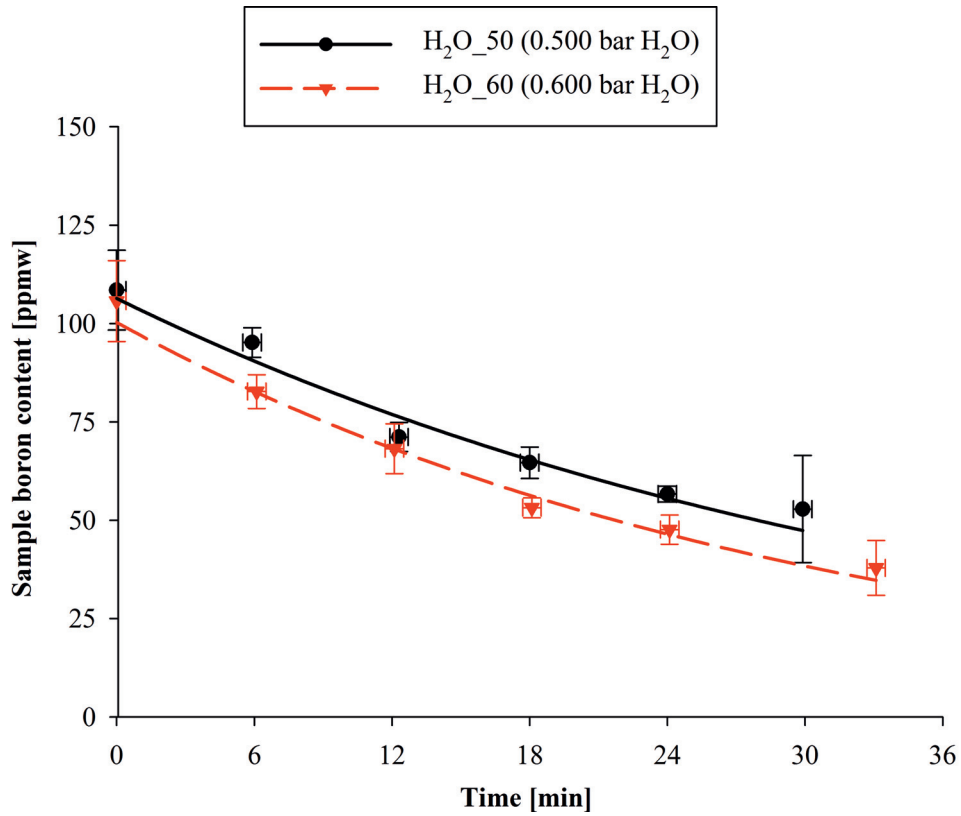
Figure 4.40: Boron content in samples as function of sampling time in experiments H_2O_50-60, with regression (thick curves). Common parameters: argon atmosphere, $p = 1.36$ bar, $Q = 2.00 \, l_N/min$, $d = 4.0$ mm, $H = 20$ mm, $m = 200$ g, EG-Si feedstock, $T = 1700$ °C, Induction 2 furnace, $d_c = 70$ mm, graphite crucible, $A_c = 36.9$ cm^2.

173
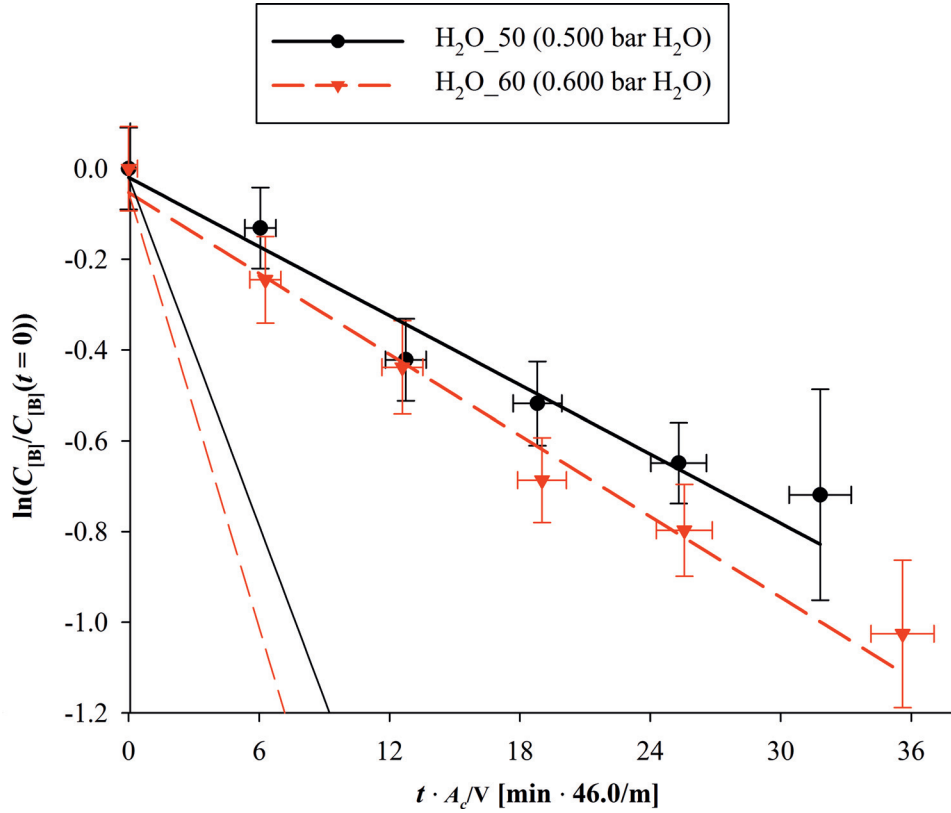
Figure 4.41: Linearized plots for regression of samples (thick lines) for experiments H_2O_50-60, compared to equilibrium modeling (thin lines). Lines have slope $-k$. Common parameters: argon atmosphere, $p = 1.36$ bar, $Q = 2.00$ l_N/min, $d = 4.0$ mm, $H = 20$ mm, $m = 200$ g, EG-Si feedstock, $T = 1700$ °C, Induction 2 furnace, $d_c = 70$ mm, graphite crucible, $A_c = 36.9$ cm^2.

Calculated rate coefficients for experiments H_2O_50-60 are listed in Table 4.16 and compared to H_2O_40 with 0.399 bar steam and no passivation. The rate coefficient of partially passivated experiments does not increase as much from the unpassivated experiment H_2O_40 as predicted by equilibrium modeling for the interface without silica formation, and the gas utilization in experiments H_2O_50-60 is significantly lower than in H_2O_40.

Table 4.16: Rate coefficients and gas utilization for experiments $H_2O\_50\text{-}60$. $A_c = 3.69 \cdot 10^{-3}$ m^2 is factored out in the unit of rate coefficients and listed values are effectively $\frac{A}{A_c}k$ to allow comparisons to values of k for other experiments. Steam partial pressure is given in the name of each experiment ($H_2O\_[\frac{1}{100}$ bar]). Common parameters: argon atmosphere, $p = 1.36$ bar, $Q = 2.00$ l$_N$/min, $d = 4.0$ mm, $H = 20$ mm, $m = 200$ g, EG-Si feedstock (FBR-Si for H_2O_40), $T = 1700$ °C, Induction 2 furnace, $d_c = 70$ mm, graphite crucible, $A_c = 36.9$ cm^2.

Experiment	Ak_t [$3.69 \cdot 10^{-3}$ m$^2 \cdot \mu$m/s]	Ak_{eq} [$3.69 \cdot 10^{-3}$ m$^2 \cdot \mu$m/s]	k_t/k_{eq} [%]
H_2O_40	9.9 ± 1.8	33.4	29.6 ± 5.2
H_2O_50	9.2 ± 2.1	46.3	19.9 ± 4.5
H_2O_60	10.8 ± 2.2	57.9	18.6 ± 3.8

4.4 Silica Passivation Threshold

"Pass" experiments was performed exclusively to estimate the passivation threshold. The partial pressure of steam set in the feed gas was increased by 0.005 bar increments until silica was observed to form on the melt surface at 1500 °C. The threshold for passivation was found to be about twice the saturation pressure of SiO in equilibrium modeling of the gas-melt interface for 2 l$_N$/min total gas flow rate. Table 4.17 lists the partial pressures of steam in the feed gas before and after the incremental increase that started passivation, and compares it to equilibrium modeling for the interface. In experiment Pass_H_2b, passivation started between 0.054-0.056 bar steam in the feed gas at 1503-1506 °C melt temperature and continued until the steam partial pressure gradually reduced to 0.050-0.051 bar at 1498-1501 °C.

Table 4.17: Passivation threshold for the feed steam partial pressure in $2\,l_N/\mathrm{min}$ total gas flow rate in "Pass" experiments at $1500\,°\mathrm{C}$ melt temperature, compared to oxygen saturation for silica formation in equilibrium modeling for the interface. Experimental observations are shown as a range representing the incremental increase in partial pressure of steam for which silica formation was observed after the increase. A clean melt was obtained for the lower value of the range and passivation was observed for the higher value in the range. The atmosphere gas is given in the name of each experiment (Pass_atmosphere). Common parameters: $p = 1.09\text{-}1.36$ bar, $Q = 1.99\text{-}10.2\,l_N/\mathrm{min}$, $d = 4.0$ mm, $H = 20$ mm, $m = 200$ g, high-purity silicon feedstock, Induction 2 furnace, $d_c = 70$ mm, graphite crucible, $A_c = 36.9\ \mathrm{cm}^2$.

Experiments	p_{H_2O} [bar] Clean-Passivated	p_{SiO}^{sat} [bar] Saturation	p_{SiO}^{sat}/p_{H_2O} [bar] Clean-Passivated
Pass_Ar	0.060-0.065	0.027	0.45-0.42
Pass_Ar,H$_2$	0.067-0.068	0.027	0.40-0.40
Pass_H$_2$a	0.060-0.065	0.027	0.45-0.42
Pass_H$_2$b	0.050-0.056	0.027	0.54-0.49

Directly above the passivation threshold, small (< 1 mm) particles formed on the surface directly beneath the lance and floated in a spinning motion to the edge of the crucible in the Induction 2 furnace, as they agglomerated/sintered into larger flakes (depicted in Figure 4.42). The formation of silica particles under the lance appeared to form instantly after increasing the steam partial pressure. There were no significant incubation time, and the onset of passivation appeared to be a local phenomenon directly below the lance, where the steam was initially supplied to the interface. It is however possible that the melt already was very close to saturation since the steam partial pressure was increased gradually before passivation was observed, and that the whole of the melt was saturated quickly after the passivation threshold was surpassed. However there would presumably be an observable delay (more than several seconds) related to surpassing saturation for the entire melt, and silica was only observed to form locally under the lance.

This slow silica formation under the lance was maintained for 1 h without observable accumulation of silica along the crucible wall. Millimeters of the surface closest to the crucible wall in the direction that the flakes moved was however in the shadow of the crucible wall above and could not be observed. It is possible that the silica was dissolved into the melt in an initial stage of passivation, although 1 h without accumulation may be judged to be longer than what would be necessary to reach oxygen saturation in the entire melt, even for the slow formation of silica represented by the small particles formed.
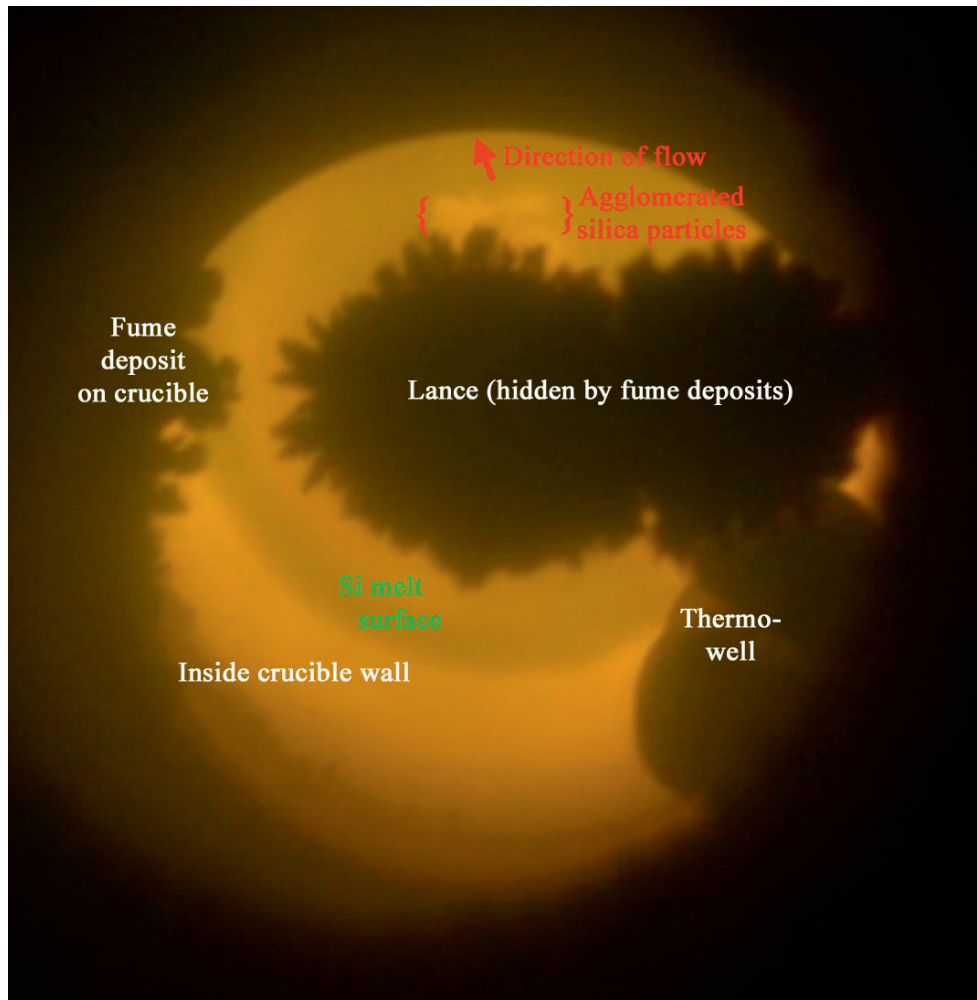
Figure 4.42: Agglomerate of silica particles formed on the melt surface beneath the lance directly above the threshold for passivation in Pass_Ar,H$_2$. For reference, the inner crucible diameter is 70 mm.

4.4.1 Reactive Gases

Changing between argon and hydrogen atmosphere had no influence on the passivation threshold in experiments with $2 \, l_N/min$ total gas flow rate in Table 4.17 and the equilibrium model. This supports the assumption that passivation is governed from Equation (4.2) after decomposition of steam and that hydrogen does not significantly change the saturation threshold for oxygen at the melt interface.

$$H_2O + [Si] \rightarrow SiO + H_2 \tag{4.1}$$
$$2\,SiO \rightleftarrows SiO_2 \text{ (s/l)} + [Si] \tag{4.2}$$

Presumably, silica passivation may also form from CO as it decomposes on the melt surface. The passivation threshold for silica formation was however not reached in experiments, among which CO_4.8 used the highest CO content of $0.048 \, bar$ in argon. CO instead forms SiC passivation as shown in Section 4.5.3.

4.4.2 Gas Flow Rate

When the total gas flow rate was increased, also the feed partial pressure of steam in argon could be increased until passivation was observed again (Table 4.18). The increased passivation threshold in the feed gas is suggested to be due to diffusion resistance in argon at $10 \, l_N/min$ total gas flow rate. Diffusion resistance may lower the fraction of steam in the gas feed that is supplied to the interface and a higher partial pressure of steam can be set in the feed gas at the passivation threshold for steam supply to the interface. This trend is opposite to that observed by Altenberend [18], which found the passivation threshold for oxygen in the feed to decrease with increasing gas flow rate as shown in Table 2.8. In experiment Pass_H$_2$b with hydrogen atmosphere, an increase of 2-$4 \, l_N/min$ total gas flow rate caused immediate passivation for $0.049 \, bar$ steam in the feed gas, which was close below the passivation threshold for $2 \, l_N/min$ total gas flow rate onto a $1500 \, °C$ melt.

Observing the passivation threshold was practically challenging at high gas flow rates like $10 \, l_N/min$ due to the large amounts of fumes formed. Large fume deposits built up on the crucible wall and lance and could fall down onto the melt and cause silica surface coverage without passivation. The fumes also impaired vision to the melt surface at the higher gas flow rate.

Table 4.18: Passivation threshold for the feed steam partial pressure in "Pass" at $1500\,°C$ melt temperature with argon and hydrogen atmospheres at different total gas flow rates. A clean melt was obtained for the lower value of the range and passivation was observed for the higher value in the range of an incremental increase in steam partial pressure. The passivation threshold increased in argon at increased total gas flow rate, but reduced in hydrogen. Common parameters: $p = 1.09\text{-}1.36\,\mathrm{bar}$, $d = 4.0\,\mathrm{mm}$, $H = 20\,\mathrm{mm}$, $m = 200\,\mathrm{g}$, high-purity silicon feedstock, $T = 1500\,°C$, Induction 2 furnace, $d_c = 70\,\mathrm{mm}$, graphite crucible, $A_c = 36.9\,\mathrm{cm^2}$.

Atmosphere Gas flow rate	Argon Experiments	p_{H_2O} [bar] Clean-Passivated	Hydrogen Experiments	p_{H_2O} [bar] Clean-Passivated
$2.01\,\mathrm{l_N/min}$	Pass_Ar,H$_2$	0.067-0.068	Pass_H$_2$a	0.060-0.065
$2.00\,\mathrm{l_N/min}$	Pass_Ar	0.060-0.065	Pass_H$_2$b	0.050-0.056
$4.00\,\mathrm{l_N/min}$	Pass_H$_2$b		Pass_H$_2$b	-0.049
$10.2\,\mathrm{l_N/min}$	Pass_Ar,H$_2$	0.093-0.097	Pass_Ar,H$_2$	-0.065

4.4.3 Temperature

The threshold for passivation increases strongly with temperature according to observations in Table 4.19. The passivation threshold in feed gas appears to follow the trend of the SiO saturation pressure with a constant ratio near 2 for the experiments at $2\,\mathrm{l_N/min}$ total gas flow rate. At $1700\,°C$, passivation was observed to occur between $0.399\,\mathrm{bar}$ in H$_2$O_40, which was not passivated and $0.500\,\mathrm{bar}$ steam in H$_2$O_50, where a characteristic passivation layer developed. It is assumed that the surface coverage is not caused by passivation in experiment H$_2$O(T_1800)_100a, with $1.03\,\mathrm{bar}$ steam at $1799 \pm 4\,°C$ melt temperature, as it could not be observed to start at the beginning of gas blowing. No experiment around $1800\,°C$ provided a reliable estimate for the steam partial pressure at passivation.

Table 4.19: Passivation threshold for the feed steam partial pressure in argon at $2 \, \mathrm{l_N/min}$ total gas flow rate, compared to oxygen saturation for silica formation in equilibrium modeling for the interface. A clean melt was obtained for the lower value of the range and passivation was observed for the higher value in the range. The passivation threshold in feed gas follows the SiO saturation pressure at a seemingly constant ratio near 2. Common parameters: $p = 1.09\text{-}1.36$ bar, $d = 4.0$ mm, $H = 20$ mm, $m = 200$ g, high-purity silicon feedstock (MG-Si in $H_2O(T\_1800)\_100a$), Induction 2 furnace, $d_c = 70$ mm, graphite crucible, $A_c = 36.9 \, \mathrm{cm^2}$.

T [°C] Clean-Passivated	Experiments	p_{H_2O} [bar] Clean-Passivated	p_{SiO}^{sat} [bar] Saturation	p_{SiO}^{sat}/p_{H_2O} [bar] Clean-Passivated
1500-1496	Pass_Ar	0.060-0.065	0.027-0.026	0.45-0.40
1501-1502	Pass_Ar,H$_2$	0.067-0.068	0.028-0.028	0.41-0.41
1703-1700	H$_2$O_40-50	0.399-0.500	0.237-0.231	0.59-0.46
1799-	H$_2$O(T_1800)_100a	1.03-	0.561-	0.54-

4.4.4 Crucible Material

The passivation threshold for different crucible materials was not directly compared, but experiments in the quartz crucibles seemed to show an increased tendency for passivation. For instance, at 0.045 bar steam in the gas feed at $1 \, \mathrm{l_N/min}$ in the Resistance furnace, passivation did not occur in a graphite crucible in experiment $H_2O/CO\_4.5/0$, but did in a quartz crucible in Crucible_Quartz, as shown in Figure 4.43.

Expansion of silicon during solidification caused some of the melt to flow out over the initially solidified surface as shown under the label "Expanded Si" in Figure 4.43(b), and only part of the original surface was visible after experiments. The part of the crucible with expanded silicon over the original surface is not included in the part of the crucible depicted in Figure 4.43(a). Expansion of silicon also frequently caused cracks in the crucible and the solidified melt after experiments. The missing piece of the surface in Figure 4.43(a) cracked completely loose. The silica crucible, spray-coated with silicon nitride, cracked into small pieces around the solidified melt and most of it was removed in Figure 4.43(b).

The crucible dissolves slightly and supplies additional oxygen to the melt, which can reduce the threshold supply of oxygen from the gas at which the melt becomes saturated at the interface and silica may form. Dissolution of silica is significantly slower than formation of SiO at the gas-melt interface, as the oxygen content in the melt may be maintained below the saturation limit during gas blowing.

(a) H$_2$O/CO_4.5/0   (b) Crucible_Quartz
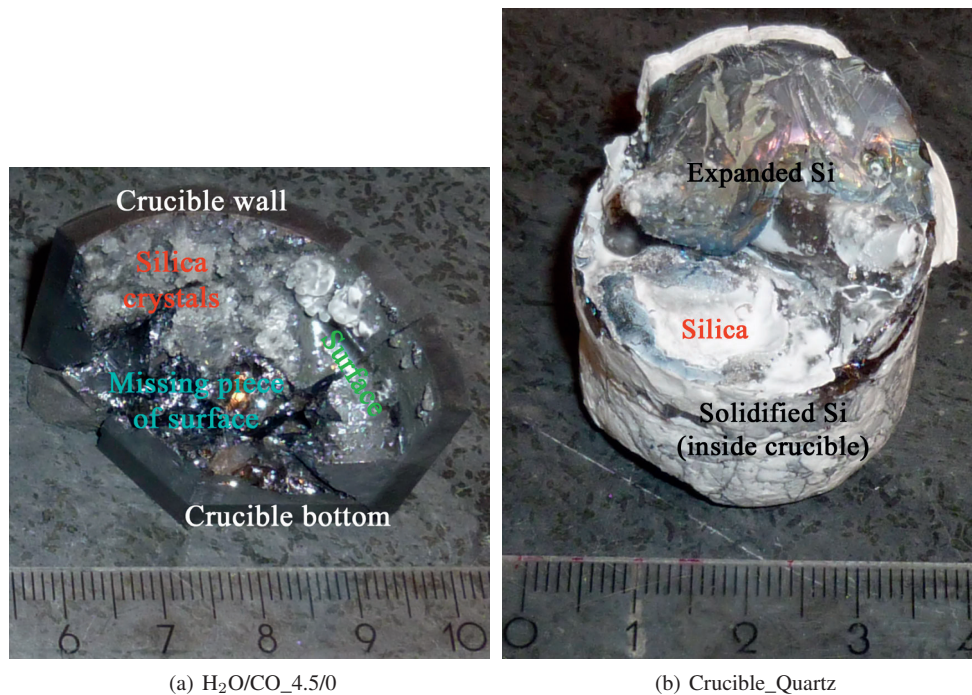
Figure 4.43: Angled pictures of silicon in graphite (a) and quartz (b) crucibles after experiments. $0.045\,\mathrm{bar}$ steam in $1\,\mathrm{l_N/min}$ total gas flow rate did not passivate the surface in a graphite crucible (left side in (a)), while a silica layer formed in a quartz crucible (b). Transparent silica crystals in the graphite crucible extend up above the silicon surface and also formed on the crucible wall, so they are not considered to be formed by passivation. The ruler measures centimeters.

4.4.5 Melt Purity

Although a direct comparison of the passivation threshold was not performed for the different silicon qualities, no obvious difference for the passivation threshold was noticed. Initial surface coverage developed as MG, UMG and FBR silicon melted in argon, presumably because of excessive oxygen inherent in surface oxides or grain boundary phases. Although FBR-Si has high purity (5-6N), the particles were an order of magnitude smaller compared to EG-Si pieces. FBR-Si could thus contain a correspondingly larger amount of silica on the surface compared to EG-Si, which did not segregate silica to the surface upon melting. After minutes of evaporation of the initial surface coverage around $1700\,^\circ\mathrm{C}$ (or higher) in inert gas, no further difference was noticed regarding passivation under gas blowing.

181

4.5 Byproducts Characterization

Byproducts of silica fume formed in all experiments as a result of active oxidation of the silicon melt. The silica fume is known to be a valuable byproduct that is currently being sold as a byproduct of metallurgical silicon production. Silica also formed transparent or white layers along the surface in cases of passive oxidation, or islands rising above the surface from dust deposits falling onto the silicon surface. Figure 4.44 identifies silicon, silica and SiC particles at the surface of experiment $H_2O/CO\_2.2/2.4$. Faceted particles of SiC with lengths up to the order of ten micrometers also formed from graphite crucibles and CO. Silica form larger irregular shapes with rounded edges on the melt surface, as it is soft and may sinter at $1500\,°C$. The phases can be recognized in BSE images by their morphology, as demonstrated in Figure 4.44(b). The sample is the cross-section opposite of the marked face in Figure 4.50 and the WDS- and BSE images are taken at the position of the arrowhead. Surfaces with SiC particles may be recognized in pictures as non-shiny with gray, brown or green coloration.

(a) WDS   (b) BSE
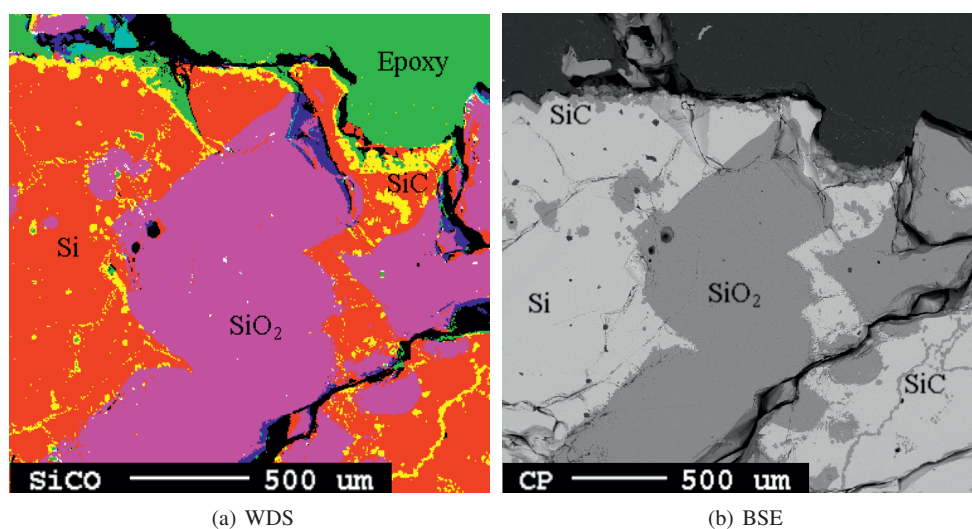
Figure 4.44: Identification of phases in WDS map and BSE image after experiment $H_2O/CO\_2.2/2.4$. Color intensities in the WDS map (a) of red, green and blue correlate to silicon, carbon and oxygen signals, respectively. Figure 4.50 shows the position of the surface where the images were acquired.

4.5.1 Silica Fumes and MG-Si Impurities

Fume deposits were collected from the furnace chamber, the crucible and the lance after experiment $Q(\text{Ind\_1})\_3$ and the samples in Figure 4.45 were analyzed by SEM imaging. The fume is typically white to brown dust of silica particles, like the deposit collected from the furnace chamber in Figure 4.45. An agglomerate of the dust collected from the furnace chamber after H_2O_35 is shown in SEM images in Figure 4.46 to consist of sub-micron particles like the fume identified from active silicon oxidation by Næss [55].

Deposits on the crucible and lance are subject to high temperature during the experiment and the particles are ripened to larger sizes (Figure 4.47(b)) and partly sintered to dense structures (Figure 4.47(a)). The morphology of the partly transparent (Figure 4.47(a)-(b)) and the white deposit (Figure 4.47(c)) in Figure 4.45 is similar.
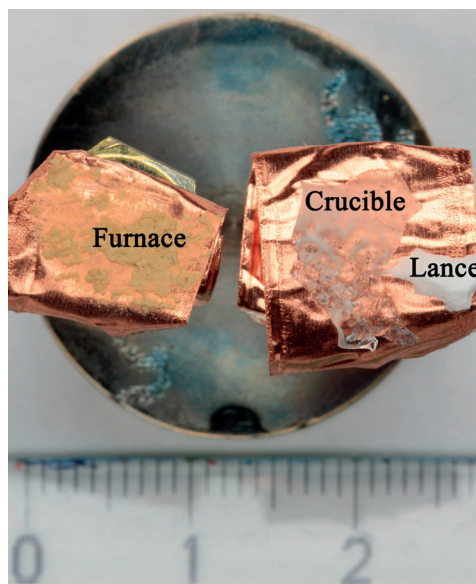
Figure 4.45: Picture of different fume deposits collected from the lance, crucible and furnace chamber after experiment $Q(\text{Ind\_1})\_3$, prepared for SEM imaging. The ruler measures centimeters.
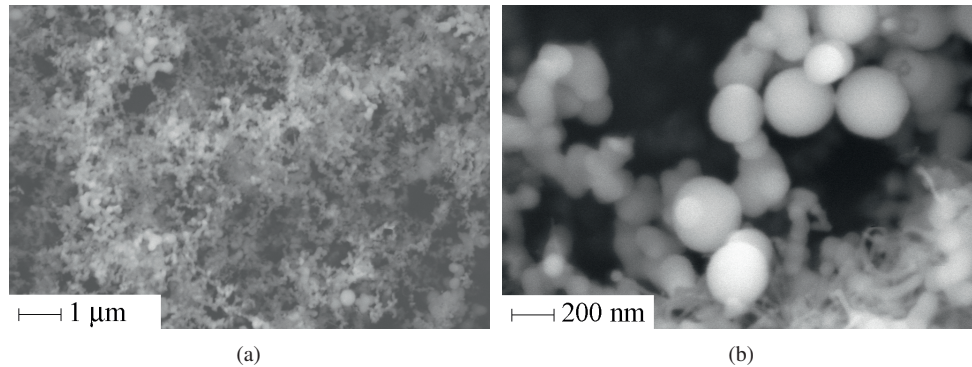
Figure 4.46: SEM images of fume agglomerate from furnace chamber after experiment H$_2$O_35, similar to the dust in Figure 4.45.

A sample of fume deposit from the crucible after experiment H$_2$O(T_1800)_100a with MG-Si was analyzed by ICP-MS. Elements of significant contents are included in Table 4.20, in which U represents uncertainty at approximately 95% confidence level. The high boron content in the fume indicates that at least part of HBO oxidizes further in the gas phase to B$_2$O$_3$ in the fume. According to equilibrium modeling, B$_2$O$_3$ may precipitate upon cooling of HBO and SiO gas below $430\ ^\circ$C. The presence of Al, Mn, Fe, Ni and Zn reveal that also these elements evaporates or reacts with oxygen and/or hydrogen to volatile gases at gas-melt interface and further condenses in the fume.

Impurities in the initial and final samples of the MG-Si melt in experiment H$_2$O(T_1800)_100a were analyzed and listed in Tables 4.21 and 4.22, respectively. Only B, Zn and Sr show a clear trend of removal during the experiment. 75% of boron, 43% of zinc and 11% of strontium in the initial sample remained in the final sample at 34.5 min. analyzes of the copper content fluctuated between samples as it was completely removed in the third sample at 12 min, but increased again to 6.2 ppmw in the next sample, so the reduction from the first sample (Table 4.21) to the fifth sample (Table 4.22) does not reliably indicate copper removal. Phosphorous was not significantly removed in the process. Dal Martello [115] found however 24% of phosphorous to volatilize during heating of quartz in a reducing atmosphere.

184
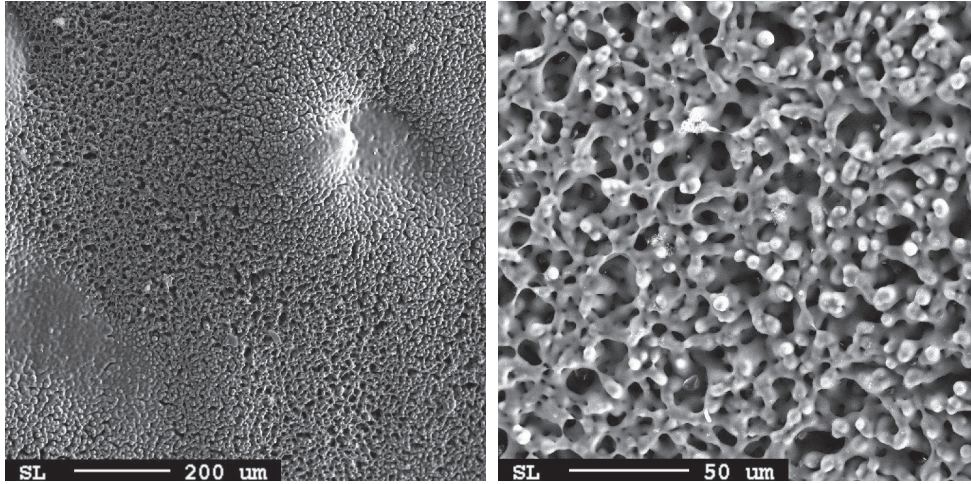
(a) Crucible deposit

(b) Crucible deposit
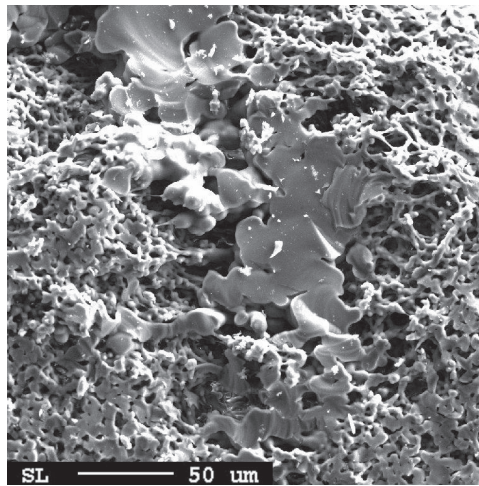
(c) Lance deposit

Figure 4.47: SEM images of fume deposits from crucible and lance after experiment $Q(\text{Ind\_1})\_3$, depicted as partly transparent (a)-(b) and white (c) deposits in Figure 4.45.

Table 4.20: ICP-MS analysis of impurity contents (with uncertainty U) in fume deposit after H$_2$O(T_1800)_100a with MG-Si. Elements P, Ti, V, Cr, Co, Cu, Sr, Mo, Zr, Y, W, Pb and U were analyzed to less than 1 ppmw and are not included.

Element	B	Al	Mn	Fe	Ni	Zn
Content [ppmw]	1005	916	4.13	22.7	13.86	47.1
U [ppmw]	53	41	0.48	2.2	0.95	2.4

Table 4.21: ICP-MS analysis of impurity contents (with uncertainty U) in MG-Si melt in initial sample of experiment H$_2$O(T_1800)_100a. Elements Y, Pb and U were analyzed to less than 0.5 ppmw and are not included.

Element	B	Zr	W	Al	P	Ti	V	Cr
Content [ppmw]	71.5	10.80	1.565	1216	13.41	201	11.92	7.64
U [ppmw]	4.5	0.52	0.082	59	0.69	17	0.71	0.56
Element	Mn	Fe	Co	Ni	Cu	Zn	Sr	Mo
Content [ppmw]	35.3	2757	1.645	8.17	5.37	16.9	0.605	1.52
U [ppmw]	3.6	139	0.083	0.50	0.27	1.4	0.069	0.14

Table 4.22: ICP-MS analysis of impurity contents (with uncertainty U) in MG-Si melt in final sample of experiment H$_2$O(T_1800)_100a. Elements Y, Pb and U were analyzed to less than 0.5 ppmw and are not included.

Element	B	Zr	W	Al	P	Ti	V	Cr
Content [ppmw]	57.4	10.37	1.75	1013	13.10	204	12.2	7.95
U [ppmw]	3.9	0.74	0.13	101	0.94	20	1.7	0.73
Element	Mn	Fe	Co	Ni	Cu	Zn	Sr	Mo
Content [ppmw]	34.8	2747	1.62	9.0	2.06	7.8	0.072	1.56
U [ppmw]	2.4	301	0.16	1.8	0.19	0.9	0.010	0.28

4.5.2 Silica Passivation Layer

Silica passivation in experiment Crucible_Quartz was found to form essentially continuous layers of silica as shown in the BSE image in Figure 4.48. The silica layer effectively blocks contact between the gas and silicon melt and is detrimental to boron removal.
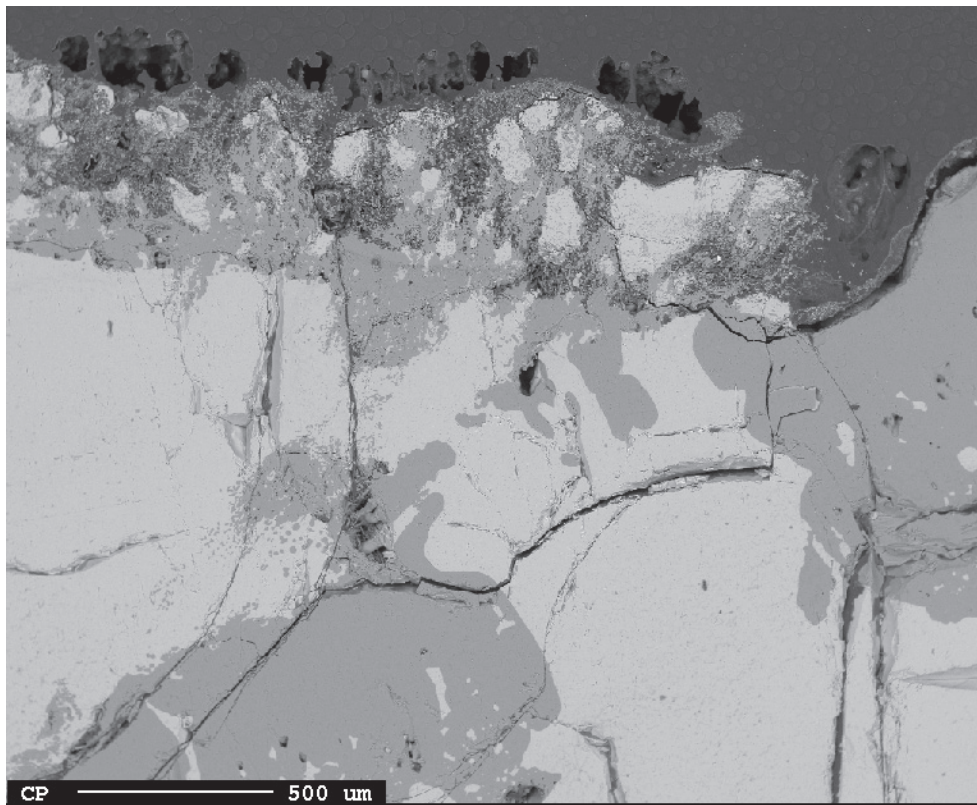
Figure 4.48: Morphology of silica on the silicon surface after Crucible_Quartz. An essentially continuous passivation layer of silica covers silicon. Also, fumes has fallen onto the surface and made an open structure of agglomerated/sintered particles above the surface.

4.5.3 SiC Particles

Decomposition of CO formed SiC particles on the melt surface. The morphology of SiC particles at the surface is magnified in Figure 4.49. SiC formed in all experiments with CO or with a graphite crucible. A graphite ring was positioned on top of the quartz crucible in experiment Q(Res)_0.14, and with $0.14\,\mathrm{l_N/min}$ total gas flow rate, back-diffusion of CO from oxidation of the graphite ring caused SiC particles on the silicon surface. The SiC particles at the surface represent local passivation. A reason why use of CO was discontinued is that an active mode of carbonation of silicon could not be achieved. This is because silicon and carbon does not form a sufficiently volatile gas, like SiO allows active oxidation of silicon. Although SiC particles are considered to be removed to the crucible wall by induction [60] and a clean surface may be maintained, use of CO results in excessive SiC formation which is conveniently avoided by using steam or other reactive gases without carbon. To avoid risks of additional byproduct phases on the melt surface or unnecessary contamination of the melt, the reactive gas is recommended to only contain the elements that react with boron, like oxygen and hydrogen for HBO formation.

Surface coverage by SiC particles is not considered to be as detrimental for boron removal as silica surface coverage, since boron was removed in experiment H_2O/CO_2.2/2.4 even though the entire surface appear to have been covered by SiC particles as seen from the non-shiny surface in Figure 4.50. The silicon carbide particles are not sintered into continuous layers like silica, and they may move with the flow of the melt so that clean silicon can be temporarily and locally exposed to the gas between the particles.

Although part of the SiC particles were entrained and settled mainly to the bottom of the crucible, most appear to remain on the gas-silicon interface in experiments in the Resistance furnace. Entrained particles had settled completely after experiments in the Resistance furnace as vertical scans across the entire silicon cross-section did not reveal SiC particles in the bulk of any sample. Boron removal is mainly affected by SiC passivation by particles at the gas-silicon interface.

An increasing content of CO in the reactive gas provide increasing SiC surface coverage as depicted in Figures 4.51-4.53 and shown in cross-section BSE images at the surface in Figure 4.54. The BSE images tend to indicate more extensive surface coverage of SiC particles than the overview photographs in Figures 4.51 and 4.52. The SiC surface layer after experiment CO_4.8 with $0.048\,\mathrm{bar}$ CO as the reactive gas shown in Figure 4.53 was thick enough to be visible by the naked eye and covered the entire original melt surface. With this extensive SiC formation at the surface, a dense and continuous layer covers the surface in Figure 4.54(c) rather than adjacent, separate particles in Figures 4.54(a)-(b) with 0.001 and $0.011\,\mathrm{bar}$ CO in argon.

188
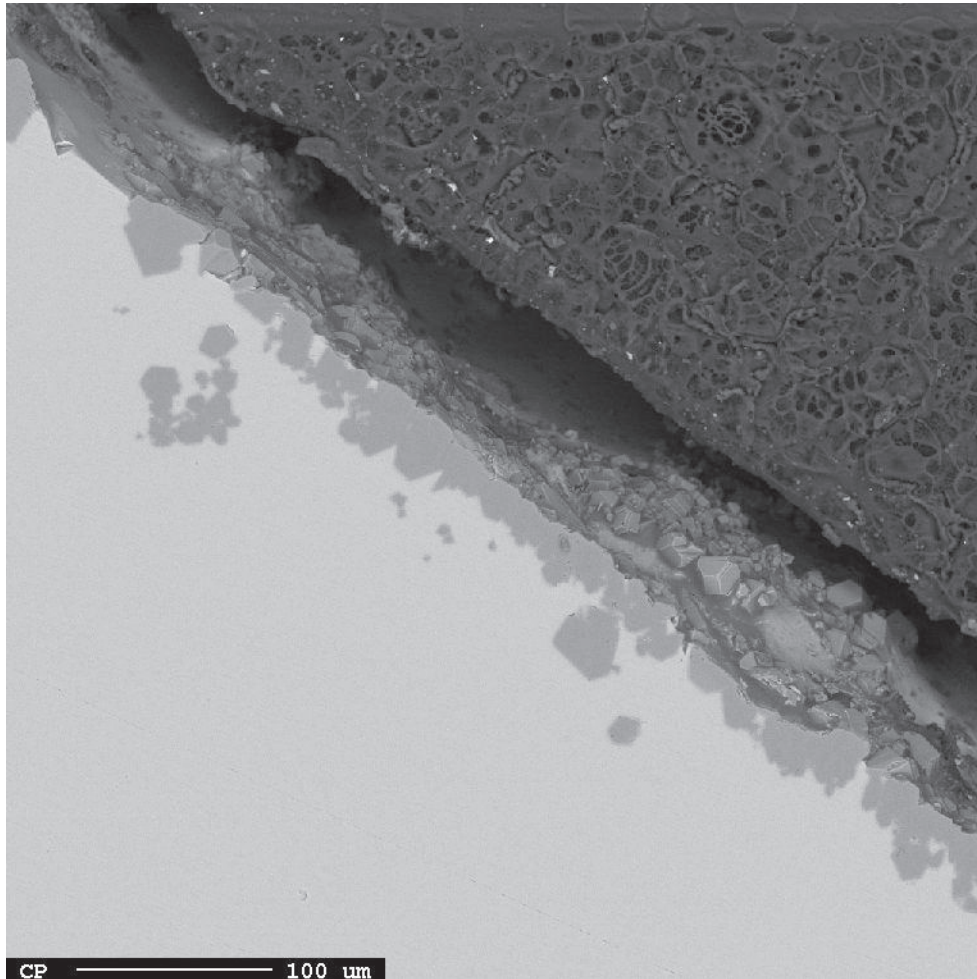
Figure 4.49: Morphology of SiC particles on the silicon surface after experiment CO_0.1 in BSE image at 200 times magnification. The black area is a gap between the silicon surface and epoxy above.

189

Figure 4.50: Overview photo of the crucible after experiment $H_2O/CO\_2.2/2.4$ with $0.022\,\mathrm{bar}$ steam and $0.024\,\mathrm{bar}$ CO. The opposite face to the half cross-section marked by the U-shape is used for microprobe analyzes, and Figures 4.44(a) and 4.44(b) are taken near the arrowhead. A piece of the surface is missing at 3-4 cm on the ruler.

Figure 4.51: Overview photo of the crucible after experiment CO_0.1 with $0.001\,\mathrm{bar}$ CO in argon. The opposite face to the half cross-section marked by the U-shape is used for microprobe analyzes, and the BSE images in Figures 4.54(a) and 4.49 are taken near the arrowhead.
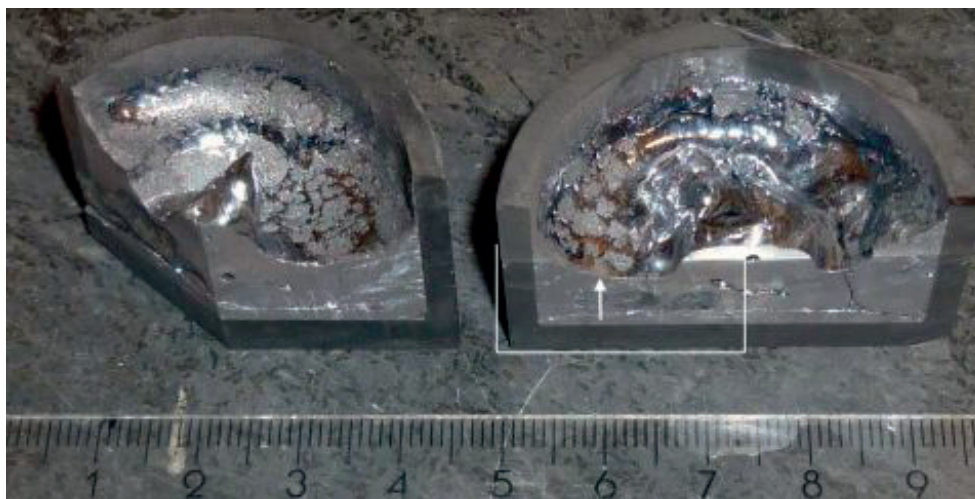
Figure 4.52: Overview photo of the crucible after experiment CO_1.1 with $0.011\,\mathrm{bar}$ CO in argon. The opposite face to the half cross-section marked by the U-shape is used for microprobe analyzes, and the BSE image in Figure 4.54(b) is taken near the arrowhead. The ruler measures centimeters.

Figure 4.53: Overview photo of the crucible after experiment CO_4.8 with $0.048\,\mathrm{bar}$ CO in argon. The opposite face to the half cross-section marked by the U-shape is used for microprobe analyzes, and the BSE images in Figure 4.54(c) is taken near the arrowhead. The ruler measures centimeters.
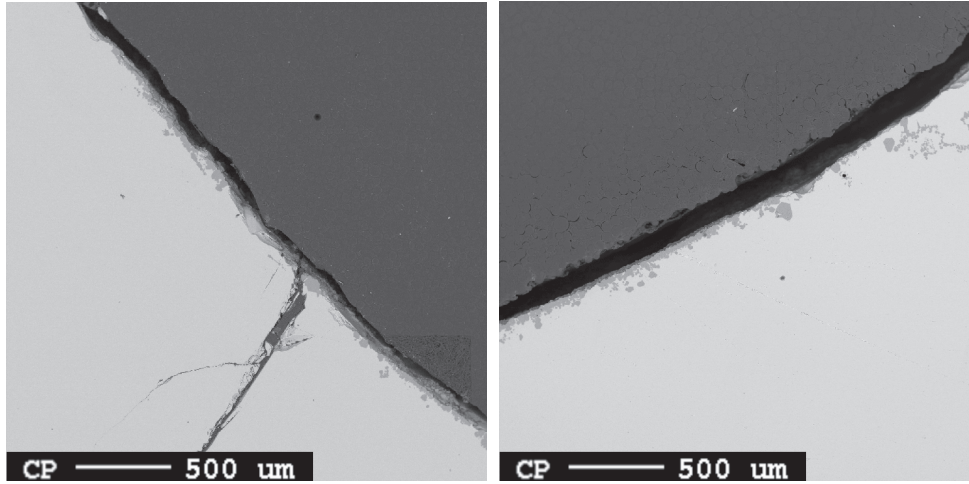
(a) CO_0.1: 0.001 bar CO

(b) CO_1.1: 0.011 bar CO
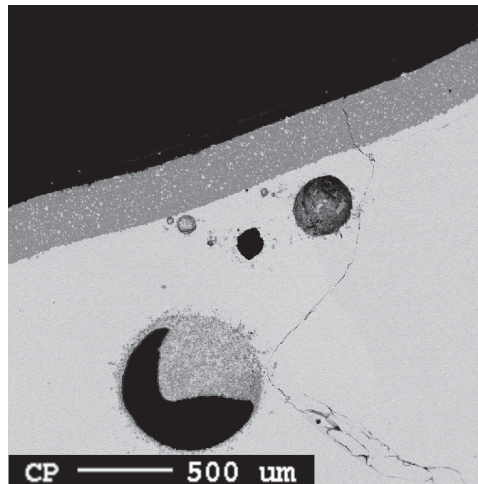
(c) CO_4.8: 0.048 bar CO

Figure 4.54: Cross-section BSE images at surface after experiments with increasing CO content. Common parameters: argon atmosphere, $p = 1.00$ bar, $Q = 2.00$ l_N/min, $d = 2\text{-}4$ mm, $H = 10$ mm, $m = 40$ g, EG-Si feedstock, $T = 1500$ °C, Resistance furnace, $d_c = 38$ mm, graphite crucible, $A_c = 11.3$ cm^2.

Chapter 5

Discussion

Equilibrium modeling for the interface introduced in Section 2.1 provide the dominant gas species and their relationship in Reactions (5.1) and (5.2).

$$H_2O + [Si] \rightleftharpoons SiO + H_2 \tag{5.1}$$

$$[B] + SiO + \tfrac{1}{2} H_2 \rightleftharpoons HBO + [Si] \tag{5.2}$$

Studies of silicon oxidation (Sections 2.3.6 and 2.3.7) use equilibrium conditions at the interface, for which modeling shows that the silicon melt reduces steam essentially stoichiometrically. Section 5.1 accordingly uses equilibrium modeling to estimate the fraction of steam in the gas feed that is supplied to the interface based on weightloss measurements representing SiO formation. A maximum steam supply fraction of 50% is explained by complete fuming in Reaction (5.3) in the gas phase.

$$H_2O + SiO \rightleftharpoons SiO_2 \text{ (l/s)} + H_2 \tag{5.3}$$
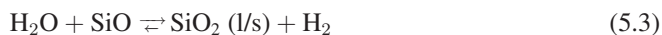
Næss [55] found that the rate of oxidation of liquid silicon is determined by the supply of oxygen in gas-blowing experiments similar to the present setup. The rate of boron removal is in Section 5.2 found to follow the rate of silicon oxidation at a constant fraction determined by equilibrium conditions of Reaction (5.2). Accordingly, the rate of boron removal is not determined by kinetics or mass transfer of boron itself, and supply of the steam as the oxidizing agent is rate determining for boron removal and silicon oxidation alike. The combination of gas-phase mass transfer of steam and equilibrium modeling for the interface provides reasonable agreement to experimental observations of the maximum steam partial pressures that can be used without passivating the melt in Section 5.3. The passivation threshold for steam supply to the interface correspond to oxygen saturation for silica formation according to Equation (5.4) as $p_{H_2O}^s(\max) \approx p_{SiO}^{sat}$.

$$2\,\text{SiO} = [\text{Si}] + \text{SiO}_2\ (\text{s/l}) \tag{5.4}$$

Also the dependence of boron removal on different experimental parameters in Section 5.4 may be explained by the combination of gas-phase mass transfer of steam and equilibrium modeling for the interface. By using equilibrium expressions for Reactions (5.1) and (5.2) at the interface and the steam supply fraction, accounting for Reaction (5.3) and mass transfer in the gas, Section 5.5 presents an analytical expression for the total mass transfer coefficient for boron removal.

5.1 Steam Supply Fraction

Experiments in which the weightloss could be fully accounted for in Section 4.2 are used to estimate the fraction of steam supplied to the interface equilibrium, that is how much of the total oxygen in the feed gas that produces SiO gas. By inserting the feed gas flow and its steam partial pressure for an experiment into the equilibrium model, the weightloss of silicon calculated over the time of steam blowing in the experiment assumes that all of the steam in the feed is supplied to the interface equilibrium. The steam supply fraction is calculated as the ratio of the weightloss in experiments to this weightloss modeled for 100% supply of steam from the feed gas to the interface ($\frac{p_{\text{H}_2\text{O}}^{\text{s}}}{p_{\text{H}_2\text{O}}} = \frac{-\Delta m}{-\Delta m_{eq}}$). The steam supply fractions is shown for representative experiments with varying gas flow rates in Figure 5.1. At $2\,\text{l}_\text{N}/\text{min}$, 50% steam supply agrees with complete consumption of SiO by fuming Reaction (5.3) and complete depletion of steam by diffusion along the wall jet. There is a trend of decreasing steam supply fraction with higher gas flow rates, which indicate a loss of steam, as the rate of steam diffusing to the interface in the flow along the wall jet does not keep up with the rate of steam feeding at increased gas flow rates and part of the steam remains in the gas as the wall jet is deflected away from the surface by the crucible wall. The diffusion resistance increases with increasing gas flow rates as a larger fraction of steam remains unreacted after deflection by the crucible wall.

The fuming Reaction (5.3) is assumed to consume all SiO into silica fume so that the maximum reliable steam supply fraction is assumed to be 50%, and the "H$_2$O" series in Figure 5.2 is not considered to provide representative steam supply fractions. For steam supply fractions higher than 50%, there would not be enough steam to consume all SiO. Remains of SiO would condense according to Reaction (5.4) in the gas leaving the melt as it cools down, but no such condensate could be noticed and only silica was identified in the fumes. Furthermore, the rate of reactions for fuming are expected to increase with temperature and thus decrease the tendency for SiO to diffuse past steam without reacting, so that the steam supply fraction would not be expected to increase from $1500\,^\circ\text{C}$ in experiments with $2\,\text{l}_\text{N}/\text{min}$ in Figure 5.1 to $1700\,^\circ\text{C}$ in experiments in Figure 5.2. Higher steam supply fractions could also indicate

that the weightloss measured for the crucible assembly is larger than the weightloss of the silicon melt, for instance if oxidation of graphite in the crucible becomes significant. Accordingly, the steam supply fractions calculated for "H_2O" experiments at 1700 °C in Figure 5.2 are considered as outlayers, and also $H(d\_35)$, H_10a-b in Figure 5.1. Experiments Q_4 at $4\ l_N/\mathrm{min}$ and Q_8a-b at $8\ l_N/\mathrm{min}$ in Figure 5.1 are considered to be outliers due to a too low weightloss measurement, because the steam supply fraction is too low for equilibrium modeling using the estimated steam supply to the interface (Section 5.2) to achieve as high boron removal rates as in the experiments, and the fraction of HBO in the gas leaving the melt system in experiments is not expected to surpass the equilibrium limit.
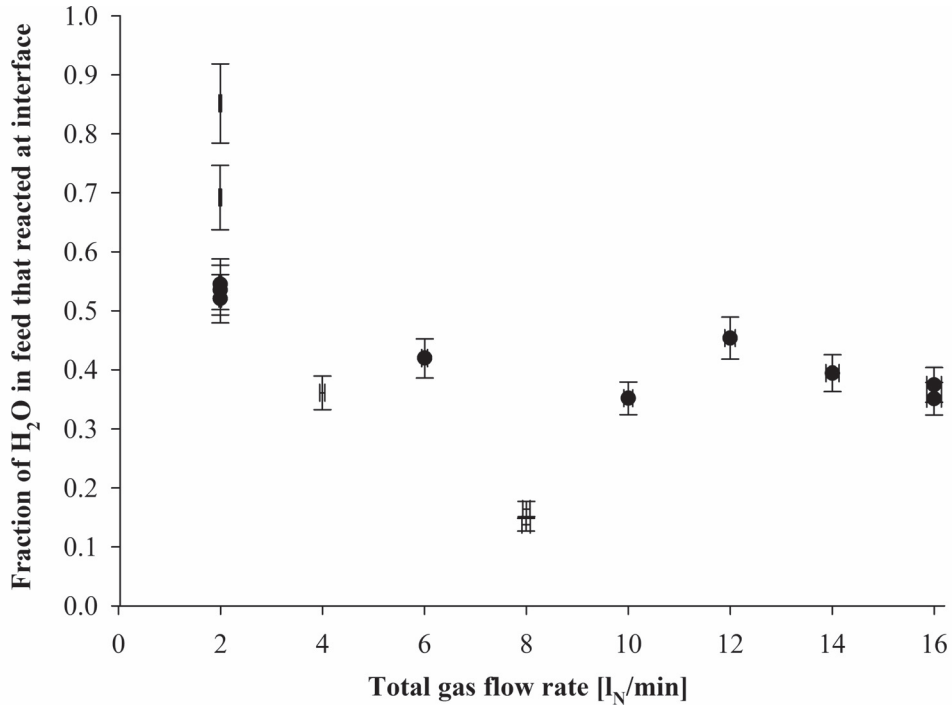
Figure 5.1: Steam supply fraction ($\frac{p^s_{H_2O}}{p_{H_2O}}$) as function of total gas flow rate in "Q" experiments together with H_10-30 and "$H(d\_35)$" at $2\ l_N/\mathrm{min}$, all with optimal lance heights and fully accounted weightloss. Experiments without symbols are considered outlayers. 50% steam supply is considered maximum due to fuming Reaction (5.46) and is achieved at $2\ l_N/\mathrm{min}$. The decreasing trend indicates additional loss by diffusion resistance at higher gas flow rates. Common parameters: $p_{H_2O} = 0.032$ bar, hydrogen atmosphere, $p = 1.12$ bar, $d = 4.0$ mm ($d = 35.0$ mm for "$H(d\_35)$"), $H = 5$-30 mm, $m = 200$ g, EG-Si feedstock, $T = 1500$ °C, Induction 2 furnace, $d_c = 70$ mm, graphite crucible, $A_c = 36.9$ cm².
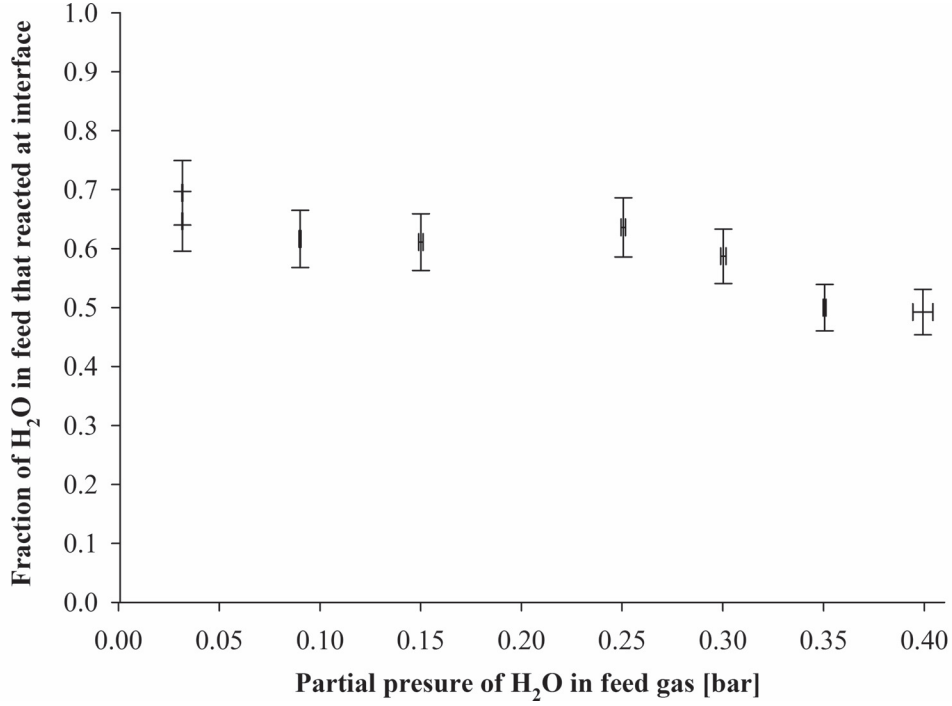
Figure 5.2: Steam supply fraction ($\frac{p_{H_2O}^s}{p_{H_2O}}$) as function of partial pressure of steam set in the feed gas (p_{H_2O}) in "H_2O" experiments without passivation. 50% steam supply is considered maximum due to Reaction (5.46) as silica fumes were observed, but no SiO condensate, so the weightloss measurements are not considered representative for silicon oxidation. Common parameters: argon atmosphere, $p = 1.36$ bar, $Q = 2.00$ l_N/min, $d = 4.0$ mm, $H = 20$ mm, $m = 200$ g, high-purity silicon feedstock, $T = 1700$ °C, Induction 2 furnace, $d_c = 70$ mm, graphite crucible, $A_c = 36.9$ cm^2.

5.2 Boron Equilibrium Fraction

This section compares boron removal in experiments to equilibrium modeling using the estimated steam supply to the interface ($p_{H_2O}^s$), which is accounted for by the steam supply fraction in Section 5.1 based on weightloss measurements. The comparison provides what is called the boron equilibrium fraction, which estimates the fraction at which the total mass transfer of boron from the bulk melt and out of the system approach the maximum rate limit determined from the supply of steam to the interface and is calculated as $\frac{k_t}{k_{eq}(p_{H_2O}^s)}$. Equivalently, the boron equilibrium fraction estimates the ratio of the HBO partial pressure in the gas

196

leaving the system to the maximum partial pressure that can be achieved with no resistance to mass transfer of boron, which means that boron has uniform concentration from the bulk to the interface, where reactions are fast and at equilibrium, and the partial pressure of HBO is fully accumulated along the wall jet so that the same equilibrium partial pressure is obtained in the gas flow out of the system. Thus, the boron equilibrium fraction can also be understood as the fraction of the equilibrium HBO partial pressure determined from steam supply that is actually achieved in the gas flow leaving the melt in experiments ($\frac{k_t}{k_{eq}(p_{H_2O}^s)} = \frac{p_{4,\text{HBO}}}{p_{eq,\text{HBO}}(p_{H_2O}^s)}$). The boron equilibrium fraction is used to assess the resistance to mass transfer of boron in experiments as separate from mass transfer of steam. The boron equilibrium fraction differs from the gas utilization in that gas utilization also includes losses for steam in addition to losses by resistances for boron removal. In the following, it is shown mathematically how the boron equilibrium fraction expresses resistances to mass transfer of boron.

The feed gas flow is input to the equilibrium model, except only the part of steam that is estimated to be supplied to the interface in the experiment ($p_{H_2O}^s = \frac{p_{H_2O}^s}{p_{H_2O}} p_{H_2O}$) is used to estimate the equilibrium limit for mass transfer of boron. The model simulates the course of refining in time steps of one minute. In each step, equilibrium compositions are calculated between the whole of the melt and the amount of gas input in one minute of gas flow. The partial pressure of HBO can be estimated from boron distribution Equation (2.4) for equilibrium Reaction (5.2) with $C_{i,\text{SiO}} = p_{H_2O}^s$. The gas at equilibrium with the bulk of the melt is discarded, while the melt is transferred to the next step. The disregarded gas represents the flow of gas away from the melt in experiments. The partial pressure of HBO and all other gases are in equilibrium with the bulk of the melt, which is the maximum HBO partial pressure that can be expected to form in the gas flow that leaves the melt in experiments. The rate of boron removal in the equilibrium model is also the maximum rate that can be expected, since the rate that boron is removed from the system is given by its concentration in the gas flow that leaves the melt according to Equation (2.59).

Equilibrium modeling with the estimated steam supply to the interface thus estimates the rate limit for boron removal in step 4 (Equation (2.60)). Equations (5.5)-(5.6) relate the rate limit for boron removal by bulk convection in the gas flow out of the system as calculated by equilibrium modeling to the mass transfer coefficient for step 4 ($k_4 = k_{eq}(p_{H_2O}^s)$), which relates to the concentration of boron in the melt like the total mass transfer coefficient for boron. The maximum partial pressure of HBO and the gas flow rate is given by the supply of steam and hydrogen from the feed gas and bulk concentration of boron in the melt. The rate limit for removal of HBO in the gas flow out of the system is actually equivalent to the rate limit for boron removal when supply of steam is rate determining, in the same way that the removal rate of boron in equilibrium modeling can be said to be determined either from supply of steam as the input of the model or by the gas flow carrying HBO out of the system. The boron equilibrium fraction thus reveals if there in experiments is any resistance to mass transfer of boron separate from mass transfer of steam. For simplicity, $k_{eq}(p_{H_2O}^s)$ is here expressed using the concentration ratio of HBO in the gas in the interface equilibrium

($C_{eq,\text{HBO}}$) to the concentration of boron equal to that in the bulk melt.

$$\frac{\mathrm{d}n}{\mathrm{d}t} = -QC_{eq,\text{HBO}}(p_{\text{H}_2\text{O}}^s) = -A_c k_{eq}(p_{\text{H}_2\text{O}}^s)C_{[\text{B}]} \tag{5.5}$$

$$k_{eq}(p_{\text{H}_2\text{O}}^s) = \frac{Q}{A_c}\frac{C_{eq,\text{HBO}}(p_{\text{H}_2\text{O}}^s)}{C_{[\text{B}]}} \tag{5.6}$$

The total mass transfer coefficient for boron removal in experiments can be lower than $k_{eq}(p_{\text{H}_2\text{O}}^s)$ due to any kinetic resistance against boron removal. Kinetics of boron removal is considered to include steps that involve the interface, namely transfer of boron from the bulk of the melt to the interface (step 1), interphase reactions for HBO formation (step 2) and diffusion of HBO from the interface and into the bulk gas flow (step 3). Equation (5.7) expresses the total resistance to boron removal from the bulk of the melt and out of the system in the gas flow leaving the melt, as the sum of the kinetic resistances and the resistance posed by supply of steam from the feed gas. The equation can be rearranged to the boron equilibrium fraction as shown in Equation (5.8).

In the case that supply of steam from the feed gas is rate determining for boron removal, the mass transfer coefficients for all the kinetic steps of boron removal are high compared to the equilibrium limit for mass transfer of HBO in the gas flow out of the system ($k_{\text{k}} \gg k_{eq}(p_{\text{H}_2\text{O}}^s)$ for k = 1, 2 and 3). Accordingly, all kinetic resistances for boron removal are negligible ($\frac{1}{k_{\text{k}}} \ll \frac{1}{k_{eq}(p_{\text{H}_2\text{O}}^s)}$ in Equation (5.7)) and the boron equilibrium fraction $\frac{k_t}{k_{eq}(p_{\text{H}_2\text{O}}^s)} = 1$. If however any of the kinetic resistances for boron removal is significant ($\frac{k_{eq}(p_{\text{H}_2\text{O}}^s)}{k_{\text{k}}} \not\approx 0$ in Equation (5.8)), the boron equilibrium fraction $\frac{k_t}{k_{eq}(p_{\text{H}_2\text{O}}^s)} < 1$.

$$\frac{1}{k_t} = \frac{1}{k_1} + \frac{1}{k_2} + \frac{1}{k_3} + \frac{1}{k_{eq}(p_{\text{H}_2\text{O}}^s)} \tag{5.7}$$

$$\frac{k_t}{k_{eq}(p_{\text{H}_2\text{O}}^s)} = \frac{1}{\frac{k_{eq}(p_{\text{H}_2\text{O}}^s)}{k_1} + \frac{k_{eq}(p_{\text{H}_2\text{O}}^s)}{k_2} + \frac{k_{eq}(p_{\text{H}_2\text{O}}^s)}{k_3} + 1} \tag{5.8}$$

The dependence of the boron equilibrium fraction on the gas flow rate gives another indication of significant resistances to boron removal, in addition to its actual value. Mass transfer from melt (k_1) is not expected to depend on the gas flow rate, particularly in the induction furnace where convection of the melt by drag from the gas flow is expected to have an negligible contribution to the mass transfer coefficient k_1 compared to the induction stirring. Also reaction kinetics at the interface (k_2) does not depend on the gas flow rate. As a result, the fraction $\frac{k_{eq}(p_{\text{H}_2\text{O}}^s)}{k_{\text{k}}}$ for k = 1 or 2 in Equation (5.8) increases with gas flow rate as shown in Equation (5.9) and the boron equilibrium fraction in Equation (5.8) would be expected to decrease with increasing gas flow rate if either step 1 or 2 posed a significant resistance to

boron removal. The mass transfer coefficient for diffusion of HBO in the wall jet increases with flow rate as $k_{\text{HBO}} \propto Q^{\frac{3}{4}}$ (Equation (2.57)). The dependence is however weaker than proportional and the term $\frac{k_{eq}(p_{\text{H}_2\text{O}}^s)}{k_3}$ in Equation (5.8) is expected to increase with increasing gas flow rate as shown in Equation (5.10), so that the boron equilibrium fraction would be expected to decrease with increasing gas flow rate if diffusion of HBO posed a significant resistance to boron removal. A similar analysis like in Equations (5.5) and (5.6), finds $k_3 = k_{\text{HBO}}(Q^{\frac{3}{4}})\frac{C_{eq,\text{HBO}}(p_{\text{H}_2\text{O}}^s)}{C_{[\text{B}]}}$ (Equation (2.58) without inserting equilibrium distribution coefficient). The boron equilibrium fraction is thus expected to be constant with increasing gas flow rate only if there is no kinetic resistance to removal of boron.

$$\frac{k_{eq}(p_{\text{H}_2\text{O}}^s)}{k_{\text{k}}} = \frac{\frac{Q}{A_c}\frac{C_{eq,\text{HBO}}(p_{\text{H}_2\text{O}}^s)}{C_{[\text{B}]}}}{k_{\text{k}}} \propto Q \quad \text{for step k = 1 and 2} \tag{5.9}$$

$$\frac{k_{eq}(p_{\text{H}_2\text{O}}^s)}{k_3} = \frac{\frac{Q}{A_c}\frac{C_{eq,\text{HBO}}(p_{\text{H}_2\text{O}}^s)}{C_{[\text{B}]}}}{k_{\text{HBO}}(Q^{\frac{3}{4}})\frac{C_{eq,\text{HBO}}(p_{\text{H}_2\text{O}}^s)}{C_{[\text{B}]}}} \propto Q^{\frac{1}{4}} \tag{5.10}$$

The boron equilibrium fractions were calculated for experiments in which the weightloss could be fully accounted for (in Section 4.2) and are presented in Figures 5.3 and 5.4. A pre-requisite for obtaining representative estimate for the boron equilibrium fraction is that a representative estimate for the steam supply fraction in Figures 5.1 and Figure 5.2 is used in the input to equilibrium modeling, and only Figure 5.3 includes representative boron equilibrium fractions. Experiments Q_4, $Q_$8a and $Q_$8b are not shown in Figure 5.3 because underestimation of the steam supply fraction yielded too high boron equilibrium fractions ($\frac{k_t}{k_{eq}(p_{\text{H}_2\text{O}}^s)} > 1$). The boron equilibrium fraction in experiments H$_2$O_03a-b is also higher than the possible range in Figure 5.4, as the duration of the experiments was not sufficient to provide a reliable estimate of the total mass transfer coefficient for the low concentration reduction achieved with $0.032 - 0.090$ bar steam, which also is the case for experiment H$_2$O_09.

The experiments with representative steam supply fractions achieve a constant boron equilibrium fraction in spite of increasing rate of boron removal with increasing gas flow rate, which in the analysis of resistances in Equations (5.8), (5.9) and (5.10) indicate fast kinetics for boron removal compared to steam supply. The mass transfer coefficient from equilibrium modeling with the estimated steam supply is however slightly higher than the total mass transfer coefficient for boron removal in experiments, as the boron equilibrium fraction averages $81\% \pm 5\%$ for the representative experiments, although the value $\frac{k_t}{k_{eq}(p_{\text{H}_2\text{O}}^s)} = 1$ is expected for a constant trend with no signs of kinetic resistances for boron removal. Due to uncertainties in the thermodynamic data for boron in the equilibrium model, the constant trend is considered a stronger indication of equilibrium boron removal than the actual value. The offset between $k_{eq}(p_{\text{H}_2\text{O}}^s)$ and k_t in experiments suggest an systematic error. The 3% systematic

underestimation in weightloss measurements is not significant and it is accounted for in the boron equilibrium fraction by a 3% decrease compared to using the raw measurements. There is however a large scatter in literature values of thermodynamic data for boron in silicon and particularly HBO gas, and tabulated data for HBO have been disputed [30].
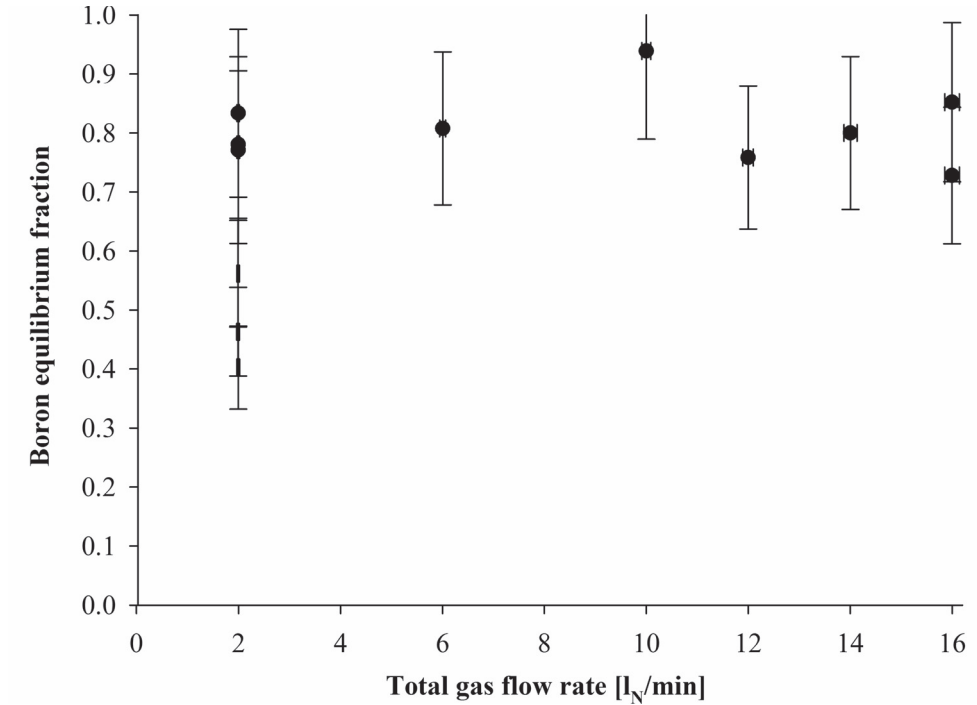
Figure 5.3: Boron equilibrium fraction ($\frac{k_t}{k_{eq}(p_{H_2O}^s)} = \frac{p_{4,HBO}}{p_{eq,HBO}(p_{H_2O}^s)}$) as function of total gas flow rate in "Q" experiments together with H_10-30 and $H(d\_35)\_5$ at 2 l_N/min, all with optimal lance heights and fully accounted weightloss. Experiments without symbols are considered outlayers, and are the same as for steam supply in Figure 5.1. Representative experiments achieve a high and constant boron equilibrium fraction, with average of $81\% \pm 5\%$. Common parameters: $p_{H_2O} = 0.032$ bar, hydrogen atmosphere, $p = 1.12$ bar, $d = 4.0$ mm ($d = 35.0$ mm for $H(d\_35)\_5$), $H = 5$-30 mm, $m = 200$ g, EG-Si feedstock, $T = 1500\,°C$, Induction 2 furnace, $d_c = 70$ mm, graphite crucible, $A_c = 36.9$ cm^2.
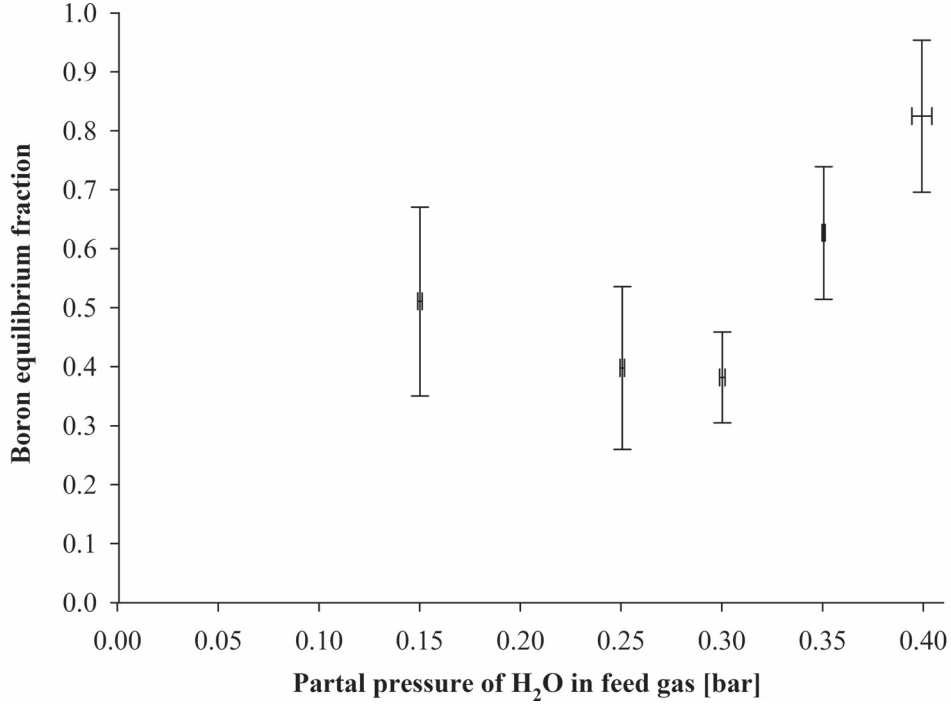
Figure 5.4: Boron equilibrium fraction ($\frac{k_t}{k_{eq}(p_{\text{H}_2\text{O}}^s)} = \frac{p_{4,\text{HBO}}}{p_{eq,\text{HBO}}(p_{\text{H}_2\text{O}}^s)}$) as function of partial pressure of steam set in the feed gas ($p_{\text{H}_2\text{O}}$) in "H$_2$O" experiments without passivation. As the steam supply fractions in Figure 5.2 are considered to be overestimated, the boron equilibrium fractions are considered to be underestimated (outliers). The boron equilibrium fraction is not expected to increase as the removal rates increases with increasing steam partial pressures, according to analyzes of resistances in Equation (5.8). Common parameters: argon atmosphere, $p = 1.36$ bar, $Q = 2.00$ l$_\text{N}$/min, $d = 4.0$ mm, $H = 20$ mm, $m = 200$ g, high-purity silicon feedstock, $T = 1700$ °C, Induction 2 furnace, $d_c = 70$ mm, graphite crucible, $A_c = 36.9$ cm^2.

Tang et al. [30] was first to observe an off-set between gas blowing experiments and the current equilibrium model, and related the difference to the standard enthalpy of formation of HBO ($\Delta_f H_{\text{HBO}}^{\ominus}(298$ K)). They found the tabulated value in JANAF [44] Thermochemical Tables too high, while ab-initio calculations found the same standard entropy. Their experimental boron removal rates is reproduced in the equilibrium model with $\Delta_f H_{\text{HBO}}^{\ominus}(298$ K) $= -229.4$ kJ/mol, which they calculated by ab-initio calculations. However, when accounting for the fraction of steam that is actually supplied to the interface equilibrium, the removal rate in equilibrium modeling is reduced approximately by the steam supply fraction. Only the lowest literature values can be used in combination with $\gamma_{[B]}$ from data in COST 507 [40]

Thermochemical Database for Light Metal Alloys to explain the experimental removal rates, as they presumably do not surpass the actual equilibrium limit represented by equilibrium modeling with accurate thermodynamic data. The average boron equilibrium fraction of 81% for representative experiments with the selected value of $\Delta_f H_{\mathrm{HBO}}^{\ominus}(298\ \mathrm{K}) = -251\ \mathrm{kJ/mol}$ by Page [51] for the equilibrium model, allows for a slightly higher value.

The boron equilibrium fraction $\frac{k_t}{k_{eq}(p_{\mathrm{H_2O}}^s)} = 1$ allows for $\Delta_f H_{\mathrm{HBO}}^{\ominus}(298\ \mathrm{K}) \leq -248 \pm 1\ \mathrm{kJ/mol}$, which is shown in calculation at the end of this section. Although the constant boron equilibrium fraction for representative experiments in Figure 5.3 suggest that boron removal in experiments achieves the actual equilibrium limit ($\frac{k_t}{k_{eq}(p_{\mathrm{H_2O}}^s)} = 1$), $\Delta_f H_{\mathrm{HBO}}^{\ominus}(298\ \mathrm{K}) = -248\ \mathrm{kJ/mol}$ is not recommended for use due to its highly indirect method of measurement and it depends on a range of parameters and simplifications. It is listed together with a compilation of literature values in decreasing order in Table 5.1 to show which values can explain the experimental removal rates and thus why the value by Page [51] was selected for the equilibrium model. The enthalpy of formation of HBO has an exponential effect on the boron removal rate in equilibrium modeling and determination of a reliable value is considered important for further investigation and development of the gas refining process.

Table 5.1: Literature values for the standard enthalpy of formation of HBO, compiled and reviewed by Vadon et al. [34], compared to the maximum limit set by $\frac{k_t}{k_{eq}(p_{\mathrm{H_2O}}^s)} \leq 1$.

Reference (Year)	Method	$\Delta_f H_{\mathrm{HBO}}^{\ominus}(298\ \mathrm{K})$ [kJ/mol]
Gurvich et al. (1994) [45]	Review of Farber and Frisch [48]	-188.6 ± 25
Farber and Frisch (1969) [48]	Mass Spectrometry	-196 ± 13
JANAF (1985) [44]	Review	-198.3 ± 3.0
Vadon et al. (2015) [34]	Review of Farber and Frisch [48]	-211.8 ± 12
Vadon et al. (2015) [34]	Review of Dill et al. [49]	-212.8 ± 19.5
Vadon et al. (2015) [34]	Review of Gorokhov et al. [46] (1)	-228.0 ± 27.0
Gurvich et al. (1994) [45]	Review of Gorokhov et al. [46]	-228.6 ± 20
Tang et al. (2012) [30]	Ab initio	-229.4
Duan et al. (1999) [50]	Ab initio	-233.9
Vadon et al. (2015) [34]	Review of Tang et al. [30]	-234.7
Vadon et al. (2015) [34]	Review of Page [51]	-236.7
Vadon et al. (2015) [34]	Review of Duan et al. [50]	-242.8 ± 8.4
Representative experiments	$\frac{k_t}{k_{eq}(p_{\mathrm{H_2O}}^s)} \leq 1$ ($\gamma_{[B]}$ from COST 507 [40])	≤ -248 ± 1
Vadon et al. (2015) [34]	Review of Gorokhov et al. [46] (2)	-250.2 ± 38.0
Page (1989) [51]	Ab initio	-251

202

Under the assumptions that the offset in boron equilibrium fraction is due to an inaccurate standard enthalpy of formation of HBO ($\Delta_f H^{\ominus}_{\mathrm{HBO}}(298 \text{ K})$) in the equilibrium model, and that HBO accumulates to the actual equilibrium partial pressure in the gas flow out of the system (step 4) in the experiments, the boron equilibrium fraction equals the ratio of the equilibrium constant for Reaction (5.2) in the experiments compared to the equilibrium model as shown in Equation (5.11).

$$\frac{k_t}{k_{eq}(p^s_{\mathrm{H_2O}})} = \frac{p_{4,\mathrm{HBO}}}{p_{eq,\mathrm{HBO}}(p^s_{\mathrm{H_2O}})} = \frac{K_{\mathrm{HBO/SiO}}}{K_{eq,\mathrm{HBO/SiO}}} \tag{5.11}$$

The equilibrium constants at the experimental temperature of $T = 1500\ ^\circ\text{C}$ relates to the standard Gibbs energy of reaction ($\Delta G^{\ominus}$ in Equation (5.12)), which in Equation (5.13) is expressed through the standard reaction enthalpy and entropy ($\Delta S^{\ominus}$) at 298 K and heat capacity (Δc_p) functions, as well as enthalpies and entropies of phase transitions of species in Reaction (5.43) between 298 K and the reaction temperature T (collected in $\Delta_{trs}H^{\ominus}$. and $\Delta_{trs}S^{\ominus}$). The reaction enthalpy can be expressed as the sum of formation enthalpies and the stoichiometric coefficient (ν_j) for the species "j" in Reaction (5.2) as in Equation (5.14). The same relationship applies to entropy and heat capacity.

$$-RT \ln K = \Delta G^{\ominus} \tag{5.12}$$

$$
\begin{aligned}
-RT \ln K = {} & \Delta H^{\ominus}(298 \text{ K}) + \int_{298 \text{ K}}^{T} \Delta c_p^{\ominus}\, dT + \Delta_{trs} H^{\ominus} \\
& - T\left(\Delta S^{\ominus}(298 \text{ K}) + \int_{298 \text{ K}}^{T} \frac{\Delta c_p^{\ominus}}{T}\, dT + \Delta_{trs} S^{\ominus} \right)
\end{aligned} \tag{5.13}
$$

$$\Delta H^{\ominus} = \sum_j \nu_j \Delta_f H_j^{\ominus} \tag{5.14}$$

Inserting Equation (5.12) for both equilibrium constants in the experiments and in the equilibrium model into Equation (5.11) shows the exponential dependence of the boron equilibrium fraction on offsets in the Gibbs free energy of the boron distribution Reaction (5.2) between experiments and the equilibrium model. The right side of Equation (5.15) assumes that the offset is only in the standard enthalpy of formation of HBO, and that all other data (equivalent to Equations (5.13) and (5.14)) in the equilibrium model equals the actual values. HBO is a product in Reaction (5.2) and its stoichiometric coefficient is $\nu_{\mathrm{HBO}} = 1$ in Equation (5.14). In Equation (5.16), the $19\% \pm 5\%$ offset in boron equilibrium fraction translates to 3 ± 1 kJ/mol offset in the Gibbs free energy of reaction and the standard enthalpy of formation of HBO compared to $\Delta_f H^{\ominus}_{eq,\mathrm{HBO}}(298 \text{ K}) = -251$ kJ/mol by Page [51] in the equilibrium model. The resulting maximum standard enthalpy of formation of HBO that can explain the experimental removal rates is -248 ± 1 kJ/mol for which the boron equilibrium

fraction $\frac{k_t}{k_{eq}(p^s_{\mathrm{H_2O}})} = \frac{p_{4,\mathrm{HBO}}}{p_{eq,\mathrm{HBO}}(p^s_{\mathrm{H_2O}})} = 1$. Lower standard enthalpies of formation of HBO is also reasonable as they provide a boron equilibrium fraction $\frac{p_{4,\mathrm{HBO}}}{p_{eq,\mathrm{HBO}}(p^s_{\mathrm{H_2O}})} < 1$, but higher values would suggest that reactions for HBO formation proceed past the equilibrium partial pressure of HBO.

$$-RT \ln \frac{p_{4,\mathrm{HBO}}}{p_{eq,\mathrm{HBO}}(p^s_{\mathrm{H_2O}})} = \Delta G^{\ominus}(T) - \Delta G^{\ominus}_{eq}(T)$$

$$= \Delta_f H^{\ominus}_{\mathrm{HBO}}(298\ \mathrm{K}) - \Delta_f H^{\ominus}_{eq,\mathrm{HBO}}(298\ \mathrm{K}) - T(\underbrace{\Delta S^{\ominus} - \Delta S^{\ominus}_{eq}}_{0}) \quad (5.15)$$

$$\Delta_f H^{\ominus}_{\mathrm{HBO}}(298\ \mathrm{K}) = -251\ \mathrm{kJ/mol} - RT \ln \frac{p_{4,\mathrm{HBO}}}{p_{eq,\mathrm{HBO}}(p^s_{\mathrm{H_2O}})} \quad (5.16)$$

The boron equilibrium fraction was not obtained for most experiments. However, the gas utilization is typically 25%-40%, which can be factored into $\frac{k_t}{k_{eq}} = \frac{p_{4,\mathrm{HBO}}}{p_{eq,\mathrm{HBO}}} = \frac{p^s_{\mathrm{H_2O}}}{p_{\mathrm{H_2O}}} \cdot \frac{p_{4,\mathrm{HBO}}}{p_{eq,\mathrm{HBO}}(p^s_{\mathrm{H_2O}})}$ with typical values of 30%-50% steam supply and 80% boron equilibrium fraction compared to the present equilibrium model. Considering instead an actual boron equilibrium fraction of 100% as indicated by constant $\frac{k_t}{k_{eq}(p^s_{\mathrm{H_2O}})}$ with increasing removal rates, all of the supplied steam is utilized for boron removal in the interface equilibrium so that $\frac{p_{4,\mathrm{HBO}}}{p_{eq,\mathrm{HBO}}} = \frac{p^s_{\mathrm{H_2O}}}{p_{\mathrm{H_2O}}}$ in which $p_{eq,\mathrm{HBO}} = \frac{K_{\mathrm{HBO/SiO}}}{p^{\ominus\frac{1}{2}}} \gamma_{[\mathrm{B}]} x_{[\mathrm{B}]} p^{\frac{1}{2}}_{\mathrm{H_2}} p_{\mathrm{H_2O}}$.

5.3 Passivation Threshold

The threshold for silica passivation set the limit to the partial pressures of steam that are suitable for refining of boron, as the surface becomes passivated by a silica layer if the supply of steam to the interface is higher than the passivation threshold. "Pass" experiments were conducted to observe the passivation threshold experimentally, which is found to agree with oxygen saturation in the equilibrium around the interface. A representative estimate for the steam supply to the interface could be measured for Pass_H$_2$a because the steam partial pressure was varied minimally ($60\ \mathrm{mbar} \leq p_{\mathrm{H_2O}} \leq 65\ \mathrm{mbar}$) as the passivation threshold was passed in the first incremental increase. Also the weightloss measurement was representative as silica particles did not accumulate on the surface and there were no passivation layer after the experiment. The steam supply fraction was estimated to $43\% \pm 4\%$ in Pass_H$_2$a. The part of steam that was supplied to the interface is estimated to $p^s_{\mathrm{H_2O}} = 26 \pm 3\ \mathrm{mbar}$ for $p_{\mathrm{H_2O}} = 60\ \mathrm{mbar}$ without passivation and $p^s_{\mathrm{H_2O}} = 28 \pm 3\ \mathrm{mbar}$ for $p_{\mathrm{H_2O}} = 65\ \mathrm{mbar}$ for which passivation was observed. The range between the observations provide an experimental range for the passivation threshold for steam supply to the interface and is in excellent agreement with the saturation pressure of SiO over silicon and silica of $p^{sat}_{\mathrm{SiO}} = 27\ \mathrm{mbar}$ at $1500\ °\mathrm{C}$. A similar comparison can be made for estimates of the steam supply in experiments H$_2$O_40-50,

for which the passivation threshold was crossed in the increment $\Delta p_{\text{H}_2\text{O}} = 0.10$ bar between these experiments. Numerical values for these experiments in Table 5.2 also show agreement between the experimental range of passivation threshold for steam supply and the saturation pressure of SiO over silicon and silica at 1700 °C.

It should be noted that thermodynamic modeling using HSC in Section 2.1 differ from the equilibrium model using ChemSheet with the database described in Section 3.6.1. HSC provides a threshold steam supply for formation of silica at 1500 °C of 37 mbar (3.7 vol% in Figure 2.1), which is outside the experimental range. The agreement between experiments the ChemSheet equilibrium model demonstrate the advantage of using the specialized database by Tang et al. [30, 39] for this H-B-O-Si system.

Table 5.2: Passivation threshold for steam supply between experiments with observation of clean surface and passivation. The experimental range covers the saturation pressure of SiO in the interface equilibrium and increases with the temperature of the melt. The steam supply fraction for H_2O_50 is approximated to that in H_2O_40 because the steam supply fraction for H_2O_50 is underestimated by the silica passivation layer. Common parameters: $p = 1.09\text{-}1.36$ bar, $Q = 2.00$ l_N/min, $d = 4.0$ mm, $H = 20$ mm, $m = 200$ g, high-purity silicon feedstock, Induction 2 furnace, $d_c = 70$ mm, graphite crucible, $A_c = 36.9$ cm^2.

T [°C]	Experiment	$p_{\text{H}_2\text{O}}^s$ [bar] (highest $p_{\text{H}_2\text{O}}^s$ without passivation)	p_{SiO}^{sat} [bar]	$p_{\text{H}_2\text{O}}^s$ [bar] (lowest $p_{\text{H}_2\text{O}}^s$ with passivation)	Experiment
1500	Pass_H$_2$a	0.026 ± 0.003	0.027	0.028 ± 0.003	Pass_H$_2$a
1700	H$_2$O_40	0.197 ± 0.016	0.231	0.246 ± 0.020	H$_2$O_50

The agreement between passivation threshold for the steam supply to the interface and the saturation pressure for SiO suggest that the passivation threshold for steam in the feed gas can be estimated from the steam supply fraction and the saturation pressure of SiO in the interface equilibrium as $\frac{p_{\text{SiO}}^{sat}}{p_{\text{H}_2\text{O}(\text{max})}} \approx \frac{p_{\text{H}_2\text{O}}^s}{p_{\text{H}_2\text{O}}}$. In Pass_H$_2$a, observations around the passivation threshold for the partial pressure of steam in the feed gas provide $0.42 \leq \frac{p_{\text{SiO}}^{sat}}{p_{\text{H}_2\text{O}(\text{max})}} \leq 0.45$ and agrees with the estimated steam supply fraction of $\frac{p_{\text{H}_2\text{O}}^s}{p_{\text{H}_2\text{O}}} = 0.43 \pm 0.04$. Using the partial pressure of steam in the feed gas for observations around the passivation threshold with 2 l_N/min total gas flow rate for the other "Pass" experiments from Table 4.17 provide $0.40 \leq \frac{p_{\text{SiO}}^{sat}}{p_{\text{H}_2\text{O}(\text{max})}} \leq 0.54$ as an estimate for the steam supply fraction which is similar to that in Pass_H$_2$a. A representative weightloss could not be estimated for the steam supply fraction in the other "Pass" experiments due to large variation of the partial pressure of steam during the experiments.

Argon atmosphere was used in Pass_Ar and Pass_Ar,H$_2$ while Pass_H$_2$a used hydrogen, and a similar steam supply fraction close to 50% indicates that resistance to diffusion to of steam to the interface is relatively low in both Ar and H$_2$ at 2 l$_N$/min total gas flow rate, meaning that steam is depleted along the wall jet flow in experiments with both atmospheres. This is also indicated by weightloss measurements for the steam supply fraction in experiments H$_2$O_03a-b at 0.032 bar steam feed partial pressure in argon atmosphere (Figure 5.2), which is no less than the steam supply fraction in comparable experiments at 2 l$_N$/min total gas flow rate in Figure 5.1. Resistance to diffusion is however expected to be higher in argon than in hydrogen due to the higher viscosity of argon, even though it is not pronounced in current experiments with 2 l$_N$/min total gas flow rate. The precise effect of the atmosphere gas on the diffusion of steam to the interface thus requires a more targeted investigation.

Figure 5.5 plots the partial pressure of steam set in the feed gas flow for the experiments in Table 5.2 and H$_2$O(T_1800)_100a at 1799 °C, for which a representative weightloss and steam supply fraction was not obtained. The experiments used 2 l$_N$/min total gas flow rate for which diffusion resistance is not considered to be large. Accordingly, the experimental observations of passivation agrees roughly with the passivation threshold for the stoichiometric limit of 50% steam supply for fuming Reaction (5.3), providing $p_{\text{H}_2\text{O}}(\text{max}) \approx 2p_{\text{SiO}}^{sat}$. Although the partial pressure of steam in experiment H$_2$O(T_1800)_100a at 1799 °C was near atmospheric pressure, argon was used as a carrier gas and the total pressure was 1.46 bar. Consequently, there was presumably a gas boundary layer through which steam diffused and partly reacted with SiO before reaching the interface.

Feeding of pure steam at atmospheric pressure presumably increases the possibility that the fuming reaction may not be fast enough to consume all SiO and 50% of the steam before steam reaches the interface. A melt temperature higher than 1800 °C might in that case be necessary to avoid passivation, although a boundary layer for steam may still be expected as SiO dominates near the surface and steam would need to diffuse through SiO. However, equilibrium modeling indicate an opposite effect of high steam fractions, and does not predict passivation from supply of 1 bar steam for melt temperatures above 1785 °C, as steam decomposes to 50% SiO and 50% hydrogen at the interface. Equilibrium modeling does not predict passivation as observed in experiments H$_2$O_50-60, and the saturation pressure of steam is considered to be a better estimate for the steam supply fraction at high fractions of steam in the feed, although it may probably not be accurate either. The passivation threshold for the temperature with pure steam is in any case not expected to be higher than 1875 °C for which the saturation pressure of SiO is above atmospheric pressure.
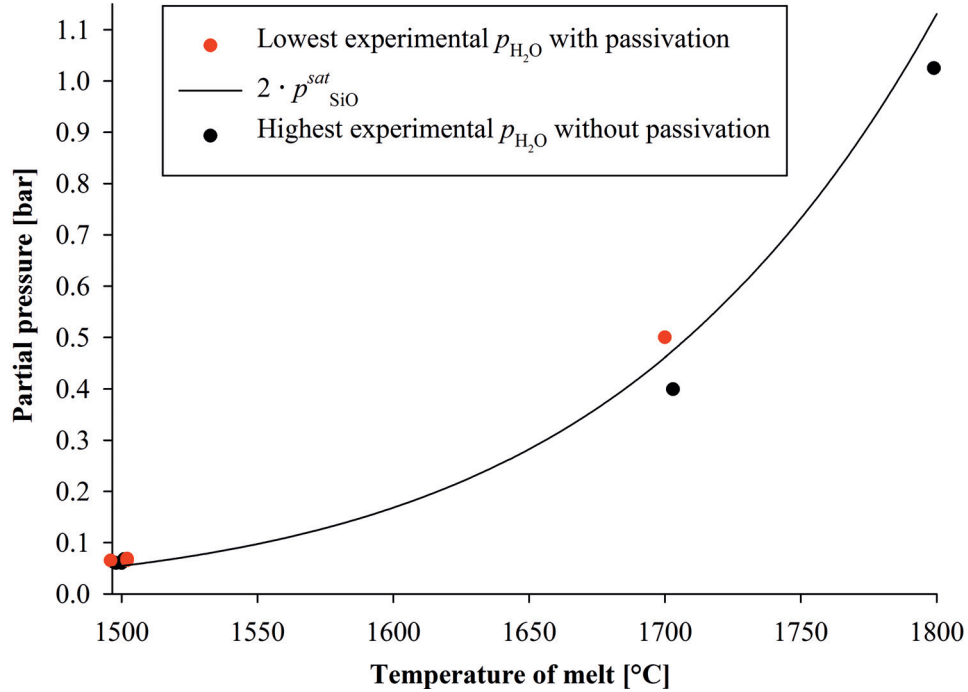
Figure 5.5: Experimental range for the passivation threshold in $2\,\mathrm{l_N/min}$ feed gas compared to stoichiometric limit for SiO saturation at interface $(0.5p_{\mathrm{H_2O}}(\max) \approx p_{\mathrm{SiO}}^{sat})$. The experimental range is represented by the highest $p_{\mathrm{H_2O}}$ without passivation and lowest $p_{\mathrm{H_2O}}$ for which passivation was observed. The experimental passivation threshold agrees with SiO saturation in the interface equilibrium for a steam supply close to the stoichiometric limit of 50%, considering that diffusion resistance is found to be relatively low in experiments with $2\,\mathrm{l_N/min}$ total gas flow rate. "Pass" experiments are around $1500\,°\mathrm{C}$, $\mathrm{H_2O\_40\text{-}50}$ around $1700\,°\mathrm{C}$ and $\mathrm{H_2O}(T\_1800)\_100a$ at $1799\,°\mathrm{C}$. Common parameters: argon atmosphere, $p = 1.09\text{-}1.36\,\mathrm{bar}$, $Q = 1.00\,\mathrm{l_N/min}$, $d = 4.0\,\mathrm{mm}$, $H = 20\,\mathrm{mm}$, $m = 200\,\mathrm{g}$, high-purity silicon feedstock (MG-Si in $\mathrm{H_2O}(T\_1800)\_100a$), Induction 2 furnace, $d_c = 70\,\mathrm{mm}$, graphite crucible, $A_c = 36.9\,\mathrm{cm^2}$.

The passivation threshold appears to increase exponentially with temperature like the saturation pressure of SiO in the interface equilibrium. This is in agreement with approximately complete decomposition of steam supplied to the interface like for equilibrium in Reaction (5.17), and passivation for oxygen saturation in Reaction (5.18). The passivation threshold for steam supply to the interface approximately equals the saturation pressure of SiO with the exponential temperature dependence in Equation (5.21) given by the reaction enthalpy in Equation (5.19) through the equilibrium constant for Reaction (5.18) in Equation (5.20).

The passivation threshold for the feed gas in a gas blowing experiment by Altenberend [18] reported in Table 2.7 show the same general trend that the passivation threshold increases more strongly as the temperature is increased. By accounting for the oxygen stoichiometry of $p_{O_2} = 2p_{H_2O} = 2p_{SiO}$, the passivation thresholds in Table 2.7 appear slightly higher than for current experiments, particularly towards lower temperatures.

$$H_2O + [Si] \rightleftharpoons SiO + H_2 \tag{5.17}$$

$$2\,SiO \rightleftharpoons [Si] + SiO_2\,(s/l) \tag{5.18}$$

$$-RT \ln K_{SiO_2/SiO} = \Delta G^{\ominus}_{SiO_2/SiO} = \Delta H^{\ominus}_{SiO_2/SiO} - T\Delta S^{\ominus}_{SiO_2/SiO} \tag{5.19}$$

$$p^s_{H_2O}(\text{max}) \approx p^{sat}_{SiO} = \sqrt{\frac{1}{K_{SiO_2/SiO}}} \tag{5.20}$$

$$p^s_{H_2O}(\text{max}) \approx p^{sat}_{SiO} = e^{\frac{1}{2R}\Delta S^{\ominus}_{SiO_2/SiO}} \cdot e^{\frac{1}{2R}\Delta H^{\ominus}_{SiO_2/SiO} \cdot \frac{1}{T}} \tag{5.21}$$

5.4 Boron Removal Dependencies

This section seek to identify dependencies of the rate and total mass transfer coefficients for boron removal on different experimental parameters and compare the trends to related theory and literature (predominantly in Section 2.3). Section 4.1 includes straightforward explanations for the effect of some experimental parameters and all of its subsections are not repeated in this discussion. The dependencies of the total mass transfer coefficient for boron removal on selected experimental parameters represents the initial strategy for identifying rate determining steps and is used in assessment of process kinetics in Section 5.5 with the rate law conforming to all dependencies.

5.4.1 Steam Content

The effect of partial pressure of steam on the rate of boron removal was investigated in the "H_2O" series. The experiments used different high-purity silicon materials, but they showed no obvious difference for boron removal from clean surfaces. The least pure material was the directionally solidified UMG-Si, which was analyzed by ICP-MS to less than $1\,\text{ppmw}$ of each of 19 impurity elements (those in Table 4.21). Figure 5.6 shows plots of the total mass transfer coefficients in experiments with increasing partial pressure of steam below the passivation threshold. The total mass transfer coefficient and the rate of boron removal increases with increasing partial pressure of steam while the total gas flow rate is constant for all experiments and the flow of diluting gas is reduced. A given amount of boron is thus removed at shorter times and the total amount of gas used to remove the given amount of boron is reduces as the steam partial pressure increases.
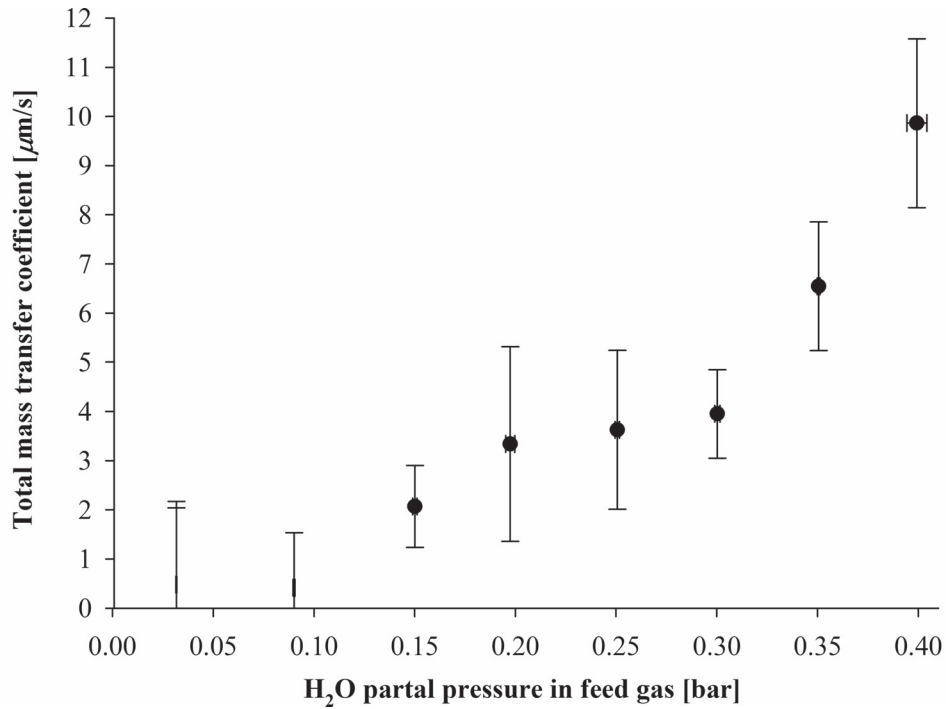
Figure 5.6: Total mass transfer coefficients in H_2O_03-40 experiments plotted as function of partial pressure of steam set in the feed gas. H_2O_03-09 are outliers due to insufficient boron removal. Common parameters: argon atmosphere, $p = 1.36$ bar, $Q = 2.00$ l_N/min, $d = 4.0$ mm, $H = 20$ mm, $m = 200$ g, high-purity silicon feedstock, $T = 1700$ °C, Induction 2 furnace, $d_c = 70$ mm, graphite crucible, $A_c = 36.9$ cm^2.

The weightloss is used to estimate the part of the partial pressure of the steam in the feed gas that was supplied to the interface, which is used in Figure 5.7. This fraction accounts for losses for steam supply to the interface, which represents a resistance for boron removal. The trend of mass transfer coefficients in equilibrium modeling is plotted to represent the maximum limit for which the equilibrium partial pressure of HBO is accumulated in the gas flow out of the system. The experimental mass transfer coefficients approach a large fraction of the equilibrium limit, which indicate low resistance losses to boron removal from the melt and out in the gas flow leaving the system in the experiments. It is not reasonable that mass transfer coefficient in experiments increases towards the equilibrium limit with increasing absolute values of the mass transfer coefficient, which thus is considered to be due to experimental scatter.
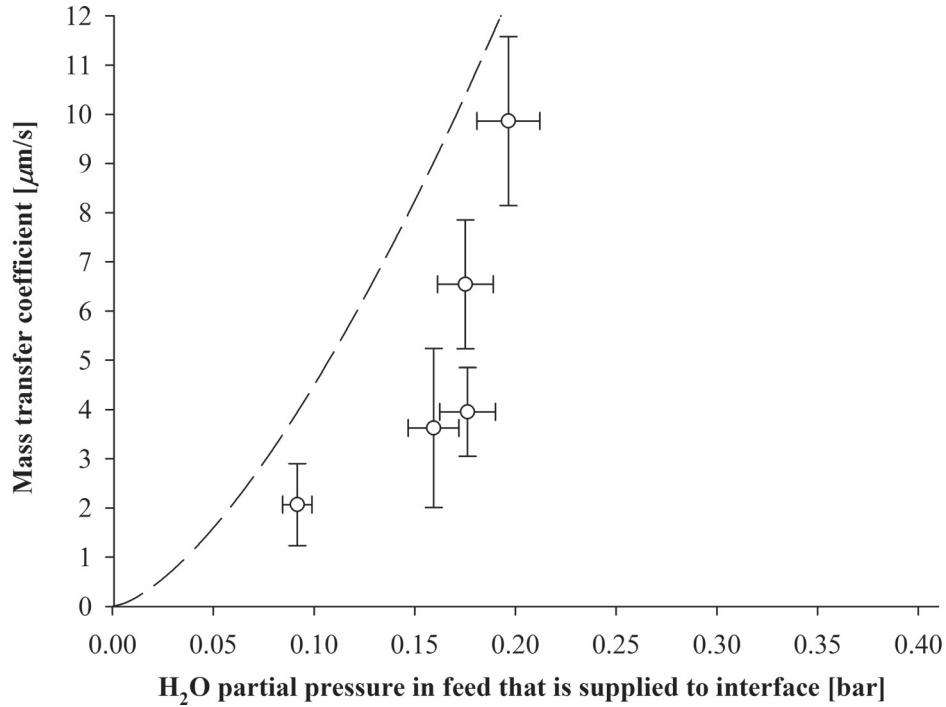
Figure 5.7: Total mass transfer coefficients in H_2O_15-40 experiments (circles) plotted as function of partial pressure of steam supplied to the interface. H_2O_03-09 are excluded due to insufficient boron removal and H_2O_20 because the weightloss was not measured. The trend line for equilibrium modeling represents the maximum limit. Common parameters: argon atmosphere, $p = 1.36$ bar, $Q = 2.00$ l_N/min, $d = 4.0$ mm, $H = 20$ mm, $m = 200$ g, high-purity silicon feedstock, $T = 1700\,°C$, Induction 2 furnace, $d_c = 70$ mm, graphite crucible, $A_c = 36.9$ cm^2.

The mass transfer coefficient is expected to depend on the partial pressure of steam as the power function in Equation (5.22), where the reaction order for steam (α_{H_2O}) is the exponent for the steam content in feed gas. The reaction order is the slope of lines in the order plot with logarithmic axes in Figure 5.8. Reaction orders for steam was calculated as the slope in linear regression with uncertainties (method by York et al. [105]) according to Equation (5.23) (u is used as a generic term for the standard uncertainty for the value it follows, and is not to be considered as a constant). Regression is performed for equilibrium modeling (k_{eq}) of the experiments, which compares to regression $k_t(p_{H_2O})$ for experiments using the steam partial pressure in feed gas (Figure 5.6) and $k_t(p^s_{H_2O})$ using the part that is supplied to the interface (Figure 5.7). The regression lines are shown in Figure 5.8 for the mean values of the regression parameters in Equations (5.24)-(5.25).

$$k_t = k_t(p_{H_2O} = p^\ominus) \cdot \left(\frac{p_{H_2O}}{p^\ominus}\right)^{\alpha_{H_2O}} \qquad (5.22)$$

$$\ln k_t \pm u = \alpha_{H_2O}(\ln p_{H_2O} \pm u) + \ln k_t(p_{H_2O} = p^\ominus) \qquad (5.23)$$
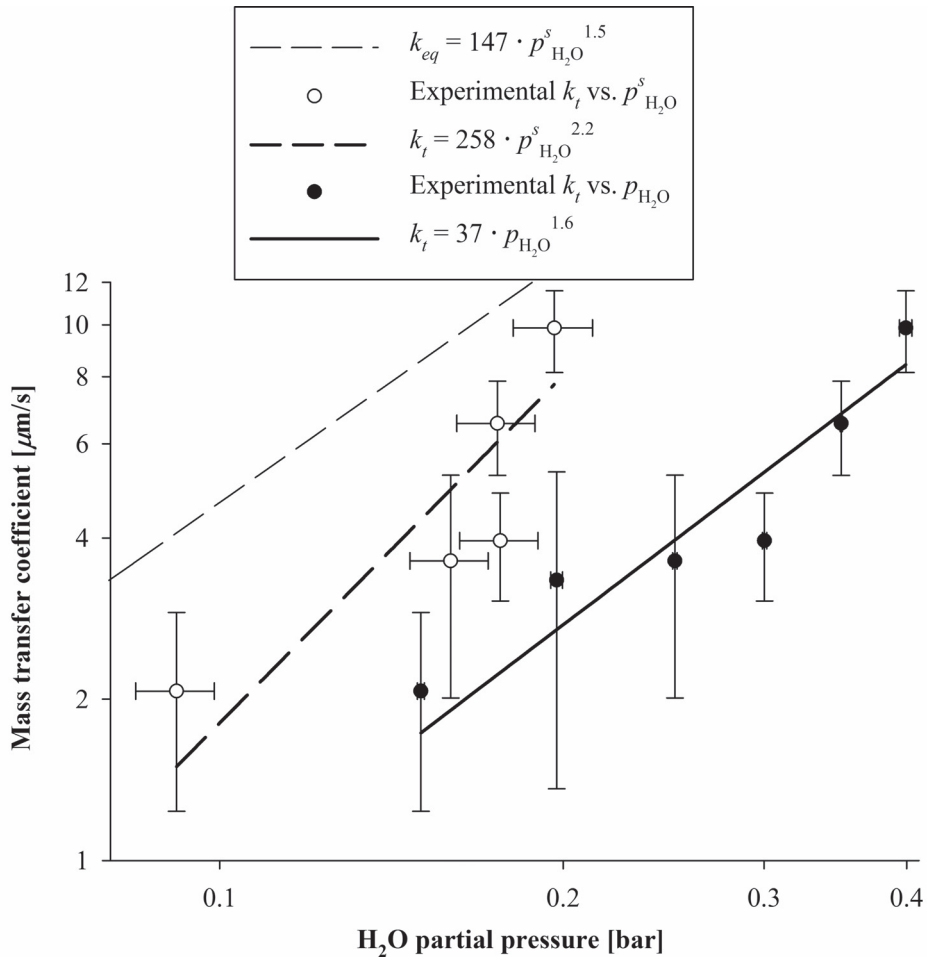
Figure 5.8: Order plot showing the reaction order for steam as the slope of regression lines (Equation (5.23)) of mass transfer coefficients from equilibrium modeling (k_{eq}) and experiments as function of steam supply ($k_t(p_{H_2O}^s)$) and as function of steam partial pressure in feed gas ($k_t(p_{H_2O})$). Common parameters: argon atmosphere, $p = 1.36$ bar, $Q = 2.00$ l$_N$/min, $d = 4.0$ mm, $H = 20$ mm, $m = 200$ g, high-purity silicon feedstock, $T = 1700$ °C, Induction 2 furnace, $d_c = 70$ mm, graphite crucible, $A_c = 36.9$ cm^2.

211

The apparent reaction orders for steam from experiments is found to be higher than for the equilibrium limit, in spite of the large fraction of equilibrium for boron removal (based on the estimated steam supply to the interface). The regression line for $k_t(p_{H_2O}^s)$ is not expected to cross above the limit for equilibrium boron removal, which it tends to do for higher steam partial pressures than in Figure 5.8, and the slope of $k_t(p_{H_2O}^s)$ is unreasonably high. Experiments H$_2$O_25-30 stand most clearly out of the trend and contributes most to the unreasonably high slope. The total mass transfer coefficients in these experiments also fall below the trend based on the partial pressure in the feed gas, indicating that the cause for the unreasonably high slope of $k_t(p_{H_2O}^s)$ is in part due to scatter in the estimates of the total mass transfer coefficient calculated from analysis of melt samples. The most important error source is however in the estimate of the steam supply. Section 5.1 find the estimated steam supply fraction to be unreasonable high for experiments H$_2$O_15-35 and it also increase with decreasing steam partial pressure. This contributes to increase the slope of $k_t(p_{H_2O}^s)$ as the experimental values of $p_{H_2O}^s$ in Figure 5.8 are unreasonably high for these experiments and the offset is highest for the experiments with lowest steam partial pressure.

$$\ln \frac{k_{eq}}{\text{m/s}} = 1.5 \cdot \ln \frac{p_{H_2O}}{\text{bar}} - 8.8 \tag{5.24}$$

$$\ln \frac{k_t}{\text{m/s}} = (2.2 \pm 0.9) \cdot \ln \frac{p_{H_2O}^s}{\text{bar}} - (8.3 \pm 1.5) \tag{5.25}$$

The apparent reaction order for steam based on the partial pressure of steam set in the feed gas ($\alpha_{H_2O} = 1.6 \pm 0.5$ from Equation (5.26)) is considered to be a more reliable estimate for the interface reactions than that base on the estimated supply of steam to the interface ($\alpha_{H_2O}^s = 2.2 \pm 0.9$ in Equation (5.25)) for the "H$_2$O" experiments. Ideally, α_{H_2O} represents a lower limit to the reaction order for steam in interface reactions because it includes the dependence of steam supply from the feed gas to the interface, which at most is proportional. Regression for the weightloss $\ln -\Delta m \pm u$ to $\ln p_{H_2O} \pm u$ for representative experiments H$_2$O_03-40 in Figure 4.30 provides $-\Delta m \propto (p_{H_2O})^{0.88 \pm 0.04}$, and combines to $\alpha_{H_2O}^s = \frac{\alpha_{H_2O}}{0.88 \pm 0.04} = 1.8 \pm 0.5$ for supply of steam to the interface. Again, the trend of an increasing offset to unreasonably high steam supply fractions for experiments with decreasing steam partial pressures (Section 5.1) suggest that the exponent 0.88 ± 0.04 from regression of the weightloss measurements is underestimated. Reliable values for the reaction order for steam in the interface reactions are thus considered to be below 1.8 ± 0.5. Since the dependence of steam supply is relatively close to proportional, it might be compensated by experimental scatter of the total mass transfer coefficient estimates in experiments H$_2$O_15-40, and its effect on $\alpha_{H_2O}^s$ is likely within the uncertainty estimate for α_{H_2O}, which agrees reasonably well with $\alpha_{eq,H_2O} = 1.5$ for equilibrium in reactions at the interface (Equation (5.27)).

$$\ln \frac{k_t}{\text{m/s}} = (1.6 \pm 0.5) \cdot \ln \frac{p_{\text{H}_2\text{O}}}{\text{bar}} - (10.2 \pm 0.6) \tag{5.26}$$

$$\alpha_{\text{H}_2\text{O}}^s \approx \alpha_{\text{H}_2\text{O}} = 1.6 \pm 0.5 \approx 1.5 = \alpha_{eq,\text{H}_2\text{O}} \tag{5.27}$$

The reaction order for steam for equilibrium is compared to experimental estimates in current experiments and experiments with inert atmospheres in previous studies of boron removal from silicon melts by gas or plasma refining in Table 5.3. The reaction order for steam is higher for equilibrium and in present experiments compared to experiments in previous studies, which typically find $\alpha_{\text{H}_2\text{O}} = 1$ in Table 5.3 and does not verify that the equilibrium reaction order for steam is generally applicable. It should however be noted that the range of partial pressures used in previous studies is relatively narrow compared to the "H$_2$O" series, and different trends could be more difficult to distinguish even for accurate data points. Higher steam partial pressures could be used in the "H$_2$O" series because the higher melt temperature provided a higher passivation threshold than in previous studies. No attempt to estimate the steam supply has been reported in previous studies, and accounting for the dependence of steam supply could have provided a slightly higher estimate for the reaction order of steam in the reactions with the interface.

Table 5.3: Reaction orders for steam in experiments without hydrogen in the "H$_2$O" series and literature, compared to equilibrium boron removal in Equation (5.24). Atm. denotes the atmosphere gas with content given as the rest after summarizing the contents of all other gases.

Reference	Process	H$_2$O content	O$_2$ content	H$_2$ content	Ar	$\alpha_{\text{H}_2\text{O}}$
Interface equilibrium		Limiting	0	0		1.5
"H$_2$O" experiments	Gas	0.15-0.40 bar	0	0	Atm.	1.6 ± 0.5
Suzuki et al. [25]	Plasma	0-1.4%	0	0	Atm.	1
Nakamura et al. [11]	Plasma	0-7.2%	0	0	Atm.	1

Table 5.4 compares equilibrium reaction orders for gases to apparent reaction orders in experiments with excess hydrogen in previous studies. The reaction order for steam is expected to be different when excess contents of hydrogen is used in the gas compared to steam in an inert atmosphere. With excess hydrogen contents in the gas, decomposition of steam can not significantly change the content of hydrogen, which instead is predominately supplied from the feed gas. In effect, steam only supplies oxygen in this case and its reaction order is expected to be equal to that of oxygen ($\alpha_{eq,\text{H}_2\text{O/H}_2} = \alpha_{eq,\text{O}_2} = 1$). Previous studies do not find a difference in the reaction order for steam between gases with and without excess hydrogen contents. Reports by Theuerer [28] and Nordstrand and Tangstad [17] is based on respectively three and two experiments and the reaction order of 0.5 for steam in hydrogen is

not considered to be reliable. It still remains to verify whether the reaction order for steam is different in gas and plasma refining experiments. The reaction order for steam in hydrogen is found to be 1 in studies of plasma refining, which agrees with equilibrium boron removal. The reaction order for hydrogen is reported to 0.5, which also agrees with equilibrium boron removal.

Table 5.4: Review of reaction orders for hydrogen and for steam or oxygen in the gas feed with excess of hydrogen, compared to equilibrium around interface. Atm. denotes the atmosphere gas with content given as the rest after summarizing the contents of all other gases.

Reference	Process	H_2O content	O_2 content	H_2 content	Ar	α_{H_2O/H_2}	α_{O_2}	α_{H_2}
Interface equilibrium		Limiting	Limiting	Excess		1	1	0.5
Theuerer [28]	Gas	1.3-13 mbar	0	Atm.	0	0.5		
Nordstrand and	Gas	3.2%, 7.4%	0	Atm.	0	0.5		
Tangstad [17] (α_{H_2} in [18])		3.20 %	0	0-96.8%	Atm.			0.5
Nakamura et al. [11]	Plasma	2.7-5.0%	0	51 %	Atm.	1		
Alemany et al. [69]	Plasma	0	0-15%	40 %	Atm.		1	
Altenberend [18]	Plasma	0	0.80 %	0-6%	Atm.			0.5

5.4.2   Gas Flow Rate and Crucible Diameter

The effect of gas flow rate on boron removal is shown in Figure 5.9. With increasing gas flow rate, the rate of steam supply from the feed gas increases and so does the removal rates. Mass transfer in the gas phase is thus rate determining, either by bulk gas flow or by boundary layer diffusion. The mass transfer coefficient for the bulk gas flow increases as the amount of steam introduced in the system per time increases with total gas flow rate and the mass transfer coefficient for diffusion increases as the gas velocity increases with the total gas flow rate through the lance of constant diameter. In the "Q" series, the lance was positioned within the optimal height region, where the lance height does not affect mass transfer in the gas [75]. The rate of steam feeding in the gas flow from the lance sets a maximum limit to the removal rates in which all of it reacts to equilibrium. The removal rates may be further limited by diffusion to the interface. Such kinetic losses may however be minimized by proper scaling of the surface area through reactor design.
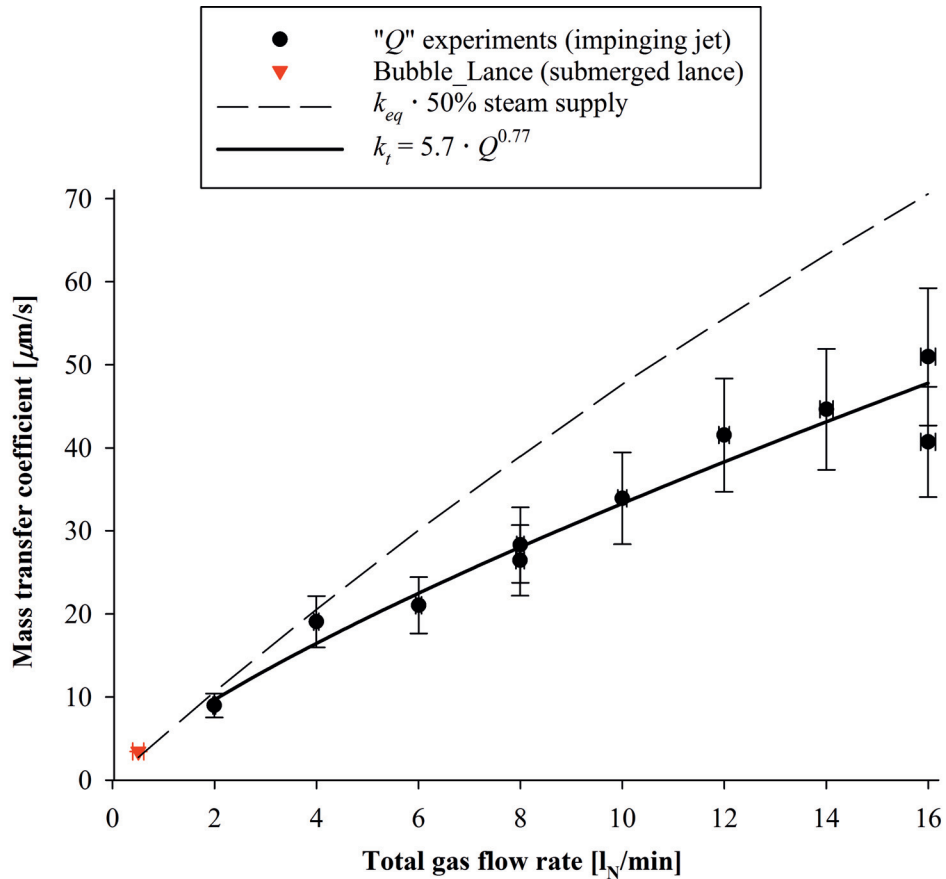
Figure 5.9: Total mass transfer coefficients in impinging jet "Q" experiments and bubbling experiment Bubble_Lance plotted as function of total gas flow rate. All experiments used 0.032 bar steam in hydrogen and EG-Si melt at 1500 °C in an induction furnace. The experiments are compared to models of the equilibrium limit, accounting for fuming ($k_{eq} \cdot 50\%$ steam supply). Common parameters: $p_{H_2O} = 0.032$ bar, hydrogen atmosphere, $p = 1.12$ bar, $d = 4.0$ mm, $H = 20$ mm, $m = 200$ g, EG-Si feedstock, $T = 1500$ °C, Induction 2 furnace, $d_c = 70$ mm, graphite crucible, $A_c = 36.9$ cm^2.

Regression of total mass transfer coefficients to the total gas flow rate in "Q" experiments agrees with the dependence for diffusion resistance in the wall jet region. Diffusion resistance in the wall jet region means that diffusion does not complete within the wall jet and part of the steam remains unreacted at the end of the wall jet and is lost in the gas flow out of the system. This diffusion loss is seen in Figure 5.9 as the gap between equilibrium modeling for 50%

steam supply and experimental mass transfer coefficients. The method by York et al. [105] was used to take experimental uncertainties into account like in estimation of reaction orders for steam by Equation (5.23), and provided the parameters in Equation (5.28) and (5.29). The regression agrees well with the rate limit for diffusion in the wall jet region ($k_w \propto Q^{0.75}$ in Equations (2.53) and (2.57)) for the "Q" experiments with total gas flow rate increasing from $2\,l_N/min$ of steam diluted in hydrogen blown from a $4\,mm$ diameter lance optimally close to the melt surface in a $70\,mm$ diameter crucible. The uncertainty is estimated for approximately 95% confidence level and excludes rate limitation in the stagnation region ($k_s \propto Q^{0.5}$ in Equation (2.52)) and a proportional dependence (Equation (2.60)).

$$\ln \frac{k_t}{m/s} = (0.77 \pm 0.08) \cdot \ln \frac{Q}{l_N/min} - (12.1 \pm 0.2) \tag{5.28}$$

$$k_t \propto Q^{0.77 \pm 0.08} \tag{5.29}$$

Steam supply and the weightloss follow $-\Delta m \propto Q^{0.87 \pm 0.09}$ (regression in Figure 4.31), which is in between theoretical dependencies for the rate limit of diffusion in the wall jet ($k_w \propto Q^{0.75}$ in Equation (2.53)) and of equilibrium silicon loss ($-\Delta m_{eq} \propto Q$). Steam supply is still found to account for the total resistance to boron removal (Section 5.2) as equilibrium modeling provides $k_{eq} \propto Q^{0.91}$. Modeling of the equilibrium limit from supplied steam can be approximated to the equilibrium modeling from the feed gas (without silica formation) multiplied by the steam supply fraction in Equation (5.30), as steam decomposes approximately stoichiometrically in equilibrium with silicon. Insertion of the gas flow rate dependence for each factor (Equations (5.31) and (5.32)) provides the dependence of the equilibrium boron removal limit (determined by steam supply) in Equation (5.33), and the total mass transfer coefficients in "Q" experiments follow this trend (Equation (5.29)).

$$k_{eq}(p^s_{H_2O}) \approx k_{eq} \cdot \frac{p^s_{H_2O}}{p_{H_2O}} \tag{5.30}$$

$$k_{eq} \propto Q^{0.91} \tag{5.31}$$

$$\frac{p^s_{H_2O}}{p_{H_2O}} = \frac{-\Delta m}{-\Delta m_{eq}} \propto \frac{Q^{0.87 \pm 0.09}}{Q} \tag{5.32}$$

$$k_e q(p^s_{H_2O}) \propto Q^{0.80 \pm 0.09} \approx Q^{0.77 \pm 0.08} \propto k_t \tag{5.33}$$

Diffusion resistance becomes evident in experiment Q_6 at $6\,l_N/min$ total gas flow rate in Figure 5.9, as the total mass transfer coefficient for Q_6 fall below the equilibrium limit determined by steam feeding in the bulk gas flow from the lance and the maximum of 50% steam supply for complete fuming. The offset occur because diffusion does not complete along the wall jet and a significant fraction of the steam in the feed gas remains at the end of the wall jet and escapes with the gas flow out of the system. Q_6 also has the lowest gas

flow rate for which the wall jet becomes constrained by the crucible wall in modeling of the gas flow in Figure 5.10. With increasing gas flow rate above $4\,l_N/min$ in Q_4, the crucible constrains the wall jet to a lower and lower fraction of the length in unconstrained flow, and an increasing fraction of steam remains unreacted as the wall jet is deflected away from the surface, which is seen in Figure 5.9 from the decreasing ratio between Q experiments below "$k_{eq} \cdot 50\%$ steam supply" for increasing gas flow rate above $4\,l_N/min$.

Constrainment of the wall jet by the crucible wall in "Q" experiments is found by comparing models for the gas flow in experiments to unconstrained flow in Figure 5.10. The wall jet ends in a vortex, at which boundary layer separation occurs and the diffusive mass transfer coefficient rapidly diminishes to that for stagnant gas outside of the vortex [74]. The distance of the wall jet increases with increasing gas flow rate (Figure 5.10(c)-(d)) and the position of the vortex is not constrained by the crucible wall in Q_4 (Figure 5.10(a) and (c) show identical vortex positions). At $6\,l_N/min$ total gas flow rate in Q_6, the wall jet extends far enough to be constrained by deflection by the vertical crucible wall, as the vortex is at a shorter radius in Figure 5.10(b) than in part (d).

Two experiments in the "d_c" series compared the rate of boron removal across different interface areas between crucibles of $38\,mm$ and $70\,mm$ diameter as shown in Table 4.7. These experiments used $0.032\,bar$ steam in 50:50 Ar:H_2 at $3\,l_N/min$ total gas flow rate through a $4\,mm$ diameter lance positioned $50\,mm$ above the melt surface, which was found to be above the optimal lance height region (Section 5.4.4). The boron removal rate and gas utilization was reduced to half in the $38\,mm$ crucible compared to in the $70\,mm$ crucible. The wall jet was most likely constrained in the $38\,mm$ crucible and diffusion resistance in the wall jet can explain the reduced gas utilization.

As the deflection of the wall jet by the vertical crucible wall stagnates the gas towards the edge of the melt surface (lower right corner in Figures 5.10(a) and (b)), the surface area may be better utilized in setups where the vortex flow can continue out to the side of the melt, either by a sloped crucible wall at the surface of the melt or complete filling of the crucible. Complete filling of the crucible was not practical in the graphite crucibles in present small-scale experiments because interfacial tensions lifted silicon a few centimeters up along the graphite wall, and a higher crucible wall was necessary to contain the melt.

The total mass transfer coefficients in Q_2-4 are close to the equilibrium rate limit for the maximum of 50% steam supply in Figure 5.9, which means that the removal rates are limited by feeding of steam in the bulk gas flow. Experiments at $2\,l_N/min$ gas flow rate from lances optimally close to the melt surface in $70\,mm$ diameter crucibles also had weightlosses corresponding to 50% steam supply in Figure 5.1. Accordingly, diffusion to the interface can keep up with the rate of steam feeding in Q_2-4, as all of the steam is consumed by fuming and decomposition at the interface before the gas flows away from the surface at the end of the wall jet. HBO is also fully accumulated to the equilibrium partial pressure determined by steam supply like in all Q experiments.

(a) Q_4 (crucible wall at 35 mm radius)　　(b) Q_6 (crucible wall at 35 mm radius)

(c) 4 l_N/min (unconstrained flow)　　(d) 6 l_N/min (unconstrained flow)
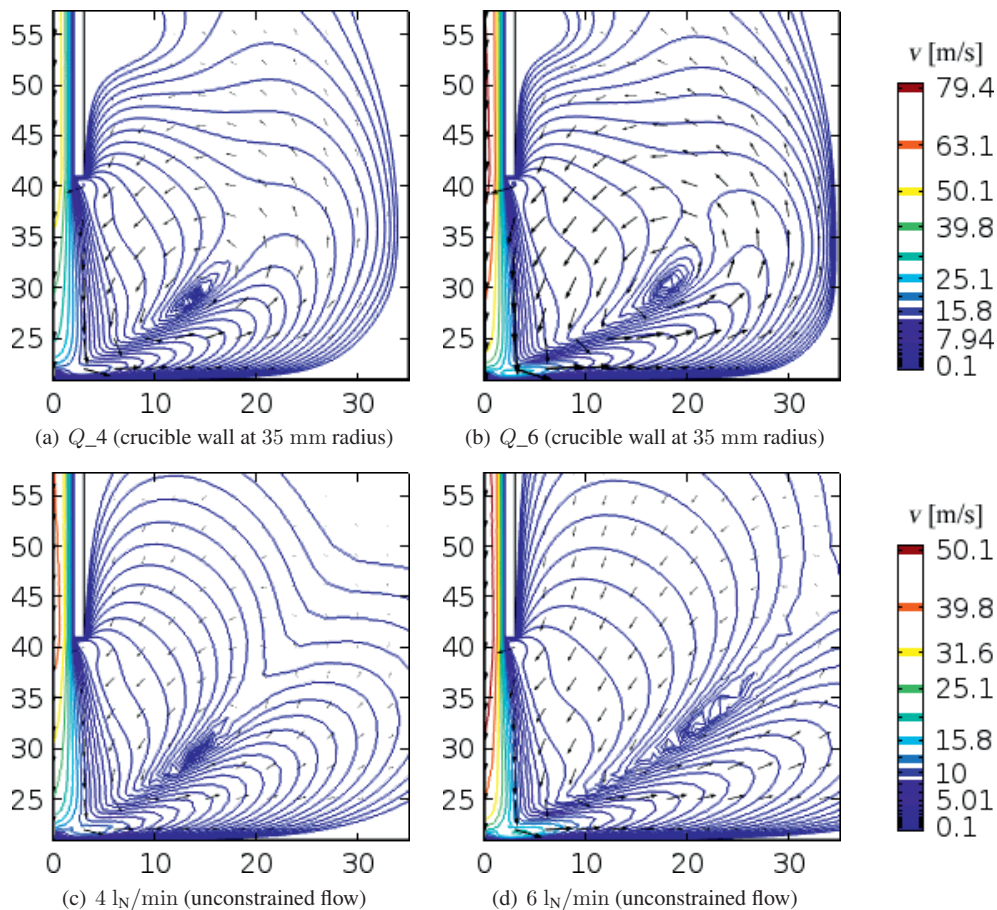
Figure 5.10: Axisymmetric CFD models of laminar ($Re < 10$) impinging jet gas flow made in COMSOL Multiphysics 4.4 with parameters representing experiment Q_4-6. 4-6 l_N/min hydrogen is fed through a 4 mm diameter lance (left in images) 20 mm above the melt surface in a 70 mm diameter crucible (a)-(b), compared to unconstrained flow (c)-(d) (crucible wall removed to 350 mm radius). The bottom axis represents the radius [mm] along the melt surface approximated to a flat no-slip wall, and the vertical axis is height [mm] in the crucible. The color legend represents the gas velocity [m/s], which is constant along each contour line. The spacing of the contour lines follow a logarithmic scale for the gas velocity while the color follows a linear scale. The arrows show the direction of flow at the base and the size scales logarithmically with the gas velocity. A vortex marks the end of the wall jet and the crucible wall start to constrain its position between 4-6 l_N/min total gas flow rate, which is the same range where incomplete diffusion becomes evident for experiments Q_4-6 in Figure 5.9.

218

Since the removal rate of boron is determined by the rate of steam feeding from the lance in experiments Q_2-4 and not by diffusion or reaction kinetics around the interface, increasing the interface area can not further increase the removal rate. While the interface area was significantly increased by bubbling the gas from a submerged lance in experiment Bubble_Lance, the removal rate remained around the equilibrium limit determined by the steam feed rate. In crucibles, bubbling is actually considered less advantageous than the impinging jet setup in "Q" experiments because the gas flow rate of $0.5\,\mathrm{l_N/min}$ in Bubble_Lance splashed the melt and it solidified on the crucible wall, while bulk gas feeding of steam remained rate determining at higher gas flow rates in impinging jet experiments Q_2-4.

Formation of droplets in the gas, for instance by splashing with fast impinging jet gas flow or bubbling, may however prove beneficial for the gas utilization for upscale gas flow rates as a larger interface area is required to maintain bulk gas rate limitation for increasing rates of steam feeding. It would however require a more sophisticated reactor design with temperature controlled walls that can contain the splashing melt, compared to impinging jet setups without splashing. Supposing that droplets capture silica fumes in the gas, they may potentially increase the steam supply fraction beyond 50%, and it may contribute to boron removal if the melt temperature is high enough so that it reforms SiO at the interface instead of accumulating into a passivation layer. Further research may assess the necessity and practicality of droplet formation in the gas. First of all, it may determine whether 50% steam supply may be maintained for upscale gas flow rates by scaling the crucible diameter to allow unconstrained wall jet flow, or if it requires distribution of the gas flow into multiple lances with lower flow rates. The onset of diffusion resistance with constrainment of the wall jet may be a coincidental observation for the conditions in "Q" experiments and further research may determine whether this is a generally applicable principle. It also remains to see if practical crucible diameters provide sufficient surface area for fast refining of any amount of melt, or whether systems for increased interfacial area are beneficial, for instance by splashing of droplets or division into modular systems.

5.4.3 Lance Diameter

Different lance diameters were used in experiments with identical gas flow rates in order to study the effect of gas velocity without changing the rate of steam feeding. The mass transfer coefficient for gas diffusion is however expected to increase with decreasing lance diameter, as this increases the gas velocity at constant total gas flow rate. The gas velocity averaged over the melt surface varied orders of magnitude in CFD modeling of the experiments. $0.1\,\mathrm{mm}$ above the surface (inside the gas boundary layer), the average velocity was a factor 166 higher in modeling of d_1 with $1.05\,\mathrm{mm}$ lance diameter than in modeling of $H(d\_35)\_10$ with $35\,\mathrm{mm}$ lance diameter. The longest wall jet was found in modeling of d_1 with the thinnest lance, for which the vortex was around $12\,\mathrm{mm}$ radius. The wall jet was not constrained by the crucible wall.

The total mass transfer coefficients in Figure 5.11 are all within the experimental uncertainty, so no effect of lance diameter is pronounced in the total mass transfer coefficient of the experiments with 2 l_N/min total gas flow rate. Accordingly, diffusion in the gas boundary layer is not a rate determining step for the experiments in Figure 5.11. The lance diameter may be revealed to have an effect on boron removal in further experimentation with a sufficiently high gas flow rate for gas diffusion to be rate determining.
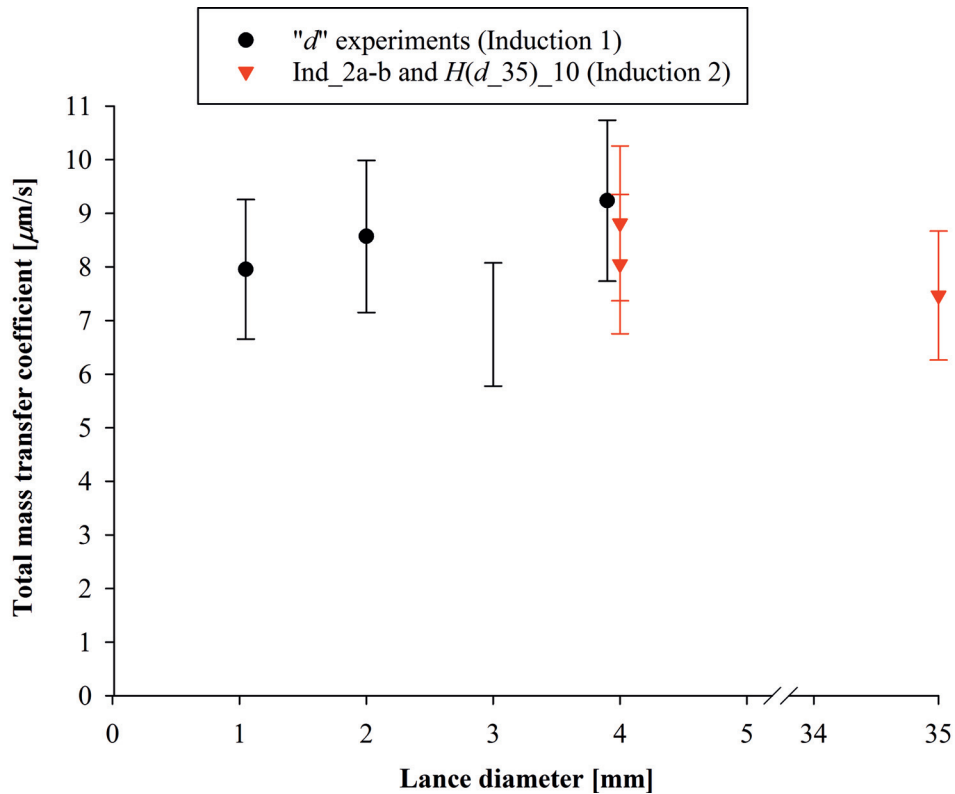
Figure 5.11: Total mass transfer coefficients in experiments with different lance diameters. No effect of lance diameter is pronounced in the total mass transfer coefficient in the experiments with 2 l_N/min, because the removal rates were limited by bulk gas feeding and not diffusion. Experiment d_3 is an outlier (no symbol) because the lance tip bent. Common parameters: $p_{H_2O} = 0.032$ bar, hydrogen atmosphere, $p = 0.99$ bar ($p = 1.2$ bar for Ind_2a-b and $H(d\_35)\_10$), $Q = 2.0$ l_N/min, $H = 10$ mm, $m = 200$ g, EG-Si feedstock, $T = 1500$ °C, $d_c = 70$ mm, graphite crucible, $A_c = 36.9$ cm^2.

In Section 5.4.2, the rate of boron removal in experiment Q_2 with a 4 mm diameter lance positioned 20 mm above the melt surface was found to be limited by the rate of steam feeding in the bulk gas flow of 2 l_N/min from the lance. The experiments with different lance diameters in Figure 5.11 also used 2 l_N/min total gas flow rate and their boron removal rates are also limited by gas feeding. Equilibrium modeling provides $k_{eq} \cdot 50\% = 10\text{-}11$ μm/s, assuming 50% steam supply fraction for experiments in Figure 5.11, and adjusted for around 20% offset between the equilibrium model and experiments (Section 5.2), this agrees with the total mass transfer coefficients in Figure 5.11.

5.4.4 Lance Height

The effect of lance height on boron removal and weightloss was investigated to assess whether the expected dependence for impinging jet mass transfer is followed and find optimal lance heights for the experiments. Impinging jets are expected to provide constant mass transfer to/from the interface in a range of lance heights close to the surface [75]. For lance heights above this range, the mass transfer coefficient for diffusion is expected to decrease with increasing lance height. The dependence of the lance height on the total mass transfer coefficient for boron removal is shown by comparing "H" experiments in Figure 5.12. Since steam supply is found to be rate determining for boron removal in current experiments (Section 5.2), the dependence of the total mass transfer coefficient for boron removal represents the dependence of steam supply by bulk gas feeding from the lance, fuming and diffusion through the gas boundary layer.

Constant mass transfer is achieved with lance heights at least up to 30 mm which together with lower lance heights are considered optimal for the gas flow of 2 l_N/min hydrogen with diluted steam blown through a vertical lance with 4 mm inner diameter. Representative weightloss measurements provide around 50% steam supply fraction for "H" experiments with up to 30 mm lance height (at 2 l_N/min in Figure 5.1) and equilibrium boron removal (at 2 l_N/min in Figure 5.3). Although "$H(d\_35)$" experiments with 35 mm lance diameter had no impinging jet out of the lance according to CFD modeling, the total mass transfer coefficient for these experiments is constant with lance height as seen in Figure 5.12.

Like in experiment Q_2 with 20 mm lance height at 2 l_N/min total gas flow rate in Figure 5.9, the rate of boron removal is also limited by bulk gas steam feeding in other "H" experiments with optimal lance height. Since the total mass transfer coefficient in "H" experiments with up to 30 mm lance height is found to be determined by the feed gas flow, and not boundary layer diffusion, the total mass transfer coefficient in these experiments is constant because a constant gas flow rate and steam partial pressure was used, and not because of diffusion from/to the impinging jet flow pattern. As the lance height is reduced below 30 mm in Figure 5.12, the mass transfer coefficient for diffusion may potentially continue to increase, because the total mass transfer coefficient becomes limited by feed gas flow instead. The lance height region of constant diffusion mass transfer (if any) may thus be lower than 30 mm.
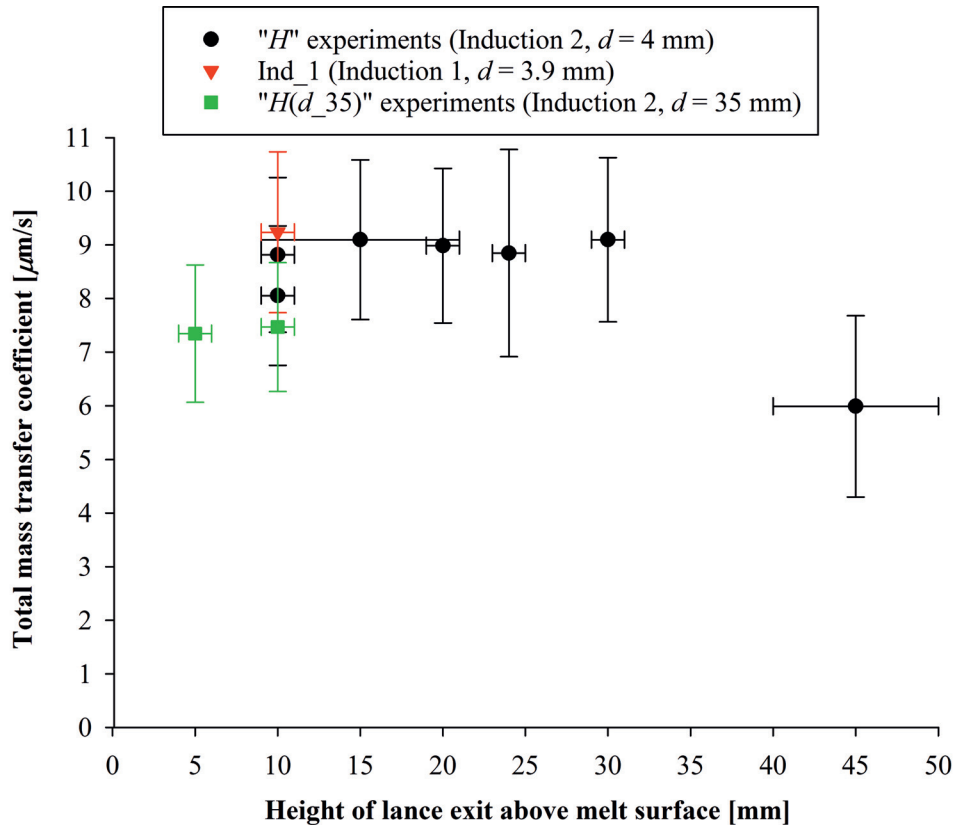
Figure 5.12: Total mass transfer coefficients in experiments with different lance heights. The lance height region of constant mass transfer is considered optimal. Common parameters: $p_{H_2O} = 0.032$ bar, hydrogen atmosphere, $p = 1.2$ bar ($p = 0.99$ bar for Ind_1), $Q = 2.00\ l_N/min$, $m = 200$ g, EG-Si feedstock, $T = 1500\ °C$, $d_c = 70$ mm, graphite crucible, $A_c = 36.9\ cm^2$.

Between experiments H_30-45 with 30-45 mm lance height in Figure 5.12, the total mass transfer coefficient drops significantly. In experiment H_45, the part of the jet from the lance that provides optimal boundary layer diffusion does not extend far enough to reach the surface, and diffusion of steam becomes rate determining.

By comparing gas utilizations in experimental series with increasing total gas flow rate using different lance heights in Figure 5.13, it is concluded that the part of the gas jet providing optimal diffusion mass transfer extends further from the lance with increasing total gas flow rate and thus increasing gas velocity through lances of identical diameters. The "Q" experiments in Figure 5.13 used a lance height within the optimal region for $2\ l_N/min$ and presumably

higher total gas flow rates. The lance height in "Q(Ind_1)" experiments was however above the optimal region for "H" experiments, which also was the case for an atmosphere of 50:50 H_2:Ar as seen from the lower gas utilization for Q(Ind_1)_2 compared to Q_2 at 2 l_N/min total gas flow rate in Figure 5.13. With an increased total gas flow rate of 6 l_N/min, the optimal lance height region has extended to at least 50 mm, as the gas utilization in experiment Q(Ind_1)_6 has caught up with that in Q_6 with lower lance height.

There is a peak in gas utilization around 1 l_N/min total gas flow rate from lances positioned 50 mm above the melt surface in "Q(Ind_1)" experiments. Experiment Q(Ind_1)_1 reaches the equilibrium rate limit determined from steam feeding at 40% gas utilization, which factors into 50% steam supply fraction and approximately 80% boron equilibrium fraction most likely due to offset in equilibrium modeling (Section 5.2). CFD modeling reveal that the impinging jet flow pattern is not developed in Q(Ind_1)_1. The model used pure hydrogen and the more viscous atmosphere of 50:50 H_2:Ar is expected to give less developed flow pattern in the experiment, like modeling with nitrogen provide a shorter jet compared to hydrogen. The peak in gas utilization around 1 l_N/min may be due to a combination of the gas flow bringing steam sufficiently close for diffusion to the interface, increased residence time available for diffusion due to the low flow rate through the system and a relatively low equilibrium rate limit determined from the rate of steam feeding. The gas utilization dropped to around zero at a further decreased total gas flow rate of 0.5 l_N/min in Q(Ind_1)_0.5, as the gas flow out of the lance did not extend far enough out from the lance 50 mm above the melt to supply steam to the interface and most of the steam appear to have escaped directly out of the system with the gas flow.

The lance height in Q(Ind_1)_3.5 was offset to 46 mm, which explains why it appears to achieve higher gas utilization compared to the trend for other "Q(Ind_1)" experiments above 3 l_N/min total gas flow rate in Figure 5.13. Above the optimal region, diffusion mass transfer increases as the lance height is decreased towards the optimal region.

Experiment Q(Ind_1)_3 was reproduced from experiment 12 by Nordstrand and Tangstad [17], except the lance diameter was 4 mm in Q(Ind_1)_3 while a nozzle of 1 mm inner diameter formed the lance exit in 12[17]. The total mass transfer coefficient of boron removal was higher in 12[17] than in Q(Ind_1)_3, giving a higher gas utilization in Table 5.5. Although the lance diameter was not found to have a significant impact on the removal rate of boron in the d series with a lance height within the optimal range and 2 $_N$/min total gas flow rate, the difference in lance diameter between Q(Ind_1)_3 and 12[17] at 3 l_N/min may offer a plausible explanation for the difference in mass transfer because the lance height was above the optimal range. The higher gas velocities through the 1 mm diameter nozzle in 12[17] may allow the free jet out of the lance to extend further, so that the 50 mm lance height comes closer to the optimal range and the rate limit for diffusion increases towards that in the optimal region.
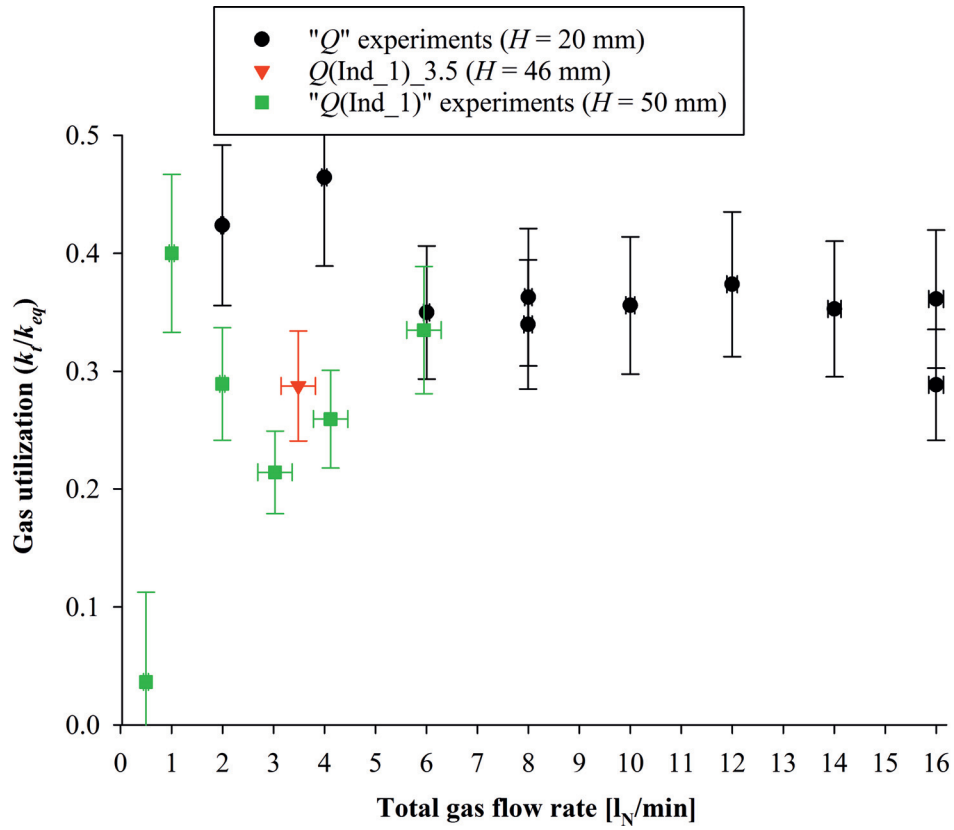
Figure 5.13: Gas utilization as function of total gas flow rate in experimental series with different lance heights. The gas utilization in "Q(Ind_1)" experiments increases towards that of "Q" experiments with optimal lance height as the optimal region extends further with increasing gas flow rate. "Q(Ind_1)" experiments used 0.49 bar hydrogen and argon at 1.00 bar total pressure in Induction 1 furnace while "Q" experiments used hydrogen atmosphere at $p = 1.12$ bar in Induction 2 furnace. Common parameters: $p_{H_2O} = 0.032$ bar, $d = 4.0$ mm, $m = 200$ g, EG-Si feedstock, $T = 1500\ °C$, $d_c = 70$ mm, graphite crucible, $A_c = 36.9\ cm^2$.

Table 5.5: Total mass transfer coefficients and gas utilization for $Q(\text{Ind\_1})\_3$ compared to 12[17] with reduced nozzle diameter. Common parameters: $p_{H_2O} = 0.032$ bar, $p_{H_2} = 0.49$ bar, argon atmosphere, $p = 1.00$ bar, $Q = 3.0$ l_N/min, $d = 4.0$ mm, $H = 50$ mm, $m = 200$ g, EG-Si feedstock, $T = 1500\,°C$, Induction 1 furnace, $d_c = 70$ mm, graphite crucible, $A_c = 36.9$ cm^2.

Experiment	k_t [μm/s]	k_t/k_{eq}
$Q(\text{Ind\_1})\_3$	5.16 ± 0.85	$21\% \pm 10\%$
12 by Nordstrand and Tangstad [17]	8.4	35%

5.4.5 Melt Convection

In Section 4.1.9, total mass transfer coefficients between experiments in different furnaces was not found to depend significantly on melt convection. Thus, mass transfer from the melt is not considered rate determining for boron removal for total mass transfer coefficients of 8-10 μm/s in the experiments. Mass transfer from the melt was also modeled and the estimated melt mass transfer coefficient for experimental conditions at $1500\,°C$ in the Induction 2 furnace is in Table 5.6 compared to the highest experimental total mass transfer coefficient achieved in experiment Q_16b with 16 l_N/min total gas flow rate. Also this comparison indicates that the boron removal in experiments is not limited by mass transfer from the melt. The ratio of these mass transfer coefficients estimates a resistance to boron removal of $\frac{k_t}{k_1} = 27\%$ in Q_16b. However, such a resistance is not observed experimentally as the boron equilibrium fraction is equally high as in experiments with lower total mass transfer coefficients like $k_t \approx 9$ μm/s for Q_2 at 2 l_N/min for which modeling of the melt mass transfer predicts a significantly lower resistance of $\frac{k_t}{k_1} = 5\%$.

Table 5.6: Highest total mass transfer coefficients in experiments compared to MHD modeling with boron diffusion in silicon melts (k_1) using similar parameters for the melt in the Induction 2 furnace. Modeling indicates that the total mass transfer coefficient is not limited by melt mass transfer for the fastest boron removal in experiment Q_16b. Parameters: $p_{H_2O} = 0.032$ bar, hydrogen atmosphere, $p = 1.12$ bar, $Q = 16.0$ l_N/min, $d = 4.0$ mm, $H = 20$ mm, $m = 200$ g, EG-Si feedstock, $T = 1500\,°C$, Induction 2 furnace, $d_c = 70$ mm, graphite crucible, $A_c = 36.9$ cm^2 ($A_c = 38.5$ cm^2 for MHD model).

Furnace (frequency)	Experiment	k_t [μm/s]	k_1 [μm/s]
Induction 2 (10750 Hz)	Q_16b	51.0 ± 8.3	191

The mass transfer coefficient for boron diffusion from the melt (k_1) was found from modeling magnetohydrodynamics (MHD) of silicon in the Induction 2 furnace with a Comsol Multi-

physics model made by Mark Kennedy and expanded to include diffusion of boron. Figure 5.14 shows the content of boron distributed over the radius and height of the melt heated to $1500\,°\mathrm{C}$, during mass transfer from 30 ppmw at the bottom and 0 ppmw at the top. The Model indicates that the melt is sufficiently stirred to achieve a uniform boron concentration around 15 ppmw, although the concentration is slightly elevated near the center (left in Figure 5.14). The bulk concentration extends $0.1 - 0.3$ mm towards the surface, making a steep concentration gradient to 0 ppmw at the surface as cause for the relatively high mass transfer coefficient. The mass transfer coefficient was calculated from the diffusion flux as an averaged across the surface divided by the bulk concentration ($k_1 = \frac{-J_{[\mathrm{B}]}}{C_{[\mathrm{B}]}}$).
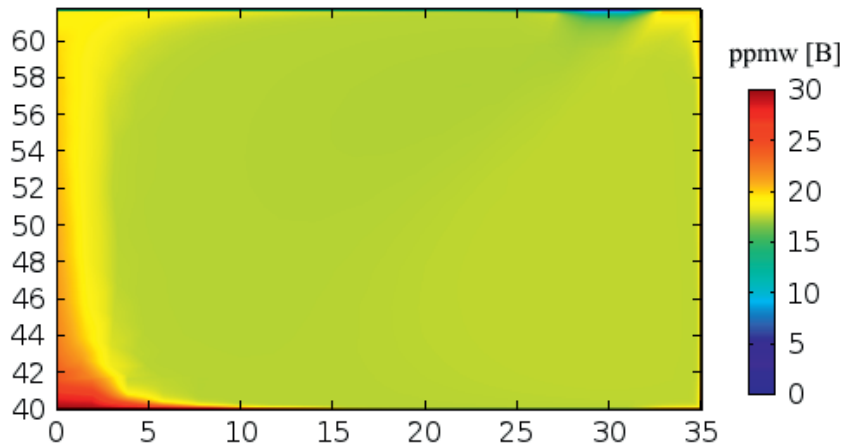
Figure 5.14: Boron content [ppmw] in silicon melt modeled in axisymmetric MHD model with diffusion made in COMSOL Multiphysics 4.4 for the Induction 2 furnace. The axes show height and radius [mm] inside a 200 g silicon melt heated to $1500\,°\mathrm{C}$ in a 70 mm diameter graphite crucible. The bottom axis represents the bottom of the crucible where a constant boron content of 30 ppmw is set to study mass transfer and the top represents the gas-melt interface and is modeled as slip wall with 0 ppmw boron as for the rate limit of melt mass transfer.

5.5   Process Kinetics

Reactive gas refining allows for semi-continuous refining of boron in simple setups. There is in principle no limit to the amount of impurities that can be removed as any amount of gas can be purged through the reactor system. However, only impurities that are enriched to a higher fraction compared to silicon in the gas than in the melt may be refined from the melt. Impurities that are not enriched in the gas may be up-concentrated in the melt.

Gas refining of silicon melts show promising results for removal of boron by reactions with oxygen and hydrogen to form HBO at the gas-melt interface. Also zinc was observed to be effectively removed from MG-Si in the process, and Ikeda and Maeda [62] removed calcium with Ar/O_2 and Ar/H_2O plasmas. Oxygen mainly reacts with silicon in parallel, which represents a loss of the silicon melt. Melt loss may in theory be suppressed by supplying oxygen in the form of SiO gas, which is the dominant gas product of silicon oxidation. SiO gas or condensate will still flow out of the system together with HBO and the silicon will be needed in production of high-purity SiO. For silicon melts with dilute concentrations of boron and other impurities, oxygen reacts mainly with silicon and a minor fraction reacts with boron. The limiting reactant in the process of boron removal is the oxidizing agent as long as the gas contains any practical levels of hydrogen.

Hydrogen alone has also been demonstrated by Nordstrand and Tangstad [17] to remove boron, as the relative stability of dominant gas species BH_3 and SiH_x allows enrichment of boron in the gas. However, the stability of HBO over BH_3 allows higher partial pressures of HBO than BH_3 in the gas so that less gas is necessary for the same amount of boron removal by introducing oxygen in a hydrogen gas. Equivalently, faster boron removal is achieved with steam than pure hydrogen [17] for identical total gas flow rates, as HBO attains higher concentrations than BH_3 in the gas flow carrying boron out of the system. Thermodynamic studies may further suggest new systems in which boron may be efficiently removed to gas.

Steam is selected as the oxidizing agent in the present study for the following reasons. The highest boron removal rates in gas/plasma refining to date has been achieved with oxygen and hydrogen (Section 2.2.2), which is contained in steam. The number of atoms in steam also provides a relatively high density of hydrogen and oxygen, so that steam can supply oxygen in a hydrogen gas without diluting hydrogen atoms. Finally, steam does not introduce additional contaminants than those necessary for HBO formation. An important reason for discontinuing use of CO as the oxidizing agent (Section 4.1.1) was that CO decomposed to SiC particles at the interface, which locally blocked contact between the gas and the melt, reducing the available reaction area. The melt surface may also be passivated by formation of silica, if the melt becomes saturated in oxygen at the interface. Silica forms continuous layers over the interface and effectively stops boron removal to gas in areas where it forms (Section 4.3). Efficient boron removal to gas thus requires control of the oxygen potential at the interface, or effective renewal of the melt-gas interface. A clean silicon surface can be maintained in practice with steam as the reactant. This is because both hydrogen and oxygen form gases with silicon (SiH_x and SiO) that are relatively stable compared to condensed phases (silica) and allow a practical operational window for the pressure of steam that can be used without saturating the interface in terms of formation of any condensed phase. There is however no gases containing carbon and silicon (and potentially oxygen and hydrogen) with high saturation pressure for SiC formation. This explains why introducing carbon (in CO) in addition to oxygen and hydrogen elements in the reactive gas was not found advantageous.

Silicon and boron are oxidized in parallel reactions. Silicon is lost by formation of SiO as

the dominant product from active oxidation of the interface, and boron is removed to the gas by formation of HBO as the dominant gas containing boron. SiO is further oxidized to silica fume particles inside the gas. Supply of the steam to the interface is found to be the rate determining step for both silicon oxidation and boron removal in experiments. The rate of silicon oxidation equals the rate of steam supply, as steam decomposes essentially stoichiometrically to SiO gas in the equilibrium around the interface. The total mass transfer coefficient for boron removal follows the rate of silicon loss at a constant ratio determined by equilibrium around the interface and depends on the partial pressure of hydrogen and the temperature of the melt. The ratio between the rates of boron removal and silicon oxidation also depends on the concentration of boron in the melt, while the concentration of silicon can be approximated to be constant for molten silicon materials. For melts with ppmw levels of boron, the rate of boron removal is orders of magnitude lower than the rate of silicon oxidation. The limiting reactant in the process of boron removal is the oxidizing agent as long as the gas contains any practical levels of hydrogen atoms.

The rate of supply of steam as the oxidizing agent is considered to be the most important factor also for the rate of boron removal. It depends on the flow rate of steam in the gas feed, and increasing the melt temperature allows to increases the partial pressure of steam that can be used in the gas flow without causing passivation and thus reduces the amount of gas needed to dilute steam. Using hydrogen as the diluting gas increases the ratio between rates of boron removal and silicon loss. Only a minor fraction of the hydrogen actually reacts to HBO for ppmw levels of boron in the melt, and steam is more effective in terms of the rate of boron removal (Section 5.4.1). The ratio between HBO and SiO formation also increases with decreasing temperature of the melt, like the stability of the HBO gas. Reactions and mass transfer of boron from the melt was comparably fast and did not pose any significant resistance to boron removal in experiments (Section 5.2).

Bulk species around the interface are found to be in equilibrium, as no effects from kinetic resistances for interface reactions, adsorption or desorption was identified for the rate of boron removal or silicon oxidation. Thus, the current results does not reveal the nature of the adsorbed species and whether or not part of the reactions involves dissolved species in the top layer of the melt, only the extent of equilibrium achieved for conversion of the reactants. The results of boron removal and silicon oxidation do not reveal information about the reaction kinetics or any sequence of reactions for silicon oxidation and boron removal. Effects of concentrations and temperature are instead related to shifting of the equilibrium conditions.

5.5.1 Interface Equilibrium

Experimental results reveal that local equilibrium is achieved around the interface, as a result of fast chemical reactions including adsorption and desorption. Supply of steam to the interface is found to be slower than all other steps and determines the removal rates, both for silicon oxidation and boron removal in experiments. Effects of varying experimental param-

eters on the rate of boron removal and silicon loss agree with expected dependencies of steam supply with equilibrium at the interphase (Section 5.4.1 and 5.4.2). No effects expected from reaction kinetic resistances including adsorption and desorption reactions are observed, neither for silicon oxidation nor boron removal. Equilibrium modeling of boron removal using the actual supply of steam to the interface agrees closely with boron removal in experiments in Section 5.2. Finally, the threshold steam supply for the onset of passivation in experiments in Section 5.3 agrees with oxygen saturation in the equilibrium around the interface.

Figure 5.15 illustrates how equilibrium in surface reactions, adsorption and desorption combines to equilibrium between bulk species in the gas and the melt around the interface. The experimental agreement with equilibrium around the interface implies that reaction kinetics and mechanisms are masked by back-reactions and the reactants and products are related through the thermodynamic state, irrespective of how it is achieved. Section 5.5.2 includes adsorbed species from literature review of kinetic studies in the representation of equilibrium around the interface, although reaction kinetics does not relate to the results of current experiments. The measurable net rate of reactions is found to be determined from the rate of steam supply only, so this study of boron removal rates is in effect a study of steam supply in combination with equilibrium relations around the interface.
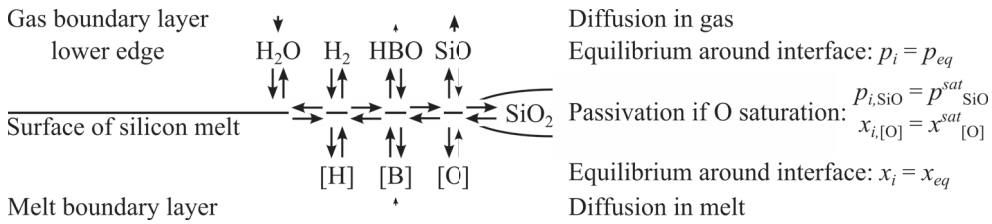
Figure 5.15: Schematic of equilibrium between bulk species around the interface (x_{eq} is mole fraction at equilibrium with gases at partial pressures p_{eq}), including adsorption, reactions at the interface and desorption.

Silicon Oxidation

For equilibrium around the interface, essentially all of the supplied steam decomposes at the surface of silicon melts due to the high oxygen affinity of silicon. Under active oxidation of a clean silicon surface in Reaction (5.34), steam decomposes to SiO as the dominant oxide. The equilibrium constant in Equation (5.35) is $K_{\text{SiO/H}_2\text{O}} = 671$ at 1500 °C and increases with increasing temperature. Activities of silicon and silica are not included in equilibrium expressions as they are approximated to unity due to high purities. The fraction of steam remaining in the established equilibrium is represented by the fraction $\frac{p_{i,\text{H}_2\text{O}}}{p_{i,\text{SiO}}}$, which is $1.5 \cdot 10^{-3}$ at equilibrium with 1 bar hydrogen at 1500 °C. This ratio decreases with increasing temperature and decreasing partial pressure of hydrogen. Conditions of active oxidation in present exper-

iments are thus in the range where steam at equilibrium with the silicon surface decomposes essentially stoichiometrically to SiO as the dominant oxide gas as approximated in Equation (5.36).

$$H_2O + [Si] \rightleftharpoons SiO + H_2 \tag{5.34}$$

$$\frac{p_{i,H_2O}}{p_{i,SiO}} = \frac{1}{K_{SiO/H_2O}p^{\ominus}}p_{i,H_2} \tag{5.35}$$

$$p_{i,SiO} \approx p_{H_2O}^s \tag{5.36}$$

The partial pressure of SiO is thus limited to p_{SiO}^{sat} and excessive oxygen forms silica. Reaction (5.37) shows the global reaction for passive oxidation from steam.

$$2\,H_2O + [Si] \rightleftharpoons SiO_2 \text{ (s/l)} + 2\,H_2 \tag{5.37}$$

The passivation threshold hardly depends on the hydrogen partial pressure, neither in equilibrium modeling or in experiments (Table 4.17). Only the partial pressure of steam in the equilibrium for Reaction (5.37) changes with the partial pressure of hydrogen. This effect is explained by de-coupling steam decomposition in Reactions (5.34) from oxygen saturation in Reaction (5.38). The reactions express equilibrium relations and it is not to be presumed that Reaction (5.38) follow sequentially after Reaction (5.34). Both reactions may proceed in parallel from intermediate species adsorbed to the interface. Passivation was in Section 5.3 observed to start when the steam supply equaled the saturation pressure of SiO at which silica become stable on the melt as expressed in Equation (5.39), assuming unit activities of silica and silicon, at least when the fraction of steam in the gas is not very high. Increasing the temperature of the melt increases the saturation pressure of SiO and so the maximum supply of oxygen to the interface for which a clean melt surface can be maintained.

$$2\,SiO = [Si] + SiO_2 \text{ (s/l)} \tag{5.38}$$
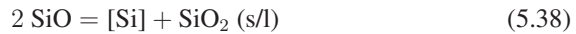
$$p_{H_2O}^s(\text{max}) \approx p_{SiO}^{sat} = K_{SiO_2/SiO}^{-\frac{1}{2}} \tag{5.39}$$

SiO accommodates essentially all oxygen contributing to the oxygen potential. SiO is here used to represent the oxygen potential, as the equilibrium partial pressure of oxygen and its potential is directly related to the partial pressure of SiO over the silicon melt as shown by Reaction (5.40) and its equilibrium constant in Equation (5.41). Oxygen saturation in the equilibrium model at 1500 °C provide $p_{O_2}^{sat} = 2.8 \cdot 10^{-18}$ bar together with $p_{SiO}^{sat} = 0.032$ bar and 56 ppmw [O] in the melt.

230

$$2\,[\text{Si}] + \text{O}_2 \rightleftarrows 2\,\text{SiO} \tag{5.40}$$

$$p_{\text{O}_2} = \frac{p_{\text{SiO}}^2}{K_{\text{O}_2/\text{SiO}}} \tag{5.41}$$

Like steam, CO also decomposes essentially stoichiometrically at the interface under equilibrium, according to Equation (5.42). Carbon in CO is however a contaminant that produce SiC particles at all practical partial pressures of CO. SiC particles locally passivate the interface (Section 4.5.3) and reduce the active area of the silicon melt from which boron can be removed.

$$\text{CO} + 2[\text{Si}] \rightleftarrows \text{SiO} + \text{SiC (s)} \tag{5.42}$$
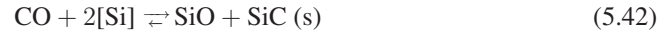
Boron Distribution

The rate of boron removal is found in Section 5.2 to follow the rate of steam supply and SiO loss according to the fraction $\frac{p_{eq,\text{HBO}}}{p_{i,\text{SiO}}}$ for equilibrium around the interface. The equilibrium relation for distribution of boron in the melt and in HBO gas is shown in Reaction (5.43) and the distribution coefficient for boron is expressed through the equilibrium constant in Equation (5.44). As no significant resistance was identified in Section 5.2 for mass transfer of boron from melt and to gas, HBO is assumed to accumulate to its equilibrium partial pressure in the gas leaving the surface (step 4) and the concentration of boron at the interface is approximated to that in the bulk melt. Thus, the effective distribution coefficient between HBO leaving the system and [B] in the bulk melt ($\frac{x_{4,\text{HBO}}}{x_{[\text{B}]}}$) in experiments is directly expressed from equilibrium at the interface in Equation (5.44). The dominant species under experimental conditions with active oxidation are used in Reaction (5.43), as these accommodate approximately the total amount of the elements and may be directly related to the potential of the elements.

Like SiO accommodates approximately all oxygen atoms in the gas and represents the oxygen potential, H_2 accommodates essentially all hydrogen atoms in the gas and represents the hydrogen potential, HBO contains approximately all boron in the gas while the boron potential is represented by the boron content in the melt. SiO also accommodates approximately all silicon atoms in the gas. Reactions (5.34) and (5.43) is used to express the relationship between partial pressures around the interface in the equilibrium established from the supply of steam, and reflects that the experimental results agrees with equilibrium partial pressures around the interface without giving information about the reaction mechanisms that produce them. They do not suppose any reaction mechanism or sequence of silicon and boron oxidation, as SiO and HBO may form in parallel reactions between intermediate species.

231

$$[B] + SiO + \tfrac{1}{2} H_2 \rightleftarrows HBO + [Si] \tag{5.43}$$

$$\frac{p_{4,HBO}}{x_{[B]}} = \frac{K_{HBO/SiO}}{p^{\ominus \frac{1}{2}}} \gamma_{[B]} p_{i,SiO} p_{i,H_2}^{\frac{1}{2}} \tag{5.44}$$

In the equilibrium model, the activity coefficient of boron at infinite dilution in silicon $\gamma_{[B]}^0 = 3.1$ at $1500\,°C$. Adjusting to 80% boron equilibrium fraction in experiments (Section 5.2) compared to the model with $\Delta_f H_{eq,HBO}^{\ominus}(298\ K) = -251\ kJ/mol$ provides an equilibrium constant of $K_{HBO/SiO} = 43$ representative for the experimental results. At $1700\,°C$, $K_{HBO/SiO} = 16$ and $\gamma_{[B]}^0 = 2.8$. The distribution of boron between gas and melt is $\frac{x_{4,HBO}}{x_{[B]}} = 3.8$ with $1\ bar$ hydrogen and oxygen saturation ($p_{i,SiO} = p_{SiO}^{sat} = 28\ mbar$) at $1500\,°C$, and $\frac{x_{4,HBO}}{x_{[B]}} = 10$ at $1700\,°C$ ($p_{i,SiO} = p_{SiO}^{sat} = 231\ mbar$). The distribution coefficient decreases with increasing temperature if the partial pressure of SiO and the supply of steam is held constant, like the stability of HBO.

The fraction of oxygen used for boron removal as compared to silicon oxidation is represented by $\frac{p_{4,HBO}}{p_{i,SiO}}$ in Equation (5.45). Adjusting the equilibrium model to 80% boron equilibrium fraction in experiments provide $\frac{p_{4,HBO}}{p_{i,SiO}} = 1.0 \cdot 10^{-2}$ at $1500\,°C$, 29 ppmw [B] and $1\ bar$ hydrogen, and $\frac{p_{4,HBO}}{p_{i,SiO}} = 3.0 \cdot 10^{-3}$ at $1700\,°C$, 26 ppmw boron in the melt and $1\ bar$ hydrogen. Division by the mole fraction of boron in the melt gives the enrichment ratio for boron, which is estimated to $E = 162$ at $1500\,°C$ and $E = 46$ at $1700\,°C$ with $1\ bar$ hydrogen for representative experiments in Section 5.2. The values for equilibrium modeling adjusted to present experiments in similar range as enrichment ratios in plasma experiments by Altenberend [18] in Table 2.3. The modification of the enthalpy of formation of HBO necessary for explaining experimental removal rates by equilibrium simulation provide more than an order of magnitude higher HBO partial pressure, distribution coefficient, enrichment ratio and thus boron removal efficiency than expected from prior thermodynamic modeling (Section 2.1).

$$\frac{p_{4,HBO}}{p_{i,SiO}} = \frac{K_{HBO/SiO}}{p^{\ominus \frac{1}{2}}} \gamma_{[B]} x_{[B]} p_{i,H_2}^{\frac{1}{2}} \tag{5.45}$$

The ratio between the rate of boron removal and the rate of silicon loss decreases with increasing temperature. However, increasing the temperature increases the saturation pressure of SiO, and the distribution coefficient for boron may be increased by simultaneously increasing oxygen supply and temperature. As the steam supply may be increased without passivation at increasing temperature, the boron removal rate may be increased like the partial pressure of HBO in the gas flow out of the system, although at the expense of a higher relative melt loss. Increasing the steam supply may also increase the partial pressure of hydrogen at the interface from decomposition of steam, unless excessive amounts are added in the feed gas. Using hydrogen to dilute the steam is advantageous compared to other atmospheres both for

the removal rate of boron according to Equation (5.44) and the relative melt loss from $\frac{p_{4,\text{HBO}}}{p_{i,\text{SiO}}}$ in Equation (5.45). However, since steam releases hydrogen as it reacts to SiO at the silicon surface, replacing steam with hydrogen in the gas is more beneficial for the boron removal rate. This is seen in the distribution coefficient in Equation (5.44) as the partial pressure of HBO in the gas increases proportionally with the partial pressure of SiO, but with the square root of the partial pressure of hydrogen. The square root dependence of hydrogen content in the gas on the boron removal rate has been observed by [18] from experimental data. Without hydrogen in the feed gas, steam supplies both SiO and hydrogen ($p_{i,\text{H}_2} = p_{i,\text{SiO}} \approx p_{\text{H}_2\text{O}}^s$ for the approximately stoichiometric Reaction (5.34)) and $\frac{p_{i,\text{HBO}}}{x_{[\text{B}]}} \propto p_{\text{H}_2\text{O}}^{s\ 1.5}$ gives a reaction order for supply of steam to the interface of $\alpha_{eq,\text{H}_2\text{O}} = 1.5$ like in equilibrium modeling and most likely in experiments (Section 5.4.1). Reaction orders of $\alpha_{\text{H}_2\text{O}} = 1.5$ for steam in inert atmosphere and $\alpha_{\text{H}_2\text{O}/\text{H}_2} = 1$ with excess hydrogen [11], $\alpha_{\text{H}_2} = 0.5$ for hydrogen [17, 18, 67] and $\alpha_{[\text{B}]} = 1$ (boron removal follows the first order rate law in all experiments and studies) are particular to equilibrium boron removal by HBO formation as the dominant boron-containing gas.

5.5.2 Mass Transfer

Removal rates depend most directly on the rate at which reactants are supplied to the interface and the rate products are removed, as the reactions are fast and reach equilibrium. Steam and hydrogen are supplied from the gas to interface reactions, while boron is supplied from the bulk of the melt in experiments. Hydrogen does not react significantly and may be assumed to have the same partial pressure at the interface as set in the feed gas. If steam is used without hydrogen in the gas feed, the partial pressure of hydrogen around the interface may be assumed to be determined from decomposition of steam. Supply of steam is found to be the only step that limits the removal rate of boron and silicon, and as it decomposes completely at silicon surface, the rate of steam supply is estimated to equal the rate of loss of the silicon melt. As the gas flow and its concentrations are held constant during experiments, the rate of silicon loss and steam supply is assumed also to be constant over the duration of gas blowing. For gas blowing experiments, the impinging jet gas flow transfers the gas reactants steam and usually hydrogen to the reactions at the melt surface and removes the gas products and fumes.

Fuming in Active Oxidation

In active oxidation, the silicon surface is kept clean by partial oxidation to SiO, and SiO is oxidized further to silica in a feed-back reaction with steam at higher partial pressures within the gas, according to the fuming Reaction (5.46). The silica produced in the gas form spherical particles as shown in Section 4.5.1 and is similar to the fumes characterized by Næss [55] from active oxidation experiments. Kamfjord et al. [82] proposed a mechanism involving formation of liquid droplets due to the high heat of silica condensation. The nucleated droplets may grow by collision until they solidify as the observed spherical particles.

The equilibrium constant for Reaction (5.46) is large ($K_{H_2O+SiO} > 10^4$ at $< 1700\,°C$) and the reaction tends towards low partial pressures of either steam or SiO (or both) in Equation (5.47). In the equilibrium around the interface, the partial pressure of steam is low and SiO is the dominant oxide gas in what Ratto et al. [78] called the inner homogeneous layer between the surface and the heights where Reaction (5.46) occurs (the heterogeneous layer). Modeling by Næss et al. [31] shows complete consumption of SiO within the gas boundary layer in impinging jet experiments with diluted oxygen in $114\,mm$ diameter crucibles with up to $26\,m/s$ gas velocity at the lance tip, which is the same as in current impinging jet experiments with $2\,l_N/min$ gas flow rate through $4\,mm$ diameter lances. Complete consumption of SiO to silica fume is also consistent with reliable measurements for the fraction of steam in the feed gas that is supplied to the interface and reacts with silicon. Silica is also the only observed product in the crucible and furnace after experiments, and no sign of SiO condensation has been observed. Outside the heterogeneous layer where Reaction (5.46) takes place, steam is the dominant oxide gas at least towards the center of the impinging jet flow, where it is first introduced on the surface.

$$H_2O + SiO = SiO_2 \text{ (l/s)} + H_2 \tag{5.46}$$
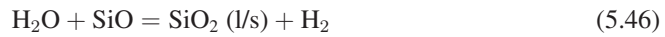
$$p_{H_2O}p_{SiO} = \frac{p_{H_2}}{K_{H_2O+SiO}} \tag{5.47}$$

Impinging Jet Flow

Figure 5.16 schematically shows the impinging jet flow pattern for gas blowing in the axisymmetric geometry of the crucible. The vertical symmetry line goes through the center of the lance in the center of the crucible. The left side of the symmetry axis in Figure 5.16 shows an ideal impinging jet flow pattern with laminar flow. Laminar flow is verified by low Reynolds numbers in computational fluid dynamic (CFD) modeling of experiments. No effect of the crucible wall is indicated except that the gas is deflected upwards as it leaves the surface. The different features of the flow pattern are not drawn to scale. The free boundary in Figure 5.16 defines the outer border of the impinging jet flow pattern and the surrounding gas above [116].

A gas jet with laminar velocity profile ($Re < 10$ in CFD models) exits the lance and impinges on the melt surface below. The area under the lance where the jet is deflected by the melt surface is called the stagnation area and there is a stagnation point at the surface under the middle of the vertical gas jet. Mass transfer by diffusion to/from the interface is constant throughout the stagnation region [75] as indicated by the constant thickness of the boundary layer in Figure 5.16. Diffusion is also fastest in the stagnation region [74]. Increasing a gas flow of argon with diluted steam to $10\,l_N/min$ Pass_Ar,H$_2$ resulted in dimple formation at the melt surface under the lance. The gas flow of $10\,l_N/min$ Ar through the $4\,mm$ diameter lance was over the limit for splashing in that some solidified silicon droplets was observed after the

234

experiment. Neither dimple formation nor splashing was observed in other experimental gas flows, of up to $16\,\mathrm{l_N/min}$ hydrogen with diluted steam and $2\,\mathrm{l_N/min}$ Ar with steam, like in fluid dynamic modeling by Nordstrand and Tangstad [17]. After the gas has been deflected in the stagnation region, it flows along the surface in the wall jet region. The gas slows down as it spreads radially over the surface and slightly upwards, and the mass transfer coefficient for diffusion to/from the interface decreases accordingly [75] as represented by an increasing thickness of the gas boundary layer. Accordingly, the total mass transfer coefficient averaged over the available cross-section area was in Section 5.4.2 found higher in a $38\,\mathrm{mm}$ diameter crucible than in a $70\,\mathrm{mm}$ diameter crucible.

Experiments with impinging jet gas blowing achieved higher removal rates than with bubbling of the gas by submersion of the lance because the gas flow rate and thus the steam feed rate that could be set in an experiment with bubbling in Section 5.4.2 was limited due to splashing. Complete diffusion of steam to the interface was achieved at higher gas flow rates in impinging jet experiments for which the length of the wall jet flow along the surface in gas flow modeling was not constrained by the crucible radius (Section 5.4.2). Further increased gas flow rates in Section 5.4.2 without scaling the area of the melt surface resulted in mass transfer resistance as diffusion to the interface did not complete so that part of the steam was lost with the gas flow out of the system. The gas velocity was increased as a result of increasing the gas flow rate, and the residence time of the gas in the wall jet flow along the surface was reduced in experiments with increased gas flow rates.
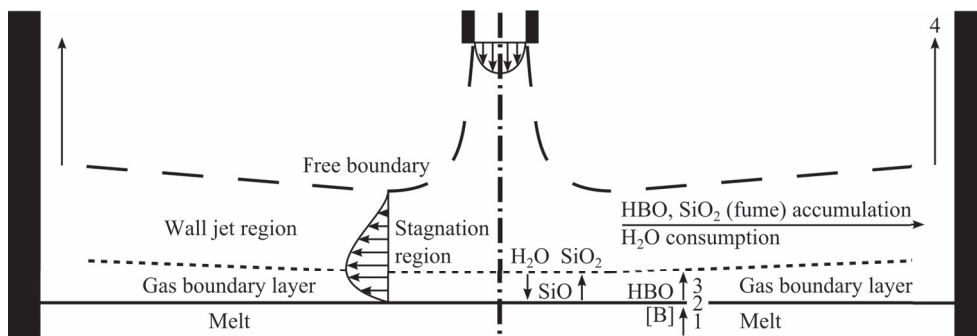

Figure 5.16: Schematic of impinging jet gas flow (left half) and mass transfer (right half). The geometry is axisymmetric around the center line. A jet of gas is fed from the lance in the top center, flows along the melt surface (full horizontal line) and leaves after deflection by the crucible wall at the edges.

The gas reactants are brought close to surface by the jet out of the lance, provided the lance exit is close enough above the surface (Section 5.4.4). According to impinging jet theory, there is a range of lance heights over the surface for which mass transfer is independent of the height. Scholtz and Trass [75, 116] relate this region to the pressure in the stagnation region and the length of the jet out of the lance in which the center velocity is maintained constant. The velocity across the jet is slowed down from the outside in due to spreading in the surrounding gas, as indicated with velocity profiles in Figure 2.7.

Steam is usually diluted in hydrogen or inert carrier gas due its threshold for passivation, and diffuses from the bulk of the gas flow to the interface through the gas boundary layer. During active oxidation of the melt surface, the fuming Reaction (5.46) influences the concentration profile and diffusion of steam to the interface. The total amount of steam available for reactions with the melt is reduced as steam is partly consumed in the gas, which thus reduces the steam concentration and the gradient towards the interface. The rate limit for diffusion of SiO is however enhanced by fuming as fuming consumes SiO within the gas boundary layer [31] and reduces the diffusion distance, and so the fuming Reaction (5.46) increases the concentration gradient for SiO.

After deflection in the stagnation region, the gas flows along the surface in the wall jet region and continued diffusion to/from the interface gradually reduces the bulk steam concentration while HBO and fume accumulates. Accumulation in the wall jet proceeds until steam is depleted or the gas flows away from the surface (step 4 in Figure 5.16) due to deflection by the crucible wall. The gas and fumes in the gas flow away from the surface that permanently leaves the melt is considered to leave the melt system.

CFD modeling of the laminar impinging jet gas flow pattern in Figure 5.17 with $2\,l_N/min$ gas flow rate of hydrogen with diluted steam shows a vortex at the end of the wall jet, which is short for this typical gas flow. The vortex recirculates part of the gas from the wall jet back to the periphery of the impinging jet from the lance and may contribute to increase the utilization of steam. Recirculating gases or fumes are not considered to leave the system, only the gas flow which continues upwards and leaves the melt permanently. Parametric studies in the model find the length of the wall jet to increase with increasing gas flow rate and decreasing lance diameter, which increases the velocity of the jet from the lance. Also the gas velocity along the surface in the wall jet region and presumably the mass transfer coefficient for diffusion increases as the thickness of the boundary layer decreases with these parameters. In experiments in Section 5.4.3, with $2\,l_N/min$ gas flow of hydrogen, no effect of lance diameter was distinguished for boron removal with lance diameters ranging from $1\,mm$ to $35\,mm$. CFD modeling does not indicate a jet out of the $35\,mm$ lance. With increasing gas flow rate, comparison of models with and without the crucible wall indicate that the length of the wall jet becomes constrained by the crucible wall at a gas flow rate of $6\,l_N/min$ hydrogen, and loss of steam by incomplete diffusion to the interface becomes apparent at this flow rate in experiment Q_6 (Sections 5.1 and 5.4.2).
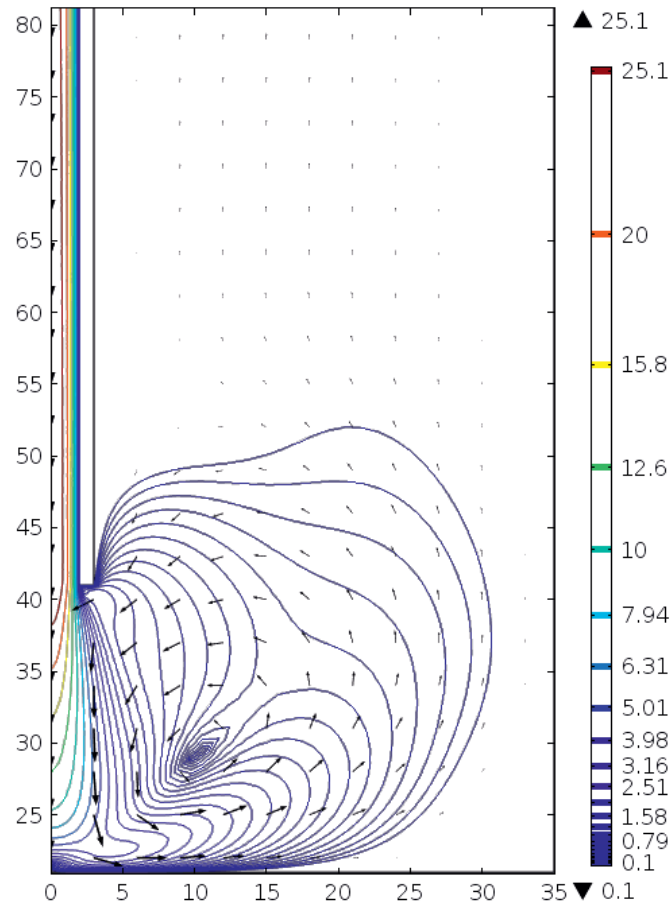
Figure 5.17: Axisymmetric CFD model of laminar impinging jet gas flow made in COM-SOL Multiphysics 4.4 with parameters representing experiment Q_2 (2 l_N/min hydrogen in 70 mm diameter crucible and 4 mm diameter lance 20 mm above the melt surface). The Model indicates a short wall jet region at these flow conditions and the gas flow turn away from the surface around the vortex marking the end of the wall jet. The vortex recirculates the upper part of the wall jet back to the periphery of the impinging jet while the lower part of the wall jet leaves the system. The axes show height and radius [mm] inside the crucible. The bottom axis represents the surface of a 21 mm deep melt (200 g silicon) and the surface is approximated to a flat no-slip wall. The color legend represents the gas velocity [m/s], which is constant along each contour line. The spacing of the contour lines follows a logarithmic scale for the gas velocity while the color follows a linear scale. The arrows show the direction of flow at the base and the size scales logarithmically with the gas velocity.

237

Steam Supply

Steam is fed in the gas flow from the lance at a rate given by its concentration ($C = \frac{p}{RT}$) in the gas flow according to Equation (5.48). It is the concentration that change with temperature in an open system, not the partial pressure because it relates to the mole fraction and the total pressure ($p_{H_2O} = x_{H_2O}p$), which both do not change with temperature. Changes in the total amount of gas by fuming (Reaction (5.46)) is not taken into account as its effect on the partial pressures in the gas is assumed negligible for most experiments, but it may likely be important for experiments with large fractions of steam in the feed gas. The fraction $\frac{Q}{RT_Q}$ in Equation (5.48) is independent of temperature because expansion of the gas upon heating is according to ideal gas law proportional to the temperature ($Qp = \frac{dn}{dt}RT_Q$), and the gas flow rate can for instance be evaluated at normal conditions with $T_Q = 293$ K which is usual for representing mass flows. Positive signs are used for flows into the system or the interface and flows out of the system or from the interface are considered to be in negative direction.

$$\frac{dn_{H_2O}}{dt} = \frac{Q}{RT_Q}p_{H_2O} \tag{5.48}$$

Steam in the feed gas may have the following three fates, considering active oxidation of a clean silicon surface.

- Consumption in fuming Reaction (5.46).

- Supply to the interface and decomposition (Reaction (5.34)).

- Escape unreacted in the gas flow out of the system.

The part of the steam that reacts with SiO in the gas (fuming Reaction (5.46)) does not reach the surface, so it is not supplied to the interface and does not contribute directly to remove boron. However, the release of hydrogen may contribute to increase the partial pressure of hydrogen around the interface and thus increase the fraction of the steam supply that removes boron compared to silicon according to Equation (5.45). The part of the steam that is consumed in the gas by fuming equals approximately the part that is supplied to the interface and decomposes, since approximately all of the supplied steam produces SiO (Equation (5.36)) and all SiO oxidizes further to silica fume in Reaction (5.46). The part of the steam in the feed gas that is supplied to the interface and decomposes is $p_{H_2O}^s$ in Equation (5.49) and it represents a fraction of the total steam feed, called the steam supply fraction $\frac{p_{H_2O}^s}{p_{H_2O}}$. Any fraction of steam that remains unreacted in the gas flow out of the system also does not contribute to the removal of boron or silicon from the melt. Considering complete decomposition of steam supplied to the interface and complete consumption of SiO by fuming, the maximum expected steam supply fraction is 50% with no additional mass transfer resistance.

$$p_{H_2O}^s = \frac{p_{H_2O}^s}{p_{H_2O}}p_{H_2O} \tag{5.49}$$

238

Section 5.1 finds no loss of steam in experiments with $2 \, l_N/\min$ gas flow rate, as the weight-loss of the melt accounted for 50% steam supply to the interface. The steam supply fraction decreased at higher gas flow rates, as diffusion from the wall jet to the interface did not complete within the crucible radius and a significant fraction of steam remained unreacted in the gas flow out of the system. The passivation threshold for the partial pressure of steam in the feed gas is estimated in Equation (5.50) from the steam supply fraction by combining Equations (5.49) and (5.39). Observations of the onset of passivation with increasing partial pressures of steam in the feed gas at $2 \, l_N/\min$ in experiments in Table 4.17 find the passivation threshold for steam in the feed gas in these experiments to be a factor 2.4 higher than the passivation threshold for supplied steam as determined by the saturation pressure of SiO over silicon and silica. The ratio between the passivation threshold for supply to the equilibrium around the interface and the passivation threshold observed in the feed gas ($p^s_{H_2O}(\max)/p_{H_2O}(\max)$) correspond to the steam supply fraction which could be measured to $\frac{p^s_{H_2O}}{p_{H_2O}} = 0.41$ in experiment Pass_H$_2$a. Both the steam supply fraction below 50% and the ratio between the passivation threshold in the feed compared to modeling of the interface equilibrium above 2 indicate slight mass transfer resistance by incomplete diffusion of steam to the interface in experiments in Table 4.17.

$$p_{H_2O}(\max) \approx \frac{p^{sat}_{SiO}}{\frac{p^s_{H_2O}}{p_{H_2O}}} \tag{5.50}$$

The amount of silicon loss over the time of gas blowing with steam (t_r in tables in Section 3.3) approximates the rate of steam supply as steam decomposes essentially completely at equilibrium around the interface. The rates of steam supply and silicon loss are assumed constant over time, like the feed gas. For active oxidation, silicon oxidizes exclusively to SiO at the interface ($\Delta n_{Si} = n_{SiO}$) and the amount of silicon loss is estimated by the weightloss of the melt ($\Delta m \approx M_{Si}\Delta n_{Si}$). Previous studies of active oxidation by molecular oxygen conclude that supply of oxygen determine the rate of silicon oxidation, and it is assumed that oxygen supply is also rate determining with steam as the oxidizing agent, providing an estimate for the rate of steam supply in Equation (5.51) as the part of the steam that is supplied to the interface from the feed gas flow. Equation (5.52) relates the rate of steam supply to the rate of steam feeding in Equation (5.48) and estimates the steam supply fraction ($\frac{p^s_{H_2O}}{p_{H_2O}} = \frac{dn^s_{H_2O}}{dt}/\frac{dn_{H_2O}}{dt}$). The steam supply fraction accounts for diffusion resistance of steam through the boundary layer in combination with consumption in the fuming Reaction (5.46).

$$\frac{\Delta n_{Si}}{t_r} \approx \frac{dn^s_{H_2O}}{dt} = \frac{Q}{RT_Q}p^s_{H_2O} \tag{5.51}$$

$$\frac{dn^s_{H_2O}}{dt} = \frac{Q}{RT_Q}\frac{p^s_{H_2O}}{p_{H_2O}}p_{H_2O} \tag{5.52}$$

Boron Removal

The removal rate of boron is expressed through the total mass transfer coefficient in Equation (5.53), which is constructed from Equation (2.16) with conversion to mole fraction of boron in the bulk of the melt ($C_{[B]} = \frac{\rho}{M} x_{[B]}$), where the average molar mass and density of the melt may be approximated to that of silicon ($M \approx M_{\text{Si}}$ and $\rho \approx \rho_{[\text{Si}]}$, respectively). The total mass transfer of boron covers all steps of mass transfer from the bulk of the melt to the gas flow leaving the melt system.

$$\frac{\mathrm{d}n_{\text{B}}}{\mathrm{d}t} = -A_c k_t \frac{\rho}{M} x_{[B]} \tag{5.53}$$

Equation (5.54) relates the removal rate of boron to the rate of steam supply as the rate determining step with equilibrium around the interface. The equation is valid under active oxidation in which approximately all of the steam supplied to the interface reacts with silicon according to Equation (5.36) and $\frac{p_{\text{H}_2\text{O}}^s}{p_{\text{H}_2\text{O}}} p_{\text{H}_2\text{O}} \leq p_{\text{SiO}}^{sat}$. The total mass transfer coefficient is expressed in Equation (5.55) from supply of steam by inserting Equations (5.53), (5.45) and (5.52) into Equation (5.54). The hydrogen partial pressure in Equation (5.55) can be taken either as that in the feed for a large fraction $\frac{p_{\text{H}_2}}{p_{\text{H}_2\text{O}}}$, from steam decomposition $p_{\text{H}_2} \approx \frac{p_{\text{H}_2\text{O}}^s}{p_{\text{H}_2\text{O}}} p_{\text{H}_2\text{O}}$ (possibly also accounting for any contribution by hydrogen from fuming in Reaction (5.46)) if hydrogen is not fed, or the sum of both sources for intermediate ratios $\frac{p_{\text{H}_2}}{p_{\text{H}_2\text{O}}}$ of hydrogen and steam feeding. The temperature T_Q and the unit of the gas constant and refer to the unit for the flow rate, and are $R = 0.082 \, \text{l}_\text{N} \cdot \text{atm/mol/K}$ and $T_Q = 293$ K for gas flow rate Q in [l_N/min]. Equation (5.55) can also be constructed from the rate HBO leaves the system (step 4 in Figure 5.16) as the factor for $k_t \approx k_4$ in Equation (2.62) with $p_{i,\text{SiO}} = \frac{p_{\text{H}_2\text{O}}^s}{p_{\text{H}_2\text{O}}} p_{\text{H}_2\text{O}}$ (combining Equations (5.36) and (5.49)).

$$-\frac{\mathrm{d}n_{\text{B}}}{\mathrm{d}t} = \frac{p_{4,\text{HBO}}}{p_{i,\text{SiO}}} \frac{\mathrm{d}n_{\text{H}_2\text{O}}^s}{\mathrm{d}t} \tag{5.54}$$

$$k_t = \frac{Q}{RT_Q A_c} \frac{M}{\rho} \frac{K_{\text{HBO/SiO}}}{p^{\ominus \frac{1}{2}}} \gamma_{[B]} p_{\text{H}_2}^{\frac{1}{2}} \frac{p_{\text{H}_2\text{O}}^s}{p_{\text{H}_2\text{O}}} p_{\text{H}_2\text{O}} \tag{5.55}$$

The rate of boron removal or the gas consumption required for a given ratio of boron removal can be calculated from equilibrium for a given melt temperature from the knowledge of the supply of steam and potentially hydrogen, as long as supply of steam is rate determining for boron removal. Like the rate of boron removal increases with increasing steam supply at a constant total gas flow rate, the total gas consumption necessary to remove boron, for instance by a factor 100, is reduced with increasing steam supply. Based on the saturation pressure of SiO in the equilibrium model, 1800 °C melt temperature allows for a steam supply above 0.5 bar, which represents 50% steam supply from pure steam at atmospheric pressure. The

model predicts that boron can be removed from 30 ppmw to 0.3 ppmw in a silicon melt at $1800\ ^{\circ}$C with the minimum requirement of $357\ \mathrm{l_N/kg}$ pure steam at atmospheric pressure in the feed gas per kg of melt, assuming a maximum of 50% steam supply and rate limitation by steam feeding. The corresponding silicon loss is 17%, which can be reduced by decreasing the temperature and adding hydrogen, at the cost of increased gas consumption since only a minor fraction of hydrogen reacts at the interface. 0.5 bar steam and hydrogen is input to the equilibrium simulation for the interface, with the assumptions that 0.5 bar of hydrogen is produced from consumption of steam and SiO above the interface and that this hydrogen is available for the interface reactions. The net diffusion of hydrogen would however be away from the interface, since hydrogen is also released from the remaining steam that reacts at the interface. As these assumptions indicate, there are uncertainties that remain to be explored regarding the supply of steam and hydrogen to the interface for high steam partial pressures in the feed.

Boron is supplied to the reactions at the interface by diffusion and convection in the melt. Mass transfer from the melt was not found to influence the rate of boron removal in Section 5.4.5, at least for the total mass transfer coefficients reached in experiments, which was up to $k_t = 51 \pm 8.3\ \mu\mathrm{m/s}$ in an induction furnace and $k_t = 8.0 \pm 1.3\ \mu\mathrm{m/s}$ in the resistance furnace without forced convection in the bulk of the melt. Drag from the wall jet gas flow may however introduce forced convection in the top of the melt and enhance mass transfer from the melt to the surface. A magnetohydrodynamic model for the melt in the Induction II furnace (Section 5.4.5) estimates a mass transfer coefficient for supply of boron of roughly $k_1 \approx 200\ \mu\mathrm{m/s}$ and uniform concentration in the bulk of the melt at steady-state.

Melt mass transfer may pose a significant resistance to the total mass transfer and become rate determining if the gas-phase mass transfer is improved further. Upscaling of the gas flow rate is expected to provide higher gas velocities and faster mass transfer to the interface than what was reached in the current experimental setup, according to impinging jet theory and extrapolation of its trend in Figure 5.9. Melt mass transfer may thus become more important for the total resistance at larger scales, particularly towards the center under the lance where gas-phase mass transfer is fastest [74] in the impinging jet flow pattern. In addition, the intensity of convection may be reduced upon upscaling and diffusion to the interface may be less enhanced as a concentration gradient may extend further into the melt. In addition to limit the rate of boron removal, resistance to mass transfer from the melt is also expected to increase the loss of silicon per amount of boron removed, since silicon is the host material and melt mass transfer resistance only reduces the concentration of boron and other impurities at the interface.

Kinetics in Interface Equilibrium

Considering chemical reactions to be fast compared to removal of products, Reactions (2.36) and (2.37) for equilibrium at the interface can be rationalized kinetically by fast reactions. Due to the low concentration of boron in MG- and SoG-Si melts it can be rationalized that steam collides much more frequently with silicon than boron atoms upon reaching the interface. The majority of steam molecules can thus be adsorbed to silicon before colliding with boron. SiO, adsorbed oxygen species or dissolved oxygen can react further with boron assuming that that SiO is not instantly removed from the surface, but have sufficient time to diffuse and collide with boron atoms. Formation of HBO requires additional reaction steps involving hydrogen and shares any of the intermediate species of adsorbed oxygen in the mechanism for SiO production.

Extensive studies of oxidation of solid silicon surfaces have identified adsorbed species and mechanism and kinetics of reactions between them [84, 117]. Figure 5.18 includes adsorbed species of hydrogen, steam and oxygen on silicon solid surfaces in a mechanistic representation of reactions at quasi-equilibrium around the interface. The term quasi-equilibrium is used in this section to indicate that equilibrium partial pressures are established around the interface even though there is a net rate of reactions, and quasi-equilibrium is the proper term when the net rate is negligible compared to the rates of individual reaction steps so that it has negligible effect on production and consumption of individual species compared to reactions and back-reactions and thus does not shift the concentrations from the equilibrium value. In lack of knowledge about adsorbed species on liquid silicon, the same species found in studies of solid silicon is used in Figure 5.18. Also, the reverse mechanism from adsorbed SiO to adsorbed steam has not been studied and reverse reactions are in Figure 5.18 indicated simply by adding reverse arrows between the surface intermediates in studies of forward reactions for silicon oxidation. Although the current analysis focuses on adsorption and desorption to/from adsorbed species at the interface, it is also expected that these dissolve into the melt (at equilibrium concentrations in the top layer) and may also take part in intermediate steps as proposed by Safarian et al. [41].

It is however not necessary to know the reaction mechanism in order to discuss the results of present experiments with quasi-equilibrium around the interface. Boron species are not included in Figure 5.18 as the intermediate species for formation of HBO at a boron-doped silicon surface has not been examined. Figure 5.18 provides a rationale for how the net reaction rate may be established at quasi-equilibrium and limited by supply of steam under the conditions of present experiments. The experimental conditions in studies of adsorption, reaction kinetics and desorption at the interface are very different from present experiments and the following discussion argues that back-reactions and re-adsorption (added in Figure 5.18) are likely to occur in present experiments, as indicated by the experimental agreement with quasi-equilibrium around the interface.

242

Gas boundary layer
lower edge

Mean free path

Adsorbed species

Surface of silicon melt

Melt boundary layer

H_2 H_2O SiO

H   H   H   O$-$H   O   O

Si   Si   Si   Si   Si   Si   Si SiO_2

[H]   [O]

Diffusion: $J_t = J_\downarrow(C_i + dC) - J_\uparrow(C_i)$
Equilibrium around interface: $p_i = p_{eq}$
Gas kinetics: $|J_\downarrow(C_i)| = J_{max} > |J_t|$

Passivation if O saturation:
$p_{i,\text{SiO}} = p^{sat}_{\text{SiO}}$
$x_{i,[\text{O}]} = x^{sat}_{[\text{O}]}$

Equilibrium around interface: $x_i = x_{eq}$
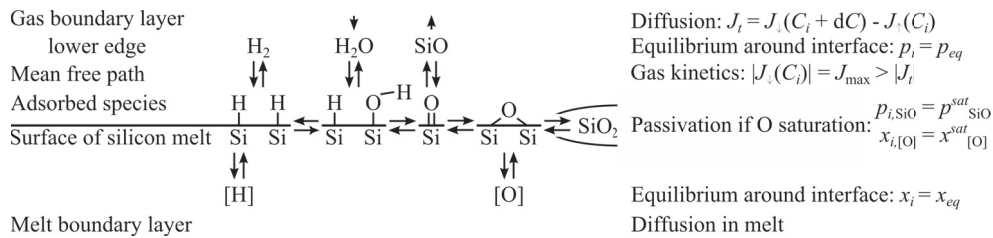Diffusion in melt

Figure 5.18: Potential mechanism of silicon oxidation with back-reaction and re-adsorption in quasi-equilibrium around the interface, showing the total flux (J_t) of diffusion as the net of upwards ($J_\uparrow$) and downwards ($J_\downarrow$)fluxes of molecular scattering.

Kinetic studies like those by Engstrom et al. [84] are not at steady-state conditions like current experiments, precisely in order to be able to study the reaction kinetics. Rather, interface reaction kinetics including adsorption and desorption kinetics is found from the change between a square wave of reactant supply, where a constant supply of reactant starts and ends instantly, and the wave of different signals produced during reactions, as illustrated by Balooch et al. [118]. Engstrom et al. [84] achieved square waves of reactant supply by periodically chopping a molecular beam in ultra-high vacuum. The signal intensity from mass spectrometric measurement of SiO desorption [84] exhibit an initial and final transient after an abrupt start or end of constant reactant supply, and interface reaction kinetics including adsorption and desorption is studied from the changes in the wave of signals produced during reactions from the square wave of reactant supply. At high temperature ($1027\,°C$ was highest by Engstrom et al. [84]), a steady rate of SiO production was stabilized within $0.2\,\text{ms}$, which show the duration of both the initial and final transient. Such fast reaction kinetics at the interface explain how silica appeared to form immediately at the interface after the steam supply was increased beyond the threshold for passivation in "Pass" experiments, in Section 4.4 .

Another important difference between kinetic studies [84, 117] and present experiments is that kinetic studies use ultra-high vacuum ($\leq 10^{-10}\,\text{bar}$) while present experiments use atmospheric pressures. In ultra-high vacuum, the mean free path of gases is in the range of kilometers [119] and reactants may be transferred by a molecular beam directly from the source to the interface. Each reactant molecule may presumably only collide once with the interface, so that the sticking coefficient can be determined for a single collision. Desorbed species move straight to the reactor wall and are unlikely to be scattered back to the interface, assuming that the field of view of the interface from the reactor wall is small. At atmospheric pressures, however, the mean free path of gases is in the range of hundreds of nanometers [119]. At the distances in the range of the mean free path above the interface, the solid angle to the interface spans the entire lower hemisphere, and a gas molecule has a 50% chance of being scattered in the direction of the interface in each collision.

Due to the short mean free path between collisions, the net transport of gases above the interface occurs by diffusion through the gas boundary layer. The gas boundary layer was modeled

243

by Næss et al. [31] to be in the order of a millimeter. As the gas boundary layer is orders of magnitude larger than the mean free path of gases, it can be understood as negligibly thin slices of gas with random scattering of the molecules. The flux of gas molecules scattered out of such a slice depends on the concentration of the molecules. In a concentration gradient, the net flux of diffusion (J_t in Figure 5.18) across a plane between two slices is the difference between the flux of molecules scattered down from above ($J_\downarrow$) and the flux of molecules scattered up from below ($J_\uparrow$). The lowermost slice at the edge of the boundary layer next to the melt surface (called Knudsen Layer [120]) is considered to be in quasi-equilibrium with adsorbed species at the interface, due to the agreement of equilibrium between bulk species to the present experimental results. The flux of molecules that collide with the interface is the total flux of molecules that are scattered down to the interface, which is higher than the net diffusion flux. In collision with the interface, molecules may be adsorbed to available atoms of the melt surface or scattered back if the site is already occupied. The maximum flux of molecules colliding on the interface is calculated by the Hertz-Knudsen [121] Equation (5.56), assuming that all molecules stick to the interface and not accounting for desorption ($p_j = 0$), and it is compared to the net flux calculated for the experiment with highest weight-loss (Q_16b).

$$J_{\text{max,j}} = \frac{p_{eq,\text{j}}}{\sqrt{2\pi M_{\text{j}} RT}} \tag{5.56}$$

For steam, the modeled equilibrium partial pressure around the interface is $p_{eq,\text{H}_2\text{O}} = 1.67 \, \text{Pa}$, and the net flux is close to the maximum estimate for adsorption ($\frac{J_t}{J_{\text{max, H}_2\text{O}}} = 0.8$). The remaining fraction (20%) is ideally the maximum fraction of steam that does not stick upon collision with the interface, based on the flux of steam consumption necessary to produce the measured weightloss in the experiment. Steam may return from the interface either by back-scattering in collisions with the interface or from re-generative desorption [122] as a back-reaction at the interface. It thus appears like most of the steam adsorb in the first collision with the interface and its adsorbed specie (Si-H + Si-OH in Figure 5.18) react further, which is reasonable in that the low partial pressure of steam in equilibrium with the silicon melt indicate significantly faster kinetics for reactions that consume steam than for back-reactions that produce steam. Also, the high ratio indicates that most of the atoms of the melt surface are unoccupied, which can indicate short residence time of adsorbed species on the interface, which may also be rationalized by fast chemical reactions and desorption. Surface renewal from convection of the melt may also contribute to clean the surface, by exposing new silicon atoms to the gas and entraining existing surface atoms with adsorbed species into the melt. J_{max} is not assumed to be accurate for the high pressure in present experiments and is mainly intended for an order-of-magnitude comparison to the net flux, and the indications are not assumed to be conclusive.

For SiO, equilibrium modeling for the estimated steam supply in in Q_16b provides $p_{eq,\text{SiO}} \approx 0.010 \, \text{bar}$, and the ratio of the net flux of silicon loss to the maximum estimate for des-

orption gives a fraction in the order of $\frac{J_t}{J_{\mathrm{max,\,SiO}}} = 2 \cdot 10^{-3}$. The desorption flux of SiO is balanced by re-adsorption, except for a negligible net flux in the quasi-equilibrium around the interface. It thus appears that up to 500 SiO-molecules are scattered back to the surface for every molecule that diffuses away. Molecules that are incident on the surface may again be scattered back to the gas or be adsorbed. Violanda and Rudolph [123] used density functional theory to predict that there is almost no energy barrier for adsorption of SiO, although on solid silicon. SiO molecules that adsorb may again desorb or feed back-reactions in the quasi-equilibrium on the surface as indicated by reverse arrows in Figure 5.18. The mismatch between the maximum flux of H_2O desorption estimated in experiment Q_16b and the flux of SiO re-adsorption suggests that most of the re-adsorbed SiO does not react in a complete sequence back to steam. Any intermediate adsorbed specie may react forwards, backwards or in parallel reactions not included in Figure 5.18, for instance with boron to produce HBO.

For impinging jet experiments of oxidation of liquid silicon by oxygen in air, Næss [55] employed a sticking coefficient of 0.01 for the probability that oxygen adsorb to the interface in order to account for differences between calculated and experimental mass transfer coefficients. Equations by Scholtz and Trass [75] was used to calculate a mass transfer coefficient for the gas boundary layer of the impinging jet experiments, as compared to estimates of the total mass transfer coefficient from the amount of fume produced during experiments. A difference between molecular oxygen and steam as oxidizing agent may be directly seen by comparing oxygen consumption. The oxygen consumption is at the highest 43%, in experiments with air by Næss et al. [31] and up to 100% (50% steam supply) in present experiments. This is in spite of a larger crucible diameter (114 mm [31]), while the lance height (25 mm), lance diameter (5 mm) and gas velocities (5-26 m/s) in experiments by Næss et al. [31] are similar to present experiments. The gas velocities compares to 2.6-21 m/s (not accounting gas expansion by heating through lance) through 4 mm diameter lances in present experiments. Næss et al. [31] reported the highest oxygen consumption in experiments with the lowest partial pressure of oxygen, of 0.042 atm for air diluted with argon.

The low oxygen consumption of 4%-10% in experiments by Næss et al. [31] with 0.21 atm oxygen in air is consistent with the absence of passivation, as the saturation pressure of SiO is 0.048 bar at the melt temperature of 1550 °C. As they did not find such low gas consumptions to be quantified solely by fluid dynamic calculations with equations by Scholtz and Trass [75] for the gas boundary layer, the use of a sticking coefficient for oxygen may also explain the elevated passivation threshold for molecular oxygen. Although consumption of steam in the gas boundary layer was not calculated, it can at most account for 50% reduced flux and mass transfer coefficient for supply of oxygen for active silicon oxidation compared to fluid dynamic calculations and not a factor 0.01 represented by the sticking coefficient. In present experiments with steam, the passivation threshold for the partial pressure of steam in the feed approached the stoichiometric limit for fuming of twice the saturation pressure of silicon for silica formation at the interface. Also the agreement of equilibrium modeling for experiments with steam feed rate limitation suggest that steam is scattered sufficiently frequent to the interface for most molecules to eventually be adsorbed. Flowers et al. [117]

measured an initial sticking probability of D_2O on Si(100) below 0.2 at $650\,^\circ C$ and found it to decrease with increasing temperature.

Chapter 6

Conclusion and Further Work

6.1 Conclusion

Gas refining experiments have removed boron in metallurgical grade silicon and highly boron-doped directionally solidified silicon, FBR-Si and EG-Si. The reactive gas used an oxidizing agent of CO or steam diluted in hydrogen and/or argon, which was blown as an impinging jet from a tubular lance above the melt surface. CO did not remove boron without additional hydrogen and HBO is considered the dominant product of boron removal to gas at relevant experimental conditions. CO also produces an additional byproduct of SiC particles at the melt surface. Based on dominant species from equilibrium modeling, Reactions (6.1) and (6.2) are constructed to represent equilibrium for active silicon oxidation and boron distribution as parallel processes at the gas-melt interface.

$$H_2O + [Si] \rightleftharpoons SiO + H_2 \tag{6.1}$$
$$[B] + SiO + \tfrac{1}{2} H_2 \rightleftharpoons HBO + [Si] \tag{6.2}$$
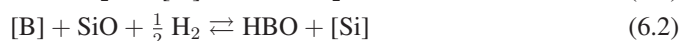
In Reaction (6.1), steam decomposes essentially stoichiometrically to SiO at the silicon surface under relevant experimental conditions, and a minor fraction of the supplied oxygen reacts with boron at ppmw levels in the melt. The highest estimate from equilibrium modeling of conditions in experiments is at $1500\,°C$ and $1\,bar$ hydrogen, for which 1% of the oxygen reacts with boron at $29\,ppmw$. Boron distributes to a factor 2.2 higher mole fraction in the gas than the melt with $0.016\,bar$ SiO in and $1\,bar$ hydrogen at $1500\,°C$ in Reaction (6.2). Boron is enriched to a factor 162 higher ratio between HBO and SiO fractions in the gas than [B] and [Si] in the melt with $1\,bar$ hydrogen at $1500\,°C$. The above ratios decreases with increasing temperature, except the distribution coefficient may be increased if steam supply and the resulting SiO partial pressure is increased simultaneously.

The experiment with the highest gas flow rate and fastest supply of steam to the interface reactions achieved the highest rate of boron removal. $16 \, \mathrm{l_N/min}$ total gas flow rate of $0.032 \, \mathrm{bar}$ steam in hydrogen removed boron from $80 \, \mathrm{ppmw}$ to $0.6 \, \mathrm{ppmw}$ in $200 \, \mathrm{g}$ silicon at $1500 \, \mathrm{°C}$ during $37.4 \, \mathrm{min}$. In this time, the gas consumption was $598 \, \mathrm{normal \, l/min}$ of which $28 \, \mathrm{g}$ steam. 4% of the silicon was lost from the melt and 37% of the steam in the feed is estimated to have been supplied to the interface reactions. Regression analysis of boron concentration in samples taken during the $37.4 \, \mathrm{min}$ estimates the total mass transfer coefficient for boron removal to $50 \, \mathrm{\mu m/s}$. Most experiments used $2 \, \mathrm{l_N/min}$ total gas flow rate with total mass transfer coefficients up to $10 \, \mathrm{\mu m/s}$.

The experimental results were compared to the state of equilibrium, which was calculated progressively during refining in an equilibrium model. The amounts in one minute of gas flow and the amounts of silicon, boron, oxygen and hydrogen in the melt from the previous minute was used to calculate equilibrium amounts and compositions of the gas, melt and potentially oxides during the course of refining. The experimental results showed a significantly higher refining rate than equilibrium simulation with most literature values for thermodynamic data for HBO, so one of the lowest literature values was selected for the standard enthalpy of formation of HBO instead of tabulated values. Representative experiments and their uncertainty indicate an upper limit of $\Delta_f H_{\mathrm{HBO}}^{\ominus}(298 \, \mathrm{K}) = -248 \pm 1 \, \mathrm{kJ/mol}$, together with data in COST 507 [40] Thermochemical Database for Light Metal Alloys for the activity coefficient of boron in silicon.

Loss of steam from the feed gas to the interface is accounted for by comparing equilibrium modeling based on the feed gas to the weightloss of the crucible during experiments, which is predominantly due to active oxidation of silicon in Reaction (6.1). Using the resulting estimate for the actual supply of steam to the interface in the input of equilibrium modeling, it was shown that interface reactions in experiments were close to the equilibrium state of Reactions (6.1) and (6.2) with selected thermodynamic data. Furthermore, there was a constant ratio of 80% between the boron removal rates from experiments and equilibrium simulations in spite of an increasing gas flow rate between the experiments. The rate determining step for boron removal was thus found to be supply of steam as the oxidizing agent to the interface, like for active silicon oxidation, and no resistance was identified for the actual transport of boron or its reactions. Using equilibrium expressions for interphase Reactions (6.1) and (6.2), an analytical expression for the mass transfer coefficient for boron removal was derived in Equation (5.55) as function of the supply of steam to the interface.

About 50% of the steam is lost by fuming in Reaction (6.3). The fuming occurs in the gas phase as SiO diffuses from the interface and towards an increasing concentration of steam. Of the remaining 50% steam, not all will potentially diffuse to the interface. A fraction of the fed steam may pass over the surface and remain unreacted in the gas flow. This stoichiometric fraction of 50% of the steam in the feed gas reacted at the melt surface in several experiments. In these experiments the flow of steam in the bulk feed gas was rate determining. The steam supply fraction decreased further in experiments with increased gas flow rates, as the rate

determining step transitioned to diffusion of steam to the interface. A low gas flow rate (in terms of requirements for rapid boron removal) was used in an experiment with bubbling to avoid excessive splashing, and the rate of boron removal was accordingly an order of magnitude lower than what was achieved without splashing by blowing the gas from a lance above the melt surface.

$$H_2O + SiO = SiO_2 \text{ (s)} + H_2 \tag{6.3}$$

Steam as the oxidizing agent is typically diluted in the gas flow in order to avoid passivation, at which a silica layer form directly on the surface of the melt and acts as a barrier between the gas and the melt which effectively stop boron removal in the covered area of the surface. The estimated steam supply at the onset of passivation observed in experiments approximated the saturation pressure of SiO, representing oxygen saturation at the melt surface at which silica becomes stable according to Reaction (6.4).

$$2 SiO = [Si] + SiO_2 \text{ (s/l)} \tag{6.4}$$

The partial pressure of steam set in the feed gas was over twice the saturation pressure of SiO at the threshold for passivation in experiments due to at least 50% loss of steam by fuming in Reaction (6.3) and additional diffusion resistance. The passivation threshold for the partial pressure of steam was strongly increased at elevated melt temperatures, like the saturation pressure of SiO. The passivation threshold for steam in the feed gas was for low diffusion resistances at 2 normal l/min observed to be 0.060-0.065 bar gas flow rate at $1500 \,°\text{C}$ melt temperature, between 0.40-0.50 bar at $1700 \,°\text{C}$ and likely above 1 bar at $1800 \,°\text{C}$. Excessive fuming at high steam fractions caused experimental challenges, as deposits of fume above the melt may fall onto the melt and partly cover the surface.

Important parameters identified in experimental series are gas composition, melt temperature, gas flow rate and interface area, which is reduced by surface coverage. For impinging jet gas blowing, the lance exit should also be sufficiently close to the melt surface. The effect of parameters is further presented from the viewpoint of optimization to provide a foundation for upscaling towards an industrial process.

Steam appears to be particularly efficient for boron removal with a reaction order of around 1.5 in argon, as it supplies both oxygen and hydrogen necessary for forming HBO gas. The gas consumption required to remove a given amount of boron may be minimized by maximizing the steam content in the gas. Maximization towards atmospheric steam partial pressure requires elevation of the temperature of the melt to avoid passivation. Hydrogen contributes to reduce the loss of silicon per amount of boron removed, although at the expense of lower refining rate if substituting steam. Decreasing temperature has the same effect by increasing the stability of HBO compared to SiO, and increasing the temperature is only beneficial for the rate of boron removal if the partial pressure of steam is increased simultaneously.

For the selected gas composition, the rate of boron removal is most directly dependent on the gas flow rate and supply of steam to the interphase reactions. Equilibrium modeling is found useful for scaling the gas flow rate to the minimum requirement for removing a given amount of boron within a desirable time, taking into account a 50% or higher loss of steam by fuming and potentially diffusion resistance. Combined with boron distribution in experiments at 80% of equilibrium calculations with current data, an equilibrium simulation indicate that a 100-fold reduction in boron content (30-0.3 ppmw) may at least require $357 \text{ m}^3_\text{N}/\text{tonne}$ steam in feed per tonne of melt at 1800 °C, with 83% silicon recovery, and that pure steam may be used at atmospheric conditions without passivation at such high melt temperature. Diffusion resistances may be minimized by scaling the interface area with the gas flow rate. Steam is gradually consumed radially along the wall jet of the impinging jet flow pattern and it may be completely consumed presumably by splashing droplets in the gas flow or using a sufficiently large crucible radius, alternatively with distribution of the gas flow over several lances as mass transfer in impinging jets are fastest under the lance. Presuming that a scaled up gas flow rate further increases the rate limit for diffusion through the gas boundary layer, mass transfer in the melt may likely become rate determining for boron removal in an upscale reactor.

6.2   Further Work

The experimental conditions that appear most beneficial for achieving a high rate of boron removal with minimal gas consumption is at high melt temperatures and high fractions of steam. It is predicted that pure steam may be used with melt temperatures of $1785 - 1875$ °C for maximum boron removal rates and with no additional gases, so such conditions are proposed for further exploring the feasibility of the process. To reduce the risk of fume deposits falling onto the melt surface, it is advised to use a setup where the gas flows out to the side over the surface. This would also improve weightloss measurements for assessment of silicon oxidation as the crucible wall that may oxidize and collect fumes above the surface is minimal. Furthermore, allowing the gas to flow out over the side of the melt surface would reduce the amount of fume above the surface and allow in-situ observation of surface coverage by imaging for higher steam contents than in current experiments. It is however not know whether the surface may be observed by simple imaging for the conditions proposed for further study. Excessively heating the melt to provide a passivation threshold that is higher than the total pressure or significantly higher than the partial pressure of steam that is supplied may destabilize silica at the interface. It would be interesting to investigate whether such a strategy could effectively evaporate islands of silica from the melt surface without stopping steam feeding, and prevent build-up of silica surface coverage during refining.

Additionally, further work may assess whether splashing droplets in the gas could be used to increase the reaction area without causing surface coverage as droplets are expected to collide with fume particles. If so, a reactor may be designed based on the basic oxygen furnace for

250

removing carbon from steel or potentially as a hood that can be lowered into a ladle so that the melt surface provides the bottom sealing. Such a hood would contain the lance and off-gas channel, and a heating element attached under the hood could heat the melt near the surface.

For impinging jet experiments without splashing, steam supply could be further investigated to provide relationships between gas flow rate, crucible diameter, lance diameter and steam consumption. It would be interesting to assess whether a low diffusion resistance for steam may be maintained during upscaling simply by increasing the crucible radius within practical limits. Such relationships may be predicted in a CFD model for the gas phase with the aim to including reactions of fuming and at the melt surface, which is being constructed by PhD candidate Mathieu Vadon at the EPM group of the SiMaP laboratory in Grenoble. Like the model by Næss et al. [31], the model by Vadon will also likely be useful for understanding active oxidation and fuming, as a determining part in the boron removal process. As melt mass transfer is suggested as a likely rate determining candidate in upscale reactors, concepts for stirring the melt like induction or bubbling a portion of the steam may prove important in further development and could be included in a complete model of the process.

Both present experiments and plasma refining experiments are intended for verification of the model by Vadon, and it may prove useful for assessing the effect of plasma species. The high temperature of the plasma may potentially destabilize silica sufficiently for significantly suppressing fuming and increasing the steam supply fraction above 50%. However, gas expansion also causes higher velocities at increased temperatures and a larger fraction of steam could remain unreacted in plasma refining. These effects could be verified by comparing experiments of reactive gas and plasma refining directly for similar geometries and parameters.

In the present study, the effect of lance diameter on the diffusion of steam should have been investigated for a gas flow rate for which the rate determining step is diffusion of steam to the interface and not the flow of steam in the feed gas as concluded for the "d_c" series. A more accurate determination of the reaction order for steam at the interface would also be desirably, which would require more accurate and reliable determination of the weightloss or another method for measuring the rate or amount of silicon oxidation. It would also be desirable to compare the reaction order for steam in hydrogen to that in argon and equilibrium considerations in Section 5.4.1. Finally, the effect of hydrogen produced by fuming could be further assessed without hydrogen in the feed. It may contribute to reduce the concentration gradient from the interface and thus slow down diffusion of hydrogen away from the interface, so that the hydrogen produced at the interface remains at a higher partial pressure than it would without hydrogen production from fuming.

It is expected that loss of silicon from the melt can be suppressed by using SiO in hydrogen as feed gas, and the feasibility of such a concept could be tested. Only minor amounts of SiO and hydrogen would be consumed, but set the environment for distribution of boron to the gas (Reaction (6.2)). Silicon would still be consumed in production of the SiO precursor. SiO gas must be produced in-situ at high temperature, presumably from silica and silicon in a heated chamber through which the hydrogen flow is blown before feeding to the melt.

As a first assessment of feasibility, it should be considered whether SiO production could be fast enough to saturate the high gas flow rates required for rapid boron removal within practical limits to the scale of the chamber. To avoid condensation of SiO prior to feeding, the temperature of the downstream gas line must be maintained higher than the temperature of silica and silicon form which the SiO gas is saturated. Also the temperature of the melt should be higher for avoiding passivation. Instead of fuming, SiO is expected to condense back into silica and silicon upon cooling. If the condensation could be controlled, it could be investigated whether this condensate could be reused to produce SiO. The condensate would however most likely contain boron like the fumes from present experiments, and boron contamination in the feed is expected to reduce its efficiency for refining. Bjerke [23] explored a similar concept in which slag refining was conducted in hydrogen atmosphere, for which boron was slowly removed from the slag at $1600\,^{\circ}\mathrm{C}$. Higher removal rates could possibly be achieved at higher gas flow rates of hydrogen.

In summary, there are still concepts and relations that can be explored in laboratory experiments in order to aid the selection of a basis for upscaling towards an industrial process. Upscaling would require careful assessment of safety issues and solutions considering the risk of condensation of steam and handling of the off-gas with both silica fume, hydrogen and potentially steam which might remain at high concentrations in case of large surface coverage. Hydrogen would preferably be burned in a controlled manner close to the reactor and it should be assessed if this can be done safely with fume particles in the gas. The released heat may be recovered during cooling of the gas before filtering and used to aid heating of water for evaporation to the steam feed gas.

The process appears to be suitable for integration in any part of a refining route from MG-Si to SoG-Si. Impurities in MG-Si were not found detrimental to boron removal in experiments. An initial surface coverage could be evaporation at lower temperatures than those proposed for further optimizing the process and the time required to heat the melt may prove sufficient for cleaning the surface. It could thus prove possible to refine boron directly after oxidizing ladle refining of silicon tapped from the electric arc furnace, providing the top slag of impurities is mechanically removed. A benefit of integrating gas refining early in the refining route is that the starting material have not accumulated a high value through previous refining processes and the loss of silicon represents a lower cost than it would later in the route. Alternatively, boron removal could be conducted after an initial solidification and potentially leaching process for removing metal impurities. The risk of surface coverage could then be minimized as segregation would remove metals which potentially could form oxides that can not be evaporated in the process. Any such oxides were however not observed to persist in noticeable amounts on the surface of MG-Si in experiments. Heat could be conserved if combined with other melt refining processes like electron beam melting for phosphorus removal, for instance in a route of leaching MG-Si, electron beam melting, gas refining, carbide settling during cooling and finally directional solidification. Any surface coverage from gas refining is expected to remain during directional solidification and would be removed with the top cut.

References

[1] H. Graßl, J. Kokott, M. Kulessa, J. Luther, F. Nuscheler, R. Sauerborn, H.-J. Schellnhuber, R. Schubert, and E.-D. Schulze. *World in Transition - Towards Sustainable Energy Systems*. German Advisory Council on Global Change. Earthscan, London, 2003. ISBN 1-84407-882-9. Pages 3, 94.

[2] P. Lorenz, D. Pinner, and T. Seitz. The economics of solar power. *McKinsey Q.*, June 26, 2008.

[3] D. Lynch. Winning the Global Race for Solar Silicon. *Sol. Cell Silicon*, 61(11):41–48, 2009.

[4] SEMI. *Metallurgical-grade Silicon Making Inroads in PV*, July 9, 2015. URL `http://www.semi.org/en/IndustrySegments/Materials/p044005`.

[5] B. Ceccaroli and O. Lohne. Solar grade silicon feedstock. In A. Luque and S. Hegedus, editors, *Handbook of Photovoltaic Science and Engineering*, pages 169–217. John Wiley & Sons, 2003. ISBN 9780470721698. URL `http://dx.doi.org/10.1002/9780470974704.ch5`.

[6] B. R. Bathey and M. C. Cretella. Review Solar-grade silicon. *J. Mater. Sci.*, 17(11): 3077–3096, 1982.

[7] Y. Delannoy. Purification of silicon for photovoltaic applications. *J. Cryst. Growth*, 360:61–67, 2012.

[8] A. F. B. Braga, S. P. Moreira, P. R. Zampieri, J. M. G. Bacchin, and P. R. Mei. New processes for the production of solar-grade polycrystalline silicon: A review. *Sol. Energy Mater. Sol. Cells*, 92(4):418–424, 2008.

[9] Elkem AS. *Elkem Solar Fiskaa*, September 16, 2011. URL `https://www.elkem.com/elkem-solar/about-elkem-solar/elkem-solar-plant-kristiansand/`.

[10] N. Yuge, H. Baba, Y. Sakaguchi, K. Nishikawa, H. Terashima, and F. Aratani. Purification of metallurgical silicon to solar grade. *Sol. Energy Mater. Sol. Cells*, 34:243–250, 1994.

[11] N. Nakamura, H. Baba, Y. Sakaguchi, and Y. Kato. Boron Removal in Molten Silicon by a Steam-Added Plasma Melting Method. *Mater. Trans.*, 45(3):858–864, 2004.

[12] R. Einhaus, J. Kraiem, F. Cocco, Y. Caratini, D. Bernou, D. Sarti, G. Rey, R. Monna, C. Trassy, J. Degoulange, Y. Delannoy, S. Martinuzzi, I. Périchaud, M. C. Record, and P. Rivat. PHOTOSIL - Simplified Production of Solar Silicon from Metallurgical Silicon. In *Proc. 21st European Photovoltaic Solar Energy Conference and Exhibition*, Dresden, September, 2006.

[13] C. Alemany, C. Trassy, B. Pateyron, K.-I. Li, and Y. Delannoy. Refining of metallurgical-grade silicon by inductive plasma. *Sol. Energy Mater. Sol. Cells*, 72 (1-4):41–48, 2002.

[14] J. Kraiem, B. Drevet, F. Cocco, N. Enjalbert, S. Dubois, D. Camel, D. Grosset-Bourbange, D. Pelletier, T. Margaria, and R. Einhaus. HIGH PERFORMANCE SOLAR CELLS MADE FROM 100THE PHOTOSIL PROCESS. In *35th IEEE Photovoltaic Specialists Conference (PVSC 2010)*, pages 1427–1432, Honolulu, June 2010. IEEE. ISBN 9781424458905.

[15] C. P. Khattak, D. B. Joyce, and F. Schmid. Production of Solar Grade (SoG) Silicon by Refining Liquid Metallurgical Grade (MG) Silicon. Technical report, National Renewable Energy Laboratory, Golden, 2001. Pages 2, 6, 8-11, 16, 21-38.

[16] A. Schei, J. K. Tuset, and H. Tveit. *Production of High Silicon Alloys*. TAPIR akademisk forlag, Trondheim, 1998. ISBN 82-519-1317-9. Pages 29, 270-272.

[17] E. F. Nordstrand and M. Tangstad. Removal of Boron from Silicon by Moist Hydrogen Gas. *Metall. Mater. Trans. B*, 43(4):814–822, 2012.

[18] J. Altenberend. *Kinetics of the plasma refining process of silicon for solar cells: experimental study with spectroscopy*. PhD thesis, Université de Grenoble, Grenoble, 2012.

[19] L. K. Jakobsson. *Distribution of boron between silicon and CaO-SiO_2, MgO-SiO_2, CaO-MgO-SiO_2 and CaO-Al_2O_3-SiO_2 slags at $1600°C$*. PhD thesis, NTNU, Trondheim, 2013.

[20] H. Nishimoto and K. Morita. The Rate of Boron Elimination from Molten Silicon by Slag and Cl_2 gas Treatment. In *Supplemental Proceedings: Materials Processing and Energy Materials*, volume 1, pages 701–708. John Wiley & Sons, March, 2011. ISBN 9781118062111. URL http://dx.doi.org/10.1002/9781118062111.ch81.

[21] T. Buseth, K. Friestad, and P. Runde. *US Patent 7,232,544*. Google Patents, 2007. URL https://www.google.com.ar/patents/US7232544.

[22] C. P. Khattak, D. B. Joyce, and F. Schmid. A simple process to remove boron from metallurgical grade silicon. *Sol. Energy Mater. Sol. Cells*, 74(1-4):77–89, 2002.

[23] H. Bjerke. Removal of boron from silicon by slag treatment and by evaporation of boron from slag in hydrogen atmosphere. Master's thesis, NTNU, Trondheim, 2012.

[24] K. Suzuki, K. Sakaguchi, T. Nakagiri, and N. Sano. Gaseous Removal of Phosphorus and Boron from Molten Silicon. *J. Jpn. Inst. Met.*, 54(2):161–167, 1990.

[25] K. Suzuki, T. Kumagai, and N. Sano. Removal of Boron from Metallurgical-grade Silicon by Applying the Plasma Treatment. *ISIJ Int.*, 32(5):630–634, 1992.

[26] A. Yvon, E. Fourmond, C. Ndzogha, Y. Delannoy, and C. Trassy. Inductive Plasma Process for Refining of Solar Grade Silicon. In *EPM 2003 4th International Conference on Electromagnetic Processing of Materials*, pages 125–130, Lyon, September, 2003. Forum Editions. URL `https://hal.archives-ouvertes.fr/hal-00551473/file/Inductive_Plasma_Process_For_Refining_Of_Solar_Grade_Silicon.pdf`.

[27] J. Van Den Avyle, P. Ho, and J. M. Gee. Silicon Purification Melting for Photovoltaic Applications. Technical report, Sandia National Laboratories, Albuquerque, 2000. Pages 9-10, 25-27.

[28] H. C. Theuerer. Removal of Boron from Silicon by Hydrogen Water Vapor Treatment. *J. Met.*, pages 1316–1319, 1956.

[29] J. Amouroux, F. Slootman, N. Madigou, T. Roger, and D. Morvan. CONTROL OF THE PLASMA REFINING OF MATERIALS BY COMPUTER ANALYSIS USING AN OPTICAL FIBER, SPECTROMETER AND O.M.A. In K. Akashi and A. Kinbara, editors, *8th INTERNATIONAL SYMPOSIUM ON PLASMA CHEMISTRY*, volume 1, pages 1868–1873, Tokyo, September, 1987. International Union of Pure and Applied Chemistry.

[30] K. Tang, S. Andersson, E. Nordstrand, and M. Tangstad. Removal of Boron in Silicon by H_2-H_2O Gas Mixtures. *JOM*, 64(952-956):814–822, 2012.

[31] M. K. Næss, J. E. Olsen, S. Andersson, and G. Tranell. Parameters Affecting the Rate and Product of Liquid Silicon Oxidation. *Oxid. Met.*, 82:395–413, 2014.

[32] J.-j. Wu, W.-h. Ma, B. Yang, Y.-n. Dai, and K. Morita. Boron removal from metallurgical grade silicon by oxidizing refining. *Trans. Nonferrous Met. Soc. China*, 19(2):463–467, 2009.

[33] B. P. Lee, H. M. Lee, D. H. Park, J. S. Shin, T. U. Yu, and B. M. Moon. Refining of MG-Si by hybrid melting using steam plasma and EMC. *Sol. Energy Mater. Sol. Cells*, 95(1):56–58, 2011.

[34] M. Vadon, C Chatillon, and I. Nuta. Données thermodynamiques nécessaires à la compréhension du procédé de purification du silicium vis-à-vis de l'impureté bore. In *Poster session of GDR ThermaTHT 2015*, Annecy, January, 2015.

[35] R. Noguchi, K. Suzuki, F. Tsukihashi, and N. Sano. Thermodynamics of Boron in a Silicon Melt. *Metall. Mater. Trans. B*, 25B(6):903–907, 1994.

[36] M. Tanahashi, T. Fujisawa, and C. Yamauchi. Activity of Boron in Molten Silicon. *Shigen-to-Sozai*, 114:807–812, 1998.

[37] G. Inoue, T. Yoshikawa, and K. Morita. Effect of Calcium on Thermodynamic Properties of Boron in Molten Silicon. *High Temp. Mater. Proc.*, 22(3-4):221–226, 2003.

[38] H. Dalaker. THERMODYNAMIC COMPUTATIONS OF THE INTERACTION CO-EFFICIENTS BETWEEN BORON AND PHOSPHORUS AND COMMON IMPU-RITY ELEMENTS IN LIQUID SILICON. *Comp. Methods Mat. Science*, 13(3):407–411, 2013.

[39] K. Tang, E. J. Øvrelid, G. Tranell, and M. Tangstad. A Thermochemical Database for the Solar Cell Silicon Materials. *Mater. Trans.*, 50(8):1978–1984, 2009.

[40] S. Fries and H. L. Lukas. In I. Ansara, A. T. Dinsdale, and M. H. Rand, editors, *COST 507: Thermochemical Database for Light Metal Alloys*, volume 2, pages 126–127, Belgium, 1998. European Commission. ISBN 92-828-3902-8.

[41] J. Safarian, K. Tang, K. Hildal, and G. Tranell. Boron Removal from Silicon by Humidified Gases. *Metall. Mater. Trans. E*, 1(1):1–7, 2014.

[42] R. R. Dirkx and K. E. Spear. Optimization of thermodynamic data for silicon borides. *Calphad*, 11(2):167–175, 1987.

[43] T. Yoshikawa and K. Morita. Thermodynamic property of B in molten Si and phase relations in the Si-Al-B system. *Mater. Trans.*, 46(6):1335–1340, 2005.

[44] M. W. Chase, Jr., C. A. Davies, J. R. Downey, Jr., D. J. Fruip, R. A. McDonald, and A. N. Syverud. *NIST JANAF THERMOCHEMICAL TABLES 1985*. National Institute of Standards and Technology, Gaithersburd, 1985. URL http://kinetics.nist.gov/janaf/.

[45] L. V. Gurvich, I. V. Veyts, and C. B. Alcock. *Thermodynamic Properties of Individual Substances. Vol. 3, Elements B, Al, Ga, In, Tl, Be, Mg, Ca, Sr, Ba and their Compounds, Part 1, Methods and Computation*. CRC Press, Reading, 1994. ISBN 0-8493-9926-2.

[46] L. N. Gorokhov, S. V. Polisadin, and A. M. Emelyanov. Theses of the reports. In *XIII AllUnion Conference on calorimetry and chemical thermodynamics*, page 58, Krasnoyarsk, 1991.

[47] N. S. Jacobson and D. L. Myers. High-Temperature Vaporization of B_2O_3(l) under Reducing Conditions. *J. Phys. Chem. B*, 115(45):13253–13260, 2011.

[48] M. Farber and M. A. Frisch. The thermodynamics of several light element high temperature species. In H. V. Kehiaian, editor, *Proceedings of the First International Conference on Calorimetry and Thermodynamics*, page 443, Warsaw, September, 1969. PWN Polish Scientific Publ.

[49] J. D. Dill, P. v. R. Schleyer, and J. A. Pople. Molecular orbital theory of the electron structure of organic compounds. XXIV. Geometries and energies of small boron compounds. Comparisons with carbocations. *J. Am. Chem. Soc.*, 97(12):3402–3409, 1975.

[50] X. Duan, D. P. Linder, M. Page, and Soto M. R. Structures and thermochemistry of $BH_lF_m(OH)_n$ and several XYBO compounds at the G-2 level of theory. *J. Mol. Struct. (Theochem)*, 465(2-3):231–242, 1999.

[51] M. Page. Multireference Configuration Interaction Study of the Reaction $H_2 + BO \rightarrow H + HBO$. *J. Phys. Chem.*, 93(9):3639–3643, 1989.

[52] Outotec. *HSC CHEMISTRY*, July 28, 2015. URL http://www.outotec.com/en/Products--services/HSC-Chemistry/.

[53] E. Fourmond, C. Ndzogha, D. Pelletier, Y. Delannoy, C. Trassy, Y. Caratini, G. Baluais, R. Einhaus, S. Martinuzzi, and I. Perichaus. REFINING OF METALLURGICAL SILICON FOR CRYSTALLINE SOLAR CELLS. In *Proceedings of the 19th European Photovoltaic Solar energy Conference*, pages 1017–1020, Paris, June, 2004. ETA-Florence. ISBN 3-936338-14-0.

[54] I. Sulentic. Removal of Boron from Silicon by Gas refining with Water and Hydrogen. Master's thesis, NTNU, Trondheim, 2012.

[55] M. K. Næss. *Mechanisms and kinetics of liquid silicon oxidation*. PhD thesis, NTNU, Trondheim, 2013.

[56] T. A. Engh. *Principles of Metal Refining*. Oxford University Press, New York, 1992. ISBN 0-19-856337-X. Pages 71-72, 114, 116, 171-178, 181-183, 206-207, 244-245, 322, 331.

[57] A. Çiftja. *Solar silicon refining; Inclusions, settling, filtration, wetting*. PhD thesis, NTNU, Trondheim, 2009.

[58] G. L. Harris. Density of SiC. In G. L. Harris, editor, *Properties of Silicon Carbide*, page 3, London, 1995. INSPEC, the Institution of Electrical Engineers. ISBN 0 85296 870 1.

[59] I. Štich, R. Car, and M. Parrinello. Bonding and disorder in liquid silicon. *Phys. Rev. Lett.*, 63(20):2240–2243, 1989.

[60] M. Kadkhodageigi, J. Safarian, H. Tveit, M. Tangstad, and S. T. Johansen. Removal of SiC particles from solar grade silicon melts by imposition of high frequency magnetic field. *Trans. Nonferrous Met. Soc. China*, 22(11):2813–2821, 2012.

[61] A. C. Akhavan. (January 12, 2014). *Overview of Silica Polymorphs*, July 28, 2015. URL http://www.quartzpage.de/gen_mod.html.

[62] T. Ikeda and M. Maeda. Elimination of Boron in Molten Silicon by Reactive Rotating Plasma Arc Melting. *Mater. Trans.*, 37(5):983–987, 1996.

[63] W. R. Imler, R. E. Haun, R. A. Lampson, M. Charles, and P. Meese. EFFICACY OF PLASMA ARC TREATMENT FOR THE REDUCTION OF BORON IN THE REFINING OF SOLAR-GRADE SILICON. In *37th IEEE Photovoltaic Specialists Conference (PVSC)*, pages 3435–3439, Seattle, June, 2011. IEEE. ISBN 978-1-4244-9966-3.

[64] G. Flamant, V. Kurtcouglu, J. Murray, and A. Steinfeld. Purification of metallurgical grade silicon by a solar process. *Sol. Energy Mater. Sol. Cells*, 90(14):2099–2106, 2006.

[65] J. S. Gulliver. *Introduction to Chemical Transport in the Environment*. Cambridge University Press, New York, 2007. ISBN 978-0-521-85850-2. Pages 212-214.

[66] R. B. Bird, W. E. Stewart, and E. N. Lightfoot. *Transport Phenomena*. John Wiley & Sons, New York, 2nd edition, 2007. ISBN 978-0-470-11539-8. Pages 513-537.

[67] J. Degoulange. *Purification et caractérisations physico-chimiques et électriques de silicium d'origine métallurgique destiné à la conversion photovoltaïque*. PhD thesis, INSTITUT NATIONAL POLYTECHNIQUE DE GRENOBLE, Grenoble, 2008.

[68] S. K. Upadhyay. *Chemical Kinetics and Reaction Dynamics*. Springer, New York, 2006. ISBN 1-4020-4546-8. Pages 1-7.

[69] C. Alemany, K.-I. Li, Y. Delannoy, B. Pateyron, P. Proulx, D. Morvan, and C. Trassy. PLASMA REFINING OF METALLURGICAL SILICON: THERMODYNAMIC AND CHEMICAL ASPECTS. In P. Fauchais, editor, *Progress in Plasma Processing of Materials 2003*, page 717, Stasbourg, June, 2002. Begell House. ISBN 1-56700-192-0.

[70] O. Levenspiel. *Chemical Reaction Engineering*. John Wiley & Sons, 3rd edition, 1999. ISBN 978-0-471-25424-9. Page 535.

[71] H. Baba, K. Hanazawa, N. Yuge, Y. Sakaguchi, H. Terishima, and F. Aratani. Metallurgical Purification for Production of Solar Grade Silicon from Metallic Grade Silicon. In P. Helm, H. A. Ossenbrink, W. Freieslenben, and W. Palz, editors, *13th European Photovoltaic Solar Energy Conference*, Nice, October, 1995. Earthscan/James & James. ISBN 9780952145271.

[72] T. L. Bergman, A. S. Lavine, F. P. Incropera, and D. P. DeWitt. *Fundamentals of Heat and Mass Transfer*. John Wiley & Sons, Hoboken, 7th edition, 2011. ISBN 13 978-0470-50197-9. Page 477.

[73] N. Zuckerman and N. Lior. Jet Impingement Heat Transfer: Physics, Correlations, and Numerical Modeling. *Adv. Heat Transfer*, 39:565–631, 2006.

[74] M. T. Scholtz and O. Trass. Mass transfer in the laminar radial wall jet. *AIChE J.*, 9 (4):548–554, 1963.

[75] M. T. Scholtz and O. Trass. Mass transfer in a nonuniform impinging jet: Part II. Boundary layer flow-mass transfer. *AIChE J.*, 16(1):90–96, 1970.

[76] C. Wagner. Passivity during the Oxidation of Silicon at Elevated Temperatures. *Metall. Mater. Trans. B*, 29(9):1295–1297, 1958.

[77] E. T. Turkdogan, P. Grieveson, and L. S. Darken. Enhancement of diffusion-limited rates of vaporization of metals. *J. Phys. Chem.*, 67(8):1647–1654, 1963.

[78] M. Ratto, E. Ricci, E. Arato, and P. Costa. Oxidation of Metals with Highly Reactive Vapors: Extension of Wagner Theory. *J. Appl. Phys.*, 32B(5):903–911, 2001.

[79] J. W. Hinze and H. C. Graham. The Active Oxidation of Si and SiC in the Viscous Gas-Flow Regime. *J. Electrochem. Soc.*, 123(7):1066–1073, 1976.

[80] K. Hildal. *Steam explosions during granulation of Si-rich alloys: Effect of Ca- and Al additions*. PhD thesis, NTNU, Trondheim, 2002.

[81] E. Arato, E. Ricci, and P. Costa. Analysis of Oxygen-Condensate Interactions in Metal Powder Production: Sprayed Particles in a Carrier Gas Phase. *Ind. Eng. Chem. Res.*, 48(7):3649–3656, 2009.

[82] N. E. Kamfjord, H. Tveit, M. K. Næss, and E. H. Myrhaug. Mechanisms of NO Formation during SiO Combustion. In T. Jiang, J.-Y. Hwang, P. Masset, O. Yucel, R. Padilla, and G. Zhou, editors, *3rd International Symposium on High-Temperature Metallurgical Processing*, pages 401–409, Florida, March, 2012. John Wiley & Sons. ISBN 9781118364987. URL http://dx.doi.org/10.1002/9781118364987.ch49.

[83] G. D. Ulrich. Theory of Particle Formation and Growth in Oxide Synthesis Flames. *Combust. Sci. Technol.*, 4(1):47–57, 1971.

[84] J. R. Engstrom, D. J. Bonser, M. M. Nelson, and T. Engel. The reaction of atomic oxygen with Si(100) and Si(111). I: Oxide decomposition, active oxidation and the transition to passive oxidation. *Surf. Sci.*, 256(3):317–343, 1991.

[85] J. R. Engstrom, D. J. Bonser, and T. Engel. The reaction of atomic oxygen with Si(100) and Si(111): II. Adsorption, passive oxidation and the effect of coincident ion bombardment. *Surf. Sci.*, 268(1-3):238–264, 1992.

[86] J. J. Lander and J. Morrison. Low Voltage Electron Diffraction Study of the Oxidation and Reduction of Silicon. *J. Appl. Phys.*, 33(6):2089–2092, 1962.

[87] W. Haldenwanger Technische Keramik. *Ceramic Materials*, June 15, 2015. URL `http://www.haldenwanger.com/download.php?` `3033644967413862654e6d556973365931386549366a7a35536951414` `c7a30535a704953643835757273744a2f413d3d`.

[88] OGT Bad Harzburg. *The material "Quartz Glass"*. 2011.

[89] P. J. Linstrom and W. G. Mallard, editors. *NIST Chemistry WebBook, NIST Standard Reference Database Number 69*. National Institute of Standards and Technology, Gaithersburd, 2011. URL `http://webbook.nist.gov/cgi/cbook.cgi?` `ID=C7732185&Units=SI&Mask=4&Type=ANTOINE&Plot=on#ANTOINE`.

[90] Fuel Cell Technologies. Flow vs Dewpoint. In *LOW-FLOW HUMIDITY BOTTLE ASSEMBLY*, July 28, 2015. URL `http://fuelcelltechnologies.com/` `humidification-bottles/low-flow-humidity-bottle-assembly`.

[91] ABB. *Data sheet DS/A61/62-EN Rev. J*, June 30, 2015. URL `search-ext.` `abb.com/library/Download.aspx?DocumentID=DS%2fA61%` `2f62-EN&LanguageCode=en&DocumentPartId=&Action=Launch`.

[92] ABB. Flow calculator. In *Flow Measurement*, June 30, 2015. URL `http://new.` `abb.com/products/measurement-products/flow`.

[93] Alicat Scientific. *Technical Data for Alicat MC and MCR Mass Flow Controllers*, March 12, 2013. URL `http://www.alicat.com/documents/` `specifications/Alicat_Mass_Controller_Specs.pdf`.

[94] J. Fenstad. *Liquidus relations and thermochemistry within the system Fe-Mn-C-O*. PhD thesis, NTNU, Trondheim, 2000. Pages 33-43, 45-47, 54-55.

[95] Nikon. *D3200*, June 15, 2015. URL `http://www.nikonusa.com/en/` `Nikon-Products/Product/dslr-cameras/25492/D3200.html`.

[96] Goodfellow Corporation. *Boron*, June 17, 2015. URL http://www.goodfellow.cn/download/metal/%E9%AB%98%E7%BA%AF%E7%A1%BCB.pdf.

[97] Toyo Tanso. *Special Graphite*, June 15, 2015. URL http://www.ttu.com/1.Special_graphite_eg.pdf.

[98] Contec. *Amplitude EcoCloth*, July 1, 2015. URL http://www.contecinc.com/products/life-sciences/wipes/nonwoven-wipes/amplitude%28tm%29-ecocloth%28tm%29.

[99] National Institute for Standards and Technology. *Certificate of Analysis Standard Reference Material 75b*, June 16, 2015. URL https://www-s.nist.gov/srmors/certificates/57B.pdf?CFID=25485582&CFTOKEN=b19fc6678bb87079-557F4EDA-E591-D999-8EF2268FFA447012.

[100] U. S. Geological Survey. (November 7, 2014). *Diabase, W-2*, July 1, 2015. URL http://crustal.usgs.gov/geochemical_reference_standards/diabase.html.

[101] Thermo Scientific. *ELEMENT 2 & ELEMENT XR*, July 1, 2015. URL http://www.thermoscientific.com/content/dam/tfs/ATG/CMD/CMD%20Documents/BR-30027-Element-2-Element-XR.pdf.

[102] Jeol (Skandinaviska) AB. *JEOL JXA-8500F Electron Probe Micro analyzer (EPMA)*, July 2, 2015. URL http://www.material.ntnu.no/lab/material/equipment/ProdInfoEPMA.pdf.

[103] Working Group 1 of the Joint Committee for Guides in Metrology. *Evaluation of measurement data - Guide to the expression of uncertainty in measurement*, 2010.

[104] Travis Wiens. *Linear Regression with Errors in X and Y*, June 16, 2015. URL http://www.mathworks.com/matlabcentral/fileexchange/26586-linear-regression-with-errors-in-x-and-y.

[105] D York, N. M. Evensen, M. L. Martínez, and J. De Basabe Delgado. Unified equations for the slope, intercept, and standard errors of the best straight line. *Am. J. Phys.*, 72 (3):367–375, 2004.

[106] K. Mukai and Z. Yuan. Measurement of the Density of Molten Silicon by a Modified Sessile Drop Method. *Mater. Trans., JIM*, 41(2):323–330, 2000.

[107] GTT-Technologies. *ChemSheet*, July 2, 2015. URL http://gtt.mch.rwth-aachen.de/gtt-web/chemsheet.

261

[108] Microsoft. *Excel*, July 2, 2015. URL `https://products.office.com/en-us/excel`.

[109] COMSOL. *Multiphysics Software Product Suite*, July 6, 2015. URL `https://www.comsol.com/products`.

[110] H. Kobatake, H. Khosroabadi, and H. Fukuyama. Normal spectral emissivity of stable and undercooled liquid silicon using electromagnetic levitation in a dc magnetic field. *Meas. Sci. Technol.*, 22(1):015102, 2011.

[111] H. Sasaki, A. Ikari, K. Terashima, and S. Kimura. Temperature Dependence of the Electrical Resistivity of Molten Silicon. *Jpn. J. Appl. Phys.*, 34(7A):3426–3431, 1995.

[112] Y. Sato, Y. Kameda, T. Nagasawa, T. Sakamoto, S. Moriguchi, T. Yamamura, and Y. Waseda. Viscosity of molten silicon and the factors affecting measurement. *J. Cryst. Growth*, 249(3-4):404–415, 2003.

[113] J. P. Garandet. New Determinations of Diffusion Coefficients for Various Dopants in Liquid Silicon. *Int. J. Thermophys.*, 28(4):1285–1303, 2007.

[114] J. Safarian and M. Tangstad. Vacuum Refining of Molten Silicon. *Metall. Mater. Trans. B*, 43(6):1427–1445, 2012.

[115] E. Dal Martello. *Impurity distribution and reduction behavior of quartz in the production of high purity silicon*. PhD thesis, NTNU, Trondheim, 2012.

[116] M. T. Scholtz and O. Trass. Mass transfer in a nonuniform impinging jet: Part I. Stagnation Flow-Velocity and Pressure Distribution. *AIChE J.*, 16(1):82–90, 1970.

[117] M. C. Flowers, N. B. H. Jonathan, A. Morris, and S. Wright. The Adsorption and Reactions of Water on Si(100)-2 x 1 and Si(111)-7 x 7 Surfaces. *Surf. Sci.*, 351:87–102, 1996.

[118] M. Balooch, D. R. Olander, and W. J. Siekhaus. Reaction of Modulated-molecular-beam Chlorine with Polycrystalline Iron. *J. Chem. Soc., Faraday Trans. 1*, 80(1):61–71, 1984.

[119] C. R. Nave. *Frequency of Molecular Collisions*, April 16, 2015. URL `http://hyperphysics.phy-astr.gsu.edu/hbase/kinetic/frecol.html`.

[120] D. A. Labuntsov and A. P. Kryukov. ANALYSIS OF INTENSIVE EVAPORATION AND CONDENSATION. *Int. J. Heat Mass Transfer*, 22:989–1002, 1979.

[121] P. Rahimi and C. A. Ward. Kinetics of Evaporation: Statistical Rate Theory Approach. *Int. J. Thermo*, 8(1):1–14, 2005.

[122] H. Ikeda, K. Hotta, T. Yamada, S. Zaima, and Y. Yasuda. Studies on Reaction Processes of Hydrogen and Oxygen Atoms with H_2O-Adsorbed Si(100) Surfaces by High-Resolution Electron Energy Loss Spectroscopy. *Jpn. J. Appl. Phys.*, 34:2191–2195, 1995.

[123] M. L. Violanda and H. Rudolph. SiO adsorption on a p(2 x 2) reconstructed Si(100) surface. *Surf. Sci.*, 603:901–906, 2009.

Appendix A

Abstracts of Scientific Papers

Boron Removal from Silicon Melts by H$_2$O/H$_2$ Gas Blowing - Mass Transfer in Gas and Melt

Øyvind Sunde Sortland and Merete Tangstad

Abstract

Metallurgical routes for solar grade silicon production are being developed as alternatives to chemical processes for their potential to achieve cost reductions, increased production volume and reduced environmental and safety concerns. An important challenge in the development of metallurgical routes relates to the higher impurity concentrations in the silicon product, particularly for boron and other elements that are not efficiently segregated in solidification techniques. The reactive gas refining process is studied for its potential to remove boron below the solar grade silicon target concentration in a single step by blowing steam and hydrogen gas jets onto the melt surface. Boron in a silicon melt is extracted to HBO gas in parallel to active oxidation of silicon. The literature is not unified regarding the rate determining step in this process. Relevant theories and equations for gas blowing in induction furnaces are combined and used to explain mass transfer in experiments. Mass transfer in the melt and gas is investigated by comparing resistance and induction heating of the melt, and varying gas flow rate, crucible diameter, diameter of the gas lance and the position of the gas lance above the melt surface. The rate of boron removal is found to increase with increasing gas flow rate and crucible diameter. A relatively high fraction of the reactive gas is utilized in the process and supply of steam in the bulk gas is the only identified rate determining step.

Boron Removal from Silicon Melts by H$_2$O/Ar Gas Blowing

Øyvind Sunde Sortland and Merete Tangstad

Abstract

Lately, blowing steam and hydrogen onto a silicon melt has shown potential for removing boron [1] and may be utilized in a metallurgical route to silicon for solar cells. The main equilibria for boron and silicon oxidation is in this work used to predict the effect of the partial pressure of steam on the removal rate of boron in terms of the reaction order. The predictions are compared to experiments, equilibrium modeling and related literature. In experiments, the partial pressure of steam in argon was varied between $0.032\text{-}0.40\ \mathrm{bar}$ in a gas flow of $2\ \mathrm{normal\,l/min}$ blown on liquid silicon at $1973\ \mathrm{K}$ ($1700\ ^\circ\mathrm{C}$) without passivation. The increased melt temperature allowed for simultaneously increasing the partial pressure of steam without passivation and then also the rate of boron removal. Without a surplus of hydrogen, the equilibrium reaction order of steam supplied to the interface is predicted to be 1.5. It is within the uncertainty of experimental estimates, and between the mean experimental values near 2 and the value 1 reported in relevant literature. With excess hydrogen, the equilibrium analysis is consistent with the linear relationship between the rate of boron removal and the partial pressure of steam, in corresponding plasma refining studies.

References

[1] E. F. Nordstrand and M. Tangstad. Removal of Boron from Silicon by Moist Hydrogen Gas. *Metal. Mater. Trans. B*, 43(4):814–822, 2012